

THE ELECTRONIC PROPERTIES OF MULTI-WALLED  
CARBON NANOTUBES

A Thesis

Submitted to the Faculty

of

Purdue University

by

Elton Daniel Graugnard

In Partial Fulfillment of the

Requirements for the Degree

of

Doctor of Philosophy

December 2000

To  
Melanie

## ACKNOWLEDGMENTS

First and foremost, I would like to thank my advisor, Ron Reifenberger. His insight, guidance, and encouragement were invaluable. His faith in my abilities often exceeded my own. I especially thank him for funding this research. I would like to thank Prof. Supriyo Datta for his interest in my work and for the many insightful discussions regarding my experiments. I thank Prof. Ron Andres for his belief in my skills and for being a never-ending source of ideas and inspiration.

Thanks to Pedro de Pablo and Brian Walsh. Without their knowledge, skill, and help, I would not have succeeded with this project. This project was truly a joint effort between the three of us. I thank Avik Ghosh for his help in developing and explaining the theoretical aspects of this work. Thanks to Dan Lovall for teaching me and sharing his expertise with me when I first started. I also thank Michael Buss for his insight and for making my first nanotube sample. I would also like to thank the members of the Purdue Nanophysics group: Seunghun Hong, Takhee Lee, Steve Howell, André Labonté, Scott Crittenden, Laetitia Soukiassian, and Dorjderem “Derem” Nyamjav. A special thanks to Takhee and Laetitia for many useful discussions and to Derem for helping me take some of the data from the Kentucky samples. Thanks to Julio Gomez, Kevin Stavens, Victor Souw, and Sunder Balasubramanian for many helpful discussions and the use of various pieces of equipment (Sunder for the lock-in and Victor for its manual).

Finally, I thank my mom, Kathryn McFadden, for being an example of hard work and my dad, Paul Graugnard, for his interesting questions about physics. I thank all my family for the many yawns and blank stares at the mention of the word nanotube. At least they listened! Their love and support were essential. Last, but not least, I thank Melanie Mendenhall for her support and expert proof-reading skills. She motivated me to finish quickly and to leave the lab once in a while.

The collaboration with Pedro de Pablo and Julio Gomez was funded in part by a joint US-Spain Science and Technology Program (1999) project No. 99040. Partial funding was also provided by NSF grant No.9708107-DMR, and by ARO Grant No.DAAD19-99-1-0198. The MWNTs used in this study were kindly supplied by R. Smalley of Rice University and A. M. Rao of the University of Kentucky (now at Clemson University).

## PREFACE

The current interest in carbon nanotubes was sparked by their rediscovery by Iijima in 1991. [1] Since that time the study of carbon nanotubes has emerged as a fast-growing sub-field of carbon science. Over the past few years, researchers published thousands of experimental and theoretical investigations regarding carbon nanotubes. The tremendous activity surrounding nanotubes is fueled by the belief that carbon nanotubes may be key components of future carbon-based nano-electronic devices.

Measurement of the electronic transport properties of carbon nanotubes is a very active micro-field of research. Many groups are trying to determine the precise, intrinsic nature of the nanotube's electronic properties. Mintmire, Dunlap, and White's question, "Are Fullerene Tubules Metallic?" [2] sparked intense interest in nanotube transport. The possibility that nanotubes could be ballistic conductors is exciting because the device applications for a truly one-dimensional ballistic wire are virtually limitless. Another reason for interest in carbon nanotubes is that depending on its diameter and the chirality (or helicity) of its carbon bonds, a nanotube can be either metallic or semi-conducting. In fact, with a few special carbon bonds in the nanotube, it can even change from a semi-conducting to a metallic conductor. Several research groups already are studying the application carbon nanotubes in field emission flat-panel displays [3, 4] and nano-scale field-effect transistors. [5-7]

Carbon nanotube research began at Purdue University in 1993 through very early low temperature STM investigations of carbon nanotubes performed by Tom Miller of the Reifenberger Research Group. Unfortunately, Miller's findings are still considered proprietary at the time of this writing. More recently, in collaboration with the Computer and Electrical Engineering groups of Profs. Supriyo Datta and David Janes, and the Chemical Engineering group of Prof. Ron Andres, the study of carbon nanotubes has been furthered. Through this collaboration these groups developed

the techniques necessary to perform investigations on the nano-scale. This ongoing research is motivated in part by a few of the possible technological applications of carbon nanotubes. One of these applications is the use of nanotubes as probe tips in scanning probe microscopy. For this purpose, Mike Buss and Katerina Moloni developed a technique of mounting a nanotube on the end of the probe of an atomic force microscope (AFM). [8, 9] This technique provides a flexible, non-destructive probe for surface imaging. Extending the mounting technique, Buss devised a method for mounting individual nanotubes onto field emission tips. This method allowed Dan Lovall to perform UHV measurements of the electron emission properties of a mounted single-walled nanotube rope. [10, 11] Such measurements are useful for studying the electronic density of states of the nanotube and for investigating the possible application of nanotubes in low-voltage flat panel displays.

Our carbon nanotube field emission and conductance measurements are the subject of this work. Similar to Lovall's nanotube measurements, we performed field emission measurements on multi-walled nanotubes. Our field emission results indicate complex electronic structure and unstable emission currents. In order to study the use of carbon nanotubes as nanometer-sized device inter-connects and to further study their electronic properties, we developed a technique to reliably attach electrodes to individual nanotubes. This provides us with the ability to perform a variety of transport measurements. These measurements reveal interesting features of the electronic properties of carbon nanotubes. Our results from conductance measurements provide some evidence for room temperature ballistic transport and the ability to maintain very high current densities. However, the results also show multi-walled nanotubes to be electrically noisier than a normal carbon resistor, which may hinder their use in device applications where high noise levels are unacceptable. Additionally, our low temperature conductance measurements show evidence for electron-electron interactions which change the intrinsic electronic properties of the nanotube. These interactions strongly suppress the low-bias conductance at low temperatures. These experiments and the results are discussed in detail in this report.

## TABLE OF CONTENTS

	Page
LIST OF TABLES . . . . .	x
LIST OF FIGURES . . . . .	xi
LIST OF ACRONYMS . . . . .	xxi
ABSTRACT . . . . .	xxii
1 INTRODUCTION . . . . .	1
2 CARBON NANOTUBES . . . . .	4
2.1 History . . . . .	4
2.2 Physical Properties . . . . .	4
2.3 Electronic Properties . . . . .	8
2.3.1 Energy Dispersion Relations . . . . .	10
2.3.2 Density of States . . . . .	13
2.3.3 Electronic Transport . . . . .	13
3 FIELD EMISSION AND TOTAL ENERGY DISTRIBUTIONS . . . . .	20
3.1 Field Emission Microscopy . . . . .	20
3.1.1 Principles of Operation . . . . .	21
3.1.2 Total Energy Distributions . . . . .	26
3.1.3 FEM Chamber . . . . .	29
3.2 FEM of Multi-walled Nanotubes . . . . .	30
3.2.1 Sample Fabrication . . . . .	30
3.2.2 FEM of Multi-walled Nanotubes . . . . .	32
3.2.3 TEDs from Multi-walled Nanotubes . . . . .	37
4 ELECTRONIC TRANSPORT MEASUREMENTS . . . . .	43
4.1 Sample Fabrication . . . . .	44
4.1.1 Tip and Substrate Preparation . . . . .	44
4.1.2 Nanotube Selection and Placement . . . . .	46

4.1.3	Support Wire Placement . . . . .	47
4.1.4	Mask Wire Placement . . . . .	47
4.1.5	Evaporation . . . . .	48
4.1.6	Mask Removal . . . . .	48
4.1.7	Characterization . . . . .	48
4.2	Room Temperature Transport Data . . . . .	53
4.2.1	Linear I(V) . . . . .	54
4.2.2	Non-linear I(V) . . . . .	57
4.2.3	Semi-metallic I(V) . . . . .	58
4.2.4	Room Temperature Zero-bias Conductance . . . . .	59
4.2.5	Estimating the Number of Conducting Paths . . . . .	61
5	TEMPERATURE DEPENDENT TRANSPORT MEASUREMENTS . . . . .	65
5.1	Temperature Dependent Conductance Data . . . . .	66
5.2	Temperature Dependent Transport Models . . . . .	74
5.2.1	The Luttinger Liquid Model . . . . .	75
5.2.2	An Improved Model: Luttinger Plus Nanotube in Series . . . . .	81
5.3	Conductance Data from Two Other Samples . . . . .	90
5.4	Noise Measurements . . . . .	100
6	CONCLUSIONS . . . . .	111
6.1	Total Energy Distributions from Multi-walled Nanotubes . . . . .	111
6.2	Electronic Transport in Multi-walled Nanotubes . . . . .	112
6.3	Recommendations and Conclusion . . . . .	115
	BIBLIOGRAPHY . . . . .	117
	APPENDICES . . . . .	124
	Appendix A: Nanotube Density of States Program . . . . .	124
	Appendix B: The FEM Chamber and an Indexed FEM of a Pt tip . . . . .	130
	Appendix C: FEM and TEDs of a Single-walled Nanotube Rope . . . . .	134
	Appendix D: Optical Microscope used for Sample Fabrication . . . . .	136
	Appendix E: Low Temperature Sample Mount . . . . .	138

Appendix F: Investigated Transport Models . . . . .	141
F.1 Thermally Activation Conduction . . . . .	141
F.2 Simple Two-band Model . . . . .	143
F.3 A Zero in the Transmission Probability . . . . .	144
F.4 1D and 2D Hopping Conduction . . . . .	145
F.5 1D and 2D Weak Localization . . . . .	148
Appendix G: Mathematica Routine for Least-squares Fits . . . . .	155
VITA . . . . .	157

## LIST OF TABLES

Table	Page
3.1 Field emission results for carbon nanotubes. Typical values for a tungsten emitter are provided for comparison. . . . .	37
4.1 Estimates for the maximum number of layers, $N_{\text{Total}}$ , in MWNTs of various outer diameters. Also listed are the approximate number of metallic layers, $N_m$ , and semiconducting layers, $N_s$ , and the minimum energy separation of the bands for each. . . . .	63
5.1 Conductance values and fractional changes for the six samples studied.	67
5.2 Relevant parameters for the six samples studied. All parameters $\pm 0.01$ . (a) not enough low temperature data to obtain a reliable fit; (b) fits not convincing for $50 \leq x \leq 100$ . . . . .	79
5.3 Fitting parameters used with Eqn. 5.8 for the six samples studied. Conductances are in units of $G_o$ , and all parameters are $\pm 0.02$ . (a) not enough low temperature data to obtain a reliable fit. . . . .	85
5.4 Electron interaction parameters for the six samples studied, calculated from Eqns. 5.6 and 5.7 for $N=1$ . All parameters $\pm 0.02$ . (a) not enough low temperature data to obtain a reliable fit. . . . .	89

## LIST OF FIGURES

Figure	Page
2.1 Schematic representations of rolling up a graphite sheet to form a (10,0) zigzag single-walled nanotube. Rolling the sheet in the direction perpendicular to the one shown above would produce a (6,6) armchair nanotube. . . . .	5
2.2 The hexagonal basis vectors for graphite can be used to uniquely define a nanotube using the $(n, m)$ coefficients of the chiral vector, $\vec{C} = n\vec{a} + m\vec{b}$ . The chiral vector is perpendicular to the axis of the tube and has a magnitude equal to the circumference of the tube. The chiral angle, $\Theta_C$ , serves to measure the helicity of the tube. Here we show $\vec{C}$ and $\Theta_C$ for a short (15,8) nanotube. . . . .	6
2.3 Examples of single-walled nanotubes (SWNTs) and multi-walled nanotubes (MWNTs). a) An individual SWNT. b) An individual MWNT. c) A small bundle or rope of SWNTs, which may have hundreds of individual tubes. d) A bundle of a few MWNTs. . . . .	7
2.4 TEM images of un-purified arc-grown SWNTs. The dark spots are the catalytic particles used to grow the nanotubes. The image at right resolves the individual tubes of some the SWNT ropes. . . . .	9
2.5 TEM images of arc-grown MWNTs. In the left image, the individual tube diameters range from $\sim 5$ to $\sim 20$ nm. In the right image the bottom MWNT terminates abruptly with a few outer shells continuing $\sim 15$ nm longer than the inner shells. . . . .	9
2.6 a) The real space unit vectors and the hexagonal lattice unit cell. The carbon-carbon distance in graphite is $a_{C-C} \simeq 1.421$ Å. b) The corresponding reciprocal space, showing the reciprocal lattice vectors, $\vec{a}'$ and $\vec{b}'$ . . . . .	10
2.7 Energy dispersion relations for two single-walled nanotubes. Each dispersion curve represents a different value of the quantization index $\nu$ in Eqns. 2.8 and 2.10. The a) zigzag (10,0) nanotube and b) armchair (10,10) nanotube. We see that the (10,10) is metallic and that the (10,0) nanotube is a direct band gap semi-conductor. . . . .	12

2.8	The $E(k)$ and $n(E)$ for two nanotubes. Graphs a) and b) are for the (10,0) zigzag nanotube, while graphs c) and d) are for the (10,10) armchair nanotube. The band gap of the (10,0) nanotube is about $\sim 1.0$ eV. The (10,10) nanotube has a finite DOS at the Fermi level. . . . .	14
2.9	Simple diagrams illustrating transport through the quantized energy levels of a carbon nanotube. a) Illustrated is a (10,10) metallic nanotube where $\Delta\epsilon_m \simeq 0.9$ eV. The electrochemical potential of contact pad 2 is lowered by an energy, $eV_{app}$ , with respect to contact pad 1, allowing electrons to travel through the first unfilled nanotube energy levels. This pure ballistic transport would lead to the I(V) shown in b), where the conductance increases by an amount $G = G_o \equiv 2e^2/h$ as new channels open. . . . .	16
3.1	A calculation of the potential barrier deformation by the applied field and the added contribution from the electron image term. This calculation is for field emission at $-1000$ V from a tungsten tip (work function = 4.5 eV) with an end radius of 700 nm. . . . .	21
3.2	A field emission micrograph from a (110) oriented platinum tip. This image, recorded with a CCD camera, was taken with $-6500$ V applied to the tip. The rather high voltage indicates that the tip has a large end radius. . . . .	23
3.3	A Fowler-Nordheim plot for a W tip. The value of beta, as determined by iteration, is $\beta \simeq 14.3 \times 10^3 \text{ cm}^{-1}$ . The best fit here gives a value for the electric field of $3.64 \times 10^7 \text{ V/cm}$ . Thus, we determine the end radius of the emitter to be $r \simeq 140$ nm. . . . .	25
3.4	A schematic representation of the field emission illustrating the contribution of the density of states to a total energy distribution, shown at the right. . . . .	26
3.5	The TED for a tungsten FEM tip. Plotted are the detected counts versus the electron energy relative to the Fermi level ( $E_F = 0$ ). Also shown is a fit to the data, which gives a FWHM of 0.80 eV for the energy resolution of the analyzer. . . . .	28
3.6	TEM images of a typical MWNT sample used in this study. a) An individual MWNT is attached to the end of a Pt FEM tip. The portion of the MWNT extending from the tip is $\sim 3.3 \mu\text{m}$ long. b) A higher magnification of the end of the tube. The outer diameter of the tube is $\sim 25$ nm. The inset is a zoom of the end of the tube, showing an inner section $\sim 13$ nm in diameter extending $\sim 6$ nm further than the outer section. . . . .	32

3.7	TEM images of an individual MWNT mounted to the end of a Pt FEM tip. In b) the end of the nanotube seems to be cut off flat. From image c) the MWNT diameter appears to be $\sim 41$ nm. . . . .	34
3.8	A plot of constant-intensity contours of the FEM image from the MWNT shown in Fig. 3.7. The oval shape is believed to stem from the end of the MWNT not being parallel to the imaging screen. . . . .	35
3.9	A Fowler-Nordheim plot for the MWNT shown in Fig. 3.7. The slope of the MWNT data is not a straight line, indicating that the field emission process involved here may not follow the standard Fowler-Nordheim theory for a metal. . . . .	36
3.10	A schematic of the field emission current from MWNT No. 1 as a function of time. Also shown are the TEDs measured at various levels of the current. The dashed lines show the corresponding current level for each TED. These TEDs were taken at room temperature with $-280$ V applied to the MWNT. The zero of the $x$ -axis in the TED plots is set at the applied voltage, giving the Fermi energy of the tube at about $-4.52$ eV. . . . .	39
4.1	A schematic of the sample fabrication procedure showing a) the selection and removal of a MWNT, b) a MWNT adhering to the etched Pt tip, c) the transfer of the MWNT to a glass substrate d) the placement of a riser wire (wire '1') parallel to the MWNT followed by the shadow mask (wire '2') perpendicular to the MWNT, e) e-beam evaporation of a thin metal film onto the ends of the MWNT, and f) the final sample after removal of the wires. The electrical contacts to the MWNT are labeled A and B. . . . .	45
4.2	A schematic of the expected nanotube/contact junction. The smaller Ti layer, evaporated first, is shown in purple. The thicker Au layer is shown in gold. A bump is formed in the contact where the Ti and Au layers build up on top of the nanotube. . . . .	49
4.3	A $1.5\mu\text{m} \times 1.5\mu\text{m}$ AFM image of MWNT sample No. 4 buried under a Ti/Au contact pad. The image shows the substrate comprised of a glass cover slide, one of the two Ti/Au contact pads, a section of the MWNT buried under the Ti/Au film, and a section of the bare MWNT which emerges from under the Ti/Au contact pad. . . . .	50

- 4.4 TEM images of the contact interface of a MWNT rope (vertical object) sample. For this sample, a TEM grid was used as the substrate. The lower portion of the MWNT rope was exposed to the evaporator and is coated in a thin film of Ti/Au. The upper portion of the rope was covered by the shadow mask. The high magnification image shows the transition region. The rope is not crushed by the contact, and there is no apparent damage to the MWNTs. . . . . 51
- 4.5 In a), an AFM image of a typical MWNT sample, No. 40. The image shows a MWNT crossing a  $4.3 \mu\text{m}$  wide trench. The two evaporated Ti/Au contact pads lie on top of the ends of the nanotube. In b), an AFM image of MWNT sample No. 5 that has been blown apart, presumably by an electrostatic discharge. Remnants of the MWNT are found scattered throughout the image. In addition, what appears to be a local melting or peeling of the Ti/Au contact pads is evident. 52
- 4.6 In a), an AFM phase contrast image of sample No. 25 showing multiple nanotubes in a MWNT rope. Taken near the middle of the sample, this image reveals the ends of several MWNTs (see arrows), suggesting that only a few MWNTs remain continuous between the two contact pads. In b), an AFM image of sample No. 49 showing the individual MWNTs unraveling at the end of the rope. . . . . 52
- 4.7 Using a two-wire shadow-mask technique, it is possible to define a third electrode in proximity to the nanotube. In a), the third electrode makes electrical contact to the middle of MWNT sample No. 66. In b), the third electrode acts as a nearby gate. . . . . 53
- 4.8 A plot of the  $I(V)$  for MWNT sample No. 4. The theoretical resistance of 27 layers conducting in parallel, with 1 mode per layer is  $478.02 \Omega$ . The resistance from the above  $I(V)$  is  $478.06 \Omega$ . The minimum diameter of this sample was  $\sim 40 \text{ nm}$ . The sample resistance was found to change abruptly with time but remained linear. . . . . 55
- 4.9 A plot of resistance versus time for sample No. 4. The sample resistance was found to change abruptly with time. The horizontal lines represent quantized resistance values of  $1/NG_o$ , with  $N = 24, 25, 26$  and  $27$ . . . 56
- 4.10  $I(V)$  data from sample No. 3 showing diode-like behavior. The minimum diameter of this rope as determined from AFM studies was  $\sim 130 \text{ nm}$ . A plot of  $\frac{k_b T}{e} \ln(|I|)$  versus  $V$  is also provided. . . . . 57
- 4.11 The conductance from MWNT sample No. 2 showing non-ohmic conduction. The minimum diameter of this tube as determined from AFM studies is  $\sim 20 \text{ nm}$ . The zero bias conductance is  $0.44 G_o$ . Typical  $I(V)$  data obtained from this sample is also plotted. . . . . 59

4.12	The zero bias conductance at room temperature plotted in units of $G_o$ for the 22 MWNT samples measured. The conductance of $27 G_o$ for sample No. 4 is not shown. Those samples marked by stars were studied more extensively as a function of temperature as discussed in Chapter 5. . . . .	60
4.13	A plot of energy separation between conduction channels for metallic and semiconducting nanotubes as a function of layer diameter. Horizontal lines are shown for $k_b T$ of 300 K and 4.2 K. The dashed line is a plot of the maximum number of layers in a MWNT as a function of the outer diameter of the MWNT. The calculation is approximate because we assume that the minimum inner layer diameter is $\sim 0.7$ nm and that the inter-layer separation is 0.34 nm. . . . .	62
5.1	$I(V)$ plots for sample No. 29 at 3 temperatures. A non-linearity near $V = 0$ appears at low temperatures. . . . .	66
5.2	The conductance $G(V,T)$ plotted in units of $G_o$ as a function of applied bias voltage $V$ for a) sample No. 25 and b) sample No. 29. Each plot shows the data for 11 different temperatures, as labeled. . . . .	68
5.3	The conductance $G(V,T)$ plotted in units of $G_o$ as a function of applied bias voltage $V$ for a) sample No. 34 at 12 temperatures and b) sample No. 41 at 10 temperatures. . . . .	69
5.4	The conductance $G(V,T)$ plotted in units of $G_o$ as a function of applied bias voltage $V$ for a) sample No. 66 at 11 temperatures and b) sample No. 87 at 9 temperatures. In sample No. 87 the nanotube was on top of the contacts. . . . .	70
5.5	A plot of conductance versus voltage from sample No. 41 at a few low temperatures. The data shows structure in $G(V,T)$ as indicated by the arrows. An asymmetry between $G(-V,T)$ and $G(+V,T)$ is also evident. These features were observed in two of the six samples studied. . . . .	71
5.6	A plot of the symmetric part a) and the asymmetric part b) of the conductance at 4 K for sample No. 41. . . . .	72
5.7	A plot of the symmetric part a) and the asymmetric part b) of the conductance at 4 K for sample No. 87. . . . .	73
5.8	The conductance at zero-bias versus temperature for the six samples studied. . . . .	74

5.9	a) A plot of $\log(G(0,T))$ versus $\log(T)$ for the six MWNT samples studied. This plot shows the power law dependence of the zero-bias conductance. A change in the slope of the data occurs near a temperature of 100 K, possibly due to a freeze out of phonon modes. b) A plot of $\log(G(V,T))$ versus $\log(V)$ for sample No. 29 at low temperatures. The dashed line is a best fit to the voltage dependent conductance at low temperatures. The values for the slopes, obtained by least-squares fits to the data are tabulated in Table 5.2. . . . . .	78
5.10	A plot of $\log[(G/G_o)/T^\alpha]$ versus $\log(eV/k_bT)$ from the low temperature data acquired from sample No. 29 indicating that the data roughly follows a scaling relationship. The dashed line is a plot of Eqn. 5.3 with $\eta = 0.095$ . The inset is a plot of the same two quantities on a linear scale and shows the deviation of the data from theory for $10 \leq eV/k_bT \leq 100$ . . . . . .	80
5.11	A schematic illustrating the location of the resistances in our MWNT samples. . . . . .	82
5.12	A plot of $G(V,T)$ versus voltage at six temperatures for sample No. 29. The data is shown as black symbols, and the theory is shown as solid colored lines. In a) we show fits using Eqn. 5.8. For comparison, in b) we show fits using Eqn. 5.3. . . . . .	84
5.13	A plots of $G(V,T)$ versus voltage for a) sample No. 66 and b) sample No. 87. The data is shown as black symbols, and the calculations using Eqn. 5.8 are shown as solid colored lines. There is a clear asymmetry in the data for sample No. 87. . . . . .	86
5.14	A plot of conductance versus voltage for sample No. 34. In (a) the fits were calculated with $\eta$ determined at every voltage and temperature. In (b) the fits calculated with $\eta$ determined only at 0.04 V and 4 K. . . . . .	87
5.15	A plot of $\eta$ versus voltage calculated for sample No. 34 at 4 K. . . . . .	88
5.16	TEM images of CVD grown nanotubes. These MWNTs have large inner diameters and kinked wall structures, which is very different from the arc-grown MWNTs used in this study. . . . . .	91
5.17	AFM images of sample No. R5. Image a) is $6 \times 6 \mu\text{m}^2$ and image b) is $3 \times 3 \mu\text{m}^2$ . Image b) shows a zoom near one of the contacts. The large diameter of this MWNT rope and the triangular features are the result of tip dilation. . . . . .	91

5.18 Conductance data for sample No. R4. The  $G(V,T)$  data are clearly different than for the other samples. In a) the conductance is shown from 250 K to 4 K. Note that the  $y$ -axis is a log scale. The data from 10 K to 4 K is shown in b). The inset in b) shows the corresponding  $I(V)$  data. . . . . 93

5.19 Conductance at zero-bias versus temperature for sample No. R4. The  $G(T)$  data saturates at low temperatures as seen in a). In b) a plot of  $\log(G)$  versus  $\log(T)$  shows that the conductance changes by several orders of magnitude from RT to 4 K. . . . . 94

5.20  $I(V)$  data at RT for sample No. R4. A large amount of noise appears as the scatter of the data points in the high bias region of the data. For the previous samples, the data points were indistinguishable. Also there is structure in the  $I(V)$  data, indicated at several points by arrows. This  $I(V)$  data is similar to the schematic  $I(V)$  shown in Fig. 2.9. . . . . 95

5.21 Figure a) shows  $I(V)$  and  $G(V)$  data from sample No. R4 averaged for 10 data sets. The structure in the  $I(V)$  data remains and is evident in the  $G(V)$  data as peaks. In (b) the conductance is shown at positive and negative voltages. The red lines, shifted from the origin by 3 mV, serve as guides to show that the peaks are roughly symmetric. . . . . 96

5.22 a)  $G(V,T)$  data for sample No. R5. This sample showed the smallest change in conductance from RT to 4 K. In b) the current ramp was increased to show that the conductance increases with voltage similar to previous samples. . . . . 98

5.23 In a) the zero-bias conductance for sample No. R5 (shown red) is plotted versus temperature along with the six samples studied in the previous sections. This sample showed the smallest change in conductance from RT to 4 K. Figure (b) shows a plot of  $\log(G)$  versus  $\log(T)$  for comparison. . . . . 99

5.24  $V(t)$  data at RT for sample No. 29 and a 10 k $\Omega$  resistor. The difference in noise levels is obvious. Although the absolute values are slightly different, both  $y$ -axes are 0.2 mV full scale. The current applied in each case was 500 nA. Both measurements were made using the dip-probe system discussed in Appendix E. . . . . 101

5.25 Typical  $V(t)$  data taken from sample No. 66. The  $V(t)$  data shown in a) was acquired at 6 K over a 4 hour period with 500 nA applied to the sample. Figure b) shows a zoom of the region from 1.5–2.5 hours. The DC offset was subtracted from the data. The bistability is clearly evident, with each level presenting a large excess noise as well. . . . . 102

5.26	V(t) data taken from sample No. 66 showing two short lived states. The V(t) data shown in a) was acquired at 4 K over a 5 hour period with 500 nA applied to the sample. Figure b) shows a histogram of the V(t) data. The two levels of the system are seen in the histogram. The histogram also shows that the lower level had a shorter lifetime. The width of each peak is indicative of the excess noise of each level.	104
5.27	V(t) data from sample No. 66 taken at 4 K for three values of the applied current: 100 nA at bottom, 500 nA in the middle, and 1 $\mu$ A at top. The voltage scale for each plot is the same size. The fluctuations and the excess noise of the system increase with current.	105
5.28	Figure a) shows a plot of lifetimes for the up and down states ( $\tau_{up}$ and $\tau_{down}$ , respectively) versus temperature for sample No. 66. The data was taken at 500 nA applied to the sample. Figure b) shows a plot of the lifetimes versus applied current acquired at 4 K.	106
5.29	Noise power for sample No. R4 at RT in a) and 4 K in b). The data was calculated by performing an FFT on the V(t) data. The maximum frequency is one half the data acquisition rate, which here was $\sim 2$ points/sec. The red line has a slope of $-1$ .	108
5.30	Noise power $\langle S_V \rangle$ versus current at RT for sample No. 66. The data is parabolic in current, consistent with Eqn. 5.13. for $1/f$ noise. The fit was determined from a least-squares fit the a plot of $\langle S_V \rangle$ versus the square of the current. The value obtained is $0.017 \Omega^2/\text{Hz}$ , which gives a value for $A$ of $4.2 \times 10^{-10}$ .	110
B.1	A labeled photograph of the front of the FEM chamber.	130
B.2	A labeled photograph of the rear of the FEM chamber.	131
B.3	A schematic top view of the FEM chamber showing some of the details of the energy analyzer.	132
B.4	A crystallographically indexed field emission micrograph from a (110) oriented platinum tip.	133
C.1	A TEM image of a SWNT rope mounted to the end of a Pt FEM tip. The diameter of the rope (as seen in the magnified region) is $D \simeq 17$ nm. Due to vibrations of the rope in the electron beam, the end cannot be resolved.	134

C.2	The TED for a SWNT rope. Here we plot the natural log of the detected counts versus the electron energy relative to the Fermi level ( $E_F = 0$ ). By subtracting the monotonically decreasing component of the data (due to the deformed barrier width), we are able to extract the peaks shown in the inset. These peaks signal peaks in the DOS of the nanotubes in the rope. . . . .	135
D.1	A photograph of the optical microscope system used to fabricate field emission and transport samples. . . . .	136
D.2	A photograph of the holders used with the manipulators on the optical microscope stage. . . . .	137
D.3	A schematic of the stainless steel tabs used to hold the Pt FEM tips. . . . .	137
E.1	A schematic of the low temperature conductance experimental setup. A Keithley 220 current source is used to send a specified current through the sample, and a Keithley 196 DMM is used to measure the voltage drop across the sample. . . . .	139
E.2	A schematic of the sample mounting plate. The plate is electrically and thermally insulated from the steel tube with a section of Bakelite. The wires from the Keithley 220 current source and the Keithley 196 DMM travel down the tube to a hole in the tube wall. The “high” wires of each instrument are attached to the upper binding-post, while the “low” wires are routed along the back of the plate to the lower binding-post. For clarification, the instrument configuration is also shown at bottom. The diode thermometer is thermally anchored to the back of the mounting plate. . . . .	140
F.1	An Arrhenius plot for the six samples discussed in Chapter 5. . . . .	142
F.2	The conductance of the simple two-band model shown with the conductance data for sample No. 29. The schematic illustrates the model. The parameters of the fit are $C = 1.7 \times 10^{-3} (\Omega\text{eV})^{-1}$ , $\Delta = 24 \text{ meV}$ and $E_F = 0$ . . . . .	144
F.3	The conductance of a ballistic conductor at several temperatures calculated with a gap in the transmission function, using Eqn. F.3. The calculations were performed at several of the temperatures shown in Fig. 5.10 for sample No. 29. . . . .	145
F.4	In (a) a plot of $\ln(G/G_o)$ versus $T^{-1/2}$ with a fit using Eqn. F.4 for 1D. In b) the $x$ -axis is $T^{-1/3}$ with a fit using Eqn. F.4 for 2D. The conductance data shown is for sample No. 29. . . . .	147

- F.5 A plot of  $G/G_o$  versus  $T^{-1/3}$  with a least-squares fit to the low temperature data for samples No. 29 and No. 87 in (a) and sample No. 66 in b). The values of the (slope,  $y$ -intercept) determined by the fits are No. 29:(-0.55, 0.55), No. 87:(-0.21, 0.26), and No. 66:(-0.53, 1.10). . . . . 150
- F.6 A plot of  $G/G_o$  versus  $T$  for sample No. 29 with least-squares fits to the data. The red curve was fit to the data below 10K using a  $T^{-1/3}$  dependence and the blue curve was fit in the region of  $\sim 20$ –60 K using a  $T^{-1/2}$  dependence. . . . . 151
- F.7 a) A plot of  $G/G_o$  versus  $\log(T)$  with a fit to the low temperature data for sample No. 29. In b) we show the same fit on a plot of  $G/G_o$  versus  $T$ . The parameters used in the fits are discussed in the text. . . . . 152
- F.8 In a) we plot  $G/G_o$  versus  $\log(T)$  with a fit to the low temperature data for sample No. 66. Figure b) shows the same fit of a linear scale. The parameters used in the fits are discussed in the text. . . . . 153

## LIST OF ACRONYMS

Acronyms used in this document:

AFM	Atomic Force Microscopy
CSA	Cylindrical Sector Analyzer
CVD	Chemical Vapor Deposition
DOS	Density of States
FEM	Field Emission Microscopy
FEED	Field Emission Energy Distribution
FIM	Field-Ion Microscopy
LL	Luttinger Liquid
MCP	Multi Channel Plate
MWNT	Multi-walled Carbon Nanotube
RT	Room Temperature
RTN	Random Telegraph Noise
STM	Scanning Tunneling Microscopy
SWNT	Single-walled Carbon Nanotube
TED	Total Energy Distribution
TEM	Transmission Electron Microscopy

## ABSTRACT

Graugnard, Elton D., Ph.D., Purdue University, December, 2000. The Electronic Properties of Multi-walled Carbon Nanotubes. Major Professor: Ronald G. Reifenberger.

Many of the physical and electronic properties of multi-walled carbon nanotubes are not well understood. Theoretical considerations of their electronic properties predict behavior characteristic of low-dimensional structures, such as the quantization of energy levels and strong electron-electron interactions. Using energy-resolved field emission, we obtained electron energy distributions from multi-walled carbon nanotubes. The measured energy distributions indicate complex yet discrete energy levels in multi-walled carbon nanotubes. In addition, the emission current is found to fluctuate in time.

To determine the source of the field emission current fluctuations and to study the fundamental electronic properties of multi-walled carbon nanotubes, we performed electronic transport measurements. For these measurements, we developed a technique for contacting the nanotubes. Measurements of the conductance at room temperature on the resulting samples displays a large amount of noise, indicating that the current fluctuations are intrinsic to multi-walled nanotubes. Low temperature conductance measurements provide evidence of a non-Fermi electron behavior known as a Luttinger liquid. The measured conductance contains contributions from the nanotube-contact interface and from the nanotube itself.

## 1. INTRODUCTION

Carbon nanotubes<sup>1</sup> are known to have very interesting electronic properties. [2, 13, 14] From a scientific standpoint, they may represent a physical realization of a one-dimensional (1D) electronic system. The relatively simple, graphite-like structure of the nanotube has led to many predictions for single-walled nanotubes (SWNTs) [2, 15–28] and multi-walled nanotubes (MWNTs). [19, 29] One exciting prediction is that carbon nanotubes can be quantum ballistic conductors with coherence lengths of several microns. [23] This prediction, based on the unique electronic band structure of the carbon nanotube, has direct implications for the use of nanotubes in future nano-electronic devices.

Given the nanometer-sized structure of the carbon nanotube, testing the predictions made for its electronic properties is an interesting problem. Two successful techniques used to test these predictions are scanning tunneling microscopy (STM) and electronic transport measurements. Past STM measurements were performed on nanotubes dispersed from suspension onto conducting substrates. [30–34] For the transport measurements, one major challenge in probing the electronic structure is how to reliably attach current and voltage leads to nanotubes. Since the mis-match between the tube diameter and the typical electrode size is considerable, a variety of innovative techniques have been investigated. The electrode attachment techniques can be sub-divided into the following categories: a) dispersing nanotubes from suspension across pre-fabricated contacts, [5, 35–38] b) growing nanotubes between pre-fabricated contacts, [6, 39] c) dispersing nanotubes, then defining contacts using focused ion-beam or electron beam lithography, [37, 40–42] d) blasting off nanotubes

---

<sup>1</sup>In 1991 Sumio Iijima of NEC found nanometer-sized graphitic needles while investigating the residue of C<sub>60</sub> production [1]. These needles are now known as carbon nanotubes. Although Iijima is generally given credit for the discovery of carbon nanotubes, evidence shows that they were produced as early as 1975. [12]

from support structures with a laser beam to disperse them over pre-defined contacts, [43] e) plunging one end of a nanotube into a liquid metal contact, [44] and f) dispersing nanotubes, then welding them to a pre-fabricated contact using an electron beam [45]. Although the above techniques provide some useful information, many of them are of limited use because they require either a serendipitous deposition of nanotubes across contacts, the exposure of the nanotube to high energy electron or ion beams, or the covering of the nanotube with lithographic chemicals. In addition, many of the above techniques result in poor electrical contact to the nanotube, as indicated by system resistances in the kilo-ohm to mega-ohm range.

To better understand the electronic properties of carbon nanotubes, we performed two sets of experiments. First, we measured the electron emission properties of individual multi-walled nanotubes. Using energy-resolved field emission, we acquired total energy distributions (TEDs) of the emitted electrons, which contain information about a nanotube's electronic density of states. Second, to address the limitations mentioned above, we developed a simple method for fabricating electrodes to multi-walled nanotubes. This method results in non-destructive, low-resistance contacts to the nanotubes and allows us to perform temperature dependent, 2-terminal conductance measurements.

The results of the field emission and transport measurements indicate that quantum mechanical effects and electron-electron interactions are very important in nanotubes. The main findings of our field emission studies show that open-ended multi-walled nanotubes exhibit an emission current which is unstable in time and that the resulting energy distributions of the emitted electrons contain several peaks, the energy of which also changes in time. The precise nature of the current instability and the electron distribution structure is not yet known.

The results of our transport measurements form the bulk of this report. We studied the conductance of the nanotube samples over a range of temperatures from room temperature to 4 kelvin. The results indicate that the electronic structure of the nanotube is non-Fermi in nature and may fit a Luttinger liquid model. Our contact

technique results in low resistance contacts to the nanotube. At room temperature, the measured resistance of the nanotube is consistent with ballistic transport. At low temperatures, the resistance of the nanotube is determined largely by the contact resistance between the Fermi liquid contacts and the Luttinger liquid nanotube. However, since our contacting technique results in strongly coupled contacts to the nanotube, there is still a significant contribution from the nanotube itself to the total resistance.

This dissertation presents and discusses in detail the above results. An outline of this report follows. Chapter 2 is an introduction to carbon nanotubes, providing background information as well as a summary of their basic physical and electronic properties. Chapter 3 describes the energy-resolved field emission experiment, and Chapter 4 describes the room temperature transport experiments, including our sample preparation technique. Chapter 5 presents the results of the temperature dependent transport measurements (including noise measurements) and discusses the data in terms of the Luttinger liquid model. Chapter 6 summarizes our findings and concludes this study.

## 2. CARBON NANOTUBES

### 2.1 History

Carbon fibers and tubes (with diameters less than 10 nm) have been known to exist since at least 1976. [12] However, it was not until the mid-1980s with the discovery of fullerenes [46] that a systematic study of nanometer-sized carbon structures began. [13] During the study of  $C_{60}$  and  $C_{70}$  in the late 80s and early 90s, speculation arose on the formation of many different graphitic structures. [47] In September of 1991, Chernosatonkii suggested a "barrel"-type structure, as a variation of the  $C_{60}$  molecule, to understand various experimental findings which were not explained by the spherical version of the fullerene. [48] Then in November of 1991 the "discovery" of carbon nanotubes was reported by Iijima. [1] In light of the ongoing fullerene research, his findings received greater attention than previous nanotube findings. Iijima was using high-resolution transmission electron microscopy (HRTEM) to investigate the byproducts of  $C_{60}$  production. He found needle-like tube structures with diameters of 4–30 nm and lengths up to 1  $\mu\text{m}$ , [1] much longer than the 10–30 nm long "tubelenes" or "barrelenes" discovered by Russian workers at about the same time. [49] Shortly thereafter in July of 1992, Ebbesen and Ajayan reported a method for producing gram quantities of carbon nanotubes, [50] and in 1994 Ebbesen reported a method for purifying nanotubes by oxidation at 1000 K. [51] Thus, by the mid 90s, there were methods in place for producing gram quantities of very pure carbon nanotubes, and the nanotube sub-field of carbon research was established.

### 2.2 Physical Properties

In the simplest case, a carbon nanotube is a seamless cylindrical shell of graphite-like,  $sp^2$ -bonded carbon atoms. In other words, rolling a certain section of graphite sheet into a seamless tube essentially creates a nanotube. This is schematically illus-

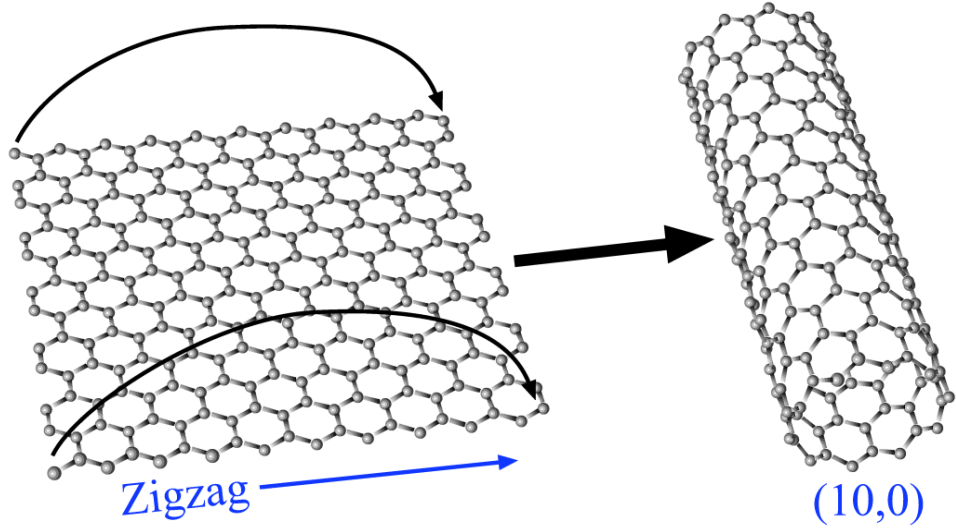


Figure 2.1. Schematic representations of rolling up a graphite sheet to form a (10,0) zigzag single-walled nanotube. Rolling the sheet in the direction perpendicular to the one shown above would produce a (6,6) armchair nanotube.

trated in Fig. 2.1. The coordinate system used to define a general individual nanotube is shown in Fig. 2.2.

The hexagonal basis vectors are  $\vec{a}$  and  $\vec{b}$ . Using a pair of integers  $(n, m)$ , we define a chiral vector  $\vec{C}$  as

$$\vec{C} = n\vec{a} + m\vec{b} \equiv (n, m). \quad (2.1)$$

The vector  $\vec{C}$  is perpendicular to the axis of the tube, and its magnitude,  $|\vec{C}|$ , is the circumference of the tube. This gives the diameter of the tube as  $d_t = |\vec{C}|/\pi$ , or in terms of  $(n, m)$ ,

$$d_t = \frac{\sqrt{3} a_{C-C}}{\pi} \sqrt{n^2 + nm + m^2} = \frac{|\vec{C}|}{\pi}, \quad (2.2)$$

where  $a_{C-C} = 1.421 \text{ \AA}$  is the carbon-carbon distance in graphite. The chiral angle,  $\Theta_C$ , is defined with respect to the  $(n, 0)$  direction as,

$$\Theta_C = \tan^{-1}\left(\frac{\sqrt{3}m}{2n+m}\right). \quad (2.3)$$

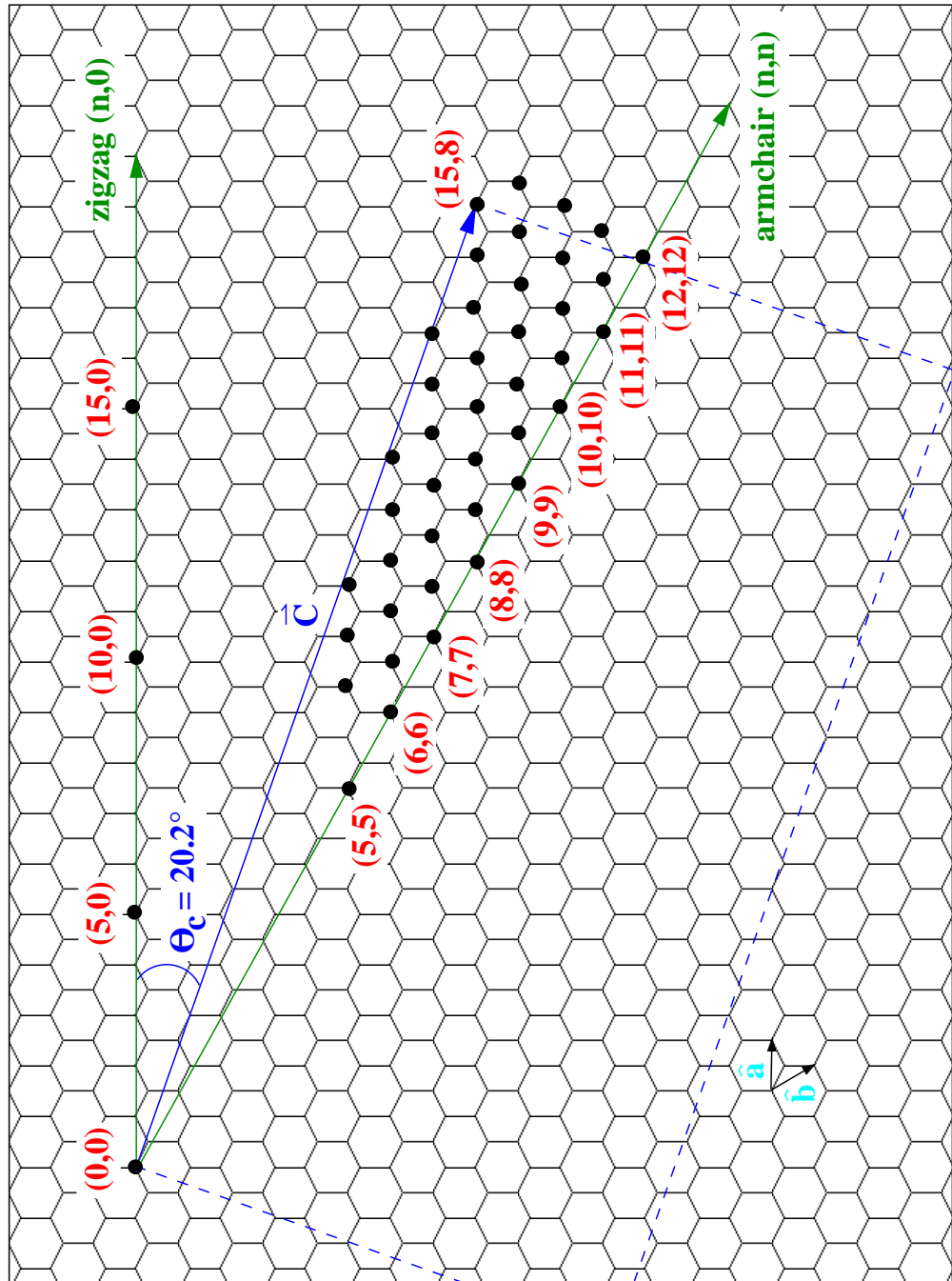


Figure 2.2. The hexagonal basis vectors for graphite can be used to uniquely define a nanotube using the  $(n, m)$  coefficients of the chiral vector,  $\vec{C} = n\vec{a} + m\vec{b}$ . The chiral vector is perpendicular to the axis of the tube and has a magnitude equal to the circumference of the tube. The chiral angle,  $\Theta_C$ , serves to measure the helicity of the tube. Here we show  $\vec{C}$  and  $\Theta_C$  for a short  $(15,8)$  nanotube.

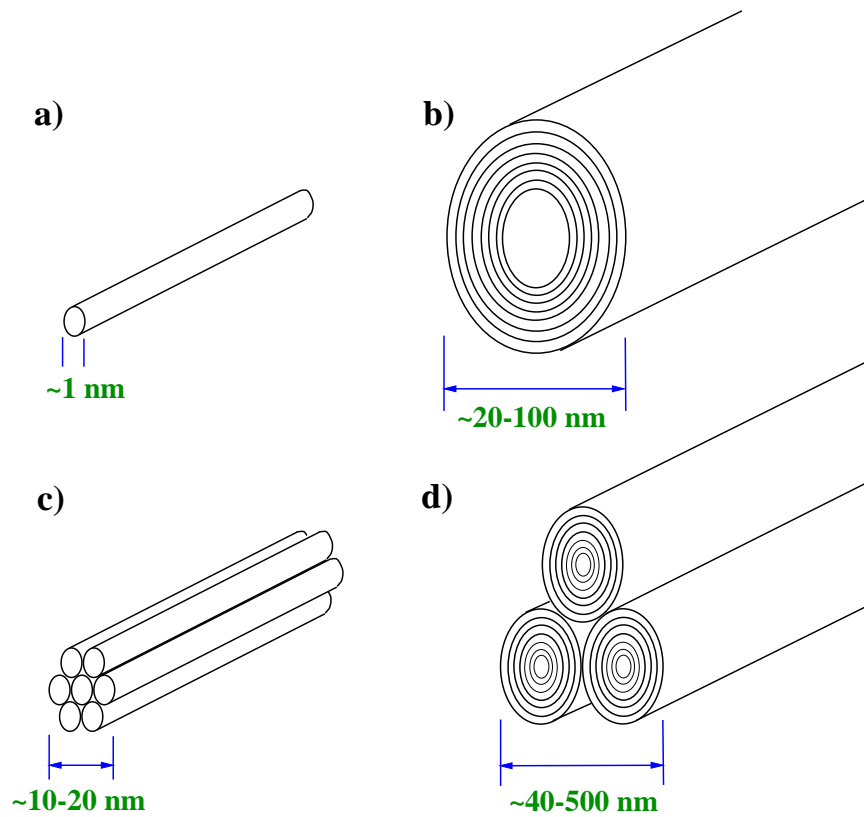


Figure 2.3. Examples of single-walled nanotubes (SWNTs) and multi-walled nanotubes (MWNTs). a) An individual SWNT. b) An individual MWNT. c) A small bundle or rope of SWNTs, which may have hundreds of individual tubes. d) A bundle of a few MWNTs.

The  $(n, 0)$  direction is called the zigzag direction due to the carbon bond pattern along this direction. The armchair direction is the  $(n, n)$  direction and has a chiral angle of  $\Theta_C = 30^\circ$ . The hexagons in the zigzag and armchair tubes will form rings perpendicular to the tube axis, whereas the hexagons of any tubes formed from the region  $0^\circ < \Theta_C < 30^\circ$  will spiral around the tube axis. The tubes with spiraling hexagons are called chiral tubes. Fig. 2.1 shows the concept of forming a  $(10,0)$  nanotube from a sheet of graphite.

So far the discussion of carbon nanotubes has been limited to single shell (single-walled) structures. Based on growth conditions, carbon nanotubes can be produced as two types: single-walled nanotubes (SWNTs) and multi-walled nanotubes (MWNTs).

A multi-walled nanotube consists of several concentric single-walled nanotubes. Thus, multi-walled nanotubes are different from the scroll-like carbon whiskers studied by Bacon in the 1950s. [51] Fig. 2.3 shows the difference between SWNTs and MWNTs and bundles of each type. The interlayer spacing in a multi-walled nanotube is 0.34 nm (a value confirmed by high-resolution TEM [1] and STM [30]) and agrees closely with the average equilibrium value obtained from self-consistent electronic structure calculations [13]. This is the same spacing as the inter-planar spacing of turbostratic graphite.<sup>1</sup> Some research suggests that there is little structure correlation between the concentric tubes in a MWNT. [1, 51] In other words, as in turbostratic graphite, there is no ABAB stacking of the carbon atoms, and the helicity of the tube changes independently from layer to layer.

MWNTs typically have diameters on the order of 10 to 20 nm, whereas SWNTs have diameters on the order of 1 nm. Even though SWNTs tend to bunch together in ropes, MWNTs are still much easier to manipulate using our techniques. Figs. 2.4 and 2.5 show some TEM images of single-walled and multi-walled nanotubes.<sup>2</sup> Although a discussion of the growth process is beyond the scope of this report, MWNTs may be produced without using catalytic particles. As a result they are generally purer than SWNTs, although the left image of Fig. 2.5 does show some contamination. The experimental work reported here is exclusively on MWNTs.

### 2.3 Electronic Properties

Based on theoretical predictions starting in 1992, [2] there has been a strong interest in the electronic properties of carbon nanotubes. Most research efforts use SWNTs to perform theoretical calculations. This research emphasizes the 1D properties of the nanotube, which are of primary interest to this work. The most striking feature

---

<sup>1</sup>In ideal graphite the graphene layers stack in an ABAB configuration. Weak disorder results in stacking faults or deviations from ABAB stacking. This deviation increases the layer separation to 0.344 nm. The resulting 2D structure of uncorrelated graphene layers is called turbostratic graphite. [13]

<sup>2</sup>These images were taken at Purdue with a JEOL 2000FX TEM. The SWNTs were produced and donated by Dr. Peter Eklund's lab at Pennsylvania State University. The MWNTs are from Dr. Richard Smalley's lab at Rice University.

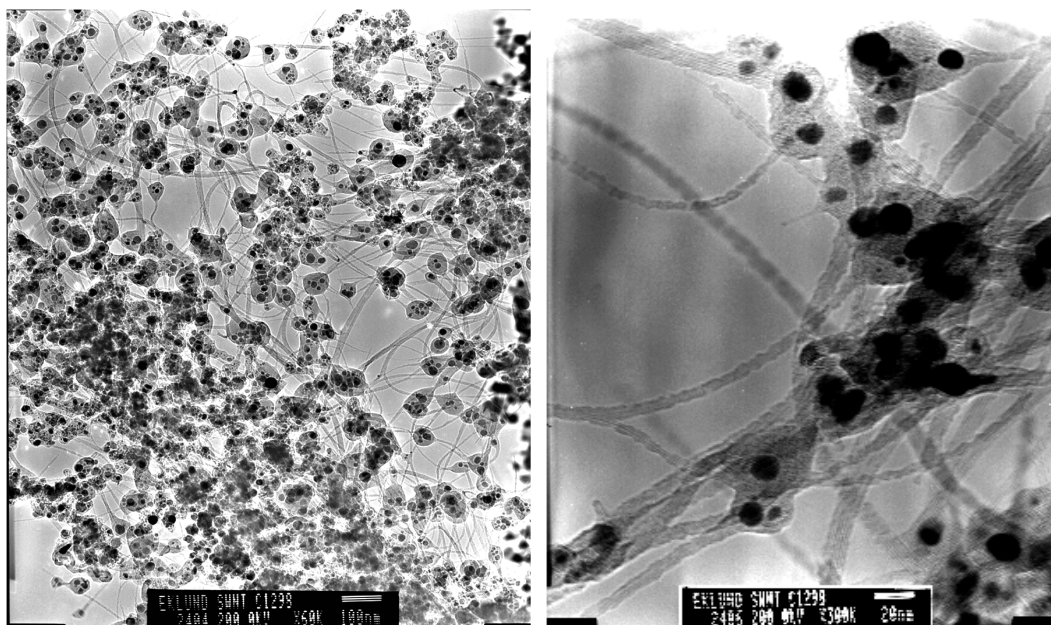


Figure 2.4. TEM images of un-purified arc-grown SWNTs. The dark spots are the catalytic particles used to grow the nanotubes. The image at right resolves the individual tubes of some the SWNT ropes.

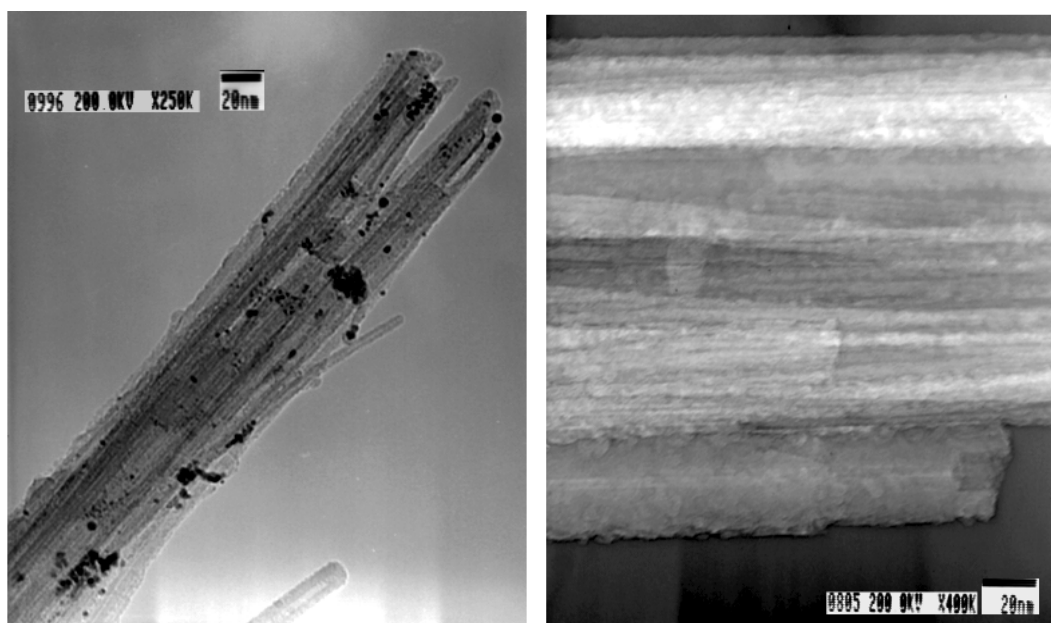


Figure 2.5. TEM images of arc-grown MWNTs. In the left image, the individual tube diameters range from  $\sim 5$  to  $\sim 20$  nm. In the right image the bottom MWNT terminates abruptly with a few outer shells continuing  $\sim 15$  nm longer than the inner shells.

of a nanotube's electronic properties is that depending on its diameter and chirality (or helicity), a nanotube can be either metallic or semi-conducting.

Researchers use a variety of techniques to make band structure calculations for nanotubes. [2, 32, 52–57] These calculations encompass work on infinite and finite tubes, capped and open tubes, and tubes with a variety of structural defects. Most of this work neglects inter-tube (in SWNT ropes) and interlayer (in MWNTs) interactions because many believe the interesting 1D features arise from interactions within the tube itself. [58] However, Delaney *et al.* suggested that interactions between the SWNTs in a rope will give rise to a small ( $\sim 0.1$  eV) band gap in an otherwise metallic tube. [52]

### 2.3.1 Energy Dispersion Relations

The two atom hexagonal unit cell of graphite is a useful starting point for understanding the electronic structure of a nanotube. Using the real space coordinate system of Fig. 2.2 and defining the reciprocal lattice vectors in terms of the real space vectors as,  $\vec{a} \cdot \vec{a}' = 2\pi$  and  $\vec{b} \cdot \vec{b}' = 2\pi$ , we arrive at the Brillouin zone in reciprocal space shown in Fig. 2.6.

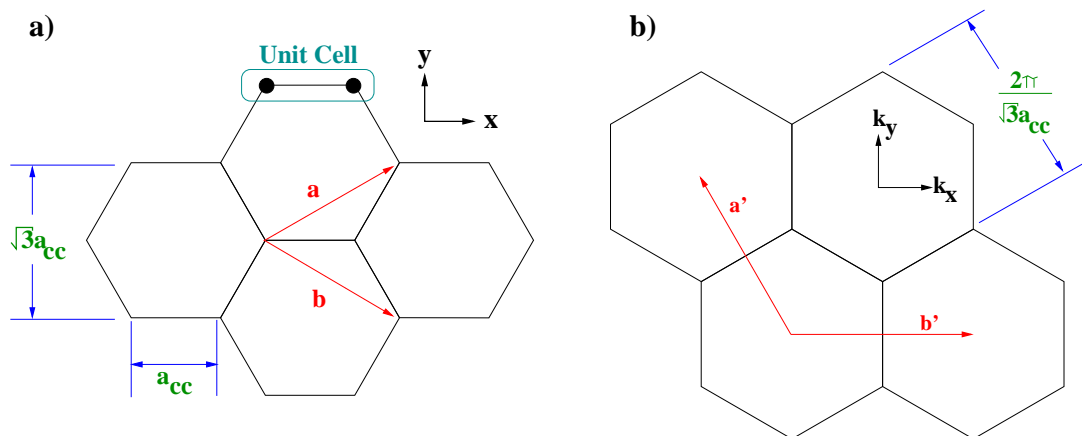


Figure 2.6. a) The real space unit vectors and the hexagonal lattice unit cell. The carbon-carbon distance in graphite is  $a_{C-C} \simeq 1.421$  Å. b) The corresponding reciprocal space, showing the reciprocal lattice vectors,  $\vec{a}'$  and  $\vec{b}'$ .

Considering only one orbital per atom and neglecting overlap along the c-axis, we find the graphite dispersion relation by solving the eigenvalue equation [57]

$$\mathbf{E} \begin{pmatrix} \phi_1 \\ \phi_2 \end{pmatrix} = \begin{pmatrix} 0 & \mathbf{h}_o(\vec{\mathbf{k}}) \\ \mathbf{h}_o^*(\vec{\mathbf{k}}) & 0 \end{pmatrix} \begin{pmatrix} \phi_1 \\ \phi_2 \end{pmatrix},$$

where

$$\mathbf{h}_o(\vec{\mathbf{k}}) = \gamma_o \left( 1 + e^{i\vec{\mathbf{k}} \cdot \vec{\mathbf{a}}} + e^{i\vec{\mathbf{k}} \cdot \vec{\mathbf{b}}} \right). \quad (2.4)$$

The general dispersion relation derived through the tight-binding approximation for 2D graphite is, [13, 57, 59]

$$E(k_x, k_y) = \pm \gamma_o \left( 1 + 4 \cos\left(\frac{\sqrt{3}k_x a}{2}\right) \cos\left(\frac{k_y a}{2}\right) + 4 \cos^2\left(\frac{k_y a}{2}\right) \right)^{1/2}, \quad (2.5)$$

where  $\gamma_o \simeq 2.9$  eV is the value of the overlap integral and  $a = \sqrt{3}a_{C-C}$ .

By rolling a general  $(n, m)$  nanotube along the chiral vector  $\vec{C}$ , Eqn. 2.1, we impose a quantization condition on the wave vectors,

$$\vec{\mathbf{k}} \cdot \vec{C} = 2\pi\nu, \quad \nu = 0, 1, 2, \dots \quad (2.6)$$

From Fig. 2.2 and Fig. 2.6, we see that to make a zigzag tube, the sheet is rolled up along the  $\vec{y}$  direction. Then, our boundary condition reduces to a condition on  $k_y$ ,

$$\vec{\mathbf{k}} \cdot \vec{C}_{zig} = nak_y = 2\pi\nu, \quad \nu = 0, 1, 2, \dots, n. \quad (2.7)$$

Thus from Eqn. 2.5, we find the *zigzag* energy dispersion relation,

$$E_{n,\nu}^{zig}(k_x) = \pm \gamma_o \left( 1 + 4 \cos\left(\frac{\sqrt{3}k_x a}{2}\right) \cos\left(\frac{\pi\nu}{n}\right) + 4 \cos^2\left(\frac{\pi\nu}{n}\right) \right)^{1/2}. \quad (2.8)$$

For an armchair nanotube, the graphite sheet is rolled up along the  $\vec{x}$  direction (see Fig. 2.2 or 2.6), so the condition becomes,

$$\vec{\mathbf{k}} \cdot \vec{C}_{arm} = n\sqrt{3}ak_x = 2\pi\nu, \quad \nu = 0, 1, 2, \dots, n. \quad (2.9)$$

Inserting this into Eqn. 2.5 gives the *armchair* dispersion relation for a nanotube,

$$E_{n,\nu}^{arm}(k_y) = \pm \gamma_o \left( 1 + 4 \cos\left(\frac{\pi\nu}{n}\right) \cos\left(\frac{k_y a}{2}\right) + 4 \cos^2\left(\frac{k_y a}{2}\right) \right)^{1/2}. \quad (2.10)$$

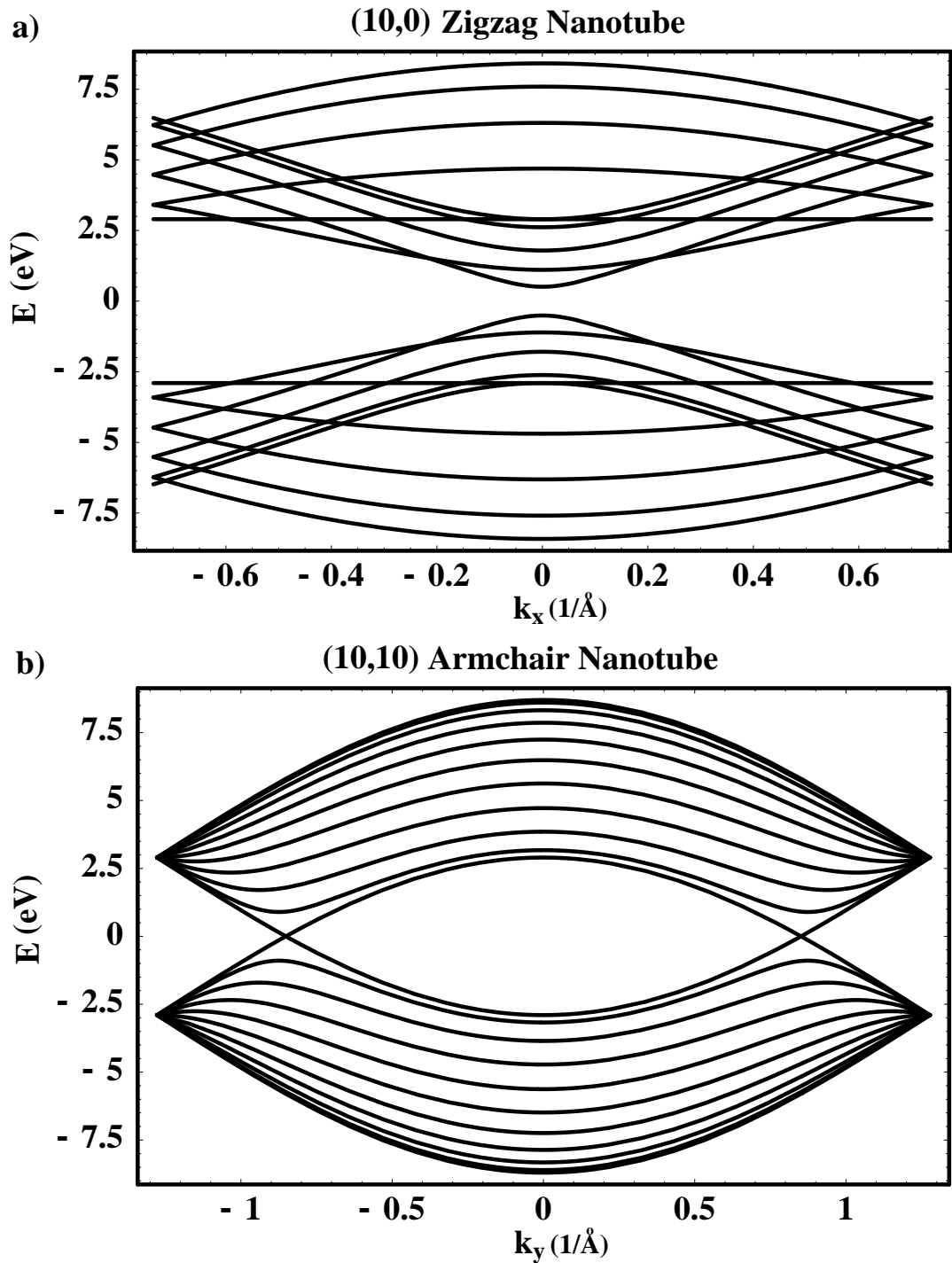


Figure 2.7. Energy dispersion relations for two single-walled nanotubes. Each dispersion curve represents a different value of the quantization index  $\nu$  in Eqns. 2.8 and 2.10. The a) zigzag (10,0) nanotube and b) armchair (10,10) nanotube. We see that the (10,10) is metallic and that the (10,0) nanotube is a direct band gap semi-conductor.

Fig. 2.7 shows an example dispersion relation for two types of nanotubes. The Fermi level  $E_F$  is at  $E = 0$ . We can see from the figure that the (10,0) nanotube is semi-conducting with a direct band gap of  $\sim 1.0$  eV at  $k_x = 0$ . The (10,10) nanotube is metallic at  $k_y = \pm 2\pi/3a \simeq \pm 0.85 \text{ \AA}^{-1}$ . These results agree with the general condition that a nanotube will be metallic if

$$n - m = 3l, \quad l = 0, 1, 2, 3, \dots \quad (2.11)$$

A dispersion relation for a general  $(n, m)$  chiral nanotube is more complicated than the simple cases shown above and is beyond the scope of this report.

### 2.3.2 Density of States

Given the dispersion relations, we may calculate the density of states of a nanotube. The electronic density of states (DOS) for a 1D material is

$$n(E) = \frac{1}{\pi \hbar v(E)}, \quad v(E) = \frac{1}{\hbar} \frac{dE}{dk}, \quad (2.12)$$

where  $v(E)$  is the group velocity for electrons moving in the  $+x$  direction. The DOS  $n(E)$  of each dispersion curve shown in Fig. 2.7 is shown in Fig. 2.8. Again we see that the metallic (10,10) nanotube has a finite DOS at the Fermi energy  $E_F = 0$ , and the (10,0) tube has a zero DOS at  $E_F$ . These density of states graphs were calculated using a C program written for armchair and zigzag tubes only and included in Appendix A. The program calculates the analytical  $E(k)$  and  $n(k)$ , then sorts the results to create the  $n(E)$  data. As discussed in Chapter 3, we investigated the DOS of several individual MWNTs through the total energy distribution (TED) of emitted electrons.

### 2.3.3 Electronic Transport

As noted above, the metallic nanotubes have energy bands crossing the Fermi energy. In Fig. 2.9, we show the energy bands at  $k_y = 2\pi/3a$  for a metallic (10,10) nanotube. The tube is ideally contacted by two contact pads with quasi-Fermi levels of  $\mu_1$  and  $\mu_2 = \mu_1 - eV_{app}$ . At the applied bias shown, the current flows only through the

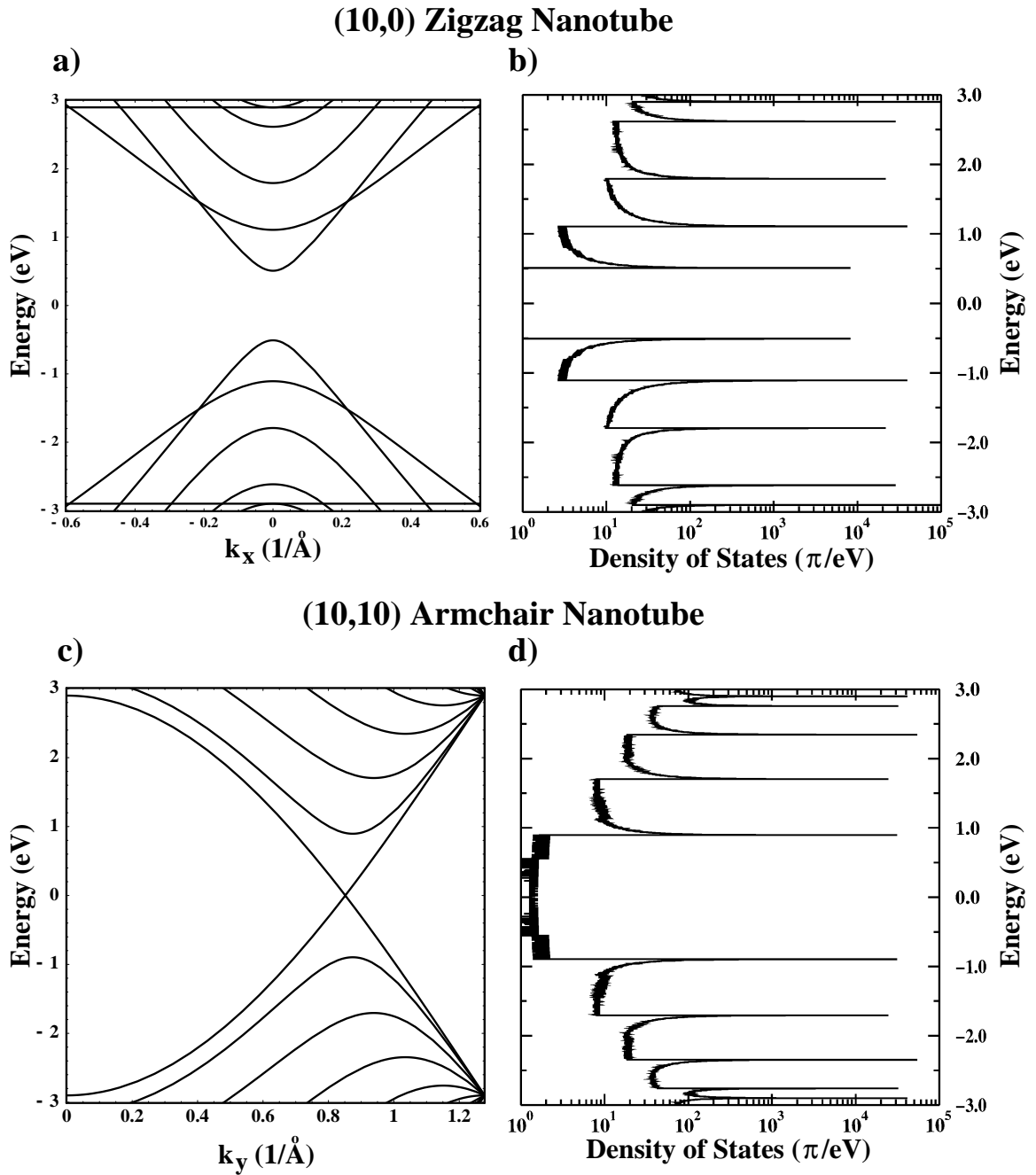


Figure 2.8. The  $E(k)$  and  $n(E)$  for two nanotubes. Graphs a) and b) are for the (10,0) zigzag nanotube, while graphs c) and d) are for the (10,10) armchair nanotube. The band gap of the (10,0) nanotube is about  $\sim 1.0$  eV. The (10,10) nanotube has a finite DOS at the Fermi level.

one level between  $\mu_1$  and  $\mu_2$  (the bands crossing the Fermi energy of the nanotube). An interesting prediction for carbon nanotubes is that transport in these metallic bands may be ballistic. [2, 60] In this case, the measured conductance is a property of the assembly of input and output contact pads coupled to the narrow constriction introduced by the carbon nanotube. Under these circumstances, current flow takes on a ‘conduction by transmission’ character, and the conductance becomes a property of the specific system rather than the material. [61] The solution of the Schrödinger equation determines the wave function of an electron in such a system.

This phenomenon is known as ballistic transport. It implies that there is no electron scattering over the length of the sample and that electrons remain in local equilibrium as they enter and exit from the contact pads. These stringent conditions are met when the phase breaking length ( $l_\phi$ ) of the electron states in the nanotube is greater than the momentum relaxation length,  $l_m$  which in turn is much greater than the length  $L$  of the nanotube. We assume that the momentum relaxation length and the elastic scattering length are equal, such that  $l_m = l_{el}$ . The phase (momentum) relaxation length is the average length over which an electron changes most of its original phase (momentum). Thus, the condition for ballistic conduction is  $l_\phi > l_m > L$ , so that  $L$  is the coherence length. Further restrictions require that the diameter  $D$  of the nanotube is comparable to the electron wavelength at the Fermi energy  $\lambda_F$  and that  $D$  is much less than  $L$ .

The net current through the nanotube is made up of the currents through the energy levels accessible between the Fermi energies of the reservoirs. As an example, the number of accessible levels in Fig. 2.9 is 1. In general, the number of accessible energy levels, called open conduction channels, is a function of energy,  $E$ , and can be written as  $N(E)$ . Depending on its diameter and chirality, a nanotube will exhibit either metallic (a finite DOS at  $E_F$ ) [62] or semiconducting (a zero value for the DOS at  $E_F$ ) behavior. The location in energy of the next available band above  $E_F$  depends on whether the nanotube is semiconducting or metallic. To first approximation, the separation in energy ( $\Delta\epsilon$ ) between energy bands may be related to the nanotube

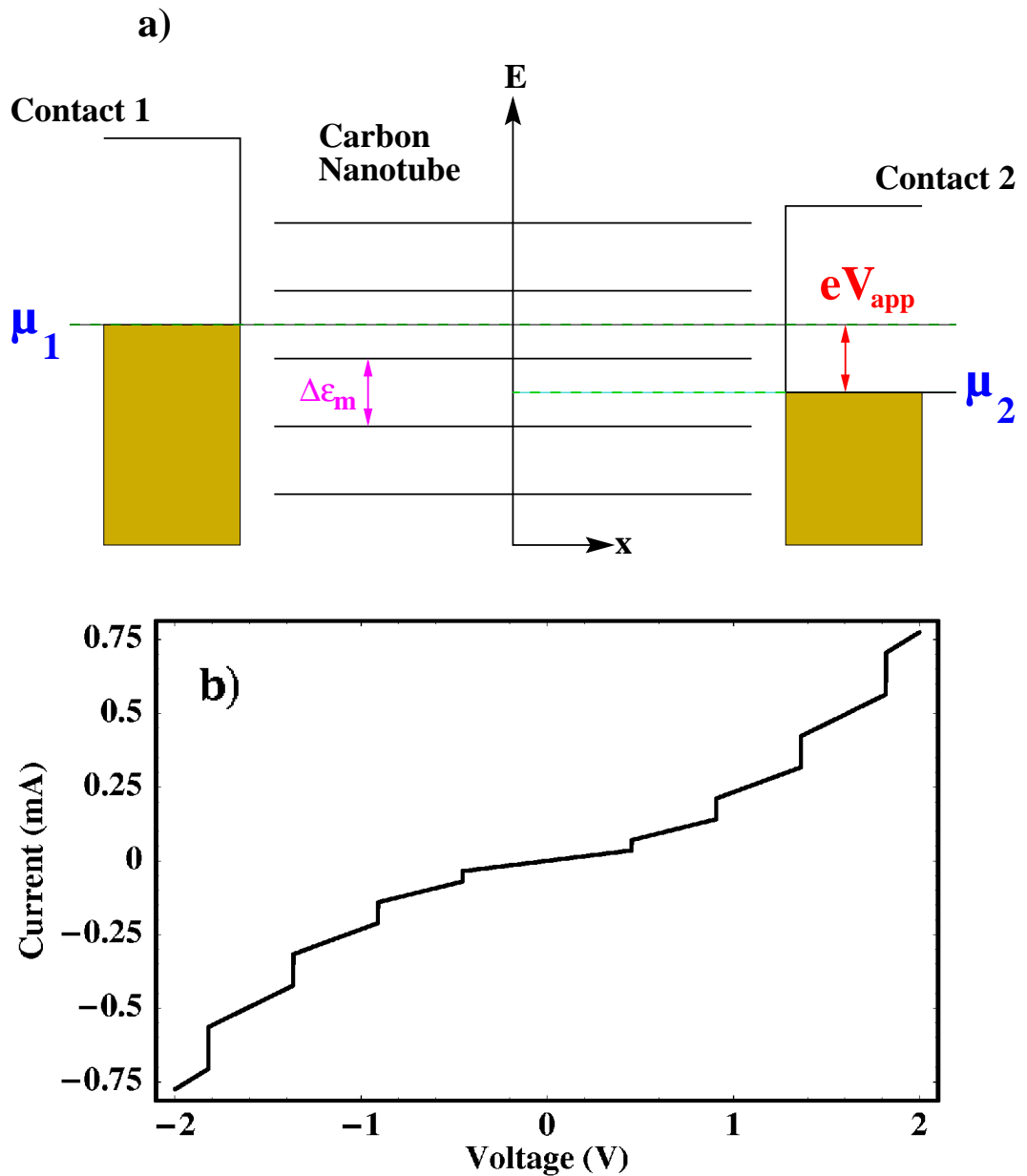


Figure 2.9. Simple diagrams illustrating transport through the quantized energy levels of a carbon nanotube. a) Illustrated is a (10,10) metallic nanotube where  $\Delta\epsilon_m \simeq 0.9$  eV. The electrochemical potential of contact pad 2 is lowered by an energy,  $eV_{app}$ , with respect to contact pad 1, allowing electrons to travel through the first unfilled nanotube energy levels. This pure ballistic transport would lead to the  $I(V)$  shown in b), where the conductance increases by an amount  $G = G_o \equiv 2e^2/h$  as new channels open.

diameter. Knowing the diameter, the following estimates can be obtained [23, 63]

$$\Delta\epsilon_m = 3\gamma_o \frac{a_{C-C}}{D} \quad (\text{metallic tubes}) \quad (2.13)$$

$$\Delta\epsilon_s = 2\gamma_o \frac{a_{C-C}}{D} \quad (\text{semiconducting tubes}) . \quad (2.14)$$

These estimates are useful for determining what values to expect for the open conduction channels,  $N(E)$ . In the case of carbon nanotubes, we must also consider the number of conducting layers (i.e., in a MWNT or a SWNT rope). We include this number in  $N(E)$ . In addition, in the Brillouin zone for a nanotube there are 2 bands crossing the Fermi level (see Fig. 2.7). This number is referred to as the number of modes per sub-band,  $M$ , and is thought to be 2. [15–17] However, recent experiments suggest  $M = 1$ , [44] and several authors have advanced theoretical arguments for  $M = 1$ . [64, 65]

Those electrons with energy  $E$ , in the range  $\mu_1 > E > \mu_2$ , and with velocity  $v(E) > 0$  may contribute to the current,  $I$ . The total current is then found to be [66]

$$I = e M \int n(E)v(E)\mathcal{T}(E)N(E) \times [f(E - \mu_1) - f(E - \mu_2)]dE , \quad (2.15)$$

where  $\mathcal{T}(E)$  is the transmission probability of an electron passing from one reservoir into the other through the open channels of the nanotube, and  $f(E - \mu_i)$  is the Fermi-Dirac distribution function with quasi-Fermi energy  $\mu_i$ . The product of the density of states and the velocity is a constant (see Eqn. 2.12), given by

$$n(E)v(E) = \left[ \frac{1}{\pi\hbar v(E)} \right] [v(E)] = \frac{1}{\pi\hbar} = \frac{2}{h} . \quad (2.16)$$

Inserting Eqn. 2.16 into Eqn. 2.15 and pulling the constants outside of the integral, we find

$$I = \frac{2e}{h} M \int \mathcal{T}(E)N(E)[f(E - \mu_1) - f(E - \mu_2)]dE . \quad (2.17)$$

The pre-factor  $\frac{e}{h}$  is the quantized current per conduction channel per energy, and the 2 accounts for the spin degeneracy of the electrons. [14] If we now assume  $\mathcal{T}(E)$  and  $N(E)$  to be constants,  $N$  and  $\mathcal{T}$ , over the range  $\mu_1 > E > \mu_2$ , we may write

$$I = \frac{2e^2}{h} \frac{(\mu_1 - \mu_2)}{e} M \sum_0^N \mathcal{T}_j , \quad (2.18)$$

where we approximate the difference in the Fermi-Dirac functions as the difference in the electrochemical potentials of the reservoirs. The transmission probability for an electron to transmit through the  $j$ th channel is  $\mathcal{T}_j$ , which we sum over the number of open channels (including all nanotube layers).

We can write the applied voltage as  $V_{app} = V = (\mu_1 - \mu_2)/e$ . Inserting this into Eqn. 2.18, we find

$$I = \frac{2e^2}{h}VM \sum_0^N \mathcal{T}_j = G_oVM \sum_0^N \mathcal{T}_j, \quad (2.19)$$

where

$$G_o \equiv \frac{2e^2}{h} \simeq 77.5 \mu S. \quad (2.20)$$

We can include the transmission probabilities into the total conductance as

$$G = G_oM \sum_0^N \mathcal{T}_j, \quad (2.21)$$

When the above conditions on the electron relaxation lengths and the electron wavelength are met, the transmission coefficients  $\mathcal{T}_j$  in Eqn. 2.21 are close to unity and the conductance becomes quantized in units of  $MNG_o$ , [61, 67]

$$G = G_oM \sum_0^N \mathcal{T}_j \Rightarrow G = MNG_o. \quad (2.22)$$

Thus, a signature of ballistic transport is a measured conductance that is close to integer units of  $G_o$ . Deviations from exact quantization can result if, for example, there is a finite contact resistance between the contact pads and the nanotube. Reflections at the entrance of any constriction will decrease the conductance through the open channels. In a similar way, backscattering of an electron upon exit from the nanotube into the contact pad will also diminish the conductance calculated from Eqn. 2.21.

Since more conduction channels are accessed as the applied bias is increased, we may allow  $N$  to increase with bias. If we write the number of open channels as  $N(V)$ , then the  $I(V)$  for a ballistic conductor is given by

$$I(V) = G(V) \times V \Rightarrow I(V) = G_oMN(V) \times V. \quad (2.23)$$

We illustrate an idealized example of this process in Fig. 2.9. Note that this behavior has not been observed experimentally with bias measurements. We measured nanotube conductances as high as  $27.0 G_o$  at room temperature, but the conductance did not increase with bias over a  $\pm 1.5\text{V}$  range. [68] Other groups have seen the conductance increase with bias, [44] but not the conductance increase predicted by Eqns. 2.19 and 2.23. Anantram provides one explanation for this lack of a conductance increase, with a discussion of scattering phenomena in the sub-bands of the nanotube. [69] He finds that in small diameter nanotubes, Bragg reflection in the sub-bands results in a “transport bottle neck,” which limits the electron transport to mainly the bands crossing the Fermi energy. In larger diameter tubes (as for MWNTs), he finds that Zener tunneling between sub-bands will increase the conductance, although not at a rate of  $MG_o$  per sub-band. The diameter determines the energy separation of the sub-bands, as given by Eqns. 2.13 and 2.14. Interestingly, Anantram also finds that defect states may assist the sub-band transport, leading to a conductance increase with bias. However, this increase is also less than  $MG_o$  per sub-band.

The potential profile of the nanotube is another important detail of ballistic transport. How the voltage drops along the length of the nanotube may result in different bias-dependent conductance values. [69] The common view is that the potential of a ballistic conductor is dropped at the contacts. Scattering within the sub-bands will locate part of the drop within the nanotube. In addition, electron-electron interactions present in the nanotube may also affect its profile. [70] With potential drops present in the nanotube, we must then consider which channels remain open over the entire length of the nanotube. Measurement of the potential profile down a nanotube, although of great interest, has been reported with limited success and is difficult to interpret. [42, 71]

### 3. FIELD EMISSION AND TOTAL ENERGY DISTRIBUTIONS

In 1937, less than ten years after Fowler and Nordheim explained the process of field emission (or cold emission) as quantum mechanical barrier penetration, [72] Erwin Müller invented the field emission microscope (FEM). [73] Energy-resolved field emission microscopy is important for the study of nanotubes since it allows for measurement of the total energy distribution (TED) of electrons field emitted from the nanotube. The TED is the energy distribution of the electrons emitted normal and transverse to the emission surface. [73] The total distribution of energies gives insight into the underlying electronic structure of the emitter. [74–76] For a 1D emitter, such as a carbon nanotube, the TED will contain information about the nanotube’s localized electronic states in the vicinity of the Fermi level. Thus, energy-resolved field emission can be a powerful tool in studying the electronic properties of carbon nanotubes. Yet, in order to understand the total energy distributions from carbon nanotubes, we must first discuss the basic principles of field emission.

#### 3.1 Field Emission Microscopy

The field emission microscope (FEM) consists of a very sharp needle (called the tip) and a viewing screen, both contained within an ultra high vacuum (UHV) chamber. A very high negative voltage ( $\sim 2\text{--}5$  kV for a standard tungsten tip) is applied to the needle while the screen is held at ground potential. The large potential difference creates a high electric field at the end of the tip. As shown in Fig. 3.1, this high electric field deforms the potential barrier at the end of the tip to a near triangular shape, which allows electrons to tunnel into the vacuum. The field required for appreciable electron emission is  $\sim 3\text{--}5 \times 10^7$  V/cm and is possible because of the very small end radius of the emitter ( $\sim 10\text{--}200$  nm). The emitted electrons are accelerated

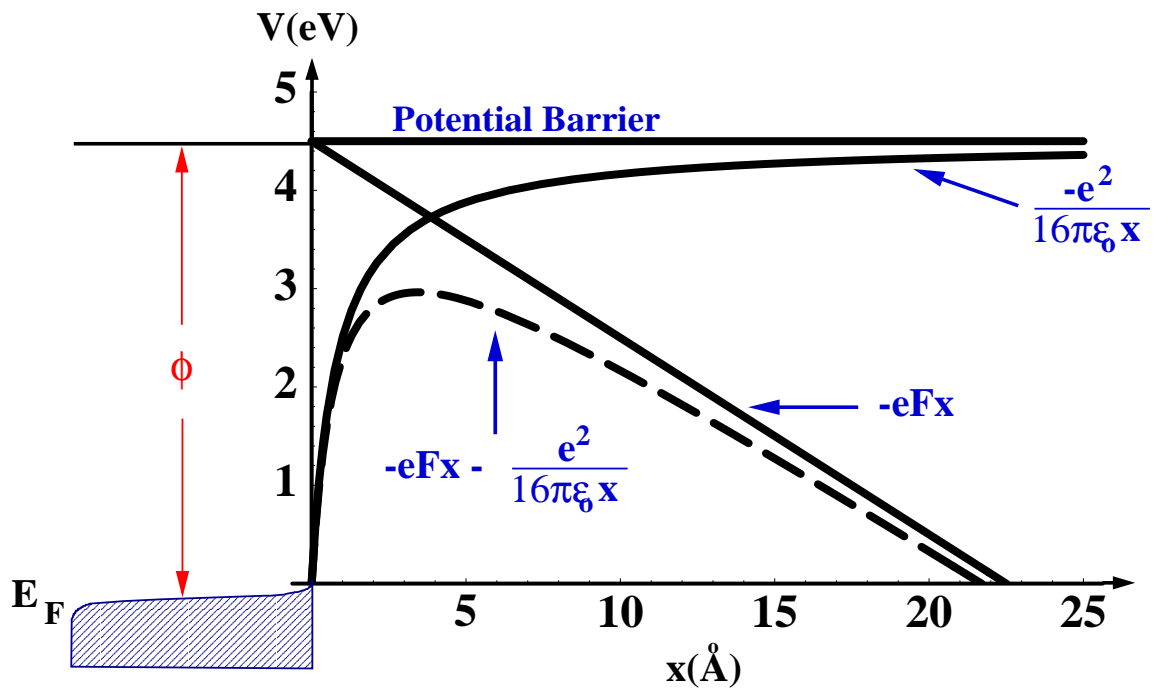


Figure 3.1. A calculation of the potential barrier deformation by the applied field and the added contribution from the electron image term. This calculation is for field emission at  $-1000$  V from a tungsten tip (work function =  $4.5$  eV) with an end radius of  $700$  nm.

toward a phosphor screen, and the pattern of the electrons striking the screen creates the visible field emission micrograph. This pattern is essentially a map of the work function at the surface of the tip.

### 3.1.1 Principles of Operation

For a tip with an end radius,  $r$ , at an applied voltage,  $V$ , the electric field at the surface of the tip is

$$F = \beta V, \quad (3.1)$$

where

$$\beta = \frac{1}{kr}. \quad (3.2)$$

Here we approximate the geometry of the tip as a hemisphere on a conical shank. The parameter  $k$  accounts for the compression of the field lines due to the conical shank of the tip. The applied electric field deforms the potential barrier at the surface

of the tip, as shown in Fig. 3.1. An additional reduction of the barrier results from the contribution of the image charge of the emitted electrons. For  $0 < x \ll r$ , where  $x = 0$  is the tip surface, the deformed potential is given by

$$U(x) = -eFx - \frac{e^2}{16\pi\epsilon_0 x} . \quad (3.3)$$

The transmission probability for an electron of energy  $E$  can be calculated using the WKB approximation for a 1D potential barrier,

$$D[U(x), E] = e^{-\frac{2}{\hbar} \int_{x_1}^{x_2} \sqrt{2m(U(x)-E)} dx} , \quad (3.4)$$

where  $x_1$  and  $x_2$  are the classical turning points, given by the zeros of the integrand.

The number of electrons emitted from the surface of a metal per second in the energy range  $E$  to  $E + dE$  is

$$P(E)dE = D[U(x), E]\mathcal{S}(E)dE . \quad (3.5)$$

The supply function,  $\mathcal{S}(E)$ , is the number of electrons incident on the surface per second and is given by

$$\mathcal{S}(E)dE = -\frac{4\pi m}{\hbar^3} \frac{dE}{1 + e^{\frac{E+\phi}{k_b T}}} , \quad (3.6)$$

where  $m$  is the electron mass and  $\phi$  is the work function of the metal.

To calculate the current density of emitted electrons, we integrate Eqn. 3.5 over all energies near the Fermi level,  $E_F$ . The result is the standard Fowler-Nordheim equation: [76]

$$j = 1.54 \times 10^{-6} \frac{F^2}{\phi t^2(y)} \exp\left[-6.83 \times 10^7 v(y) \frac{\phi^{3/2}}{F}\right] \text{ A/cm}^2 , \quad (3.7)$$

where  $F$  is the applied field in volts/cm and  $\phi$  is in electron volts. The tabulated functions  $t(y)$  and  $v(y)$  varying smoothly with the dimensionless parameter  $y$ , which is given by [73, 75, 77]

$$y = \frac{\sqrt{e^3 F}}{\phi} . \quad (3.8)$$

The applied electric field deforms the potential barrier which an electron sees at the metal surface, as shown in Fig. 3.1, by an amount  $eFx$ . The image charge of the electron provides an additional reduction of an amount  $\frac{e^2}{16\pi\epsilon_0 x}$ . At the point where  $U(x)$  is maximum, the contribution from the image term is equal to  $\sqrt{e^3 F}$ . Thus, from Eqn. 3.8,  $y$  is the ratio of the image term at  $U(x) = U_{max}$  to the work function  $\phi$ .

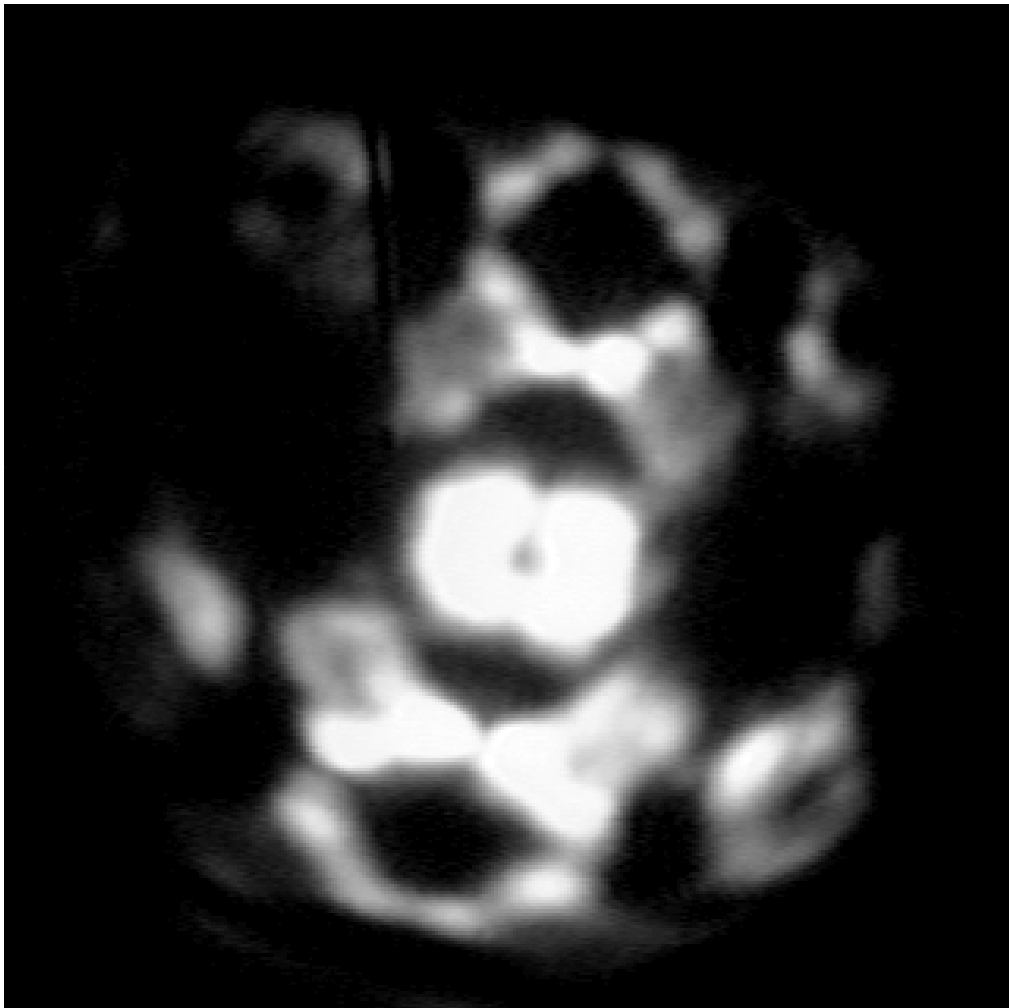


Figure 3.2. A field emission micrograph from a (110) oriented platinum tip. This image, recorded with a CCD camera, was taken with  $-6500$  V applied to the tip. The rather high voltage indicates that the tip has a large end radius.

From Eqn. 3.7 we see that the field emission micrograph is a map of the work function of the tip surface. The tip is usually made from a polycrystalline wire, but since the end of the tip is so small, it may be part of a single crystal structure (either by luck or by annealing the tip). The spherical end of the tip is actually made up of several flat facets with relatively low surface energy. These flat facets blend smoothly into each other through regions of higher surface energy. Thus, the work function  $\phi$  depends on the orientation within the crystal, where the flat low index facets have a higher work function than the high index transition regions. From Eqn. 3.7, we see that the regions with a lower work function will produce a greater emission current. The resulting pattern of the emission current displays the anisotropy of the surface energy, [73] which we see clearly in the field emission micrograph from a (110) oriented platinum tip shown in Fig. 3.2. Appendix Fig. B.4 contains a version of this micrograph indexed crystallographically.

Defining the constants  $a = \frac{1.54 \times 10^{-6}}{\phi t^2(y)}$  and  $b = 6.83 \times 10^7 v(y)$ , we can write the Fowler-Nordheim equation in its most common form:

$$j = aF^2 e^{-b\phi^{3/2}/F} . \quad (3.9)$$

Thus, for a field emission process, a plot of  $\ln(\frac{j}{F^2})$  versus  $\frac{1}{F}$  is linear. If we now insert Eqn. 3.1 into Eqn. 3.9 and rearrange it, we find that

$$\frac{I}{V^2} = A\beta a e^{-\frac{b\phi^{3/2}}{\beta V}} , \quad (3.10)$$

since  $j = \frac{I}{A}$ , where  $A$  is the relevant surface area of the emitter. A typical Fowler-Nordheim plot for a tungsten tip appears in Fig. 3.3.

Using Eqn. 3.10, we can determine the field at the surface of the tip and find an estimate of the end radius of the tip. Now a plot of  $\ln(\frac{I}{V^2})$  versus  $\frac{1}{V}$  should be linear with slope  $m$ . From the slope we can determine  $\beta$  by

$$\beta = - \frac{0.683\phi^{3/2}}{m} s(y) , \quad (3.11)$$

where the tabulated function  $s(y)$  is given by [75–77]

$$s(y) = v(y) - \frac{y}{2} \frac{dv(y)}{dy} . \quad (3.12)$$

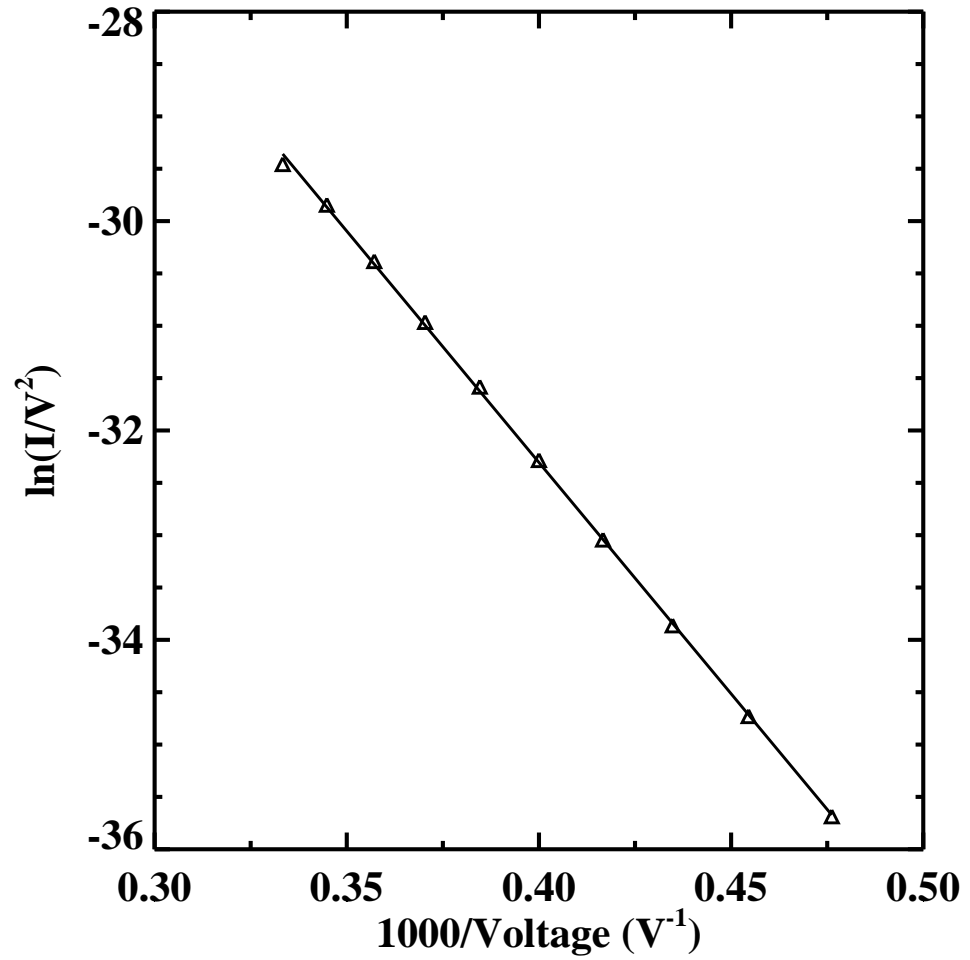


Figure 3.3. A Fowler-Nordheim plot for a W tip. The value of beta, as determined by iteration, is  $\beta \simeq 14.3 \times 10^3 \text{ cm}^{-1}$ . The best fit here gives a value for the electric field of  $3.64 \times 10^7 \text{ V/cm}$ . Thus, we determine the end radius of the emitter to be  $r \simeq 140 \text{ nm}$ .

### 3.1.2 Total Energy Distributions

Measurement of the total energy distribution (TED) of emitted electrons, also called the field emission energy distribution (FEED), gives insight into the underlying electronic structure of the emitter. [74–76] To measure the TED, an analyzer capable of counting electrons at a specific energy replaces the screen in a FEM experiment. Fig. B.3 shows a schematic of the chamber and the cylindrical sector analyzer (CSA) used for TED measurements.<sup>1</sup> The CSA and its control electronics are computer interfaced with the commercially available software, SPECTRA. Thus, all of the distributions were digitized as they were acquired.

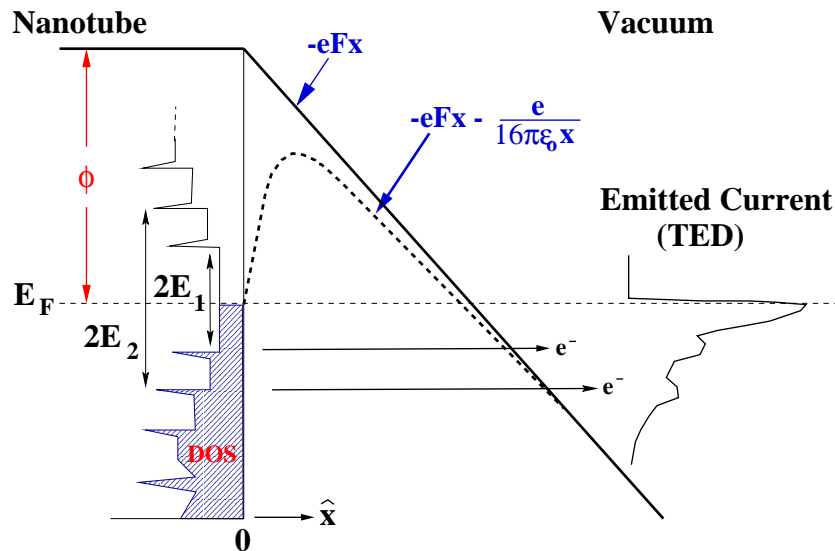


Figure 3.4. A schematic representation of the field emission illustrating the contribution of the density of states to a total energy distribution, shown at the right.

Illustrated in Fig. 3.4 is the basic mechanism of field emission and the contribution of the localized electronic states of the emitter. In this figure, we assume the singularities in the DOS (see Figs. 2.8(b) and (d)) persist at the uncapped end of the nanotube. This assumption is consistent with calculations presented by De Vita *et al.* which suggest that the singularities soften into peaks (but do not disappear) at

<sup>1</sup>The analyzer used is a commercially available Omicron CSA-300 electron energy analyzer.

the uncapped end. [78] The presence of a peak in the density of states at a particular energy level increases the relative number of electrons emitted at that energy level.

For a metal, free electron theory relates the emitted current density to the energy relative to the Fermi energy ( $\epsilon = E - E_F$ ) by [75]

$$j(\epsilon) = \frac{J_o}{d} e^{\epsilon/d} f(\epsilon), \quad (3.13)$$

where  $f(\epsilon)$  is the Fermi-Dirac distribution function.  $J_o$  is the current density at  $T = 0^\circ K$ , given by Eqn. 3.7. [75, 79] The parameter  $d$  (in eV) is related to  $F$  and  $\phi$  by [75, 79]

$$\frac{1}{d} = \frac{2\sqrt{2m\phi} t(y)}{\hbar e F} = 1.025 \times 10^8 \frac{\sqrt{\phi} t(y)}{F}, \quad (3.14)$$

where  $t(y)$  (with  $y = \frac{\sqrt{\epsilon^3 F}}{\phi}$ ) is a tabulated dimensionless constant that takes into account the surface barrier lowering by the applied electric field. In order to fit an experimental TED, Eqn. 3.13 must be convolved with a gaussian function, [80]

$$\Theta = \frac{1}{\sigma\sqrt{2\pi}} e^{-\epsilon^2/2\sigma^2}, \quad (3.15)$$

to represent the finite energy resolution of the analyzer. The full-width at half-maximum (FWHM) of the analyzer,  $\Gamma$ , is given by  $\Gamma = 2.356\sigma$ . Shown in Fig. 3.5 is the TED for a tungsten emitter with a fit to the data. Using the average work function for W of  $\phi = 4.54$  eV gives a value for  $\Gamma$  of 0.80 eV. The convolution of the Fermi-Dirac distribution with the energy resolution of the analyzer determines sharp leading edge of the TED. The broader trailing edge is largely the result of the exponential decrease with energy of the transmission function for electrons penetrating through the surface potential barrier.

As illustrated in Fig. 3.4, localized peaks in the density of states of the emitter manifest themselves as bumps in the trailing edge of a total energy distribution. A peak in the DOS at a particular energy increases the transmission probability at that energy. Thus, any feature on the trailing edge of a TED implies a corresponding feature in the DOS of the emitter. [76] As shown in Fig. 2.8, nanotubes have very sharp features in their DOS due to the 1D nature of their electronic structure. These

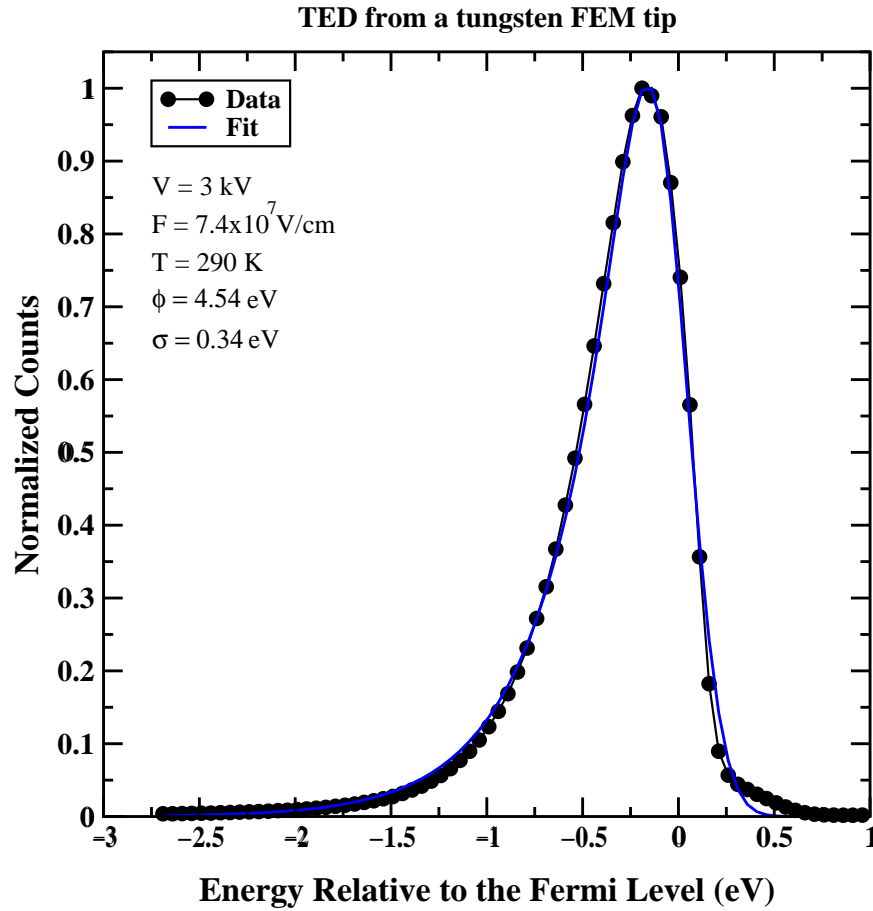


Figure 3.5. The TED for a tungsten FEM tip. Plotted are the detected counts versus the electron energy relative to the Fermi level ( $E_F = 0$ ). Also shown is a fit to the data, which gives a FWHM of 0.80 eV for the energy resolution of the analyzer.

features should be observable in the TED from a nanotube field emission tip. It may also be possible to distinguish between semi-conducting and metallic nanotubes by the location of the leading edge of the TED. The finite DOS at the Fermi energy of a metal will produce a TED with a leading edge located at the applied voltage of the emitter, minus the work function of the energy analyzer. A semiconductor will produce a TED with a leading edge that is shifted by an additional amount  $E_g/2$ , where  $E_g$  is the band gap of the semiconductor. Thus, the electron energy distribution may contain important information about a nanotube's electronic properties.

### 3.1.3 FEM Chamber

For our field emission studies, we use a UHV chamber specifically designed for the study of nanometer-sized objects. Within this chamber we are able to perform FEM, FIM (Field-Ion Microscopy), and TED measurements. Figs. B.1 and B.2 are photographs of the chamber, and Fig. B.3 shows a schematic of the chamber. We mount the tip/nanotube assembly within the chamber to an XYZ- $\Theta\Phi$  manipulator, giving us translational and rotational freedom with the tip. The entire chamber, including the phosphor screens, is at ground, and the high voltage is applied to the tip through UHV feedthroughs. We apply the bias voltage to the emission tip using very stable Fluke and Spellman power supplies. The emitted current is measured with a Keithley 485 picoammeter. The picoammeter operates with battery power, allowing it to float at the applied bias. Thus, we can measure the current flowing out of the tip, rather than the current striking the screen. This method provides a more accurate measure of the current since not all of the emitted electrons strike the screen. We take careful precautions to properly isolate the picoammeter from ground and ensure that there are no current leakage paths.

For normal FEM work, we use a UHV grade phosphor screen. The electrons striking the screen must have an energy of  $\sim 250$  eV or greater. For normal emitters, this energy requirement is easily satisfied. However, since nanotubes are so sharp, they sometimes emit electrons at very low voltages. When the electron emission occurs at a voltage too low to give the electrons enough energy to excite the phosphor, we use a multi-channel plate (MCP) electron amplifier integrated with a fluorescent screen. The MCP screen produces a higher quality image than the phosphor screen, so we also use the MCP screen for higher resolution imaging. Figs. B.1–3 indicate the locations of each of these screens. In each situation, the tip to screen distance  $R$  is approximately 13 cm. Since the FEM is essentially a point projection microscope, it has a magnification  $\mathcal{M}$  given by [73]

$$\mathcal{M} \simeq \frac{R}{\rho r_{tip}}, \quad (3.16)$$

where  $r_{tip}$  is the end radius of the emitting object. The dimensionless factor  $\rho$  accounts

for the compression of the field lines which the electrons follow, due to the presence of the tip shank. We can calculate this compression if the electron paths are known, but it is usually much simpler to estimate  $\rho$  directly from an FEM micrograph. A value of 1.5 is typical for conventional metallic emission tips. The resulting image deformation is axially symmetric and almost uniform over the emission pattern. Thus, near linear magnifications on the order of  $10^5$ – $10^6$  are readily achieved. [73]

### 3.2 FEM of Multi-walled Nanotubes

Our study of the electronic properties of carbon nanotubes began with field emission from a SWNT rope. [10, 11] Fig. C.1 shows the SWNT rope used in our study. This is one of only two quality ropes successfully mounted to an FEM tip in the space of a year. Due to the difficulty of mounting SWNT ropes, we turned our attention to field emission from MWNTs. Multi-walled nanotubes often have diameters which are larger than the diameter of a SWNT rope. Thus, a multi-walled tube is easier to mount to the end of a FEM tip.

#### 3.2.1 Sample Fabrication

The method used to mount a MWNT is the same as that for mounting a SWNT rope and is similar to the procedure described by Dai *et al.* [81] First, a 0.003 in. diameter Pt wire is spot welded to a small stainless steel tab, as illustrated in Fig. D.3. By using the steel tabs, we are able to manipulate the samples without damage and are able to transfer the samples from the TEM to the FEM with the same sample mount. The tips are formed by etching and zone electro-polishing the Pt wire in a saturated  $\text{CaCl}_2$  solution to an end radius of  $\sim 100$  nm. [82] Then the tubes are attached to the tips by using an inverted optical microscope (Nikon Epiphot 200) equipped with a 50X/0.55 objective to observe the process in dark-field at 750X magnification. Bolted onto the microscope stage, two micro-manipulators (Newport M-460A-XYZ) are used to attach the nanotubes to the Pt field emission tips. Photographs of the microscope, stage, and holders appear in Appendix D. This microscope configuration permits one to “see” the nanotubes, which have diameters much less than the average wavelength of light, but lengths of several microns.

We show a schematic of the fabrication configuration in Figs. 4.1(a) and (b). The nanotube source consists of a small copper foil with one edge wrapped with a conductive adhesive (SEM tape), onto which the nanotubes (MWNTs or SWNTs) have been deposited in several places. This nanotube tape contains thousands of nanotubes with one end protruding from the edge of the tape (see Fig. 4.1(a)). The nanotube tape and a Pt tip are mounted onto opposing micro-manipulators. Prior to mounting a nanotube, it is useful (but not necessary) to transfer a small amount of the SEM tape to the Pt tip by touching the tip to a clean portion (no nanotubes) of the adhesive and carefully removing it. This process leaves a thin coating of the adhesive on the end of the tip. Although the amount of adhesive is not usually visible in the optical microscope, it is easily seen in the TEM.

The mounting procedure consists of bringing the etched tip in the vicinity of a desired nanotube. The tip is then brought into contact with the nanotube. SWNT ropes and individual MWNTs are usually less than  $\sim 20$  nm in diameter and often cannot be seen in the dark-field microscope. Thus, contact to a rope or individual tube is realized when movement of the Pt tip produces movement in a visible part of the nanotube source. At this moment, the Pt tip is connected to the visible source through an invisible nanotube or rope. Electrical connections to the tip and the copper foil allow for the application of a voltage bias (Fig. 4.1(a)). The bias (and humidity) facilitates the adhesion of the nanotube to the Pt tip. A small DC bias ( $\sim 10$ – $15$  V) is then applied between the tip and nanotube source. With the bias applied, the tip is slowly pulled away from the source. The tip may slide along the nanotube for a short length. When successful, the tip/nanotube sliding will stop and the nanotube will slide or break free from its anchor (Fig. 4.1(b)).

We often observe a visible emission of light or spark during this break-off procedure, implying the presence of a localized, intense electrical arc. If the spark occurs in the space between the tip and the source, then sometimes a portion of a nanotube or rope is left attached to the Pt tip. We confirm the presence of a nanotube or rope of nanotubes using a TEM. It is important to note that the spark-removal

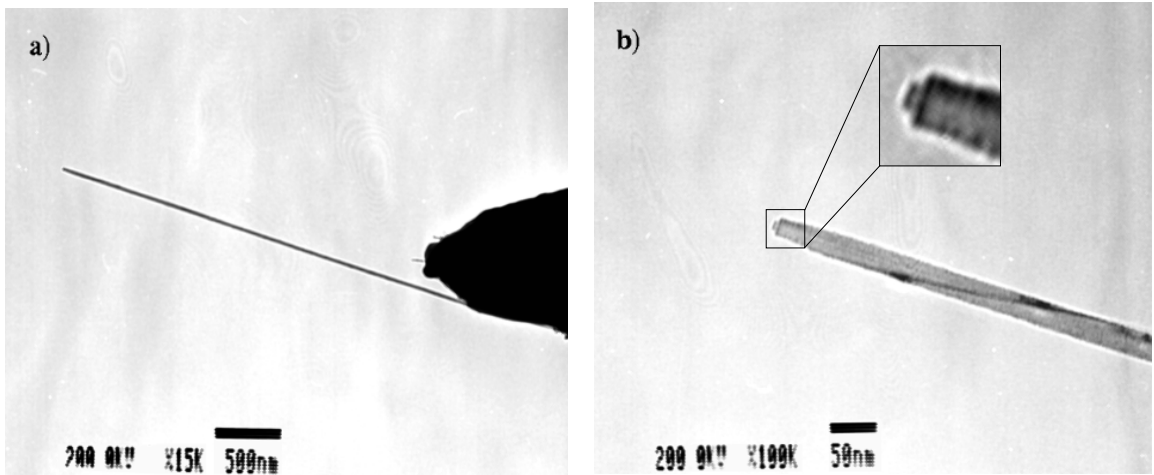


Figure 3.6. TEM images of a typical MWNT sample used in this study. a) An individual MWNT is attached to the end of a Pt FEM tip. The portion of the MWNT extending from the tip is  $\sim 3.3 \mu\text{m}$  long. b) A higher magnification of the end of the tube. The outer diameter of the tube is  $\sim 25 \text{ nm}$ . The inset is a zoom of the end of the tube, showing an inner section  $\sim 13 \text{ nm}$  in diameter extending  $\sim 6 \text{ nm}$  further than the outer section.

of the tube from the nanotube source breaks the tube somewhere along its length. Therefore it is likely that the tube remains open and does not close, as has been reported elsewhere. [83–85] Fig. 3.6 shows TEM images of one sample. In Fig. 3.6(b), we see that the end of the MWNT is not closed. After inspection of the nanotube, the tip/nanotube sample is inserted into the FEM chamber.

### 3.2.2 FEM of Multi-walled Nanotubes

Many studies of field emission from carbon fiber tips [86–88] and arrays (i.e., films) of carbon nanotubes appear in the literature. [87, 89–93] Reports of field emission studies of single MWNTs [94–96] and SWNTs [97] also have appeared. The work reported here builds on these previous studies, many of which were performed at relatively high pressures of  $10^{-4}$ – $10^{-7}$  Torr. [89, 90, 94] At these pressures, it is possible that background gases could be responsible for some of the observed instability in the emitted current and degradation of the nanotube. [88, 89, 96] For example, in contrast to carbon fiber tips, [88] reports claim that carbon nanotubes burn out or

“unravel” at emission currents greater than  $\sim 1 \mu\text{A}$ . [94] Here we describe results that characterize the electron emission properties of individual MWNTs. To ensure a clean test environment, we performed the measurements at operating pressures of  $< 2 \times 10^{-9}$  Torr.

The MWNTs studied here were first imaged using the UHV phosphor screen. Often the end radii of the MWNTs were less than 20 nm, and thus, they began field emitting at extremely low voltages (i.e.,  $\sim 200$  V at a tip to screen distance of  $\sim 13$  cm). As mentioned in Section 3.1.3 the electron beam was often not energetic enough to excite much of the phosphor, so the resulting field emission image was relatively weak. Then the MWNTs were imaged using the MCP. FEM and TED measurements were made on several samples, all of which displayed similar behavior. In this report, we discuss only the data for the MWNT sample shown in Fig. 3.7.

This MWNT was found to emit at voltages around 250 V, roughly 10 times less than a typical tungsten emitter. We recorded the field emission pattern using the MCP, and Fig. 3.8 shows a plot of the constant-intensity contours of the field emission image produced by the MWNT. Although striations or banding in the field emission patterns were reported for SWNT films and attributed to capped nanotubes, [4, 93, 98] we observed no such patterns here. The observed field emission patterns were relatively stable and continuous, although we sometimes observed flicker in the image. As discussed in Section 3.1.1, the field emission pattern often reveals the underlying symmetry of the emitter. However, we attribute the oval shape of the MWNT emission pattern in Fig. 3.8 to the misalignment of the end of the nanotube with the MCP screen due to the limited motion of the manipulator combined with the  $\sim 18^\circ$  angle of the MWNT relative to the Pt tip (as determined from Fig. 3.7(a)).

After studying the emission patterns, we performed a Fowler-Nordheim analysis on the MWNT. A representative Fowler-Nordheim plot of data from the MWNT is shown in Fig. 3.9. The slope of the plot has a slight curvature, perhaps indicating that the standard Fowler-Nordheim theory may not apply. It may not be strictly applicable because of the small radius of the MWNT [99] and the possibility that the

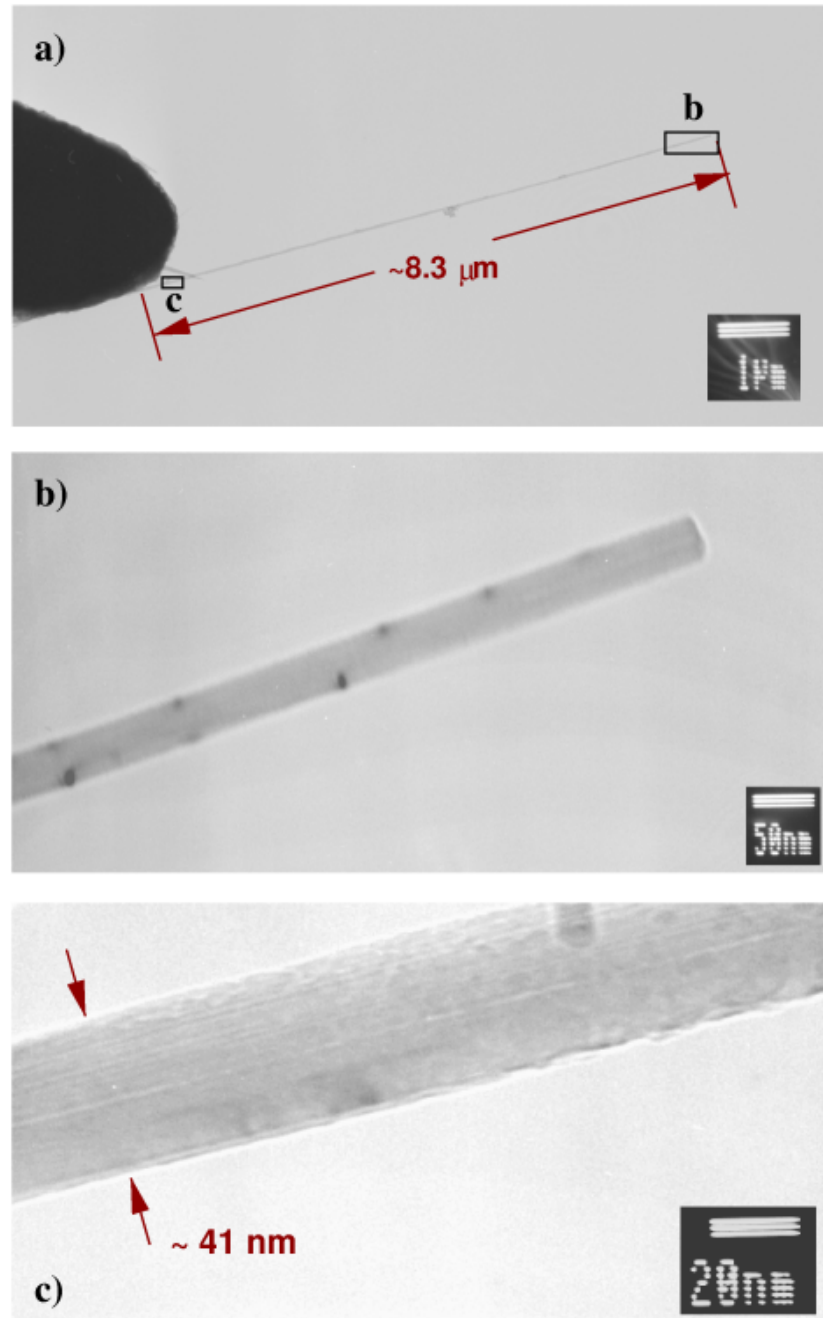


Figure 3.7. TEM images of an individual MWNT mounted to the end of a Pt FEM tip. In b) the end of the nanotube seems to be cut off flat. From image c) the MWNT diameter appears to be  $\sim 41 \text{ nm}$ .

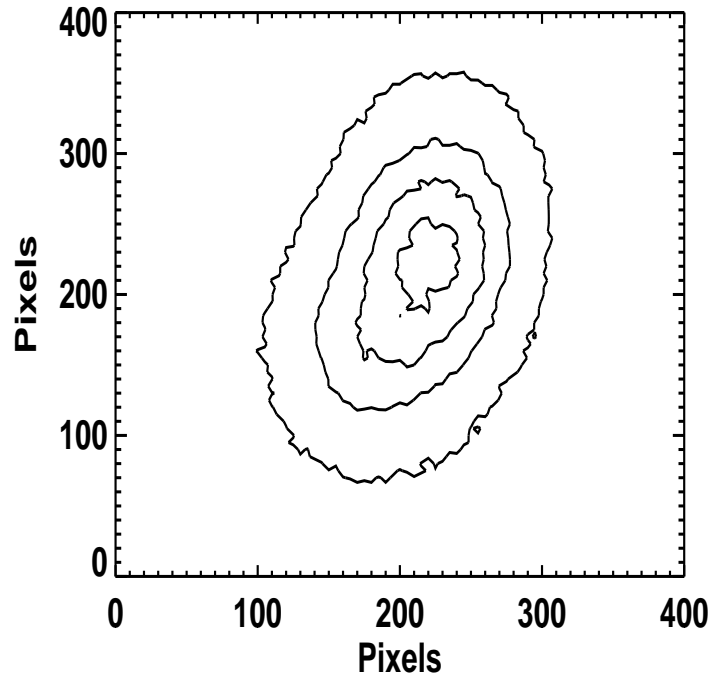


Figure 3.8. A plot of constant-intensity contours of the FEM image from the MWNT shown in Fig. 3.7. The oval shape is believed to stem from the end of the MWNT not being parallel to the imaging screen.

emitting nanotube may be semiconducting.

With the slope of the linear fit to the data in Fig. 3.9, we determined the value for  $\beta$  by iteration using Eqns. 3.1 and 3.11. Assuming a work function of  $\phi = 5.1$  eV, we determined the value for  $\beta$  of  $1.7 \times 10^5$  cm<sup>-1</sup>. It is not clear that this value is reliable because of the curvature in the Fowler-Nordheim plot. Using a radius of  $r_{tip} = 20.5 \pm 0.5$  nm (as measured from the TEM shown in Fig. 3.7) we estimate that  $\beta = (9.8 \pm 0.4) \times 10^4$  cm<sup>-1</sup> from Eqn. 3.2. Using this value for  $\beta$  and the slope of the Fowler-Nordheim plot, we can invert Eqn. 3.11 to solve for the work function of the MWNT emitter. Iteration yields an estimate of  $\phi = 3.6$  eV. This value is not consistent with a metallic nanotube, which is expected to have a work function similar to that of graphite, i.e.,  $\sim 5.1$  eV. However, given the uncertainty in the value

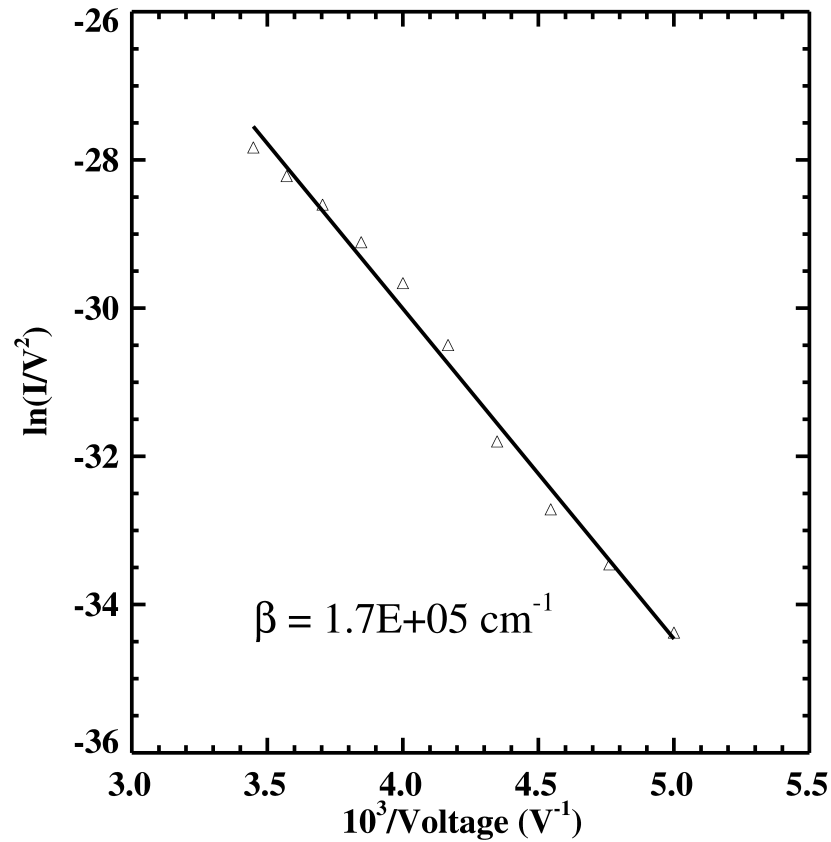


Figure 3.9. A Fowler-Nordheim plot for the MWNT shown in Fig. 3.7. The slope of the MWNT data is not a straight line, indicating that the field emission process involved here may not follow the standard Fowler-Nordheim theory for a metal.

of  $k$  for this MWNT (see Eqn. 3.2) which has an end form geometry much different than that of a normal emitter the factor of 2 difference in  $\beta$  may be reasonable.

A peculiar feature of the FEM from this MWNT is that its emission current was found to change erratically with time. At several applied voltages the current jumped by as much as an order of magnitude. Most of the jumps in current were by a factor of about 2, either up or down. The frequency of the jumps did not correlate with the applied voltage. Sometimes increasing the applied voltage by 10 V caused the current to drop to a lower level and stabilize. Sometimes the current was stable

for up to 30 minutes, but the erratic behavior usually returned. At liquid nitrogen temperatures the instability in the emission current did not decrease, although with our current system the lowest temperature achievable is about 100 K. Perhaps much lower temperatures are necessary before any change in the stability of the current will be seen. The other MWNTs we studied also exhibited this current instability, although the SWNT rope did not. [10, 11] We summarize the results in Table 3.1, including the values for a tungsten emitter for reference.

Table 3.1  
Field emission results for carbon nanotubes. Typical values for a tungsten emitter are provided for comparison.

Emitter	V needed for 1 nA	End Radius (nm)	Current Stability
W	2100 V	140	Stable
SWNT	250 V	8.5	Stable
MWNT #1	235 V	20.5	Unstable
MWNT #2	175 V	7	Unstable
MWNT #3	275 V	15	Unstable
MWNT #4	210 V	10	Unstable

### 3.2.3 TEDs from Multi-walled Nanotubes

In order to obtain information regarding its DOS, we also measured the TED for this MWNT. We shown a schematic of the chamber and analyzer in Fig. B.3. We centered the emission current from the MWNT over the entrance to the analyzer by using a rate-meter to maximize the detected counts at the Fermi energy (roughly the applied voltage minus the analyzer work function). We then recorded the counts as a function of measured kinetic energy using commercial control software. The entrance and exit slits of the analyzer were set to maximize the energy resolution. Since the MWNT field emitted at voltages less than 360 V, we used the lowest pass energy of the analyzer (1 eV) for the TED measurements.

The TEDs from the MWNT were found to have peaks in the trailing edge, several of which persisted over time. These peaks may be associated with features in the DOS of the emitting nanotube. However, the energy location of these features changed from one TED to another. The peak structure in the TEDs changed with applied bias. Interestingly, the shape of the TEDs also changed with the current level. This is well demonstrated in Fig. 3.10, where the current as a function of time is given with the TED for each region.

At the time the data was taken, we could not safely digitize the emission current in real time, which was plotted on a chart recorder, so we reproduced it schematically. This behavior is similar to that reported for carbon fibers, where the TEDs also varied with the emitted current. [88] This may suggest that MWNTs have properties more like graphite than SWNTs, which do not display these fluctuations. [10, 11] At this voltage, the TEDs appeared most free-electron-like when the emission current was highest (region 11 at  $\sim 170$  nA and region 13 at  $\sim 190$  nA).

At present, the source of the noise in the emission current is not clear. Determining the source of noise is essential due to the great interest in MWNTs for flat-panel displays and other field emission applications which require stable emission currents. If instability is inherent in the MWNTs, this will have a significant impact on their possible applications. Of the possible sources of noise, first, we discuss those not intrinsic to the MWNTs. The measurement of all TEDs were performed in a UHV environment. The typical pressure of the chamber during field emission is  $< 2.0 \times 10^{-9}$  Torr. Thus, it is unlikely that residual gas in the chamber caused the current instability. In fact, for a W field emission tip, gas adsorption onto a clean emission surface has been well studied. As gases adsorb onto the emitting surface the emission current decreases, but for low levels of gas adsorption no abrupt changes occur. More importantly, low levels of gas adsorption do not appreciably alter the shape of the TED of a W tip, they simply decrease the number of detected electrons. If the emitting tip is heavily contaminated, then the field emission current can become unstable. However, due to the low chamber pressure and observation of current

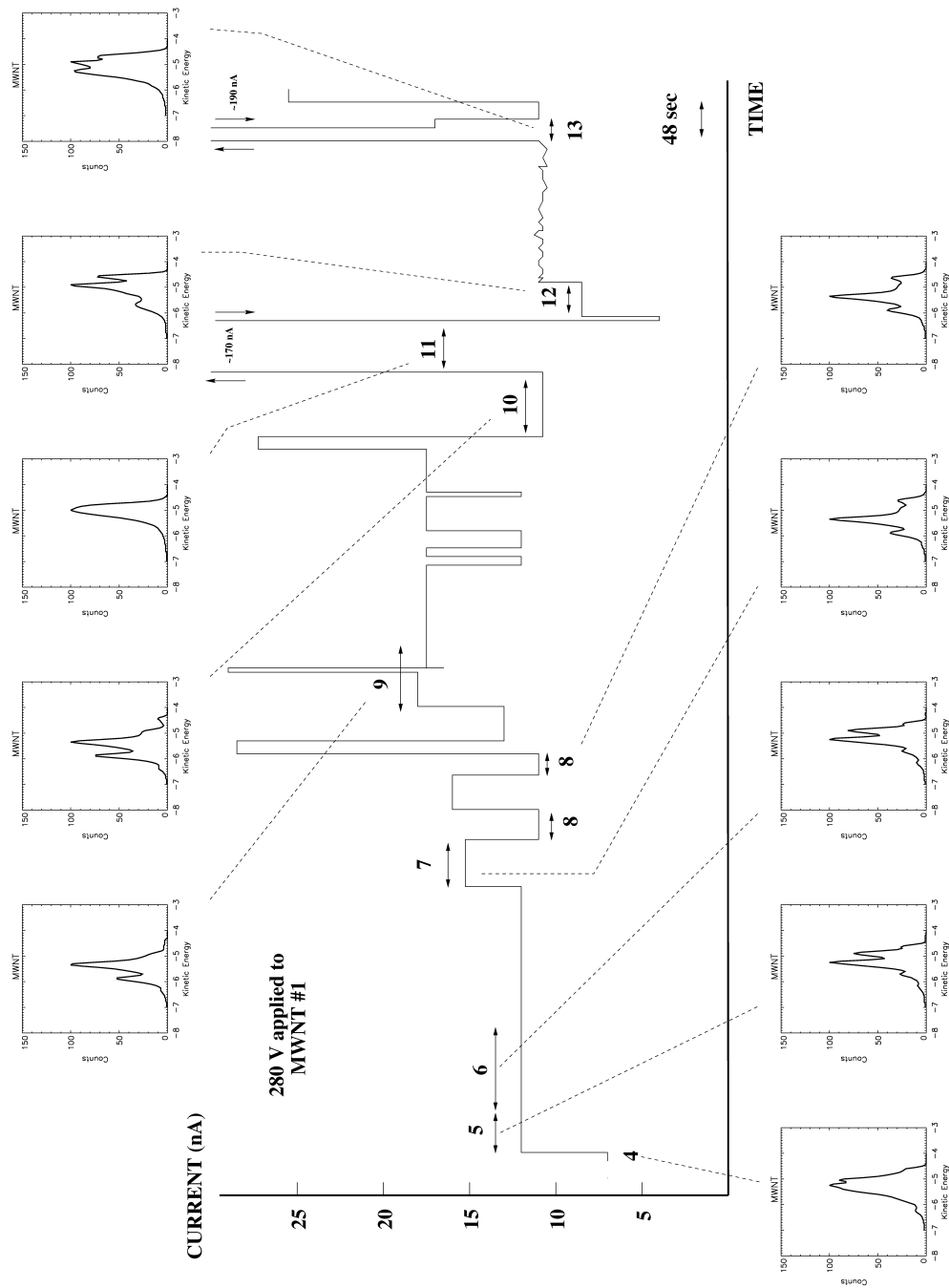


Figure 3.10. A schematic of the field emission current from MWNT No. 1 as a function of time. Also shown are the TEDs measured at various levels of the current. The dashed lines show the corresponding current level for each TED. These TEDs were taken at room temperature with  $-280$  V applied to the MWNT. The zero of the  $x$ -axis in the TED plots is set at the applied voltage, giving the Fermi energy of the tube at about  $-4.52$  eV.

fluctuations in all MWNT samples, we believe that the residual chamber gases are not the source of the MWNT current instability. Also, in a previous study, we found the field emission current and the measured TEDs for a SWNT rope to be stable and reproducible for over a week. [10, 11] This provided further evidence that the stability is not related to the residual chamber gases. Another possible noise source could be instability in the high voltage power supply. We checked and found the power supplies to be stable. Again, any noise here would not explain the change of the features in the TEDs of the MWNTs. Furthermore, we would have also detected the noise in the power supplies during the SWNT FEM experiment.

The electrical contact between the Pt tip and the MWNT is yet another possible external source of noise. During the mounting process for these MWNTs, we used a small amount of conducting adhesive (SEM tape) as glue to attach the MWNTs. Since the glue is sticky enough, sometimes it is not necessary to spark the nanotube free of the boule. It is possible, however, since we use only a small amount of glue, that the MWNT is only weakly coupled to the Pt tip. Thus, an intermittent contact resistance could explain the current instability. For an ohmic contact at a constant voltage, the resistance must change by half to achieve a factor of 2 increase in the current. For 280 V and a emission current of about 14 nA (see Fig. 3.10), we estimate a resistance of  $\sim 20$  G $\Omega$ s. Thus, the contact resistance would need to change by 10 G $\Omega$ s, a value too large to be reasonable. We find a better estimate since, for field emission, the relationship between voltage and current is given by Eqn. 3.10. Using a Fowler-Nordheim plot for a MWNT, we can estimate that a 10 volt change is needed to produce a factor of 2 change in the current. For typical current values, this requires the contact resistance to change by several hundred kilo-ohms. In both cases, the changes in the contact resistance are extremely high.

Furthermore, a changing contact resistance still does not provide a clear explanation for the changing features in the measured TEDs. It could be possible that the glue is providing intermittent current paths to different shells of the MWNT. An instable contact of the tube to the Pt tip could cause switching between different

current channels down the length of the MWNT. If the glue contact is the source of the noise, it is odd that the same instability was not exhibited by the SWNT rope. At present a method for making a more stable electrical contact at the Pt/MWNT junction is still in progress.

Other possible explanations of the current instability stem from the intrinsic properties of the MWNT itself. The MWNTs used in this study are known to have defects, as seen in the high magnification image of Fig. 3.7. It should also be noted that the TEM itself can create defects in the MWNTs, or even completely destroy them. It is also possible that the TEM creates defects which are not visible in the images. Defects in the nanotubes could cause the current path to switch between different shells. Often the fluctuations in the emission current are similar to the fluctuations in random telegraph noise (RTN), where a system switches between two or more states at random. Each of these states would have its own current path and thus, would possibly display different energy distributions. In the absence of defects, we expect that the current does not travel from one shell to another within a single MWNT. The inter-layer resistivity of a MWNT should be similar to that of graphite where the inter-planar resistivity is  $2-8 \times 10^3$  times larger than the in-plane resistivity. [100] Vibrations of the MWNT could aid in this switching, although the vibration frequency of a carbon nanotube should be on the order of many kilohertz. Vibrations of this frequency are unobservable in the time it takes to record one TED.

Another source of internal fluctuations could stem from the adsorption of oxygen or other gases in the MWNTs. Sumanasekera *et al.* recently reported significant changes in the resistance of SWNT ropes which were heated to 500 K then exposed to various gases, such as nitrogen and helium. [101] The resistance decreased over time at a constant temperature, indicative of a degassing process. As amounts of  $N_2$  and He were introduced to the ropes, the changes in resistance were believed to result from the gas collisions with the walls of the SWNTs. [101] If MWNTs are as sensitive to residual gas collisions, then the fluctuation of the emission current could be related to collisions with the small amount gases present in the UHV chamber at

$10^{-9}$  Torr. In addition, the MWNTs were never heated under vacuum to degas the nanotubes. Thus, the MWNTs could be oxygen doped, which may lead to current instabilities related to the diffusion of the oxygen within the sample.

Another explanation for the instability, based on the intrinsic properties of a MWNT, comes via comparison to the experiments of Binh and Purcell. [99]. In their experiments on nanotips, they found similar instabilities in the emission current and concomitant changes in the measured TEDs. Similar to MWNTs, the emission current from metal nanotips (ending in a single atom) is believed to come from localized energy bands at the surface of the tips. Such an emission process would enhance local heating at the tip, induced by the emission current. If this local heating is large enough, the atomic structure at the end of the MWNT could be changed. Such changes in the atomic structure of the tip would have to be un-resolvable in the TEM, as TEM studies of the MWNT tips before and after FEM experiments show no change in the tip structure.

Changes in the emission current and the measured TEDs would be related to changes in the local density of states at the end of the MWNT. Several reports show calculations illustrating how the density of states (DOS) varies near the capped [32, 53, 78] and uncapped [78] end of a nanotube. Calculations also show that defects at the tips of nanotubes create additional states. [24, 102] These features would assist local heating of the tip due to current emission from localized energy bands in the nanotube. One implication of this local heating mechanism is that the emission current must be kept below a threshold level ( $\leq 1$  nA for the metal nanotips in Ref. [99]) in order to keep the current stable.

To investigate the possibility that the current noise is an inherent property of MWNTs (whether caused by defects or otherwise) or a property of the electrical contact to the nanotube, we devised another independent experiment. Chapter 4 discusses the technique developed for measuring the conductivity of multi-walled carbon nanotubes directly.

## 4. ELECTRONIC TRANSPORT MEASUREMENTS

As mentioned in Chapter 1, the electronic transport properties of carbon nanotubes is a subject of much interest. Yet, difficulties in studying the properties of individual nanotubes arise from their nanometer dimensions. It is difficult to make good, reliable electrical contacts to a carbon nanotube. Most of the methods used to fabricate electrodes center on the use of electron-beam lithography. If the electrodes are predefined, then nanotubes are dispersed over the entire substrate, which must then be scanned to find a nanotube bridging two or more contacts. [5, 35–38, 45, 103] This technique is of limited use because it requires the serendipitous deposition of the nanotubes across the contacts. Also, this technique results in weak contact to the nanotube. If the electrodes are not already predefined, they can be placed on top of the nanotubes which have already been dispersed on the substrate. [37, 40–42, 104] Although this technique removes the chance involved in the other method, it requires that the nanotube be coated in electron beam resist. After developing and dissolving the resist, it is not clear that only a pure carbon nanotube remains between the contacts.

To address some of the issues mentioned above, we developed a simple technique for fabricating contacts to small ropes of multi-walled nanotubes. [68] This technique allows reliable electrical contacts to be made to both ends of a MWNT. We essentially combined a simple shadow mask technique, developed by Pedro de Pablo, [105] with our ability to manipulate individual MWNTs (as described in Chapter 3). Using our technique, we have studied the electrical conductance of MWNTs as a function of applied bias and temperature. A systematic study of the temperature dependence of the electrical conductance is necessary to better understand the factors which govern electron transport through nanotubes. Such studies, made with reliable contacts, also

will provide insight into the further use of nanotubes in nano-electronic applications. This Chapter describes the sample fabrication technique and the room temperature transport data obtained with the resulting samples. Chapter 5 describes the temperature dependent measurements and the conductance data obtained.

## 4.1 Sample Fabrication

Our method for making electrical contacts to nanotubes relies on the ability to manipulate individual or small ropes of nanotubes, to place them on an insulating substrate, and to position a shadow mask across the nanotube. We made most of our samples using MWNTs, although we have also made samples with networks of SWNTs. The sample preparation process is schematically illustrated in Fig. 4.1.

### 4.1.1 Tip and Substrate Preparation

The first step in the process is the fabrication of several field emission tips. Usually made from platinum, we use the tips to select and mount the desired nanotube. The end radius for the tips is usually on the order of 100 nm. An example of a typical tip, with an attached MWNT, is shown in Fig. 3.7. Since the tips are easily damaged, we prepare several tips before starting to make samples.

The next step is to prepare the substrates. We developed this fabrication process with the use of an inverted dark-field microscope. We first used transparent substrates because we placed the nanotubes on the surface opposite the microscope objective. However, we have developed a procedure which places the nanotubes on the surface facing the objective, thus lifting the transparent substrate requirement. Since the latter process is more difficult, we use the former method more commonly. All of the data reported here was taken using No. 1 (0.17 mm thick) or No. 2 (0.25 mm thick) glass cover-slips (Corning). The sizes ranged from 9 or 18 mm squares to disks of 12 mm diameter. Before measurements could be made, the 18 mm squares were cut to 9 mm squares using a diamond scribe. As illustrated in Fig. 4.1, the fabrication process described here is for the 12 mm disks, for which we designed a special mount. Dust is the main problem encountered with the cover-slips. In the sample preparation room, even after their immediate removal from the center of a

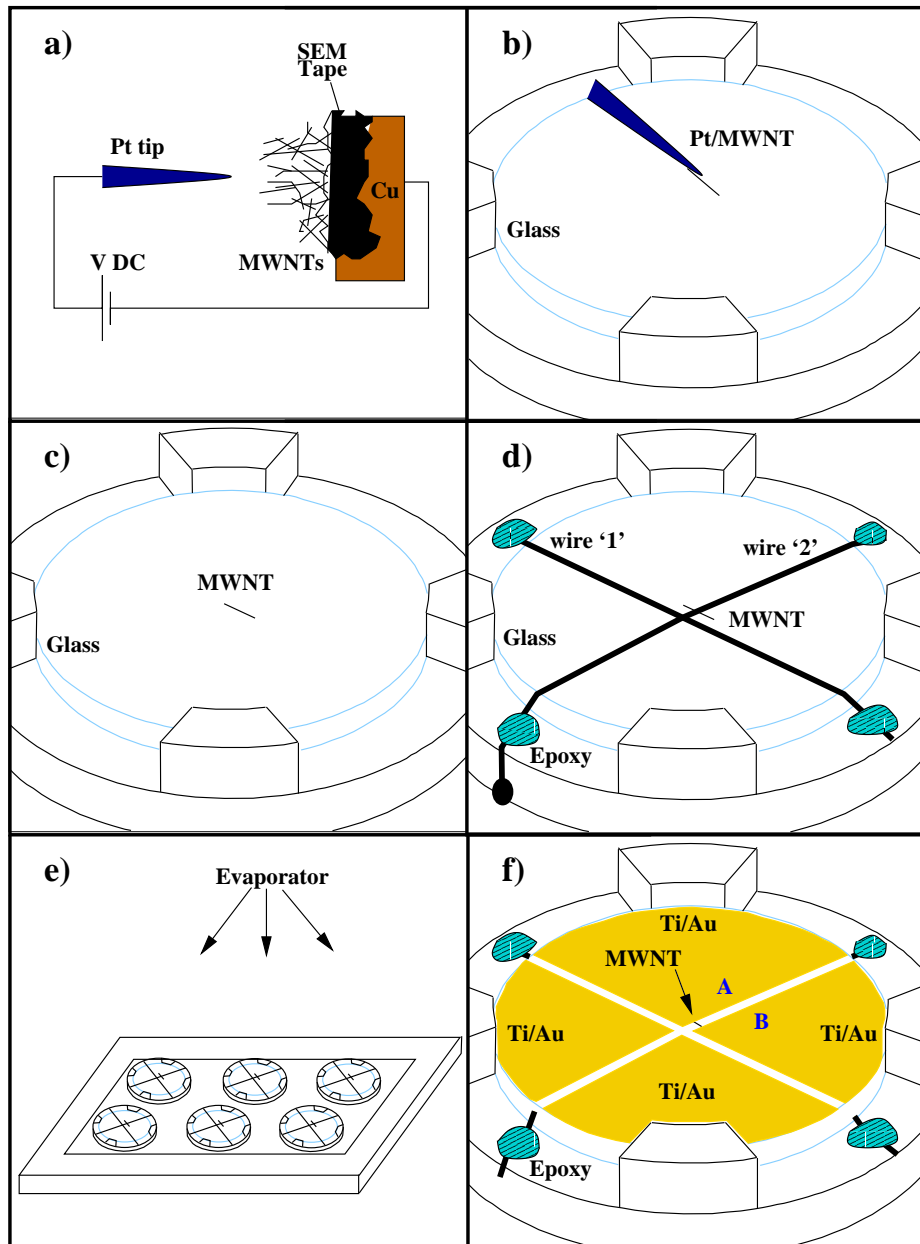


Figure 4.1. A schematic of the sample fabrication procedure showing a) the selection and removal of a MWNT, b) a MWNT adhering to the etched Pt tip, c) the transfer of the MWNT to a glass substrate d) the placement of a riser wire (wire '1') parallel to the MWNT followed by the shadow mask (wire '2') perpendicular to the MWNT, e) e-beam evaporation of a thin metal film onto the ends of the MWNT, and f) the final sample after removal of the wires. The electrical contacts to the MWNT are labeled A and B.

storage container, micron-sized or larger dust particles littered the cover-slips. Before using these cover-slips, we removed most of these particles using Fisher or Kodak lens paper. However, it is necessary to leave a few particles on the glass surface in order to be able to focus the microscope objective on the surface.

#### 4.1.2 Nanotube Selection and Placement

In Section 3.2.1 we describe the procedure for selecting and mounting a nanotube in detail. Figs. 4.1(a) and (b) illustrate this procedure. For fabrication of the transport samples, the section of the nanotube attached to the tip must be greater than  $4\ \mu\text{m}$  long, since this is the minimum size of the shadow mask used. It is believed that the spark-removal of the nanotube opens the ends, which do not re-close, possibly due to carboxylic acid groups which bond to the end.

After attaching a nanotube to the Pt tip, we remove the nanotube source from the micro-manipulator (Newport M-460A-XYZ). We attach the cover-slip substrate, in its holder, to a second micro-manipulator. The substrate is centered approximately over the microscope objective, and the base of the Pt tip is bent so that the nanotube is closest to the substrate. Then the tip/nanotube is carefully lowered to the substrate. Care must be taken to focus the microscope on the correct side of the cover-slip. Since we are looking from underneath the sample, the first surface in focus is the bottom of the substrate. The next visible surface is the top (for which the nanotube is intended), followed by the reflection of the bottom surface.

We can position the nanotube with better than  $10\ \mu\text{m}$  lateral resolution on the surface, and we lower the nanotube until its end touches the glass substrate. Then we lower the tip more while moving it away from the touching end of the nanotube. The nanotube will stay attached to the tip, sliding along the substrate, until enough of its length is in contact with the cover-slip so that it sticks and the tip slides away (Fig. 4.1(c)). We then remove the Pt tip.

### 4.1.3 Support Wire Placement

After placing the nanotube onto the cover-slip, we stretch a 4  $\mu\text{m}$  tungsten wire<sup>1</sup> across the center of the substrate and hold it under tension (Fig. 4.1(d), wire ‘1’). This is facilitated by attaching a small weight ( $\sim 5$  mm diameter solder ball) to one end of the wire and holding the other end with a miniature alligator clip in the opposing micro-manipulator. If necessary, we clean the wire by dipping it in ethanol. The substrate is positioned by use of a special sample mount, designed to hold the cover-slip in a fixed position throughout the sample preparation process. Using this sample mount, we glue the wire to the mount and not to the cover-slip as in Fig. 4.1(d). The wire acts as a riser for the shadow mask. Thus, we orient it roughly parallel to the nanotube. By placing the nanotube on the substrate first, we can position the riser wire within only a few microns from the nanotube. Once the W wire is in place, we glue the ends with Devcon 5 minute epoxy to the edges of the sample mount. After the glue dries the weight is cut free, and the wire is cut loose from the manipulator.

### 4.1.4 Mask Wire Placement

Since the first wire is a riser wire, the second wire does not contact the nanotube. After placing the first wire, the next step is to place a shadow mask wire roughly perpendicular to the first wire and the nanotube axis. We move the wire with a micro-manipulator until it is centered across the nanotube. Depending on the length of the nanotube, we use W wire of either 4  $\mu\text{m}$  or 7  $\mu\text{m}$  diameter. We lower the wire to the surface and hold it in place while we glue the ends to the edge of the sample mount (Fig. 4.1(d), wire ‘2’). This step is extremely critical as any movement of the second wire will shift it from over the nanotube. We allow the glue to dry for at least 20 minutes. Then the wire is cut free from the manipulator and the weight. We carefully remove the sample mount from the manipulator and attach it to a plate designed for use in an electron-beam evaporator. This plate holds six samples and is stored in a desiccator while we make the other samples. It typically takes 2–4 hours to prepare one sample. During the course of this thesis we prepared  $\sim 110$  samples.

---

<sup>1</sup>The 4  $\mu\text{m}$  tungsten wire is available from Goodfellow.

#### 4.1.5 Evaporation

After preparing six samples, they are ready for the evaporation process. We use an oil-free multiple source electron-beam evaporator with a base pressure of  $\sim 2 \times 10^{-8}$  Torr. The first samples were covered with 100 nm of Ti followed by 100 nm of Au. Later samples were coated with about 10 nm of Ti and 40–150 nm of Au. The Ti is used as an adhesive layer to hold the Au film to the substrate. Once the evaporation is finished the samples are removed and stored in a vacuum desiccator.

#### 4.1.6 Mask Removal

When ready for measurement a sample is mounted on the optical microscope and the wires are carefully removed in the reverse order. The wires are cut with a razor blade close to the glue drops. The wires are almost perfect shadow masks, shadowing the substrate underneath them from the evaporator sources. Thus, when the wires are removed, a trench is formed between two Ti/Au contact pads. Only the nanotube connects the two contact pads ‘A’ and ‘B’ (Fig. 4.1(f)). An advantage of this shadow mask technique is that the nanotube undergoes no chemical processing.

#### 4.1.7 Characterization

Using this technique, we can fabricate reliable contacts, which are strongly coupled to the nanotube. A schematic of the expected nanotube/contact junction is shown in Fig. 4.2. The finished samples are characterized using either a Digital Instruments or Nano-Tec [106] AFM operating in ‘tapping’ or non-contact mode. From the resulting images, it is usually clear which samples have survived the transfer into and out of the evaporation chamber. Typically, our chance for success is  $\sim 25\%$ . A 3D AFM image showing a nanotube entering one contact pad is given in Fig. 4.3 while a 2D image of the whole trench with a nanotube bridging the contact pads is shown in Fig. 4.5(a). In Fig. 4.4, we show TEM images of the contact/MWNT interface for a MWNT rope. The upper section of the rope (vertical object) was covered by the shadow mask, and the lower section was exposed to the evaporator beam and is coated in Ti/Au. The high magnification image shows no evidence for damage to the MWNTs. However, to avoid any damage to the MWNTs from the TEM beam, images were not taken for

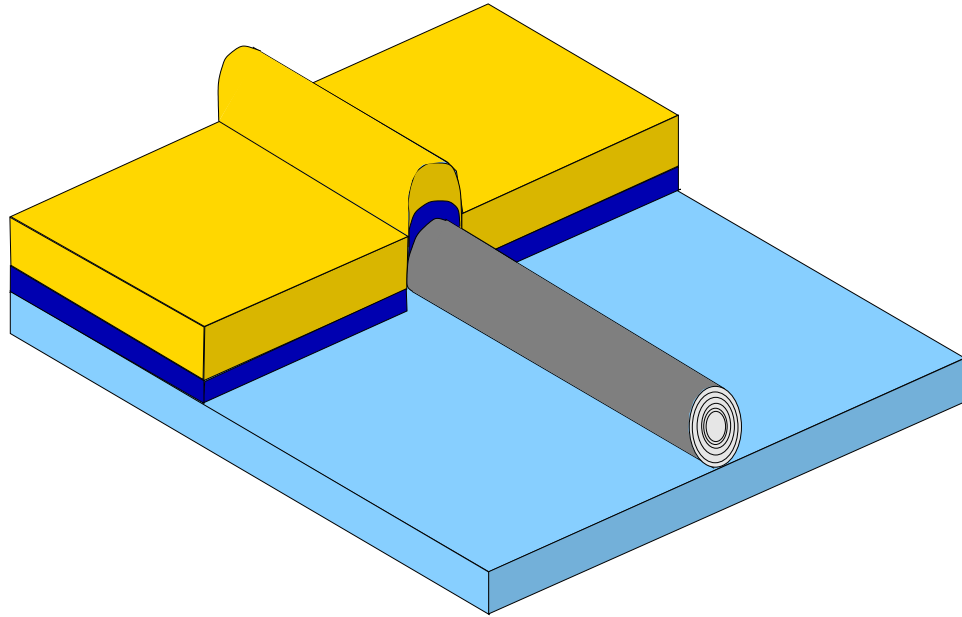


Figure 4.2. A schematic of the expected nanotube/contact junction. The smaller Ti layer, evaporated first, is shown in purple. The thicker Au layer is shown in gold. A bump is formed in the contact where the Ti and Au layers build up on top of the nanotube.

any sample on which transport measurements were performed.

We find the electrical contacts to the MWNT are reliable enough that, in some instances, the electrical resistance can be measured with a hand-held digital multimeter (although this practice is not recommended). A common failure mode for the nanotubes appears to be an electrostatic discharge, which evidently causes a high current to pass through the nanotube. In Fig. 4.5(b), we show an AFM image of a sample in which the nanotube has been destroyed. Care was taken to minimize the risk of discharge by using a grounding strap and Teflon tweezers. The typical leakage resistance between the two contact pads when no MWNT is present (or for a sample like the one in Fig. 4.5(b)) is greater than  $1\text{ G}\Omega$ .

The MWNTs studied so far typically have diameters which range between  $\sim 5\text{ nm}$  and  $\sim 20\text{ nm}$ , although the ropes of MWNTs have much larger diameters.<sup>2</sup> TEM stud-

<sup>2</sup>The diameters of the individual MWNTs in AFM images are enlarged due to tip dilation effects.

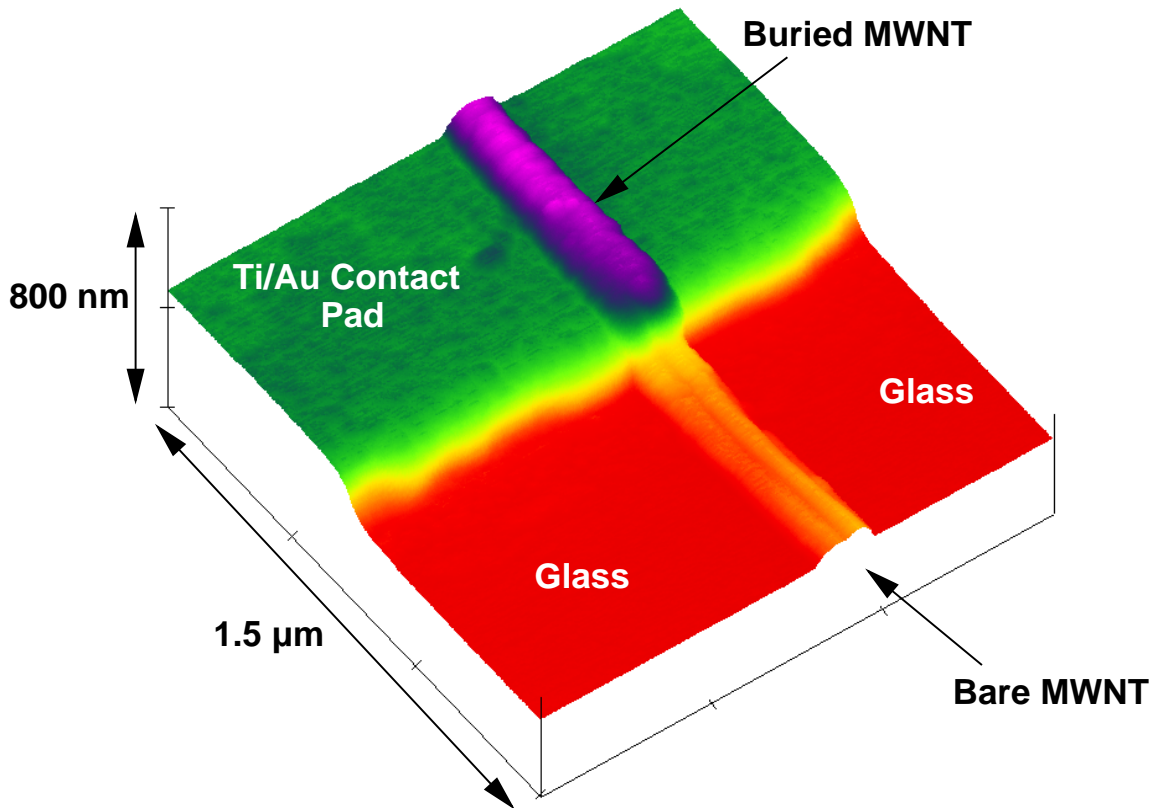


Figure 4.3. A  $1.5\mu\text{m} \times 1.5\mu\text{m}$  AFM image of MWNT sample No. 4 buried under a Ti/Au contact pad. The image shows the substrate comprised of a glass cover slide, one of the two Ti/Au contact pads, a section of the MWNT buried under the Ti/Au film, and a section of the bare MWNT which emerges from under the Ti/Au contact pad.

ies suggest that a typical MWNT sample is comprised of a few individual MWNTs. [85] Further evidence supporting this view is given in Fig. 4.6(a) and (b) which illustrates how individual MWNTs intertwine in our samples. Fig. 4.6(a) is a phase contrast AFM image taken near the center of a MWNT sample. The phase imaging mode is used to enhance contrast. [107–109] This image provides clear evidence that broken MWNTs exist along the length of the rope. Fig. 4.6(b) shows individual MWNTs that have unraveled at the end of a MWNT rope. Based on these studies, it is likely that a few, perhaps only one, of the individual MWNTs in a rope remains continuous across the entire  $4\mu\text{m}$  length between the contact pads. Thus, experi-

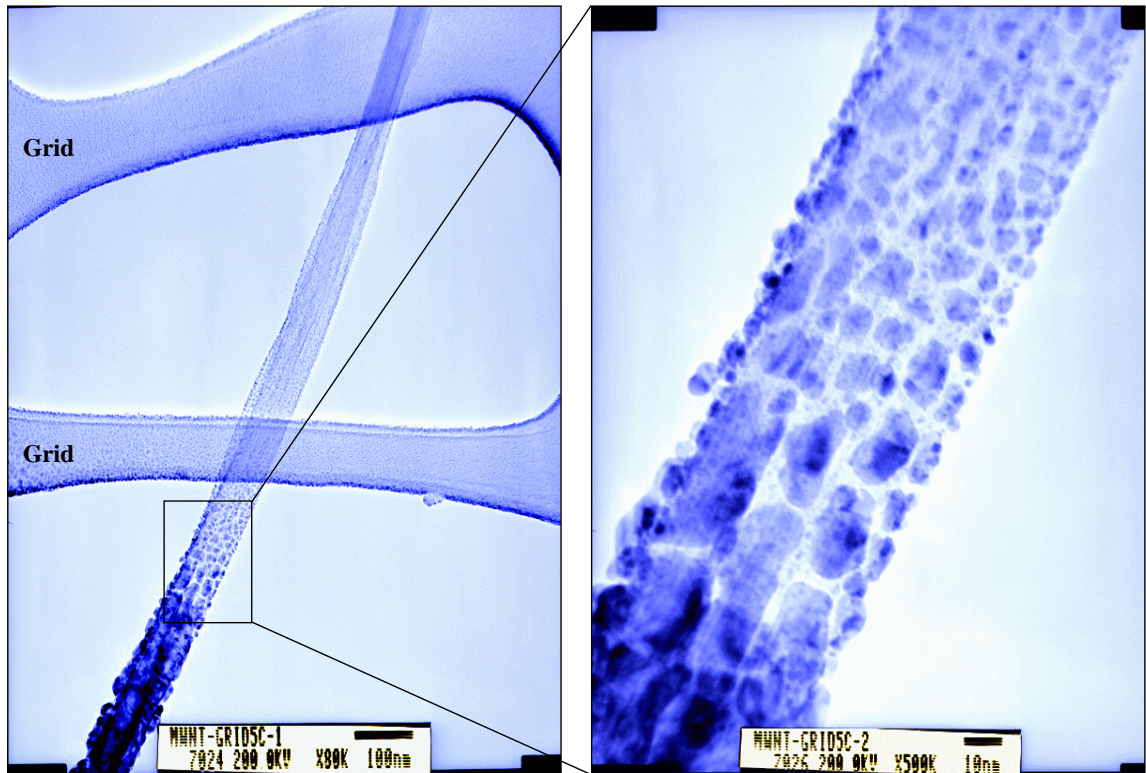


Figure 4.4. TEM images of the contact interface of a MWNT rope (vertical object) sample. For this sample, a TEM grid was used as the substrate. The lower portion of the MWNT rope was exposed to the evaporator and is coated in a thin film of Ti/Au. The upper portion of the rope was covered by the shadow mask. The high magnification image shows the transition region. The rope is not crushed by the contact, and there is no apparent damage to the MWNTs.

mental transport measurements in our samples may be dominated by the electronic properties of only one MWNT, a view which is consistent with our transport data.

One advantage of our procedure for making contacts to nanotubes is its flexibility. This is demonstrated in Fig. 4.7 which illustrates how a third electrode can be added about midway between the two contact pads. This was accomplished by carefully positioning two tungsten wires so that they crossed above and near the center of the MWNT. In Fig. 4.7(a), the third electrode makes electrical contact with the MWNT. In Fig. 4.7(b) the third electrode is used as a nearby electrostatic gate.

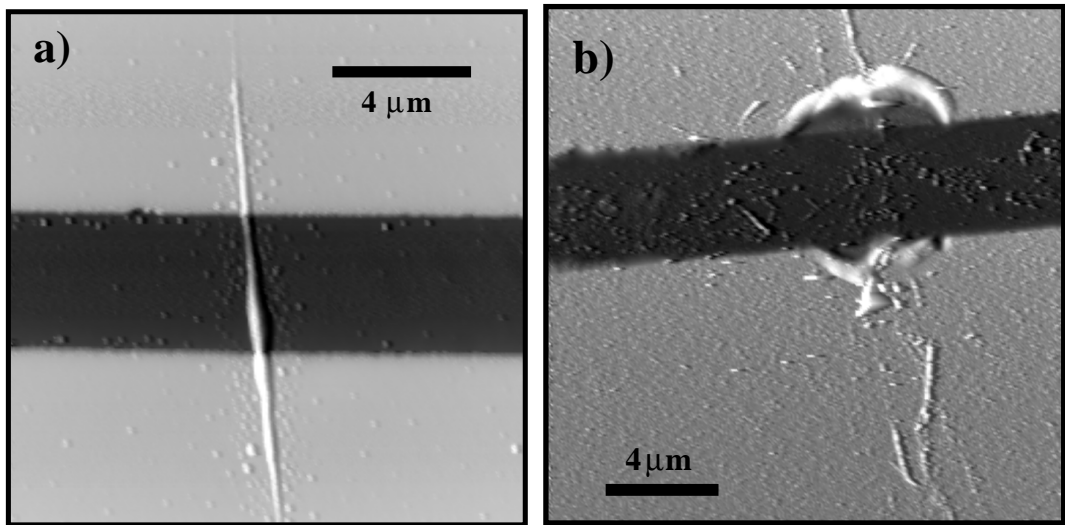


Figure 4.5. In a), an AFM image of a typical MWNT sample, No. 40. The image shows a MWNT crossing a  $4.3 \mu\text{m}$  wide trench. The two evaporated Ti/Au contact pads lie on top of the ends of the nanotube. In b), an AFM image of MWNT sample No. 5 that has been blown apart, presumably by an electrostatic discharge. Remnants of the MWNT are found scattered throughout the image. In addition, what appears to be a local melting or peeling of the Ti/Au contact pads is evident.

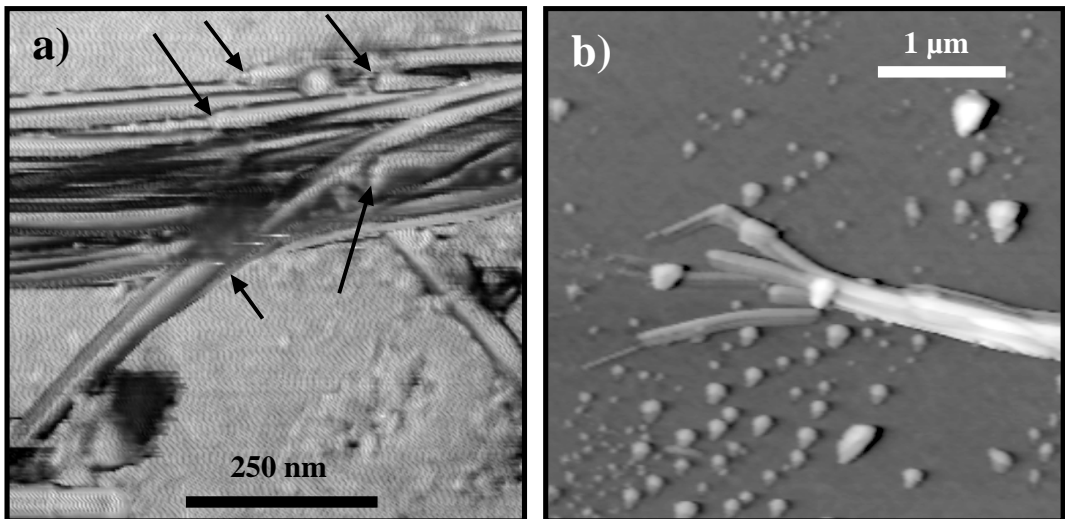


Figure 4.6. In a), an AFM phase contrast image of sample No. 25 showing multiple nanotubes in a MWNT rope. Taken near the middle of the sample, this image reveals the ends of several MWNTs (see arrows), suggesting that only a few MWNTs remain continuous between the two contact pads. In b), an AFM image of sample No. 49 showing the individual MWNTs unraveling at the end of the rope.

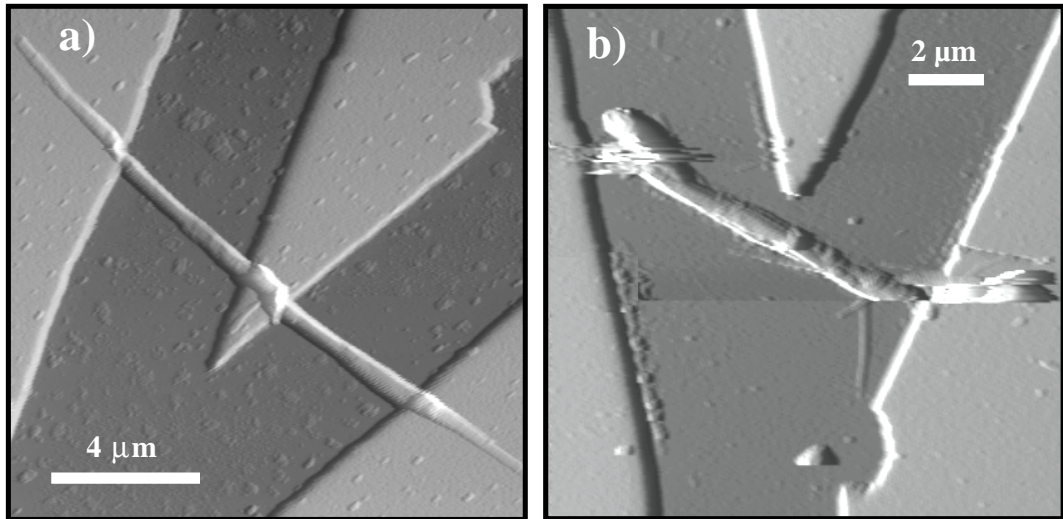


Figure 4.7. Using a two-wire shadow-mask technique, it is possible to define a third electrode in proximity to the nanotube. In a), the third electrode makes electrical contact to the middle of MWNT sample No. 66. In b), the third electrode acts as a nearby gate.

## 4.2 Room Temperature Transport Data

Using the above technique, the electrical contacts made to MWNTs are robust. With the proper precautions, the samples withstand handling as well as repetitive mounting and demounting to a variety of different sample probes. During the course of our initial measurements, we have used probe stations in two different buildings and have transported the samples between buildings without adverse effects. The  $I(V)$  data presented below are found to be very reproducible once the sample is mounted in the probe station, with the sum of contact and lead wire resistance (found to be less than a few ohms) presenting the only variable between the two stations. All measurements reported here are 2-terminal measurements, since there are only two contacts (three at most) to the nanotube.

Important information about the electronic properties of the MWNT is obtained by performing  $I(V)$  measurements. In principle, it is believed that, depending on its diameter and chirality, each layer comprising the MWNT can have either a metallic or semi-conducting band structure. This suggests that at least three types of  $I(V)$

characteristics might be anticipated. First, if the MWNT is comprised of concentric layers which are metallic, these layers will dominate current flow through the MWNT and a linear  $I(V)$  characteristic is anticipated. Secondly, if the MWNT is dominated by semi-conducting layers, then the resulting  $I(V)$  might be expected to exhibit non-linear behavior. If a MWNT has both semi-conducting and metallic layers intact, then it may be possible for a combination  $I(V)$  characteristic to result.

#### 4.2.1 Linear $I(V)$

$I(V)$  data from MWNT sample No. 4 having a minimum rope diameter (as determined from AFM scans) of  $\sim 40$  nm was found to be highly linear and is shown in Fig. 4.8. The resistance of this sample at room temperature was initially found to be  $478.06 \Omega$ , a value considerably smaller than the estimated resistance of  $\sim 3$  k $\Omega$  expected for classical (diffuse) conduction through a high quality carbon fiber ( $\rho \simeq 10^{-6} \Omega\text{cm}$ ) of the same dimensions. [110] Assuming an inter-planar separation of  $0.3$  nm between the walls in each layer of the MWNT, from the diameter measured from AFM studies, we estimate that at most,  $\sim 65$  layers comprise the nanotubes within the rope. Again, it is likely that both ends of the nanotubes are open. The  $I(V)$  data are found to be highly linear, showing only  $\sim 2\%$  deviation from non-linear behavior over the  $\pm 1.5$ V range investigated. Over this voltage range, based on Eqn. 2.23, even for a purely metallic sample, we expect to measure a non-linear  $I(V)$ . As new conduction channels are opened, the resistance of the sample should decrease, as shown in Fig. 2.9(b). Although the diameters of the conducting layers cannot be precisely known, based on Eqns. 2.13 and 2.14 at least two new channels should be accessible over this voltage range, even for the smallest nanotube diameters. As discussed in Section 2.3.3, one possible explanation for the lack of new channels could be Bragg reflection in the new sub-bands. [69] Other bias-dependent scattering mechanisms could exist, which would also limit or even cancel the increase in conductance with new channels. [57] Still, it is not clear why the  $I(V)$  does not show some small non-linearity.

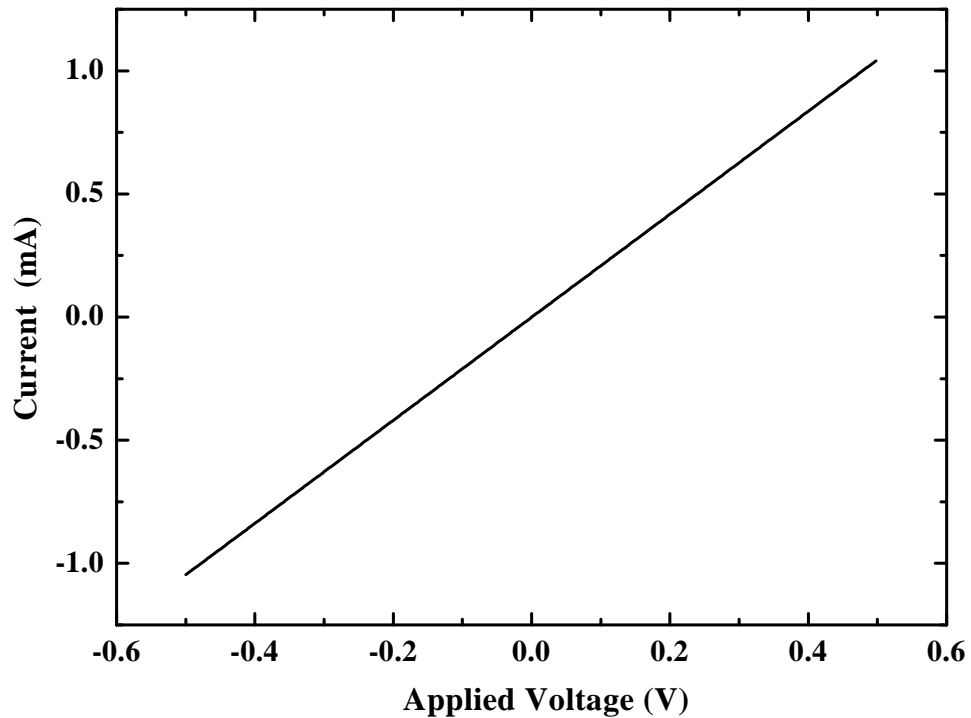


Figure 4.8. A plot of the  $I(V)$  for MWNT sample No. 4. The theoretical resistance of 27 layers conducting in parallel, with 1 mode per layer is  $478.02 \Omega$ . The resistance from the above  $I(V)$  is  $478.06 \Omega$ . The minimum diameter of this sample was  $\sim 40$  nm. The sample resistance was found to change abruptly with time but remained linear.

Assuming the initial resistance of  $478 \Omega$  is determined by  $N$  layers conducting in parallel and the  $N$  must be an integer leads to a value of  $N = 27$  and requires  $M = 1$  in Eqn. 2.23. Currents up to 3 mA have been passed through this sample without destroying it or changing its resistance due to joule heating. This implies that the MWNTs in the sample can pass a minimum current density of at least  $2.4 \times 10^8$  A/cm<sup>2</sup> without adverse effects. [111]

While the resistance of the MWNT can be measured quite accurately and is very reproducible for a given set of measurements, we find that, for this sample, the resistance increased between measurements; three of the four increases in resistance have resulted in changes that do not seem random. Surprisingly, increases in steps of  $\Delta R \simeq 21 \Omega$  have been measured as shown in Fig. 4.9.

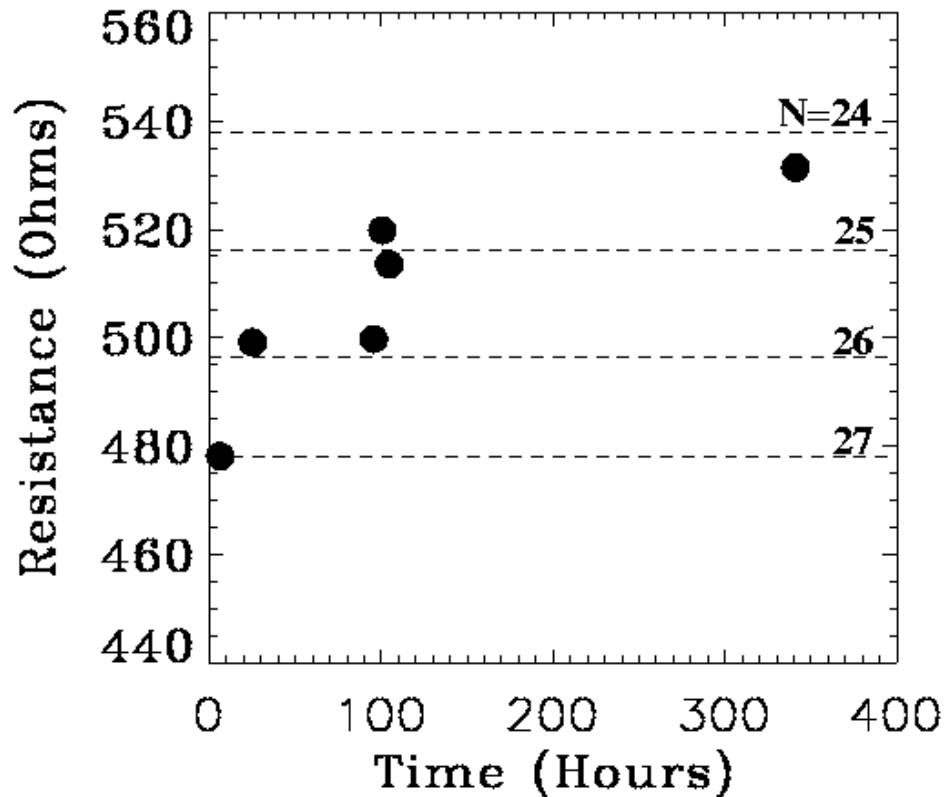


Figure 4.9. A plot of resistance versus time for sample No. 4. The sample resistance was found to change abruptly with time. The horizontal lines represent quantized resistance values of  $1/NG_o$ , with  $N = 24, 25, 26$  and  $27$ .

This result can be compared to changes in resistance expected for a ballistic quantum wire that initially conducts through  $N$  layers, but then changes to conduction through  $N - 1$  layers:

$$\Delta R = \frac{12906\Omega}{M[N(N - 1)]} . \quad (4.1)$$

The apparent quantized changes of resistance can be understood by starting with  $N = 27$  in Eqn. 4.1, implying that one layer was lost and now only 26 of the 65 possible layers carry current, and so on. To avoid values of  $N$  that are  $1/2$  integers,  $M$  must be set to equal 1. It follows that contact pads prepared in the way described above are evidently capable of making good electrical contact to many ( $26 \pm 1$ ) layers in a MWNT rope. If the resistance is quantized, then we should expect the measured

resistance to fall directly on the dotted lines in Fig. 4.9. However, since this data was taken using a 2-terminal method, the contact resistance is measured also. In addition, this sample was evaporated with 100nm Ti and 100nm of Au. It is possible that the Ti layer was slowly oxidizing over time, which may increase the contact resistance.

#### 4.2.2 Non-linear I(V)

Fig. 4.10 shows representative data from sample No. 3, exhibiting a highly non-linear I(V) behavior. It is interesting that the current measured for this sample was considerably smaller (nano-amps compared to milli-amps) than the other samples we have measured. Since the inter-layer resistivity for graphite is  $2-8 \times 10^3$  times the in-plane resistivity, [100] the small currents measured in this tube suggest a current path between two concentric layers, perhaps caused by an internal defect located

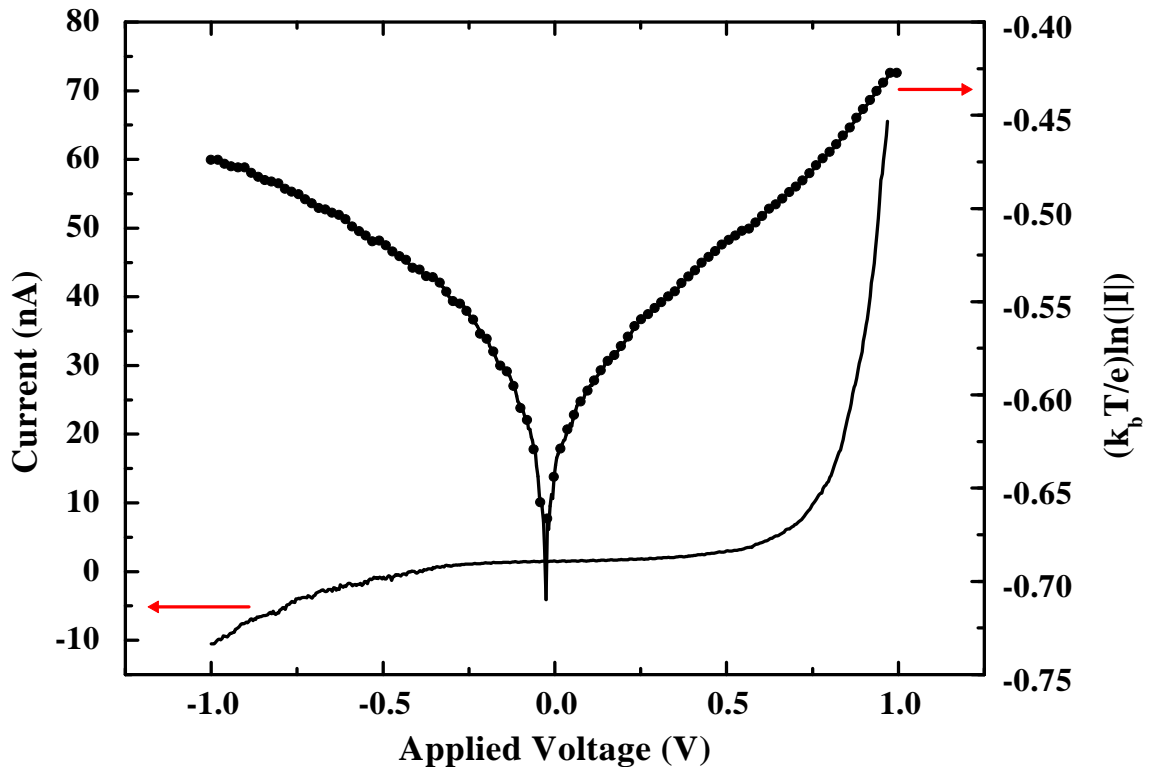


Figure 4.10. I(V) data from sample No. 3 showing diode-like behavior. The minimum diameter of this rope as determined from AFM studies was  $\sim 130$  nm. A plot of  $\frac{k_b T}{e} \ln(|I|)$  versus  $V$  is also provided.

somewhere within a nanotube. This provides one explanation for the very low currents observed. An explanation of the asymmetric  $I(V)$  data necessarily requires current flow from a metallic to semi-conducting region in the sample. This suggests the intriguing possibility of a nanometer-sized, rectifying, metal-semiconductor junction formed between two adjacent layers within a single MWNT.

The  $I(V)$  data from sample No. 3 can be further analyzed under forward bias by using the standard diode equation:

$$I = I_o \exp \left[ \frac{\Phi}{k_b T} + \frac{eV}{\eta k_b T} \right] \quad (4.2)$$

where  $I$  is the measured current,  $I_o$  is a constant,  $T$  is the temperature,  $k_b$  is Boltzmann's constant,  $\Phi$  is the Schottky barrier height in eV,  $e$  is the magnitude of the electron charge, and  $V$  is the applied bias voltage. An ideality factor  $\eta$  is often included in this diode equation to account for deviations of the data from the simple p-n junction theory. Fits to the forward bias data give values of  $\eta \simeq 5.6$ .

### 4.2.3 Semi-metallic $I(V)$

Further evidence for parallel conduction through two or more layers in a MWNT is shown in Fig. 4.11, which plots the conductance of MWNT sample No. 2 as a function of applied voltage. The original  $I(V)$  data is also provided. After acquiring  $I(V)$  data, the conductance  $G(V,T)$  was calculated by taking a numerical derivative of  $I(V)$ .<sup>3</sup> This sample exhibited a noticeable deviation from non-linear behavior, which can be understood by considering conduction through a metallic layer in parallel with conduction through a semi-conducting layer. The change may also stem from higher energy sub-bands being accessed as the applied voltage increases, although the increase in conductance is not in steps of  $1 G_o$ . The best fit to the data near  $V=0$  gives a resistance of  $\sim 29 \text{ k}\Omega$  (i.e., a zero bias conductance of  $0.44 G_o$ ). Several other samples displayed  $I(V)$  characteristics very similar to that plotted in Fig. 4.11.

---

<sup>3</sup>For all of the  $G(V,T)$  data reported here, the data are first smoothed by a five point adjacent average, then the derivative is computed using an algorithm which averages the slopes to neighboring data points.

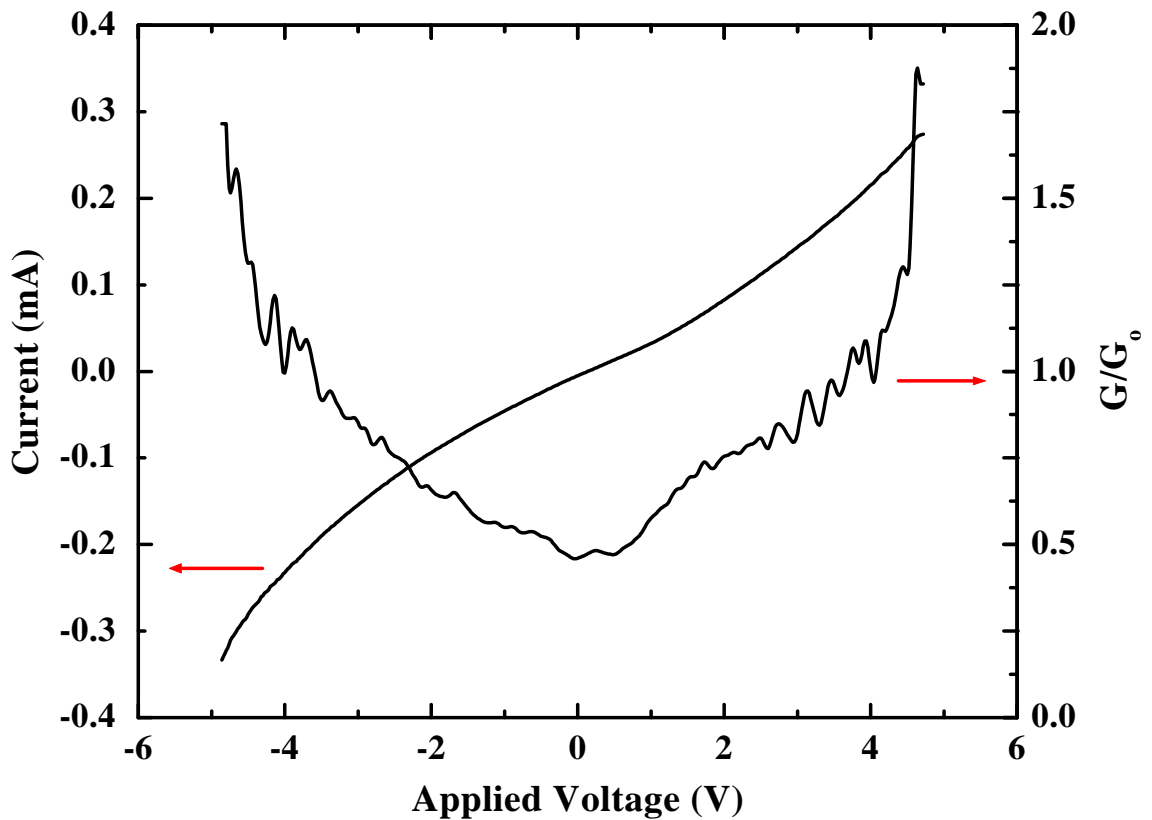


Figure 4.11. The conductance from MWNT sample No. 2 showing non-ohmic conduction. The minimum diameter of this tube as determined from AFM studies is  $\sim 20$  nm. The zero bias conductance is  $0.44 G_o$ . Typical I(V) data obtained from this sample is also plotted.

#### 4.2.4 Room Temperature Zero-bias Conductance

During the past two years, over 100 samples were prepared using the technique described above. Of these 100 samples, 75% were either deemed unacceptable after inspection in the dark-field microscope, were destroyed by electrostatic discharge, or failed for unknown reasons. Transport data was acquired from roughly 25% of the remaining samples. After acquiring I(V) data, the conductance  $G(V,T)$  was calculated by taking a numerical derivative of the I(V) data. A plot of the room temperature (RT) conductance, at zero-bias, for all 22 samples is given in Fig. 4.12. The conductance of  $27 G_o$  for sample No. 4 (discussed in Section 4.2.1) is not shown. From this figure, it is evident that  $\sim 50\%$  of the samples had a conductance greater

than  $1 G_o$ , while  $\sim 25\%$  had a conductance less than  $0.5 G_o$ . The samples indicated with stars were studied extensively as a function of temperature and voltage. The temperature dependent conductance data obtained from these samples is discussed in detail in Chapter 5. Note that we made sample No. 87 by placing the nanotube on top of pre-fabricated contacts, not by using the method described earlier.

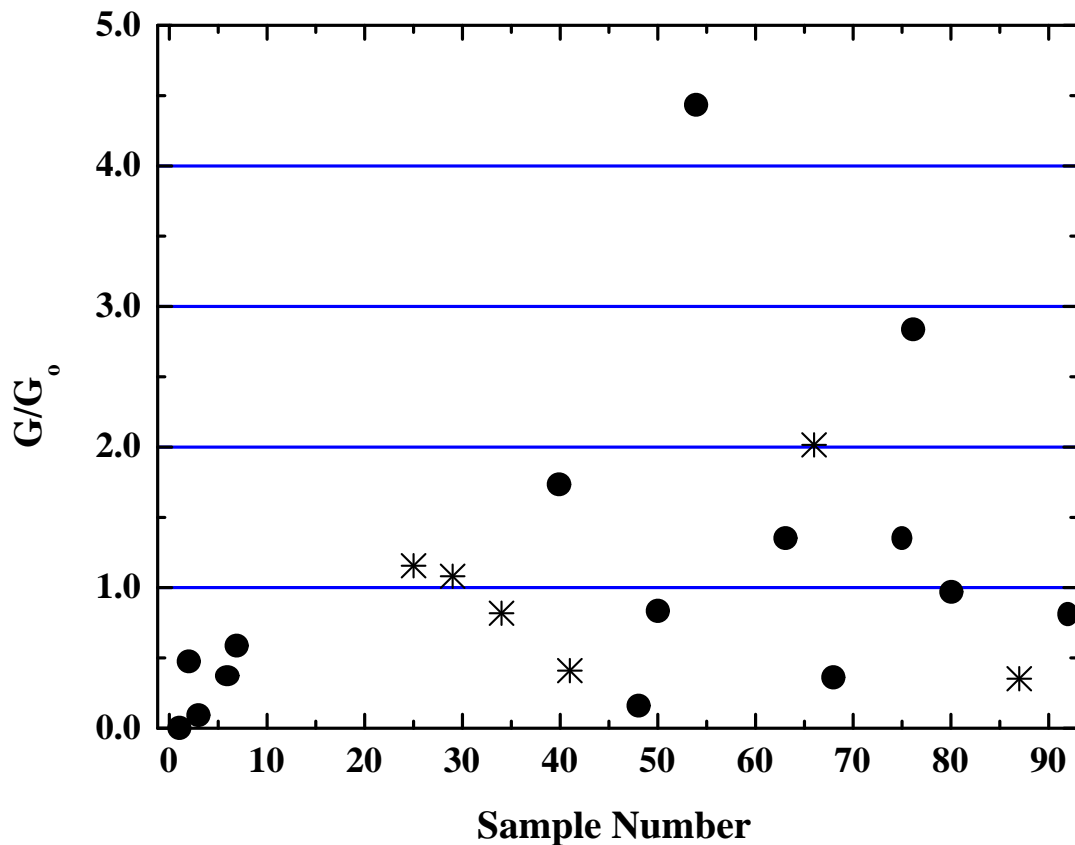


Figure 4.12. The zero bias conductance at room temperature plotted in units of  $G_o$  for the 22 MWNT samples measured. The conductance of  $27 G_o$  for sample No. 4 is not shown. Those samples marked by stars were studied more extensively as a function of temperature as discussed in Chapter 5.

#### 4.2.5 Estimating the Number of Conducting Paths

It is necessary to discuss the various factors which may influence the measured conductance of our samples. In what follows, we consider each layer of a MWNT as an individual nanotube contacted at either end. Since we are measuring MWNTs, there is always the possibility that an arbitrary number of nanotubes spans the distance between the two contacts, resulting in an aggregate conductance rather than a conductance related to the fundamental properties of an individual nanotube. In addition, each layer of a nanotube may have more than one accessible conduction band, which may also affect the measured conductance. For this reason, it is important to estimate the number of conducting layers and available bands in each MWNT that remain continuous between the two contact pads. Experimentally, it is difficult to determine this number precisely, but estimates can be made.

Depending on whether a layer is metallic (m) or semi-conducting (s), using Eqns. 2.13 and 2.14, we can relate its diameter to the location in energy of the available energy bands (above  $E_F$ ). The separation in energy ( $\Delta\epsilon_{m,s}$ ) between the lowest occupied band and the next available one is important in estimating the number of energy bands that contribute to electronic conduction in a MWNT at a given temperature. In metallic layers, for bias voltages  $V$  such that  $e|V| < \Delta\epsilon_m$ , only one band is accessible and should dominate current flow. Hence, the higher energy bands should not contribute significantly to the measured conductance. In general, at finite bias, the number of bands  $N$  carrying current through a nanotube could depend on voltage, hence  $N(V)$ , as discussed in Section 2.3.3. The approximate number of bands accessible at a given bias voltage  $V$  can be estimated by calculating the ratio of the energy difference  $\Delta\epsilon$  to  $eV$ .

A plot of  $\Delta\epsilon_m$  and  $\Delta\epsilon_s$  as a function of layer diameter is given in Fig. 4.13. Also plotted is the approximate number of layers in a MWNT as a function of the outermost layer diameter. This plot is useful in estimating the number of bands that may contribute to conduction in the following way. We have observed from AFM and TEM images that the diameters for a single MWNT range between 5 nm

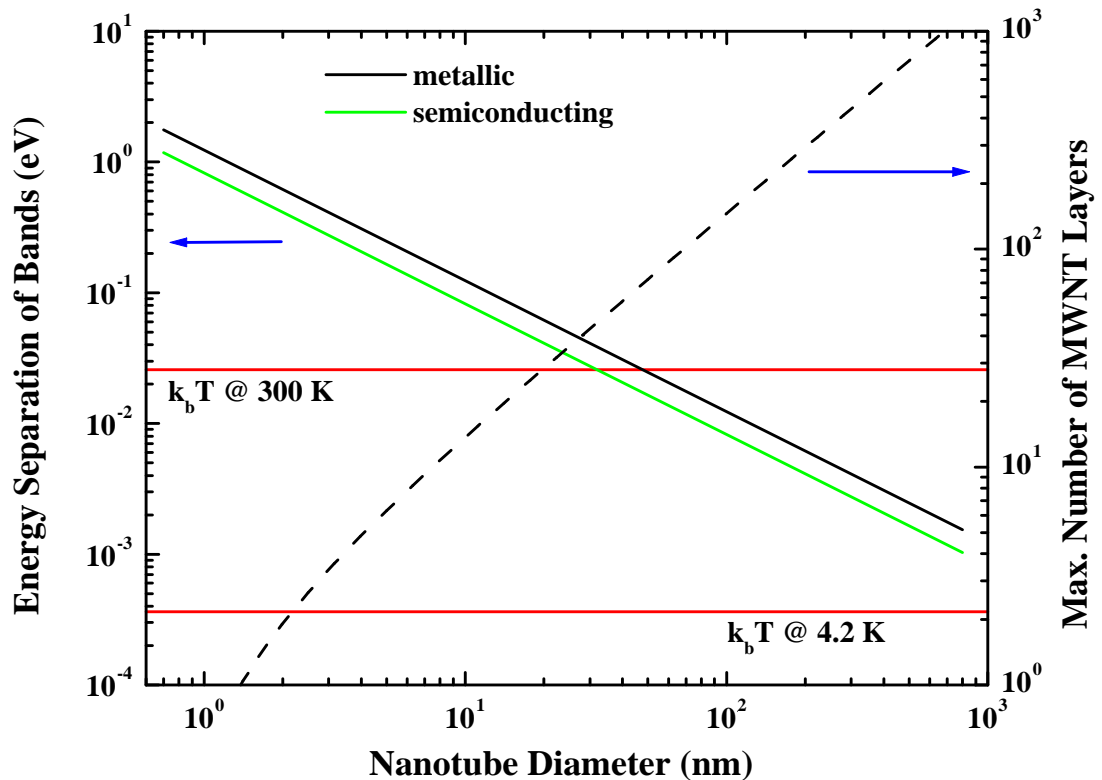


Figure 4.13. A plot of energy separation between conduction channels for metallic and semiconducting nanotubes as a function of layer diameter. Horizontal lines are shown for  $k_b T$  of 300 K and 4.2 K. The dashed line is a plot of the maximum number of layers in a MWNT as a function of the outer diameter of the MWNT. The calculation is approximate because we assume that the minimum inner layer diameter is  $\sim 0.7$  nm and that the inter-layer separation is 0.34 nm.

and 20 nm.<sup>4</sup> If we assume that a typical MWNT used in this study has an outer diameter of 10 nm, then we can estimate maximum possible values for  $N(V)$ . From the dotted line in Fig. 4.13, we estimate that approximately 13 layers comprise a nanotube with an outer diameter of 10 nm. Assuming 1/3 of these layers are metallic (see Eqn. 2.11), we infer that the MWNT will have about 4 metallic layers and about 9 semiconducting ones. At room temperature, from Fig. 4.13, we find that the energy gaps for the 9 semiconducting layers (each of which must have a diameter  $\leq 10$  nm)

<sup>4</sup>From TEM studies, we have observed a single MWNT diameter as large as 41 nm, but this was observed only once.

Table 4.1

Estimates for the maximum number of layers,  $N_{\text{Total}}$ , in MWNTs of various outer diameters. Also listed are the approximate number of metallic layers,  $N_m$ , and semiconducting layers,  $N_s$ , and the minimum energy separation of the bands for each.

MWNT Diameter	$N_{\text{Total}}$	$N_m, \epsilon_m$	$N_s, \epsilon_s$
5 nm	6	2, 0.25 eV	4, 0.16 eV
10 nm	13	4, 0.12 eV	9, 0.08 eV
15 nm	21	7, 0.08 eV	14, 0.05 eV
20 nm	28	9, 0.06 eV	19, 0.04 eV

lie above the  $k_bT$  line appropriate for 300 K. Thus, these semiconducting layers are not expected to contribute appreciably to conduction at temperatures at or below 300 K. In addition, possible values for the energy spacing between bands for the 4 metallic layers (each of which must also have a diameter  $\leq 10$  nm) also lie above the appropriate room temperature  $k_bT$  line, indicating that only the lowest energy band in each layer will significantly contribute to conduction for temperatures at or below 300 K. We conclude that for a 10 nm outer diameter MWNT at room temperature and below, the maximum number of layers contributing to conduction is 4 and that conduction through each layer at zero bias is controlled only by the lowest energy band. It then becomes important to determine how many of the 4 conducting layers remains continuous between the two contact pads, but clearly from this discussion, values of  $N$  less than or approximately equal to 4 can be expected.

As discussed in Chapter 2, the presence of ballistic transport in a MWNT will be signaled by conductance values close to  $MN(V)G_o$  (see Eqn. 2.23). Based on the above discussion, for electron transport through metallic layers at low bias, there is only one band for each continuous layer contributing to current flow, implying that at most,  $N = 4$  at zero bias. When  $eV > \Delta\epsilon$ ,  $N$  can increase and additional structure might become evident in  $G(V,T)$  as additional bands are accessed. For  $M = 1$  and a

maximum value of  $N = 4$ , one expects measured conductances to be in the range of  $1 G_o$  to  $4 G_o$ , with a few values close to integer multiples of  $G_o$ . This expectation is consistent with much of the data plotted in Fig. 4.12. Thus, it appears that for this low bias data taken at or below 300 K, only a few metallic layers in the MWNT rope are transporting the majority of the current. Hence, the high conductances we have measured for MWNTs can be related to the properties of a few layers (possibly even one) and need not necessarily be attributed to the conduction through many layers of the MWNT. Also, the likelihood that only one energy band contributes to conduction in each layer supports the idea that 1D behavior is an important consideration for this system.

## 5. TEMPERATURE DEPENDENT TRANSPORT MEASUREMENTS

To further investigate the electronic properties of carbon nanotubes, we performed transport measurements as a function of temperature from room temperature (300 K) to liquid helium temperatures (4.2 K). By performing these measurements, we obtained information about the intrinsic properties of nanotubes. The two main types of measurements made were  $I(V)$  measurements and  $V(t)$  measurements. The  $I(V)$  measurements were performed in order to study the temperature and voltage dependence of the conductance,  $G(V,T)$ . Such measurements of the DC conductance are useful for determining the dominant conduction mechanism in a carbon nanotube. Particularly interesting is the zero-bias conductance as a function of temperature. When calculating the conductance of the nanotube at low bias, a thermal average over the neighboring sub-bands is performed. This provides one explanation for non-integral values of the zero-bias conductance in units of  $G_o$ , as seen in Fig. 4.12. By cooling the samples to liquid helium temperatures ( $k_bT \simeq 0.4$  meV at  $T = 4.2$  K), we hope to greatly reduce any thermally activated components of the conductance.

Measurements of the sample voltage as a function of time,  $V(t)$ , were made at various temperatures in order to study the noise and stability of the samples. Preliminary measurements were also made using a lock-in amplifier to directly obtain noise spectrum data. In addition to providing information regarding the practical use of nanotubes in electronic circuits, noise measurements may also provide information about the mechanisms controlling the sample conduction. [112–115] The noise measurements were motivated in part by the results of our field emission studies, discussed in Section 3.2.3, but also by the temperature dependent conductance data discussed below.

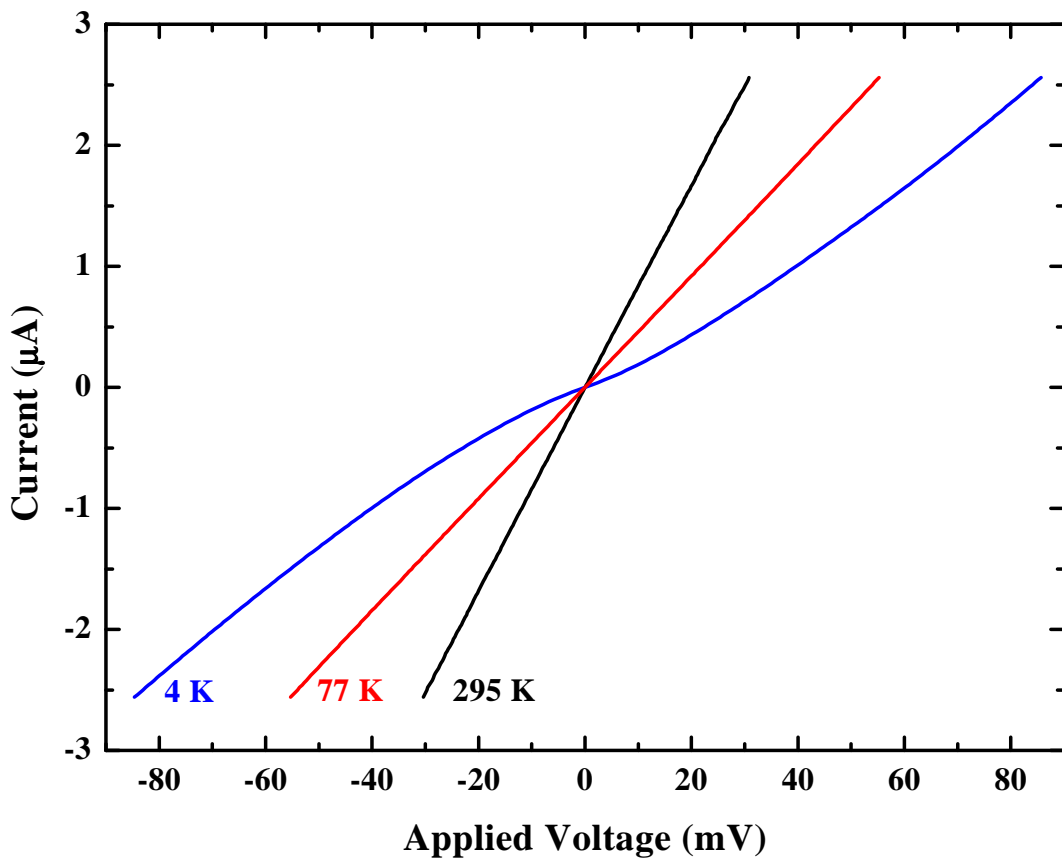


Figure 5.1.  $I(V)$  plots for sample No. 29 at 3 temperatures. A non-linearity near  $V = 0$  appears at low temperatures.

### 5.1 Temperature Dependent Conductance Data

Of the 22 samples shown in Fig. 4.12, six were chosen for further investigation. It should be noted that sample No. 87 is different than the other five samples. We made sample No. 87 by placing a MWNT on top of pre-fabricated contacts, not by using the method described in Chapter 4. For all samples, the temperature dependent measurements were performed using the dip-probe method described in Appendix E. Fig. 5.1 shows a typical set of  $I(V)$  data. A clear non-linearity appears in the  $I(V)$  data at low temperatures. We observed this  $I(V)$  behavior for all samples studied. By measuring  $I(V)$  at different temperatures, it was possible to calculate the conductance of the MWNT samples ( $G(V,T) \equiv dI/dV$ ) as a function of both applied voltage and

Table 5.1  
Conductance values and fractional changes for the six samples studied.

Sample ID	$G(300\text{ K})$	$\Delta G/G$
25	$1.26 G_o$	1.9
29	$1.08 G_o$	2.6
34	$0.82 G_o$	3.3
41	$0.41 G_o$	5.8
66	$2.03 G_o$	2.1
87	$0.35 G_o$	1.8

temperature. Table 5.1 tabulates the zero-bias conductance at room temperature (RT) for the six samples. Note that sample No. 87 has the lowest conductance value. Also listed is the fractional change in conductance  $\Delta G/G$  between RT and 4 K, calculated by

$$\Delta G/G = \frac{G(300K) - G(4K)}{G(4K)}. \quad (5.1)$$

For completeness, the conductance data for each of the six samples (indicated by stars in Fig. 4.12) are plotted in Figs. 5.2, 5.3, and 5.4. The data illustrate several important features common to data from all of the samples studied. These features include (i) the presence of nearly ohmic behavior near room temperature; (ii) the presence of temperature and voltage dependent noise in the  $I(V)$  data which is clearly present in the conductance near room temperature; (iii) the appearance of a non-linearity in  $I(V)$  which appears as a downward bow in  $G(V,T)$ ; (iv) the evolution of this bow into a conductance gap which is fully developed at temperatures near 4 K; and (v) the saturation of the low temperature conductance to a common value at higher bias.

Interesting behavior was observed in two of the six samples at temperatures near 4 K. A reproducible structure in  $G(V,T)$  became evident in the conductance as a

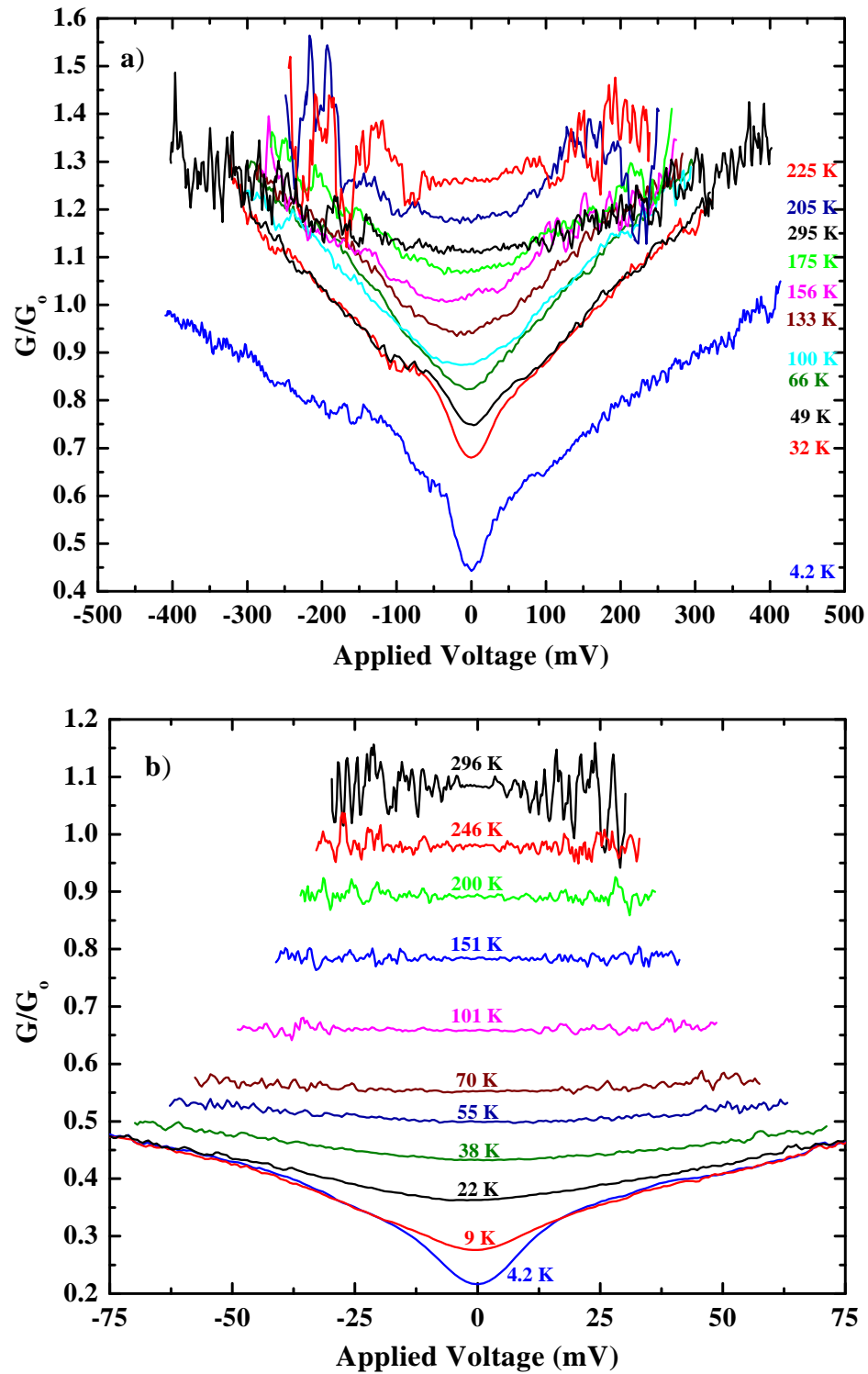


Figure 5.2. The conductance  $G(V,T)$  plotted in units of  $G_0$  as a function of applied bias voltage  $V$  for a) sample No. 25 and b) sample No. 29. Each plot shows the data for 11 different temperatures, as labeled.

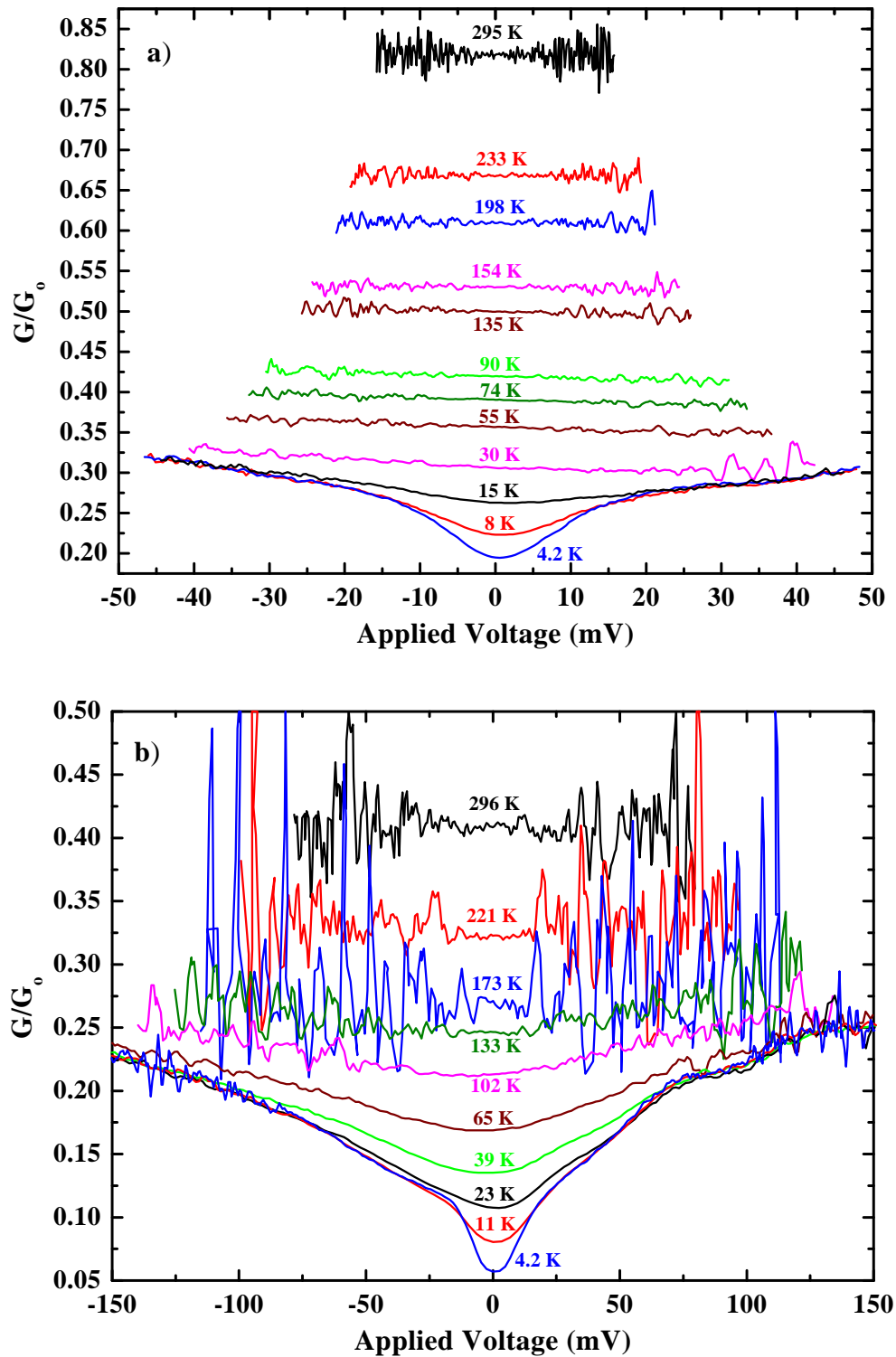


Figure 5.3. The conductance  $G(V,T)$  plotted in units of  $G_0$  as a function of applied bias voltage  $V$  for a) sample No. 34 at 12 temperatures and b) sample No. 41 at 10 temperatures.

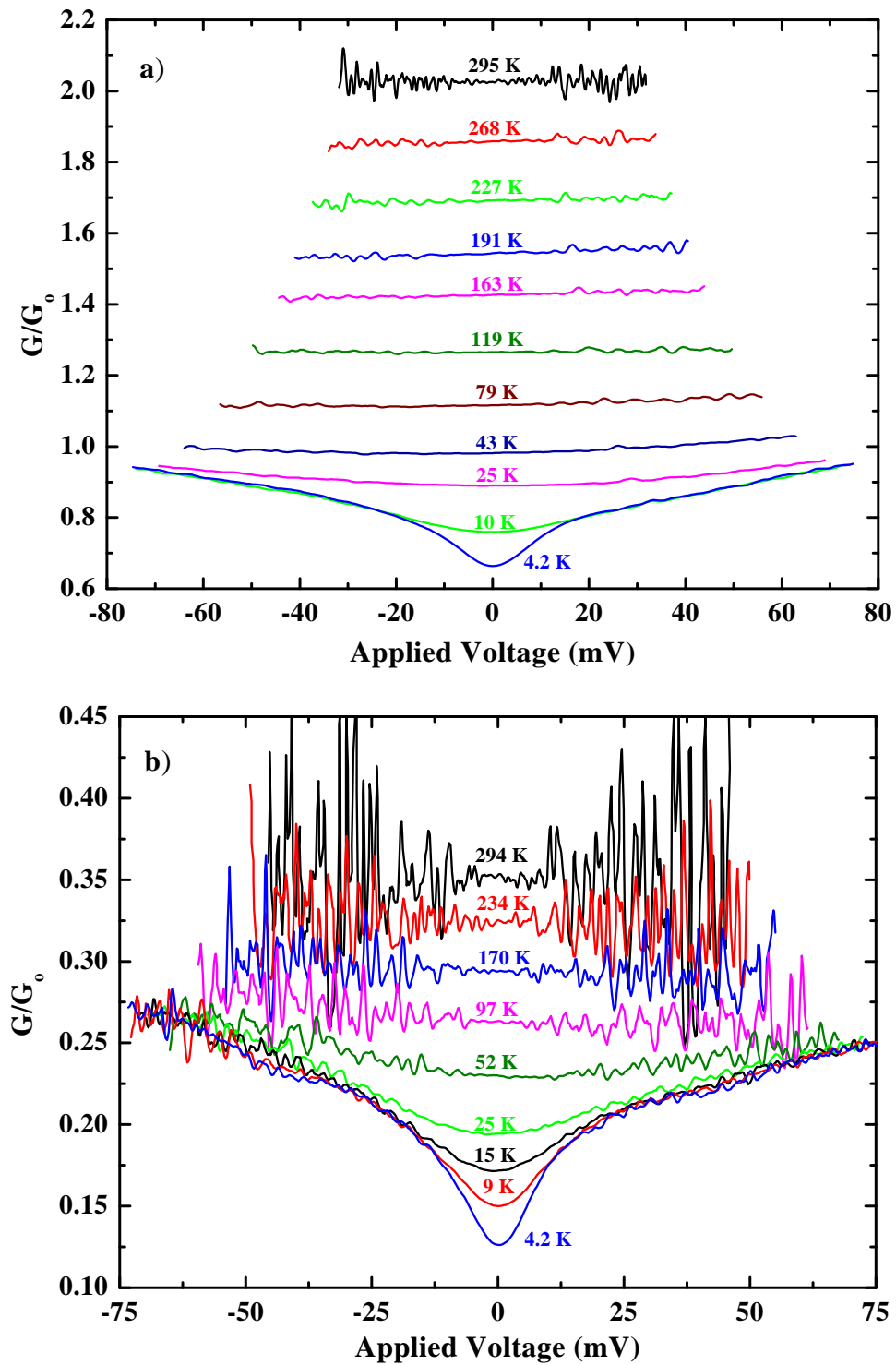


Figure 5.4. The conductance  $G(V,T)$  plotted in units of  $G_0$  as a function of applied bias voltage  $V$  for a) sample No. 66 at 11 temperatures and b) sample No. 87 at 9 temperatures. In sample No. 87 the nanotube was on top of the contacts.

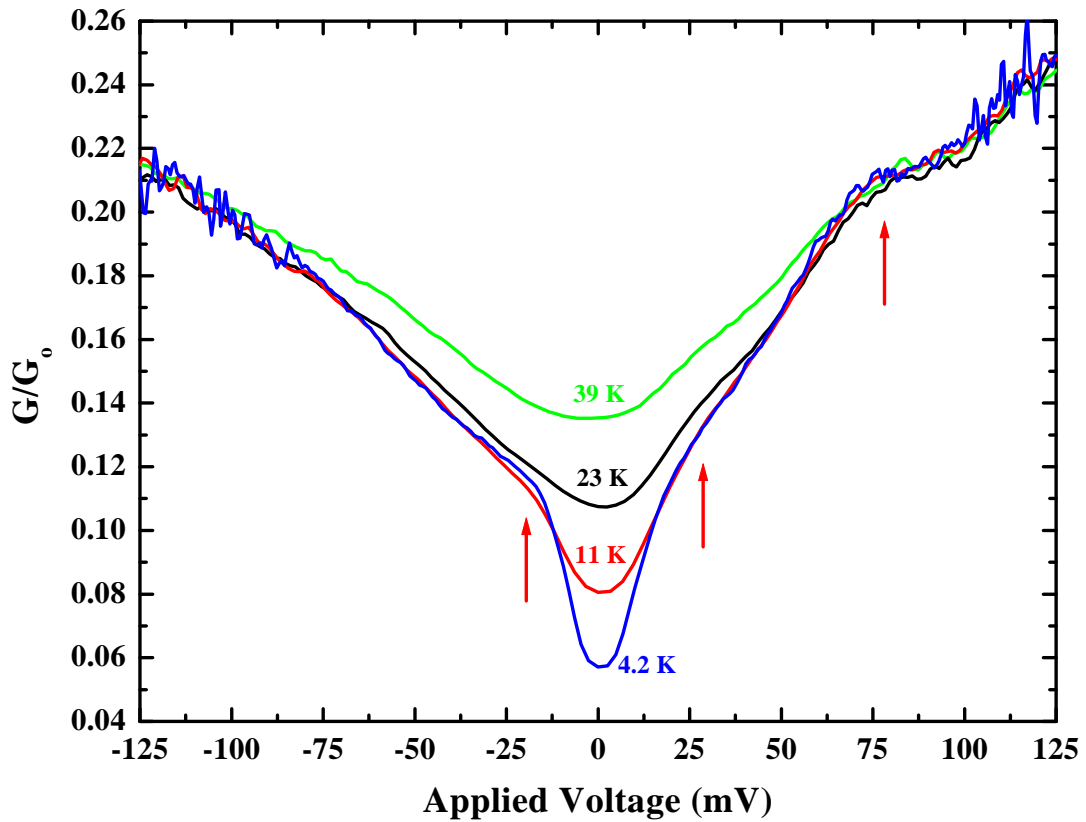


Figure 5.5. A plot of conductance versus voltage from sample No. 41 at a few low temperatures. The data shows structure in  $G(V,T)$  as indicated by the arrows. An asymmetry between  $G(-V,T)$  and  $G(+V,T)$  is also evident. These features were observed in two of the six samples studied.

function of applied bias voltage for sample No. 25 (Fig. 5.2(a)) and sample No. 41 (Fig. 5.3(b)). This structure is evident (and indicated by arrows) in Fig. 5.5 where only the low temperature data are plotted for sample No. 41. In addition, an asymmetry develops in the data, causing  $G(-V,T) \neq G(+V,T)$ . The origin of this behavior may be the influence of higher sub-bands in the conduction process. Figure 5.6 shows a plot of the symmetric part (a) and the asymmetric part (b) of the 4 K data for sample No. 41. Figure 5.7 shows the same for sample No. 87, which also displayed an asymmetry in the  $G(V,T)$  data.

Perhaps the most striking feature of the data is the evolution of a conductance gap below  $\sim 20$  K. All samples showed a similar temperature dependent behavior at

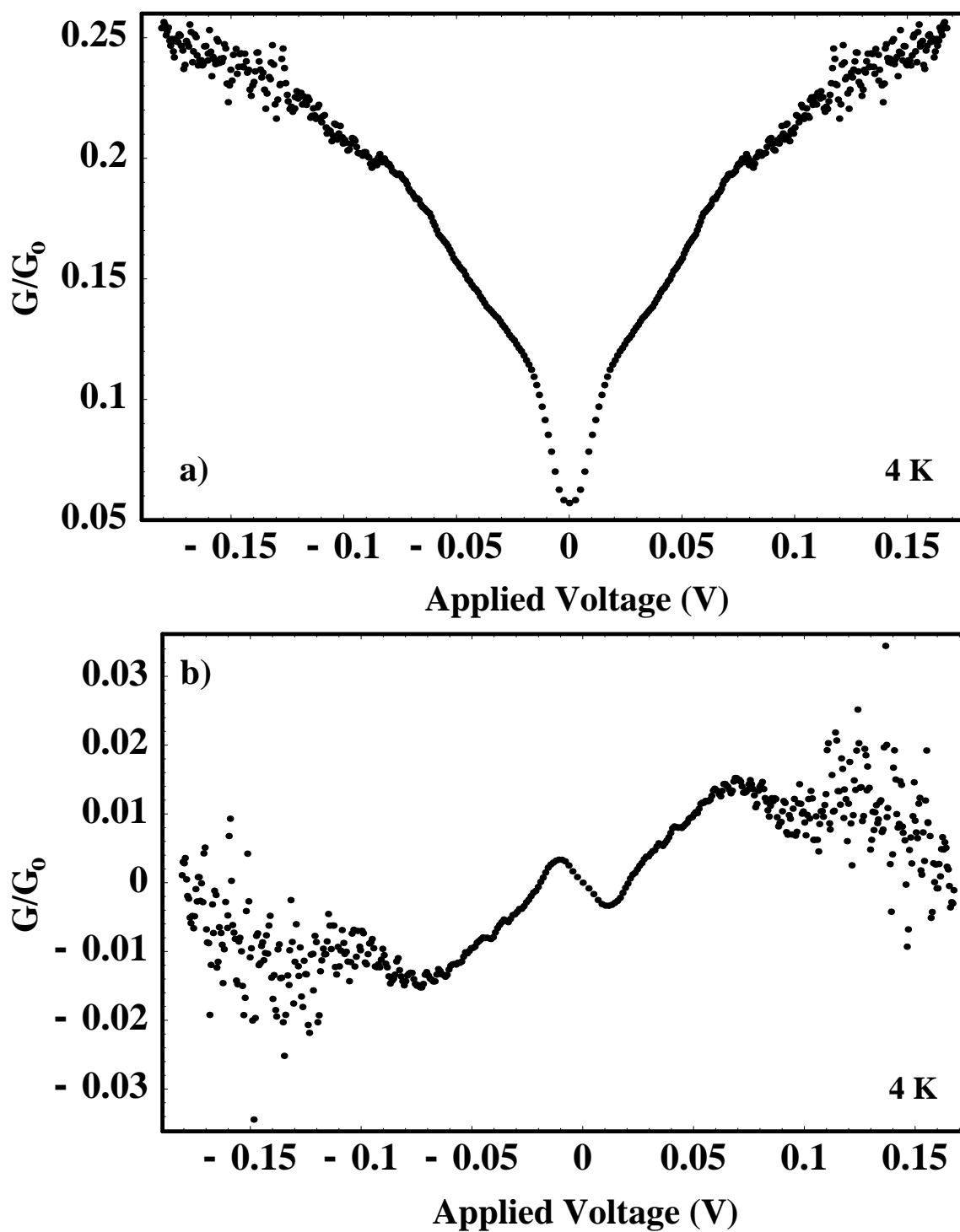


Figure 5.6. A plot of the symmetric part a) and the asymmetric part b) of the conductance at 4 K for sample No. 41.

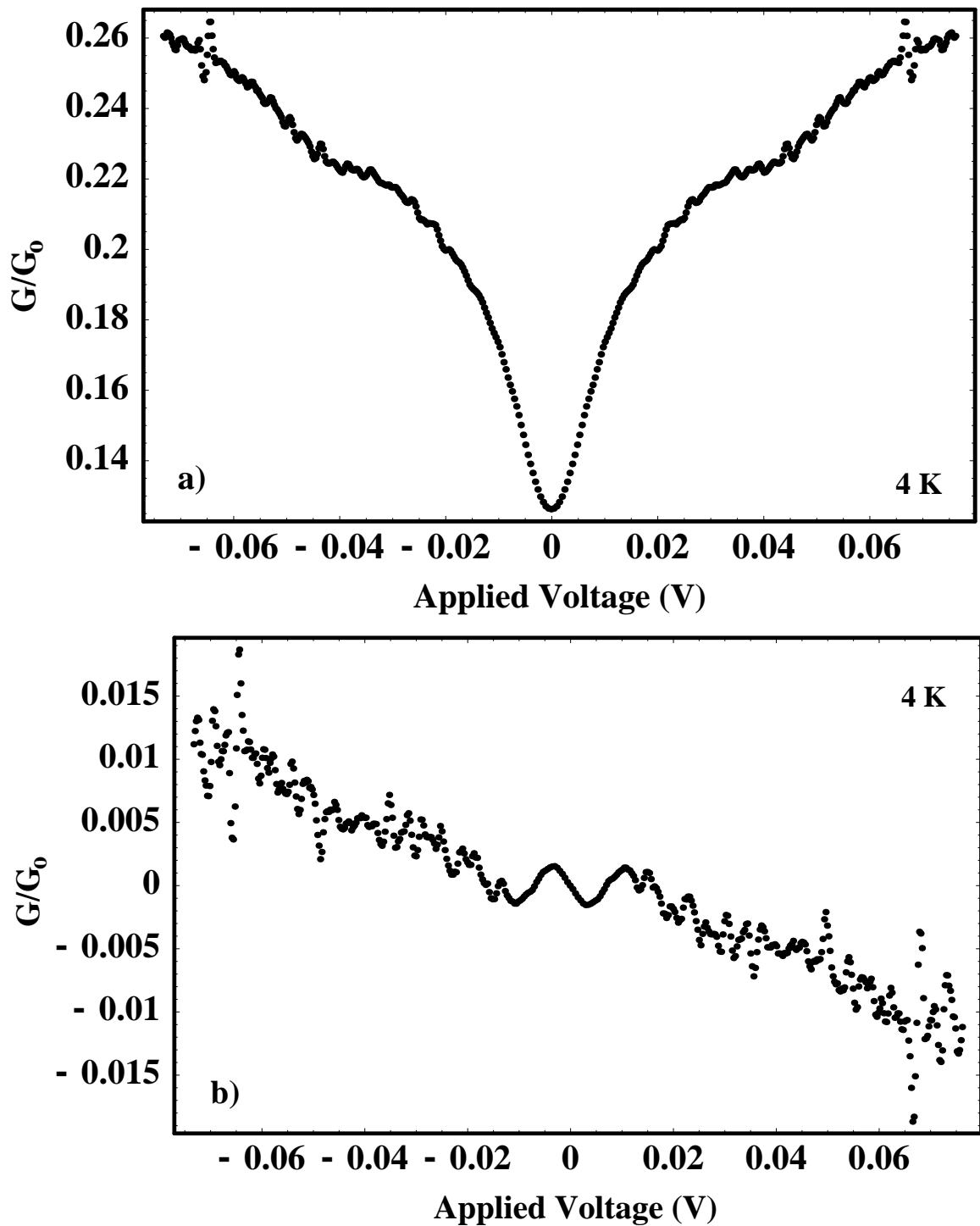


Figure 5.7. A plot of the symmetric part a) and the asymmetric part b) of the conductance at 4 K for sample No. 87.

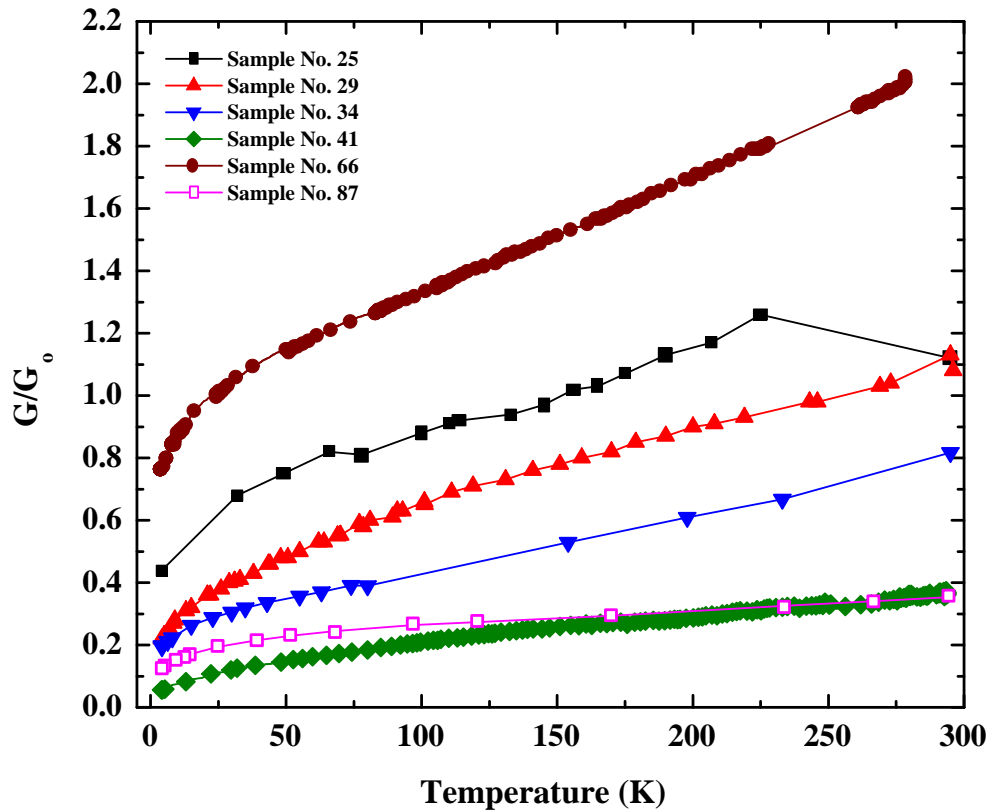


Figure 5.8. The conductance at zero-bias versus temperature for the six samples studied.

temperatures above  $\sim 20$  K. Below this temperature, the conductance near zero-bias decreased substantially faster than the conductance measured at higher bias. The temperature dependence of the conductance is clearly seen in Fig. 5.8, where we plot the zero-bias conductance versus temperature for all six samples.

## 5.2 Temperature Dependent Transport Models

It remains to describe the temperature dependence of the conductance at zero-bias. For interacting electrons in 1D, the collective system may have several interesting properties due to Coulomb interactions. In the case of a weak coupling between the nanotube and the contact pads, Coulomb blockade effects are expected and have been observed. [116, 117] Weak coupling between the nanotube and the contact exists in scanning tunneling microscope (STM) studies where the STM tip forms a weakly

coupled contact to the nanotube, [33, 34] or when a nanotube is laid on top of a metallic contact. [5, 35, 36, 38] We believe our method for sample fabrication results in strongly coupled contacts, thus the regime of Coulomb blockade is not appropriate for the experiments we performed, and we find no evidence of it in our data.

If ballistic transport is occurring in these MWNT samples, one might expect little if any temperature or voltage dependence in the conductance. In fact, as the temperature of a ballistic system is lowered, the amount of phonon scattering should decrease. Thus, one would expect the sample conductance to increase as the temperature is lowered. Clearly, our experimental data contradict this expectation. In an attempt to account for this observation, the following temperature dependent models for electron transport have been considered: i) thermally activated conduction, [118] ii) simple two-band model appropriate for graphite, [119] iii) a zero in the transmission probability induced by gap states, [24] iv) variable range hopping mechanisms, [120–122] v) 1D and 2D weak-localization, [40, 123] and vi) Luttinger Liquid behavior. [21, 22, 29] Of all these models, the Luttinger Liquid model provides the most consistent explanation for the observed temperature *and* voltage dependence of the conductance. Schönenberger *et al.* have measured MWNT conductance, which for some samples, is well described by 1D weak-localization, while for other samples is better fit to a Luttinger liquid model. [123] All of our MWNT samples studied as a function of temperature are best described by the Luttinger liquid model. The temperature dependence of the conductance is not well fit by either 1D or 2D weak localization models, but the lack of magneto-transport data at this time prevents us from excluding these models entirely. Brief discussions of the transport models i–v are given in Appendix F with representative fits to the data.

### 5.2.1 The Luttinger Liquid Model

In what follows we analyze our data in terms of the Luttinger liquid theory. [124–129] In one-dimension, strong Coulombic interactions between the electrons may modify the density of states (DOS) from that predicted by a Fermi liquid theory. The resulting system is a highly correlated electron liquid that is characterized by a power-

law vanishing of the DOS near the Fermi energy,  $E_F$ . In the event that this strongly correlated behavior exists, the transport through a nanotube might be described in terms of a low-energy theory of plasmon waves [19], more commonly known as a 1D Luttinger Liquid (LL). [21, 22, 29, 130, 131] Such a system is characterized by a power law dependence in the electronic tunneling density of states ( $DOS_{tun}$ ) with respect to energy. Specifically, one finds  $DOS_{tun} \propto (E - E_F)^\alpha$ . [22, 29] This power law suppression of the DOS gives rise to a temperature and voltage dependence in the differential conductance ( $G \equiv dI/dV$ ), given by [37]

$$G(V, T) = AT^\alpha |\Gamma(z)|^2 \cosh\left(\frac{x}{2}\right) \otimes \frac{1}{4k_b T} \text{sech}^2\left(\frac{E - eV}{2k_b T}\right), \quad (5.2)$$

where  $A$  is a constant,  $\Gamma$  is the gamma function,  $z = \frac{1+\alpha}{2} + \frac{ix}{2\pi}$ ,  $x = \eta eV/k_b T$ , and  $\otimes$  represents a convolution with the thermal broadening function of the electrical leads. [61] The multiplicative factor  $\eta$  in the definition of  $x$  is a constant that accounts for the voltage division introduced by the contact resistance. Typically,  $\eta$  is expected to have a value of 0.5 if two tunnel barriers couple the nanotube to the contact pads (i.e., weak coupling). This is the case for which the theory was developed (i.e., *tunneling* DOS).

Eqn. 5.2 can be written as [38]

$$G(V, T) = AT^\alpha |\Gamma(z + \frac{1}{2})|^2 \times \sinh\left(\frac{x}{2}\right) \left[ \frac{1}{2} \coth\left(\frac{x}{2}\right) - \frac{1}{\pi} \text{Im}\Psi\left(z + \frac{1}{2}\right) \right], \quad (5.3)$$

where  $\Psi$  is the diGamma function. Eqn. 5.3 has two important limits specified by

$$G(V, T) \propto T^\alpha \quad \text{when} \quad \frac{eV}{k_b T} \ll 1, \quad (5.4)$$

and

$$G(V, T) \propto V^\alpha \quad \text{when} \quad \frac{eV}{k_b T} \gg 1. \quad (5.5)$$

For intermediate values of  $\frac{eV}{k_b T}$ , a scaling law is expected to hold. [37, 127–129]

Depending on where the nanotube is contacted, the exponent  $\alpha$  is determined by the LL interaction parameter  $g$ . The parameter  $g$  is related to the number of conducting channels at  $E_F$  and the ratio of the charging energy of the tube to the

single particle level spacing. [37, 123] For strong electron-electron interactions we have  $g < 1$ , while in the absence of interactions  $g = 1$  (i.e., Fermi liquid). Based on estimates for  $g$ , values for  $\alpha$  range between 0.6 and 0.2. For the specific case of a MWNT with  $N$  layers, the LL model must be modified to accommodate the multiple layers involved in screening. The resulting relationships are [29]

$$\alpha_{end} = \frac{1}{4N} \left( \frac{1}{g} - 1 \right), \quad (5.6)$$

$$\alpha_{bulk} = \frac{1}{8N} \left( \frac{1}{g} + g - 2 \right), \quad (5.7)$$

where the subscript *end* designates the case of electron injection into the end of a layer, and *bulk* designates the case of electron injection into the side of a layer. The effect of the electron interaction is stronger for the *end* case because the electrons can only respond to an added electron by moving in one direction, whereas for the *bulk* case, the electrons can move in two directions. A contact may be defined as *bulk* when  $L_c > \frac{hv_F}{2\pi k_b T}$ , where  $L_c$  is the distance from the end of the nanotube to the contact and  $v_F$  is the Fermi velocity. [132] Although it is difficult to know exactly where the electrons enter our nanotube samples, we can estimate that the electrons will enter where the interaction strength is smallest. For the outer layer of a MWNT, this would be near the edge of our contacts. At 4 K we find  $L_c \simeq 1.5 \mu\text{m}$ . Since the length of the section of nanotube buried under our contacts is typically on the order of this distance and often longer, we expect to have *bulk* contacts. The above theory provides clear predictions for the behavior of the conductance for a nanotube system if it is governed by LL behavior.

In terms of the Luttinger liquid model, we analyze the temperature dependent conductance data at zero-bias  $G(0, T)$  by plotting  $\log(G(0, T))$  versus  $\log(T)$ .<sup>1</sup> Fig. 5.9(a) shows such a plot for all six samples. As evident from this plot, the data can be characterized by a power law of the form suggested in Eqn. 5.4 above. Analysis of this data shows a change in the exponent  $\alpha$  near 100 K. A least-squares fit to the data provide unbiased estimates of  $\alpha$  for  $T < 100$  K, which are given in Table 5.2.

---

<sup>1</sup>By log we always mean  $\log_{10}$ .

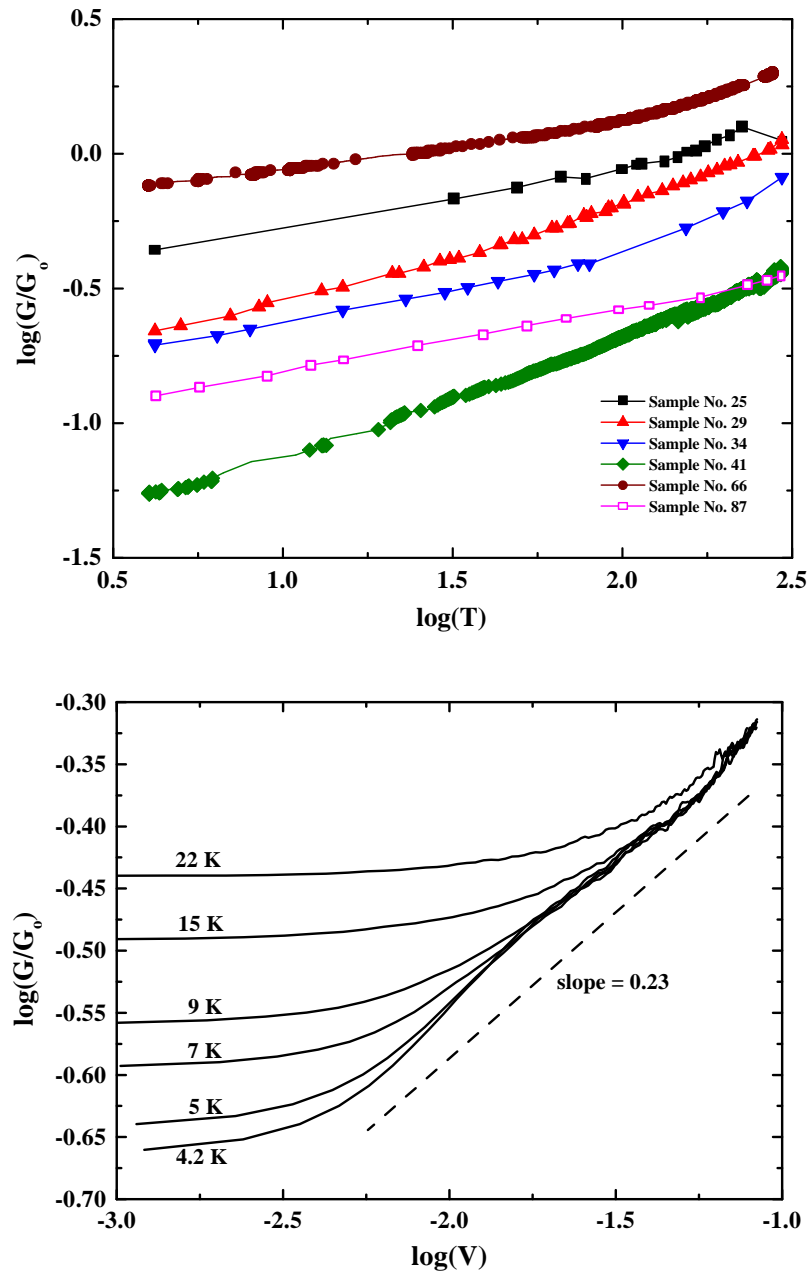


Figure 5.9. a) A plot of  $\log(G(0,T))$  versus  $\log(T)$  for the six MWNT samples studied. This plot shows the power law dependence of the zero-bias conductance. A change in the slope of the data occurs near a temperature of 100 K, possibly due to a freeze out of phonon modes. b) A plot of  $\log(G(V,T))$  versus  $\log(V)$  for sample No. 29 at low temperatures. The dashed line is a best fit to the voltage dependent conductance at low temperatures. The values for the slopes, obtained by least-squares fits to the data are tabulated in Table 5.2.

Table 5.2

Relevant parameters for the six samples studied. All parameters  $\pm 0.01$ .  
 (a) not enough low temperature data to obtain a reliable fit; (b) fits not convincing for  $50 \leq x \leq 100$ .

	Conductance	Eqn. 5.3 Fitting Parameters		
Sample ID	G (V=0,300 K)	$\alpha$ (T < 100 K)	$\alpha$ (4 K dI/dV)	$\eta$ (from scaling)
25	1.26 $G_o$	0.22	0.21	(a)
29	1.08 $G_o$	0.34	0.23	0.095
34	0.82 $G_o$	0.24	0.21	$\sim 0.09$ (b)
41	0.41 $G_o$	0.42	0.43	0.30
66	2.03 $G_o$	0.17	0.12	0.07
87	0.35 $G_o$	0.24	0.26	0.25

In addition, according to Eqn. 5.5, the conductance should follow a power law in voltage when the voltage energy scale is larger than the temperature scale. A typical plot used to estimate the power law dependence of the conductance with voltage at low temperatures is given in Fig. 5.9(b). The dashed line indicates the power law of the data. The low voltage data for these curves departs from the power law when the voltage energy scale and the temperature energy scale become comparable. [70] The values of the slope  $\alpha$  determined by least-squares fits to the 4 K data at high voltage are also listed in Table 5.2.

In accordance with Eqn. 5.3, a further consequence of LL theory is that  $G(V, T)/T^\alpha$  should scale as  $eV/k_bT$ . If LL behavior is present, the scaled conductance measured as a function of bias at different temperatures should collapse onto a universal curve. [127,133] Thus, the data were analyzed by plotting  $G/T^\alpha$  as a function  $eV/k_bT$ . The data for sample No. 29 at six temperatures between 4.2 K and 22 K are analyzed in this way, as shown in Fig. 5.10. The figure indicates that the data roughly follows a scaling relationship. For reference, the dashed line gives a plot of Eqn. 5.3 using a

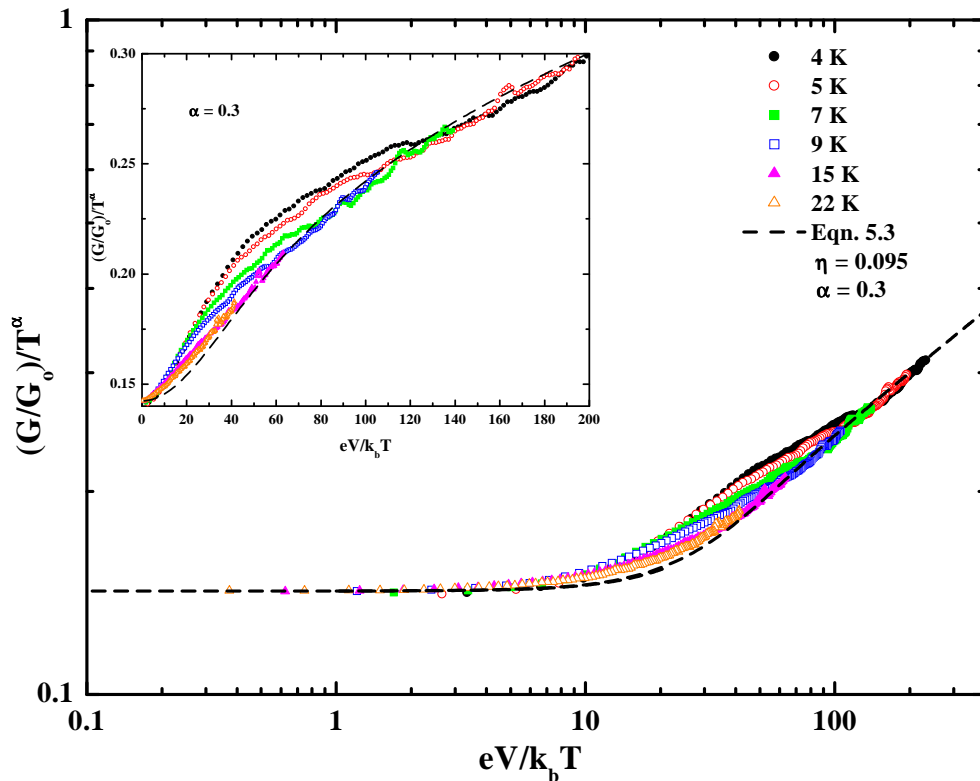


Figure 5.10. A plot of  $\log[(G/G_0)/T^\alpha]$  versus  $\log(eV/k_b T)$  from the low temperature data acquired from sample No. 29 indicating that the data roughly follows a scaling relationship. The dashed line is a plot of Eqn. 5.3 with  $\eta = 0.095$ . The inset is a plot of the same two quantities on a linear scale and shows the deviation of the data from theory for  $10 \leq eV/k_b T \leq 100$ .

value of 0.095 for  $\eta$ . Values of  $\eta$  obtained by analyzing data from the other samples in a similar way are collected in Table 5.2.

From the above analysis, we obtain the parameters listed in Table 5.2. For all of the samples except No. 29 and No. 66, the values listed for  $\alpha$  from the temperature and voltage dependencies agree within their uncertainties. This result is in agreement with Eqns. 5.4 and 5.5, which predict the same exponent for the power law behavior with temperature or voltage. Also, the data shown in Fig. 5.10 do scale approximately to a single curve, in accordance with Eqn. 5.3. These results indicate that the Luttinger liquid model is an accurate representation of the transport through

multi-walled nanotubes. This model provides a far more consistent description of the conductance than any of the other models studied (see Appendix F).

### 5.2.2 An Improved Model: Luttinger Plus Nanotube in Series

A critical reading of the previous section reveals two important features in our conductance data. First, as seen in Fig. 5.10, the data do not really collapse onto the universal curve predicted by Eqn. 5.3. The data deviate significantly in the decade of  $10 \leq eV/k_bT \leq 100$ . Second, the values of  $\eta$  obtained from this study are evidently smaller than those found in previous transport studies on SWNTs. [37] Bockrath *et al.* and Yao *et al.* have used the Luttinger model to successfully describe the conductance of SWNT systems. [37, 38] As mention above, Schönenberger *et al.* have interpreted some MWNT data in terms of the Luttinger model. [123] One important factor is that in our case, the overall system conductance is high. We believe that our high system conductance is due to the strongly coupled contacts produced using our fabrication technique. In the case of contacts strongly coupling to the nanotube, the contact resistance should be smaller than for weakly coupled contacts. Thus, our contact resistance to the nanotube is low and does not dominate the overall system resistance. If the contact resistance is on the order of the nanotube resistance, then there will be a significant voltage drop along the nanotube. Thus, the voltage division factor  $\eta$  may be less than 0.5, depending on the ratio of contact resistances to nanotube resistance. This scenario was also reported by Postma *et al.* in their study of buckled and crossed SWNTs. [133] In their case, the voltage drops at the contacts to the nanotubes and at the buckled and crossing regions. For a SWNT junction they find a value of 0.18 for  $\eta$ . [133]

Thus, how the voltage is divided is very important, and since our contact resistance is low, we must consider the resistance of the nanotube itself. This is illustrated in Fig. 5.11. For this simple picture, the total system conductance is given by

$$G_{Total} = \frac{G_{NT} \times G_{LL}}{2G_{NT} + G_{LL}}, \quad (5.8)$$

where  $G_{LL}$  is the Luttinger liquid component of the conductance (given by Eqn. 5.3)

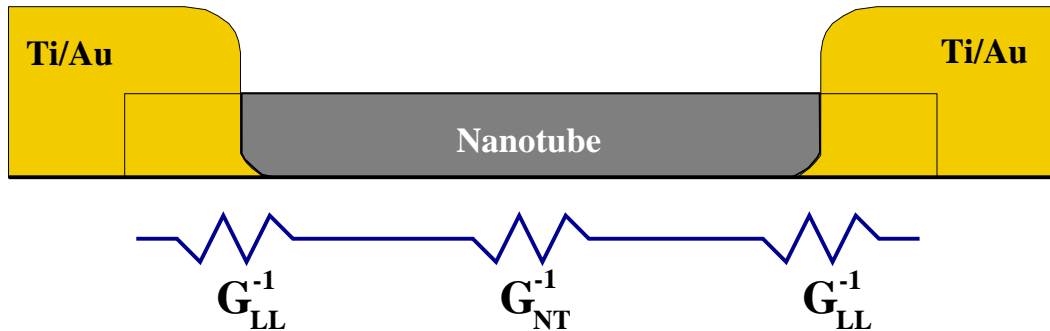


Figure 5.11. A schematic illustrating the location of the resistances in our MWNT samples.

and  $G_{NT}$  is the conductance of the nanotube itself. As shown in Fig. 5.11, the Luttinger liquid resistance ( $G_{LL}^{-1}$ ) is physically located at the contacts to the nanotube, where the Fermi liquid electrons must enter the non-Fermi liquid nanotube. The only new parameter introduced by Eqn. 5.8 is the nanotube conductance, for which we use a constant value. By using the simple model of three series resistors, the constant chosen for the nanotube conductance dictates the value of the voltage division factor  $\eta$  used in Eqn. 5.3 for  $G_{LL}$ . The total voltage drop  $V$  across the sample may be written as

$$V = 2\Delta V_{LL} + \Delta V_{NT} = 2\eta V + (1 - 2\eta)V, \quad (5.9)$$

where  $\Delta V_{LL} = I G_{LL}^{-1}$  and  $\Delta V_{NT} = I G_{NT}^{-1}$ . Thus,  $\eta$  is related to the ratio of the conductances by

$$\eta = \frac{1}{2 + G_{LL}/G_{NT}}. \quad (5.10)$$

Since  $G_{LL}$  is a function of voltage and temperature,  $\eta$  is as well.

The conductance as predicted by Eqn. 5.8 no longer necessarily follows a power law. Also, the scaling relationship no longer holds and the theory does not collapse to a universal curve for any finite values of  $G_{NT}$ . However, we can use Eqn. 5.8 to fit the low temperature conductance data. Fits to the low temperature data for sample No. 29 are shown in Fig. 5.12(a) for the same six temperatures as in Fig. 5.10. Here the data are shown as black symbols, and the theoretical curves are colored

lines. Since a scaling law does not apply for Eqn. 5.8, we include Fig. 5.12(b) for comparison. The fits shown in Fig. 5.12(b) were calculated with Eqn. 5.3 using the same parameters as in Fig. 5.10. The parameters used in Eqn. 5.8 for the calculations shown in Fig. 5.12(a) were determined using a least-squares fitting program written in *Mathematica*<sup>TM</sup>. The routine is provided in Appendix G. For these calculations, the nanotube conductance  $G_{NT}$  was a constant and was used in Eqn. 5.10 to calculate  $\eta$ . Since  $G_{LL}$  is a function of  $\eta$ , we iterate Eqn. 5.10 to find a self-consistent value for  $\eta$ .  $G_{LL}$  is also a function of temperature and voltage, so technically we must calculate  $\eta$  for every temperature and voltage as well. The change in  $\eta$  calculated at different temperatures is insignificant, however,  $\eta$  does change significantly when calculated at different voltages. When a consistent voltage-dependent value for  $\eta$  is used in Eqn. 5.8, the data for sample No. 29 is not well fit. Still, using a voltage-independent  $\eta$ , the improvement in the fits to the data is remarkable. By simply adding a single component for the nanotube conductance, we are able to fit the low temperature data much better. The data in the region  $10 \leq eV/k_bT \leq 100$  ( $\sim 3.5\text{--}35$  mV at 4 K) which departed from the Luttinger model alone, are now well described.

Given the quality of the fits calculated for a constant value of  $\eta$ , we believe that there may be an additional voltage and/or temperature dependent effect, which is not included in Eqn. 5.8. This additional effect may stem from a voltage or temperature dependence of the nanotube itself, which may partially cancel the voltage dependence of  $\eta$ . Thus, for sample No. 29 we only calculate  $\eta$  at 0.075 V, which is the high voltage range of the data. Also, the effect of  $\eta$  is reduced as the voltage goes to zero. Despite the inconsistency in the voltage dependence of  $\eta$ , we now have a natural explanation for its small value, namely a significant voltage drop along the nanotube. Interestingly, the presence of a voltage drop along the nanotube and not only at the contacts was directly observed in the Kelvin Force Microscopy measurements of Brian Walsh. [71] He observed voltage drops located at the contacts to a MWNT and a linear decrease in the potential profile along its length. From his data the value of  $\eta$  was around 0.2 to 0.27, which is the same as the values found here.

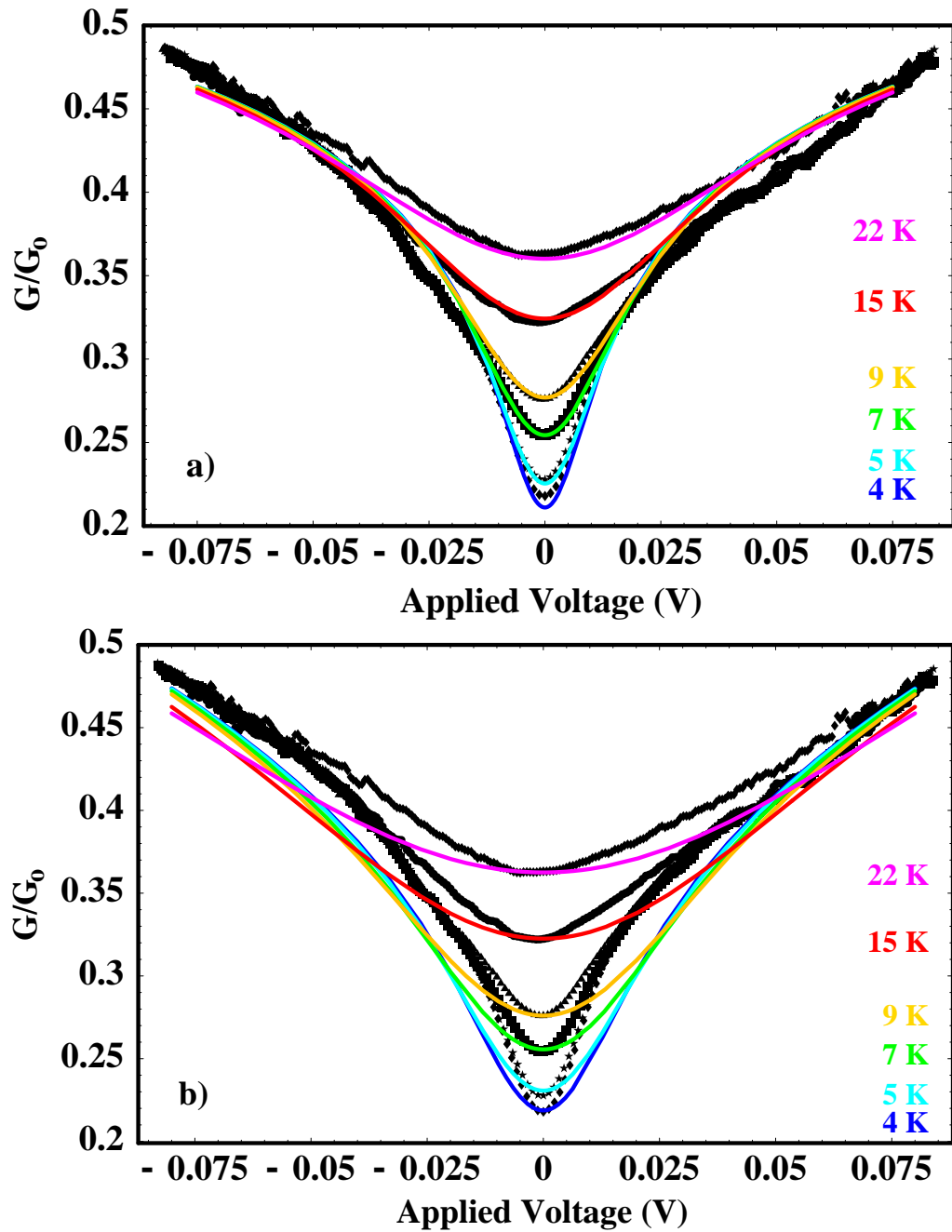


Figure 5.12. A plot of  $G(V,T)$  versus voltage at six temperatures for sample No. 29. The data is shown as black symbols, and the theory is shown as solid colored lines. In a) we show fits using Eqn. 5.8. For comparison, in b) we show fits using Eqn. 5.3.

Table 5.3

Fitting parameters used with Eqn. 5.8 for the six samples studied. Conductances are in units of  $G_o$ , and all parameters are  $\pm 0.02$ . (a) not enough low temperature data to obtain a reliable fit.

	<b>Conductance</b>	<b>Eqn. 5.8 Fitting Parameters</b>			
Sample ID	G (V=0,300 K)	$G_{NT}$	$A$	$\alpha$	$\eta$
25 (a)	1.26	0.77	1.37	0.95	0.05
29	1.08	0.67	0.68	0.56	0.16
34	0.82	0.42	0.81	0.53	0.13
41	0.41	0.34	0.14	0.58	0.23
66	2.03	1.25	3.80	0.39	0.12
87	0.35	0.50	0.47	0.36	0.24

Using the same method, we analyzed the data from the other five samples. The fitting parameters obtained from the analyses are listed in Table 5.3. In Fig. 5.13 we show the best fits obtained for two other samples using Eqn. 5.8. The parameters used for these two fits were not calculated using the least-squares program, although the least-squares values are very close to the ones used. Fig. 5.13(a) shows the fits for sample No. 66, which had a RT conductance of  $2 G_o$  at zero-bias. Fig. 5.13(b) shows the fits for sample No. 87, which had a RT conductance of  $0.35 G_o$ . There is a clear asymmetry between the  $G(-V,T)$  and  $G(+V,T)$  data for sample No. 87 (as shown in Fig. 5.7). This asymmetry may stem from poor electrical contact to the MWNT. To fabricate this sample the MWNT was placed on top of the gold contacts and not buried beneath them. We expect that this configuration results in a poor contact to the nanotube, which is why this sample had the lowest RT conductance for these six samples. A high resistance at the contacts to the nanotube is also indicated by the value for  $\eta$  of 0.24, meaning that  $\sim 50\%$  of the voltage was dropped at the contacts to the nanotube. In contrast, sample No. 66 had both the highest

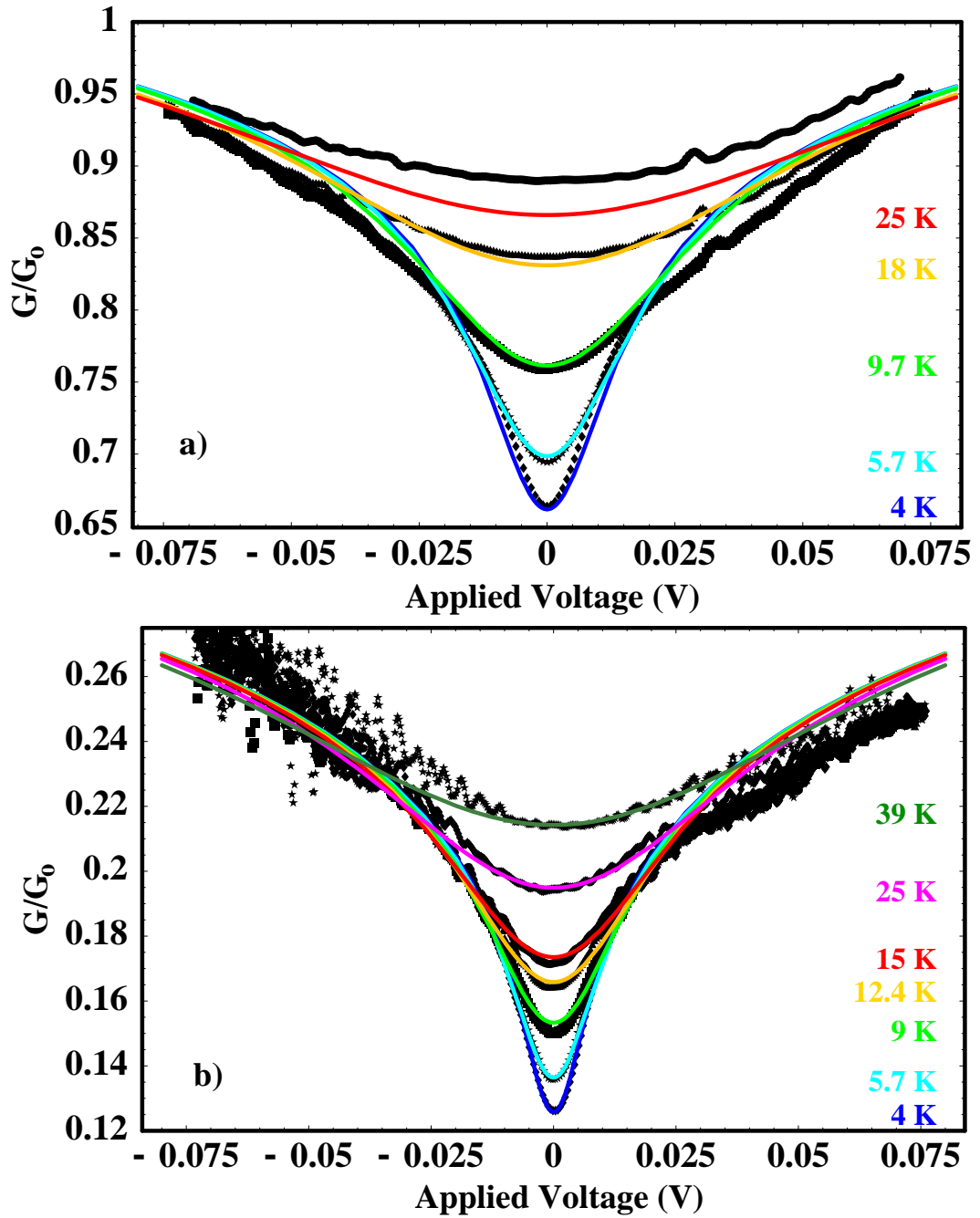


Figure 5.13. A plots of  $G(V, T)$  versus voltage for a) sample No. 66 and b) sample No. 87. The data is shown as black symbols, and the calculations using Eqn. 5.8 are shown as solid colored lines. There is a clear asymmetry in the data for sample No. 87.

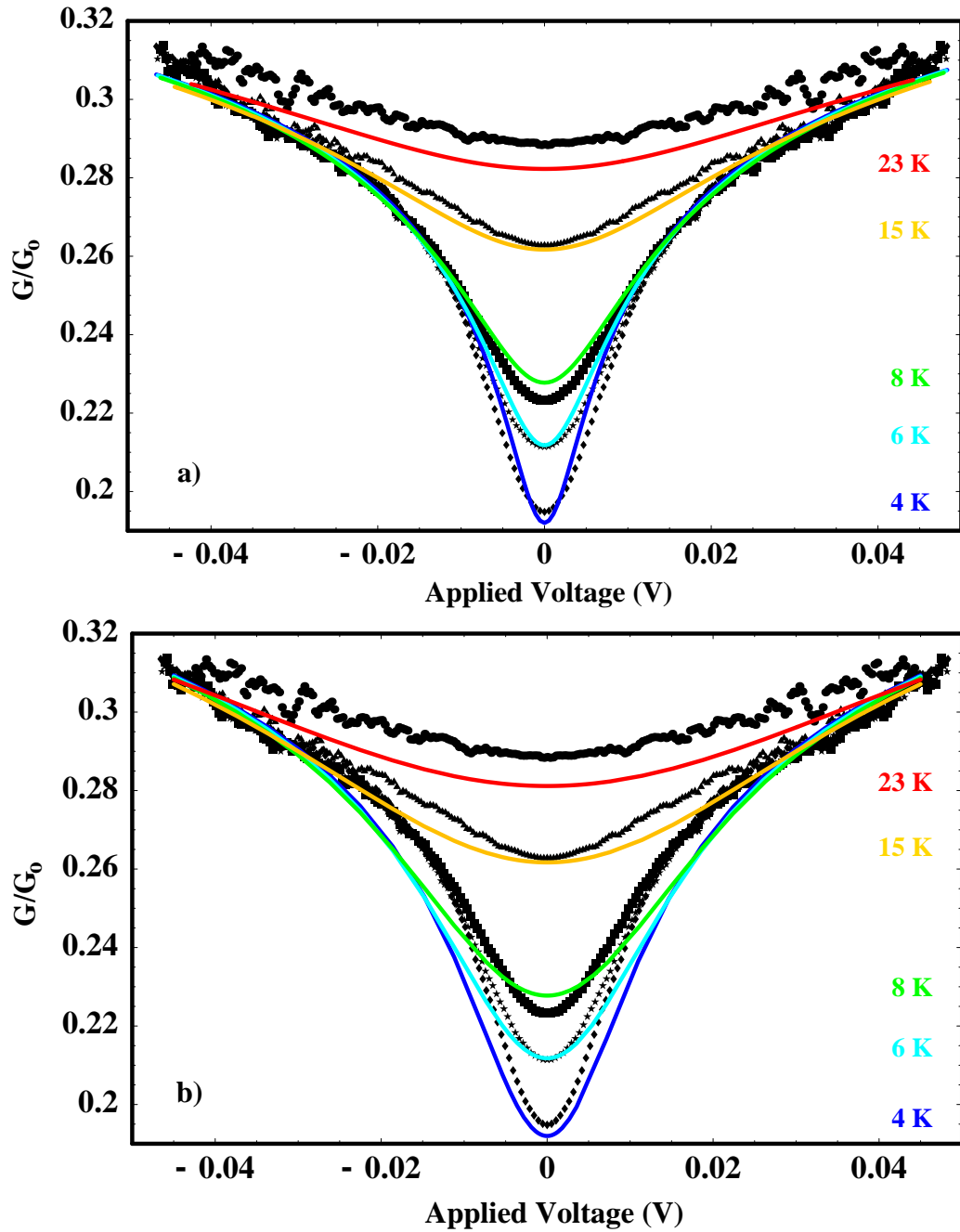


Figure 5.14. A plot of conductance versus voltage for sample No. 34. In (a) the fits were calculated with  $\eta$  determined at every voltage and temperature. In (b) the fits calculated with  $\eta$  determined only at 0.04 V and 4 K.

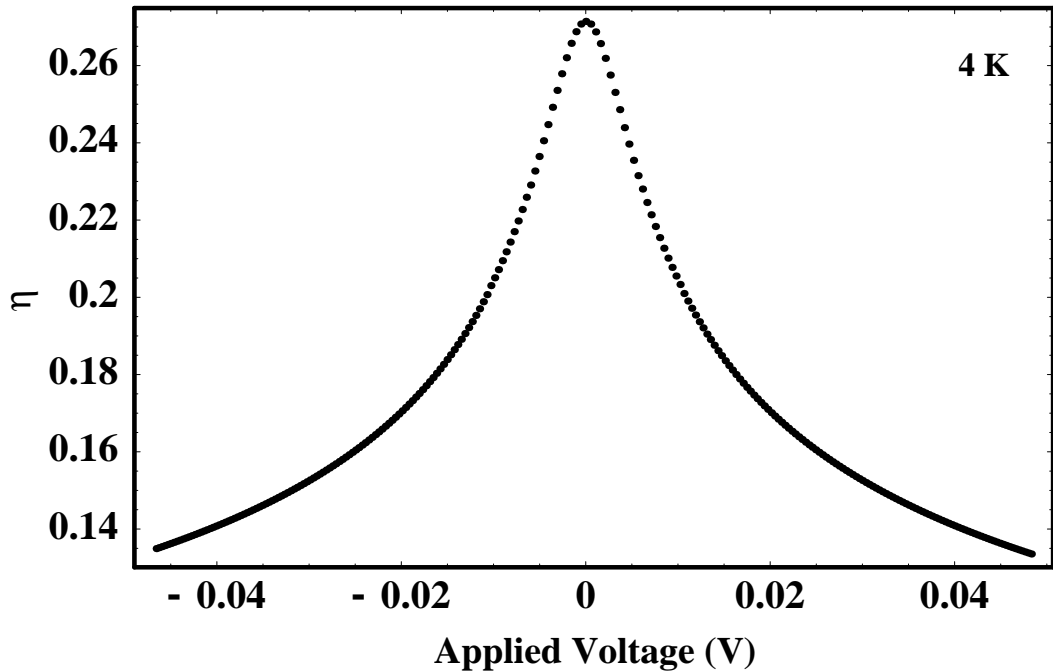


Figure 5.15. A plot of  $\eta$  versus voltage calculated for sample No. 34 at 4 K.

RT system conductance and the lowest value for  $\eta$ . The value for  $\eta$  of 0.12 means that a total of only  $\sim 25\%$  of the voltage was dropped at the contacts to this sample. The other high RT conductance sample, No. 25, also has a low value for  $\eta$ . Thus, there seems to be a correlation between the RT sample conductance and the coupling between the nanotube and contact, as characterized by the value of  $\eta$ .

For sample No. 34, we were able to fit the data using a completely self-consistent model. That is, the least-squares fit to the data, with  $\eta$  calculated self-consistently at every voltage and temperature fits the data well. Fig. 5.14(a) shows such a fit determined by the least-squares *Mathematica*<sup>TM</sup> routine given in Appendix G. Fig. 5.14(b) shows the fit calculated using the same parameters as in (a), but with  $\eta$  calculated only at 0.04 V for the 4 K data. The effect of the self-consistent determination of  $\eta$  is clear. Fig. 5.15 shows a plot of  $\eta$  versus voltage at 4 K. The value of  $\eta$  becomes larger near zero-bias, where the LL term of the total conductance has its minimum. Thus, the voltage drop at the contacts becomes larger at zero bias.

Table 5.4

Electron interaction parameters for the six samples studied, calculated from Eqns. 5.6 and 5.7 for  $N=1$ . All parameters  $\pm 0.02$ . (a) not enough low temperature data to obtain a reliable fit.

Sample ID	$g (\alpha_{bulk})$	$g (\alpha_{end})$
25 (a)	0.11	0.21
29	0.16	0.31
34	0.16	0.32
41	0.15	0.30
66	0.20	0.39
87	0.21	0.41

The values of  $\alpha$  obtained from these fits can be used to estimate values of  $g$ , the electron-electron interaction parameter, using Eqns. 11 and 12. The two cases  $\alpha_{end}$  and  $\alpha_{bulk}$  are considered separately since we cannot be sure which configuration applies in each nanotube. The results are listed in Table 5.4. Theoretical estimates for  $g$  typically lie around 0.18–0.3, [22, 29, 37, 38, 133] which can be compared to the data in Table 5.4. The data indicate that for samples No. 66 and 87 values of  $g$  calculated assuming electron injection into the sides (bulk case) of the MWNT give values close to theoretical expectations. The values of  $g$  for samples No. 29, 34, and 41 lie at the limits the expected values, but are closest for the *end*-contacted case. Sample No. 25 seems also to be *end*-contacted, but there is not enough low temperature data for this sample to make a reliable estimate. These results show that the electrons in the MWNTs are strongly interacting, since all of the values for  $g$  are less than one.

The data presented in this section provide strong evidence for the Luttinger liquid phase in multi-walled nanotubes. The model presented in this section describes both the voltage and temperature dependence of the conductance at low temperatures. Of all the models we have studied, the Luttinger liquid plus nanotube model provides

the most accurate description of the observed transport behavior. The next closest temperature dependent conductance model would be weak localization. Since we observe a strong voltage dependence for our samples, we believe the Luttinger model is appropriate. The measurements of Shea *et al.* reveal features of weak localization *and* a Luttinger liquid, where the LL was distinguished by its voltage dependence. [103] Thus, all of the features we have measured are consistent with the Luttinger liquid model, with the conductance of the nanotube included.

### 5.3 Conductance Data from Two Other Samples

In this section we briefly describe temperature dependent conductance measurements made on MWNTs provided by A.M. Rao while at the University of Kentucky. These samples are not included in Fig. 4.12 because they were made using a different growth process (chemical vapor deposition, CVD) and have different physical properties. [134] TEM images shown in Fig. 5.16 reveal that these MWNTs have a very kinked structure. Many of these MWNTs have large inner diameters, in contrast to the arc-grown MWNTs used in this study, which are typically completely filled. In addition to the kinks and bend in these tubes, the catalytic particles are also present. The presence of these particles is another side-effect of the CVD growth method, in which the nanotubes are grown from catalytic particles. In the arc-discharge method, used for the other MWNTs in this study, the nanotubes grow in plasma between two carbon electrodes, and no catalyst is needed. The structural properties of the CVD nanotubes should play a significant role in terms of their transport properties.

Two samples from the Kentucky source were successfully fabricated and mounted in the dip-probe. Fig. 5.17 shows AFM images of one of the samples. We acquired conductance data from these samples in the same manner as the other samples. In the case of sample No. R4, we initially degassed the sample by pumping on the dip-probe for several days while heating the sample to  $\sim 350$  K. The initial room temperature (RT) zero-bias conductance for this sample was  $1.4 G_o$ . Upon heating the conductance rose to  $1.44 G_o$ , then fluctuated and gradually reduced to  $\sim 0.9 G_o$  at 350 K. When the sample was cooled to RT, the conductance decreased to  $\sim 0.7 G_o$ . For some unknown

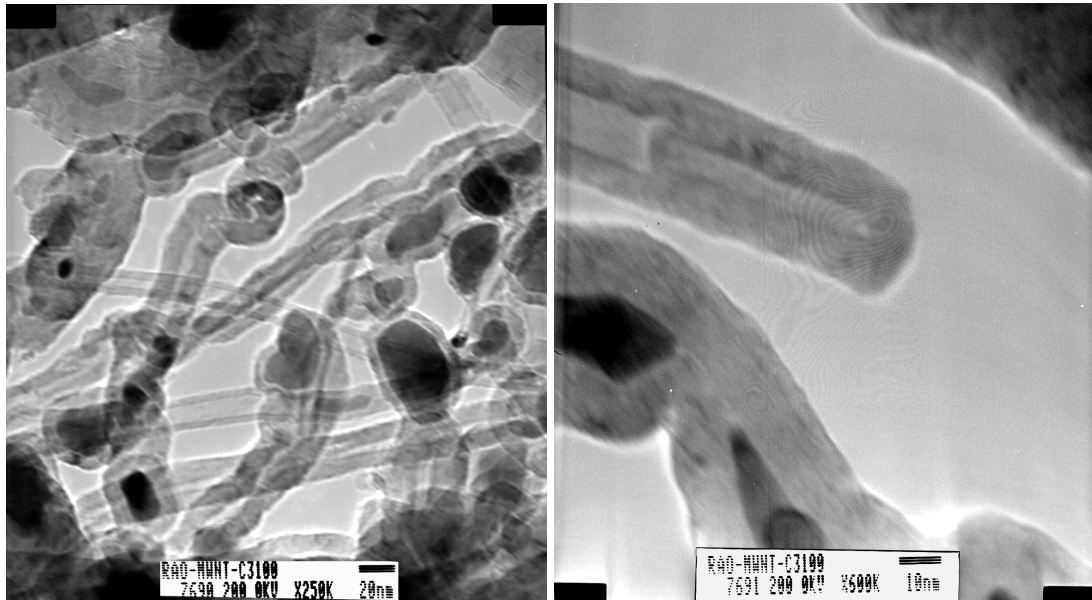


Figure 5.16. TEM images of CVD grown nanotubes. These MWNTs have large inner diameters and kinked wall structures, which is very different from the arc-grown MWNTs used in this study.

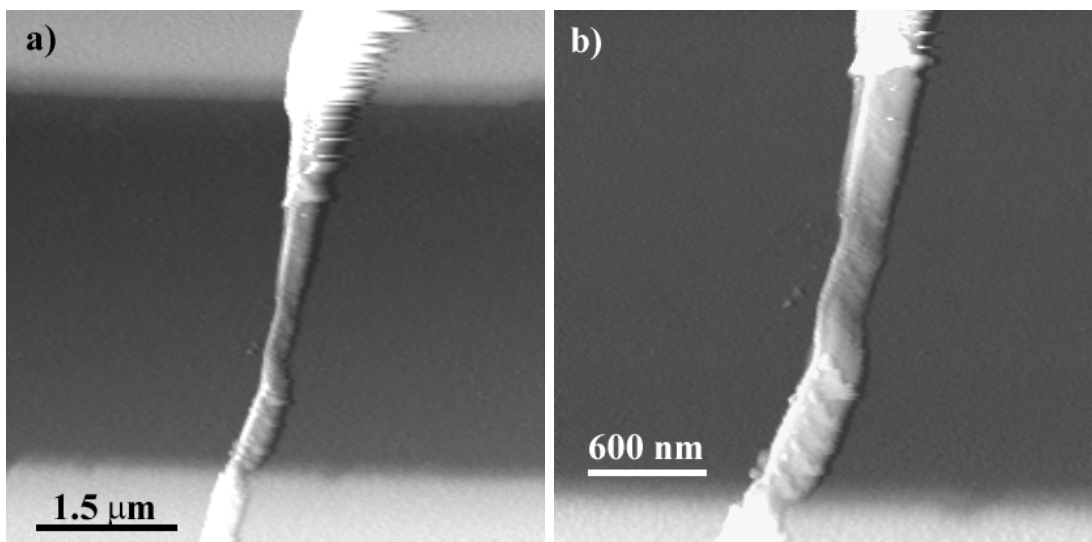


Figure 5.17. AFM images of sample No. R5. Image a) is  $6 \times 6 \mu\text{m}^2$  and image b) is  $3 \times 3 \mu\text{m}^2$ . Image b) shows a zoom near one of the contacts. The large diameter of this MWNT rope and the triangular features are the result of tip dilation.

reason, the conductance then changed overnight to  $\sim 0.08 G_0$ . Such a dramatic change in the conductance has not been observed for any other sample.

The conductance of sample No. R4 as a function of voltage at several temperatures is shown in Fig. 5.18. There is a striking difference between this  $G(V, T)$  data and the data for the previous samples. The conductance for sample No. R4 changed by over four orders of magnitude from RT to 4 K. This is the largest change in conductance that we have observed. Also, a large gap forms in the conductance at low temperatures. A voltage offset developed in the  $I(V)$  data as the sample was cooled. The offset has been subtracted from the data such that  $V = 0$  at  $I = 0$ . The affect of this offset can be seen in the asymmetry of the data in Fig. 5.18(b) and the inset where the gap spreads from  $V = 0$  to almost 400 mV at 4 K. The conductance at zero-bias is plotted versus temperature in Fig. 5.19 on a linear scale in (a), and the log of the data is shown in (b). The data clearly saturates at low temperatures, which is a feature not seen in other samples.

Also apparent in Fig. 5.18 is an extremely large amount of noise in the  $I(V)$  data near RT. This noise is seen in the  $I(V)$  data shown in Fig. 5.20 as the scatter in the data points. Since the current is applied and the voltage is measured, the data display vertical jumps on an  $I(V)$  plot. The samples analyzed in the last sections also displayed noise at high voltages. However, the noise for those samples was not nearly so easy to see in the  $I(V)$  data. The  $I(V)$  data from this sample also displayed reproducible structure, as seen in the  $I(V)$  data shown in Fig. 5.20 and indicated by arrows. This  $I(V)$  is similar to the  $I(V)$  shown in Fig. 2.9(b) for transport through several modes of a ballistic conductor.

In Fig. 5.21 we show the RT conductance versus voltage with the  $I(V)$  data. The data was taken after the conductance of the sample decreased to  $\sim 0.08 G_0$ . The data shown in this figure is the average of 10 data curves, yet several features remain. The structure in the  $I(V)$  is still present, though not as obvious as in Fig. 5.20. The structure in the  $I(V)$  is apparent in the  $G(V)$  data as well. The peaks in the  $G(V)$  data correspond to the structures seen in the  $I(V)$  data. Comparison of the  $I(V)$ 's

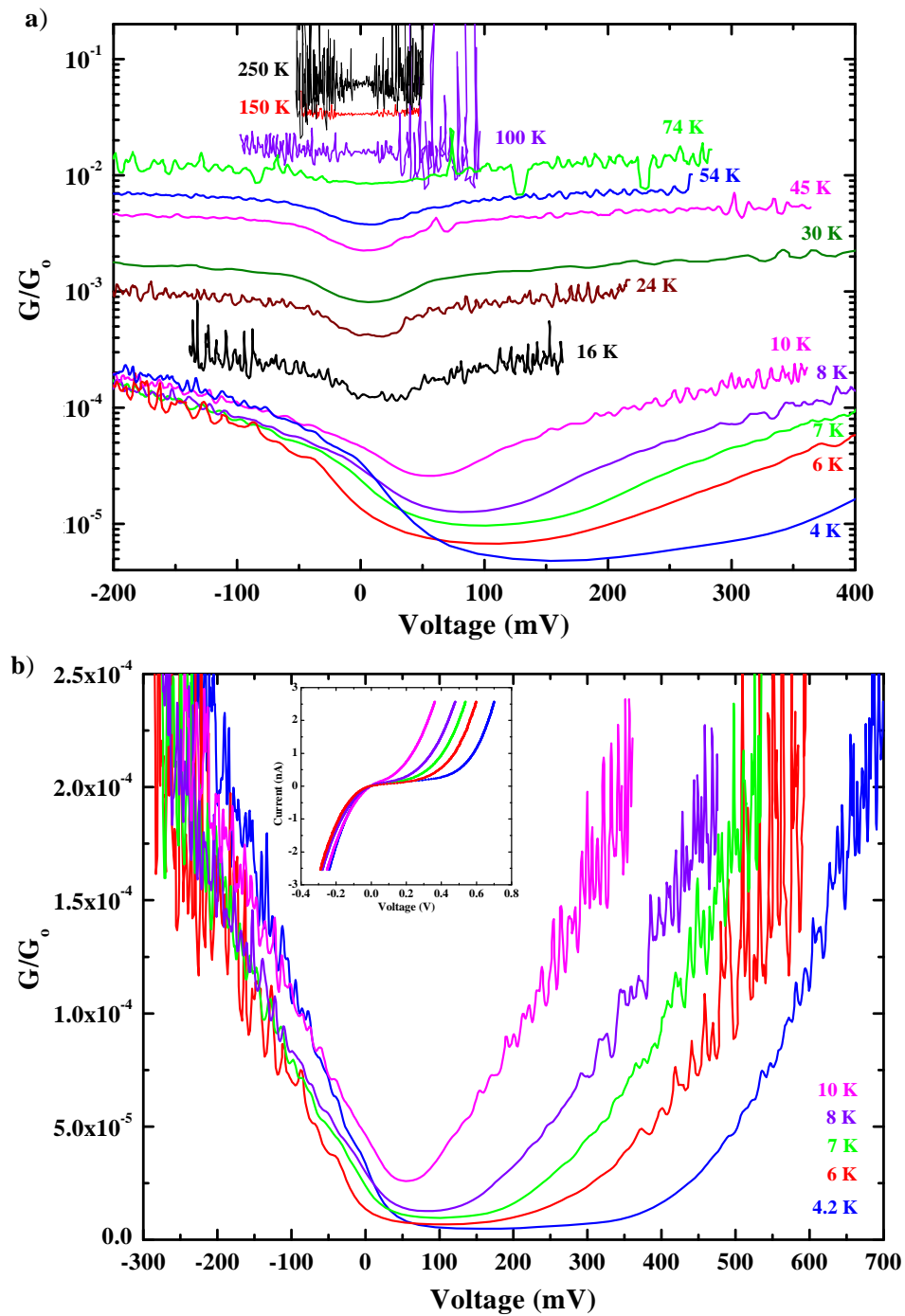


Figure 5.18. Conductance data for sample No. R4. The  $G(V,T)$  data are clearly different than for the other samples. In a) the conductance is shown from 250 K to 4 K. Note that the  $y$ -axis is a log scale. The data from 10 K to 4 K is shown in b). The inset in b) shows the corresponding  $I(V)$  data.

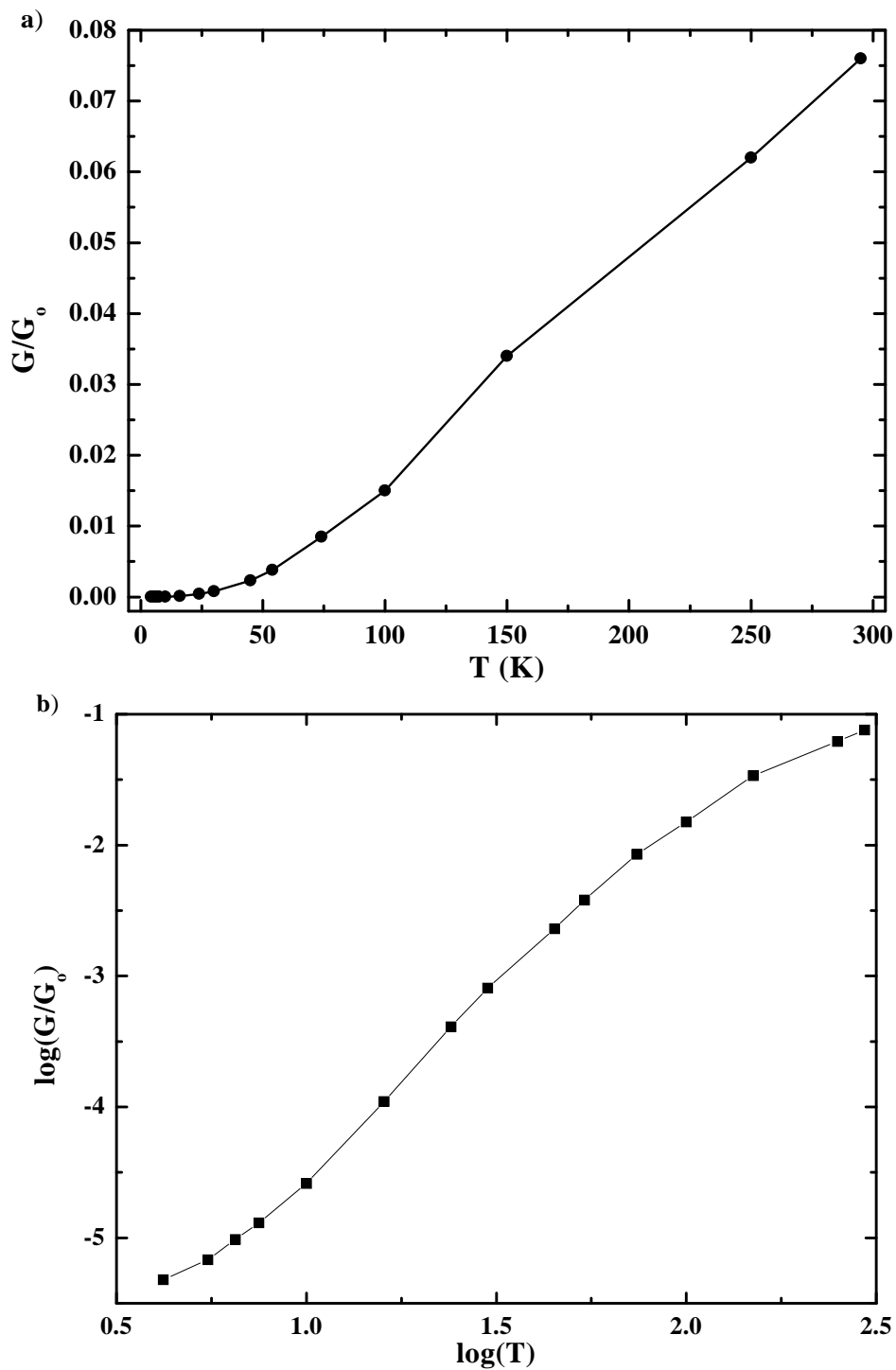


Figure 5.19. Conductance at zero-bias versus temperature for sample No. R4. The  $G(T)$  data saturates at low temperatures as seen in a). In b) a plot of  $\log(G)$  versus  $\log(T)$  shows that the conductance changes by several orders of magnitude from RT to 4 K.

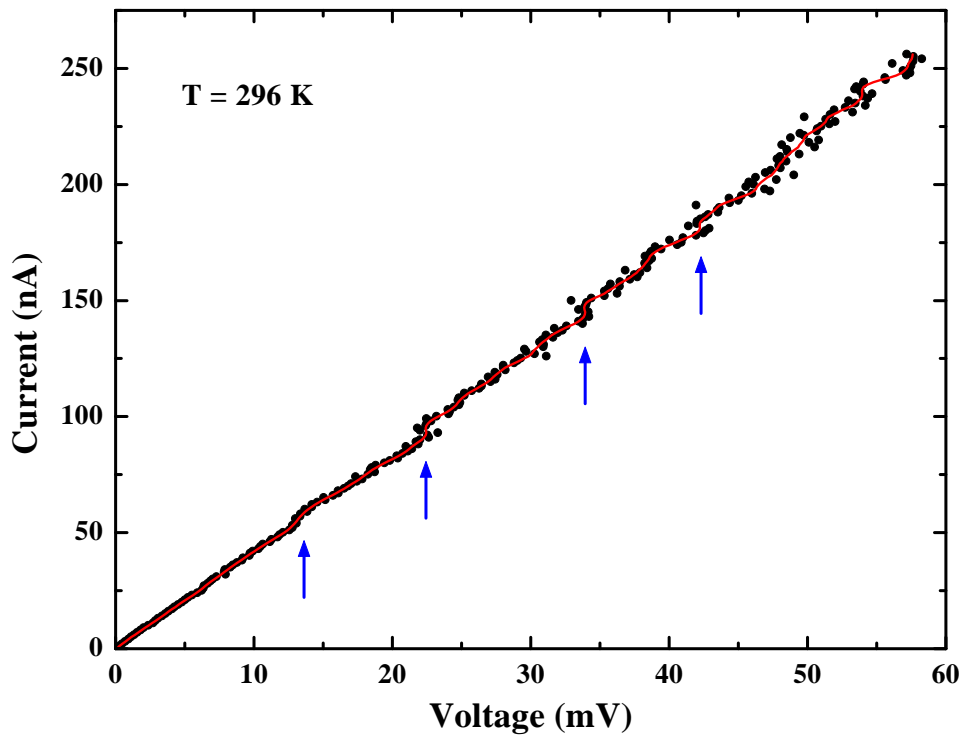


Figure 5.20.  $I(V)$  data at RT for sample No. R4. A large amount of noise appears as the scatter of the data points in the high bias region of the data. For the previous samples, the data points were indistinguishable. Also there is structure in the  $I(V)$  data, indicated at several points by arrows. This  $I(V)$  data is similar to the schematic  $I(V)$  shown in Fig. 2.9.

obtained from this sample with the  $I(V)$  shown in Fig. 2.9(b) would suggest that the structure in the data is related to the 1D density of states of the nanotube. This interpretation is also supported by the peaks seen in the  $G(V)$  data in Fig. 5.21. In Fig. 5.21(b) we show the positive and negative voltage regions of the  $G(V)$  data. The red vertical lines, shifted from the origin by 3 mV, serve as guides showing that the peak structure is roughly symmetric with voltage, although offset from  $V = 0$ . These peaks in the conductance are consistent with the peaks in the DOS for a nanotube. This low conductance indicates a weak contact to the nanotube. The asymmetry shown in the  $G(V,T)$  data of Fig. 5.18 is evidence that one contact was strongly coupled to the nanotube, while the other was only weakly coupled. Thus, the Fermi

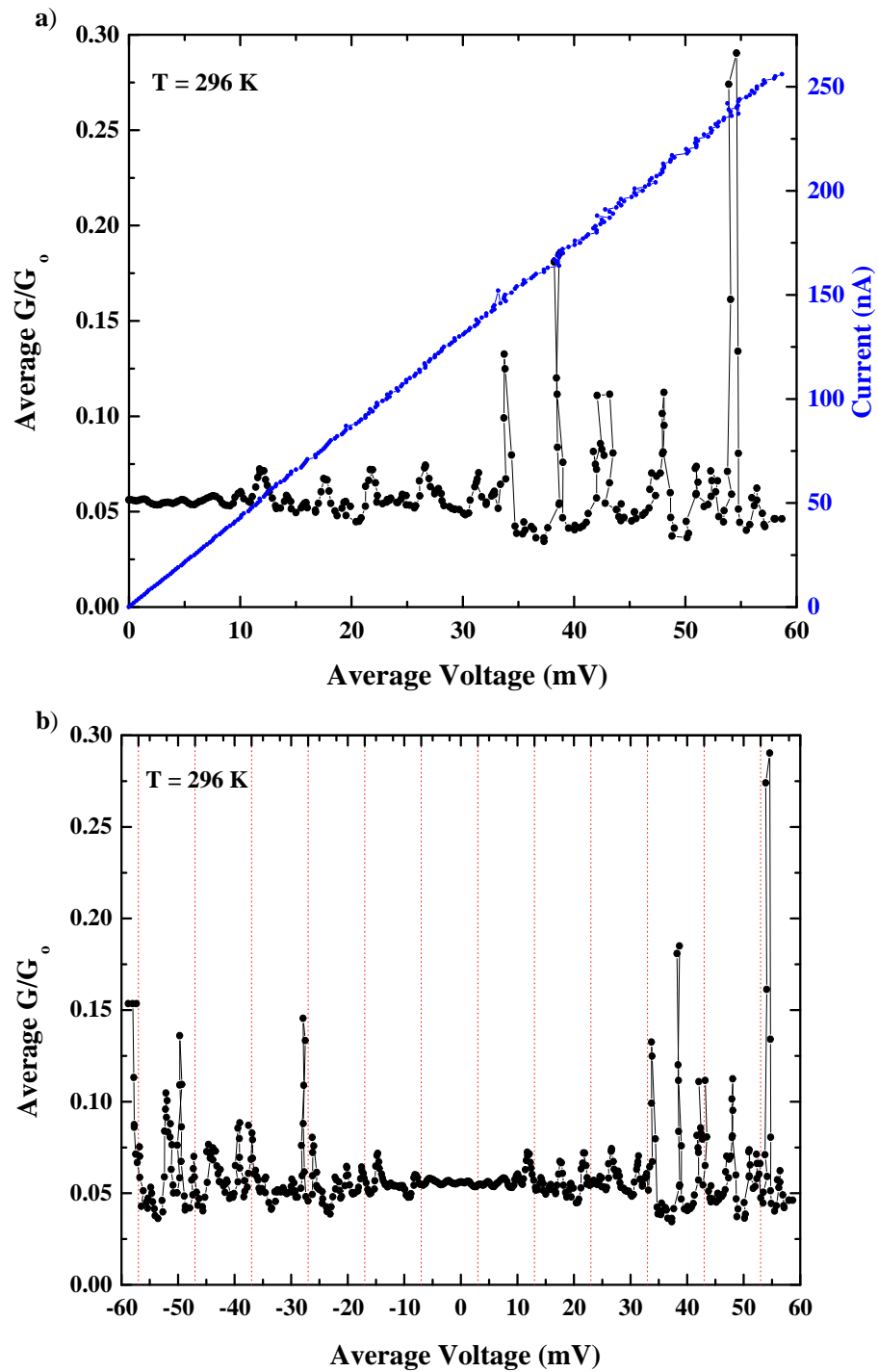


Figure 5.21. Figure a) shows  $I(V)$  and  $G(V)$  data from sample No. R4 averaged for 10 data sets. The structure in the  $I(V)$  data remains and is evident in the  $G(V)$  data as peaks. In (b) the conductance is shown at positive and negative voltages. The red lines, shifted from the origin by 3 mV, serve as guides to show that the peaks are roughly symmetric.

level of the nanotube was pinned to the strongly coupled contact. This configuration is similar to an STM and is necessary to observe the density of states features.

The other sample made with the Kentucky MWNTs again displayed completely different behavior. The RT zero-bias conductance of sample No. R5 was  $\sim 1.44 G_o$ , and the conductance at 4 K was  $\sim 1.14 G_o$ . The  $G(V,T)$  data for this sample is shown in Fig. 5.22. Since the resistance of this sample was so low, the voltage range in Fig. 5.22(a) is small and the conductance appears flat. In Fig. 5.22(b) the applied current was increased up to a factor of 10. The resulting  $G(V,T)$  at 4 K shows an increase with voltage similar to the samples of the previous sections. The  $G(V,T)$  data also display an asymmetry similar to samples No. 41 and 87. It is interesting that the  $G(V,T)$  data remains noisy at 4 K, although the noise is lower than at RT.

For comparison with the samples analyzed in the previous sections, the zero-bias conductance is plotted versus temperature in Fig. 5.23 with the data from the other six samples. The temperature dependence of sample No. R5 is clearly different from the other samples. The zero-bias conductance data for sample No. R4 is not plotted here since the scale of the conductance change is much greater for this sample.

The conductance data obtained from the CVD grown MWNTs are clearly different from the previous samples, and are even different from each other. Since only two samples with CVD nanotubes have been successfully studied to date, we do not know what the general characteristics of these tubes are. Since the CVD tubes are grown from catalysts deposited on quartz substrate the sample fabrication technique for these tubes is different that for the other samples. It has not been possible to control the voltage of the CVD nanotube source substrate, and often a large voltage is evident between the nanotubes and the Pt tip during sample fabrication. This large voltage could cause structural damage to the selected nanotube, if it is not destroyed in the spark-discharge. Also as mentioned, there are numerous structural difference between these MWNTs and the others simple based on the differences in growth technique. The resulting conductance data show both promising and not so promising results. If the majority of CVD grown nanotubes behave as sample No. R5, then these tubes

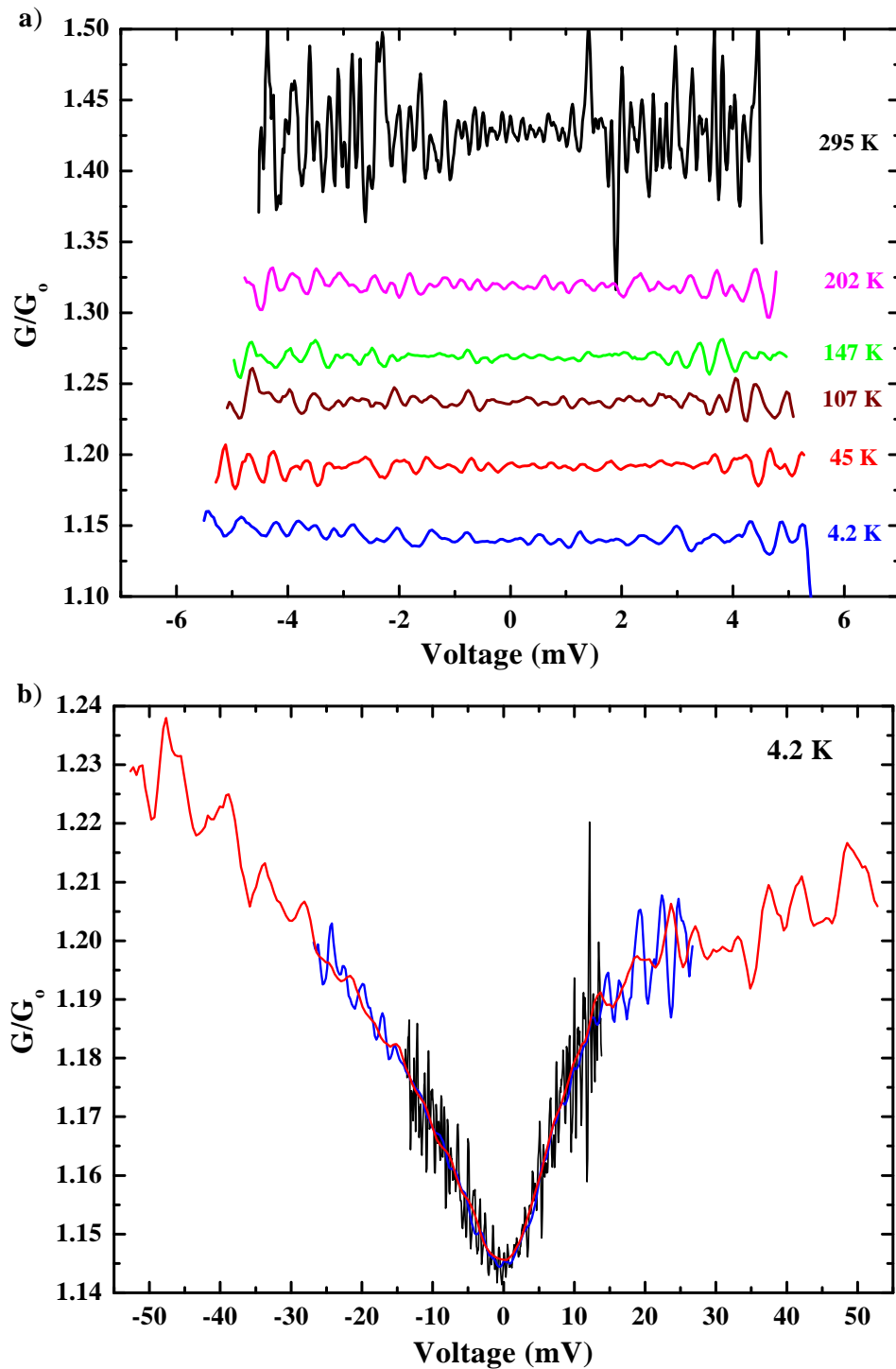


Figure 5.22. a)  $G(V,T)$  data for sample No. R5. This sample showed the smallest change in conductance from RT to 4 K. In b) the current ramp was increased to show that the conductance increases with voltage similar to previous samples.

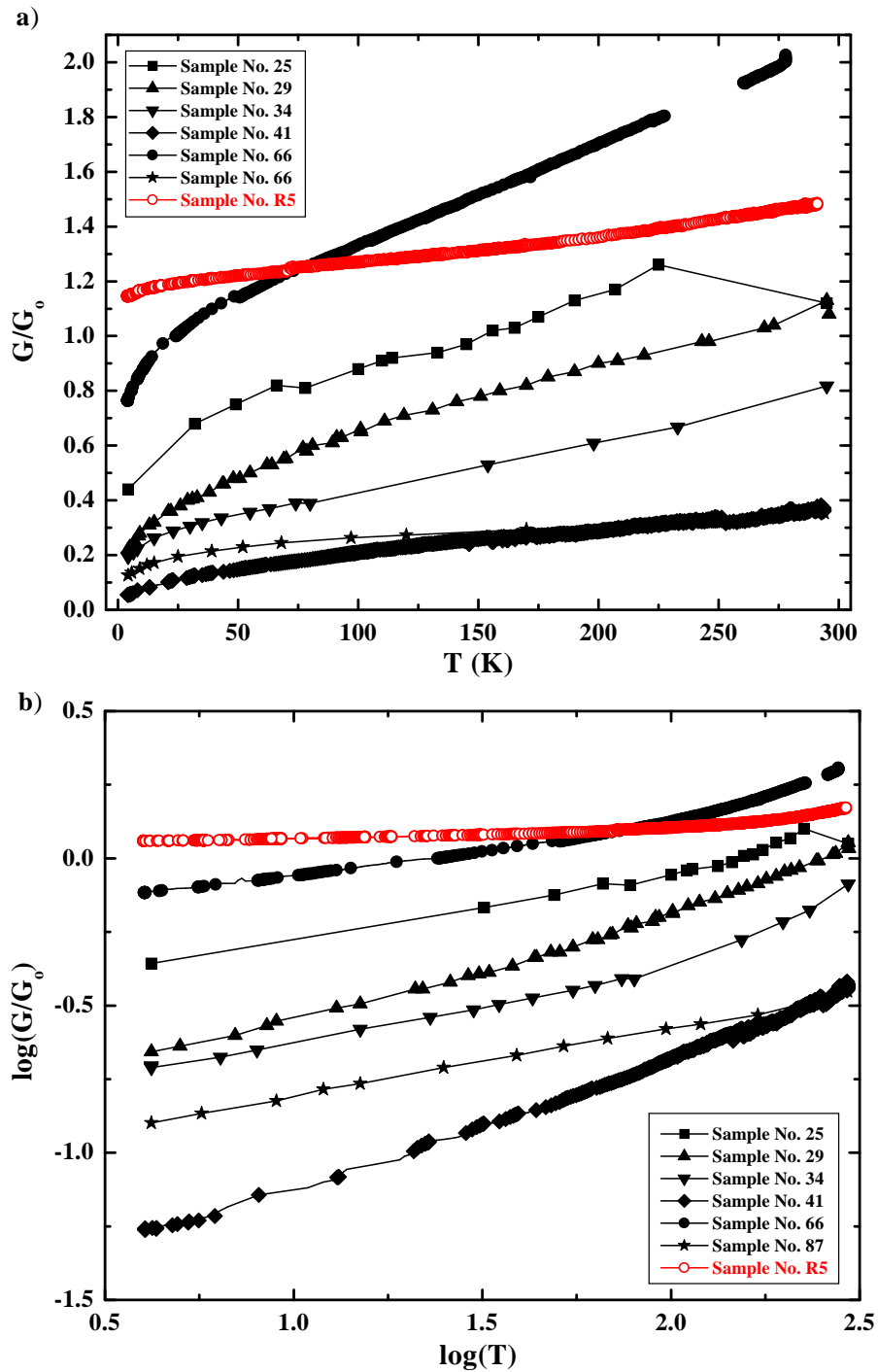


Figure 5.23. In a) the zero-bias conductance for sample No. R5 (shown red) is plotted versus temperature along with the six samples studied in the previous sections. This sample showed the smallest change in conductance from RT to 4 K. Figure (b) shows a plot of  $\log(G)$  versus  $\log(T)$  for comparison.

may be better candidates for molecular wires. CVD grown nanotubes are especially convenient since the catalysts may be patterned as desired, then the nanotubes grown in these specified locations, as has already been demonstrated. [6, 39]

#### 5.4 Noise Measurements

As discussed in the previous sections, the  $I(V)$  obtained from all of the nanotube samples exhibited a significant amount of noise at room temperature and high bias. In order to better characterize this noise, initial measurements of the noise characteristics from the nanotube samples have been made. Most of our noise studies were performed by measuring the sample voltage as a function of time,  $V(t)$ , at a constant applied current.  $V(t)$  measurements were made at various temperatures in order to study the reduction of the noise with temperature that is apparent in the conductance data. For sample No. R4, preliminary measurements were also made using a lock-in amplifier, which directly measures the noise voltage at a specified frequency.

The  $V(t)$  measurements on MWNTs have shown them to be noisy conductors. The MWNTs we have studied are noisier than a common carbon resistor, which has the highest noise value for typical lab resistors. For immediate comparison Fig. 5.24 shows the voltage measured over an 8 hour period at RT for sample No. 29 and a 10 k $\Omega$  resistor. The red data is the resistor and the black points are the nanotube data. Both  $y$ -axes are 0.2 mV full scale. Both measurements were performed using the dip-probe discussed in Appendix E, with 500 nA as the applied current in each case. The large scale fluctuations of the voltage across sample No. 29 are due to slight temperature fluctuations of the probe. The faster fluctuations are intrinsic to the nanotube sample.

In many cases the voltage across the sample shows a bistability indicative of a two-level system. [114, 135–137] In such a system, there are two stable states between which the system randomly fluctuates. For this reason, the noise present in a two-level system is often called random telegraph noise, RTN. In Fig. 5.25, this behavior can be seen in the  $V(t)$  data for sample No. 66. This data was acquired over a 4 hour period with 500 nA applied to the sample at a temperature of 6 K. The DC offset

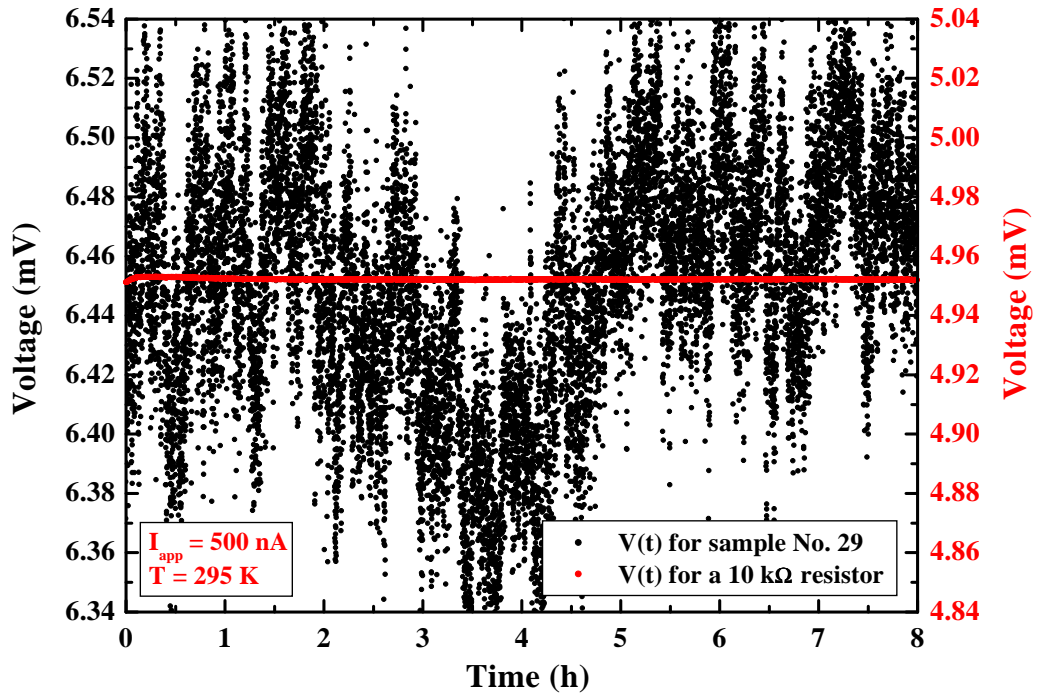


Figure 5.24.  $V(t)$  data at RT for sample No. 29 and a 10 k $\Omega$  resistor. The difference in noise levels is obvious. Although the absolute values are slightly different, both  $y$ -axes are 0.2 mV full scale. The current applied in each case was 500 nA. Both measurements were made using the dip-probe system discussed in Appendix E.

has been subtracted from the data. Each of the two levels seen in Fig. 5.25(b) also displays a large excess noise. In many two-level systems the RTN is the dominant noise of the system. Here the size of the RTN is comparable to the excess noise of the system. Thus, the overall noise of a nanotube sample with RTN has an amplitude almost twice as large as a sample with out such fluctuations. In this case, the overall peak-to-peak noise voltage is  $\sim 12 \mu\text{V}$  (Fig. 5.25(a)), while the peak-to-peak noise voltage for each level is  $\sim 6 \mu\text{V}$  (Fig. 5.25(b)).

In Fig. 5.25(b) the lifetime of the lower level is slightly longer than the lifetime of the upper level. Often the fluctuation between levels is on average faster than the data acquisition rate. If the lifetime of only one level is smaller than the voltage integration period of the Keithley 196 DMM, the system may appear to exist in only

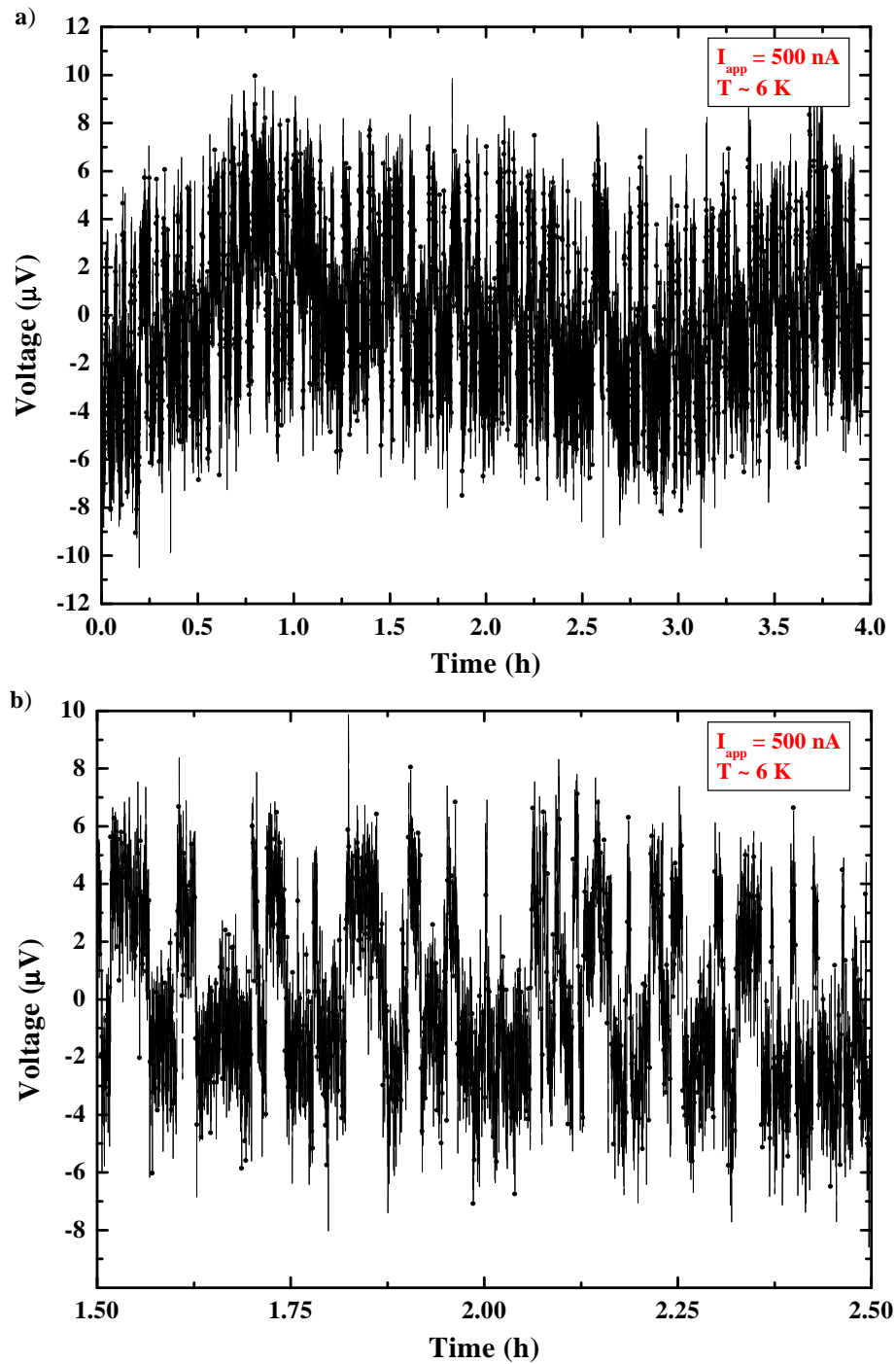


Figure 5.25. Typical  $V(t)$  data taken from sample No. 66. The  $V(t)$  data shown in a) was acquired at 6 K over a 4 hour period with 500 nA applied to the sample. Figure b) shows a zoom of the region from 1.5–2.5 hours. The DC offset was subtracted from the data. The bistability is clearly evident, with each level presenting a large excess noise as well.

one state. However, when the lifetime of *each* level is short, the system may appear to be in a combination of the two levels. This is shown in Fig. 5.26(a) where  $V(t)$  data for sample No. 66 is plotted. This data was taken at 4 K with 500 nA applied to the sample. The upper lifetime is slightly longer than the lower lifetime, but both are short. The two states of the system are more clearly seen in a histogram of the  $V(t)$  data shown in Fig. 5.26(b). Also evident from the histogram is that the lifetime of the lower level was shorter than the lifetime of the upper level. Thus, the higher voltage peak is taller. The width of each peak displays the excess noise of the system.

Random telegraph noise is a thermally activated process. [114, 135–137] The lifetime of the low state is expected to decrease with increasing voltage, or in our case, current. [136] To study this aspect of the noise,  $V(t)$  data was acquired from sample No. 66 for several applied currents. Fig. 5.27 shows the  $V(t)$  data acquired for three values of the current at 4 K. The data show an increase in fluctuations and excess system noise as the currents increase. In the low current plot (bottom) the two-level system is well defined. As the current is increased however, the two-level system becomes more ambiguous. At this current level, other states of the system are being activated, so there are more than two levels. Also, the lifetime of the levels has decreased which makes them blur together. It should be noted that sample No. 66 was lowered into the helium bath several times during this noise study. Each time the sample was cycled, a new multi-level system was formed due to microscopic changes within the sample.

During a single dip-cycle, the RTN was studied more extensively for sample No. 66. During this dip, the noise was measured for several current values at a constant temperature, then for several temperatures at a constant current. For each data set, the average lifetime of the up-state,  $\tau_{up}$ , and the average lifetime of the down-state,  $\tau_{down}$ , was extracted. Fig. 5.28 shows plots of the lifetimes as a function of temperature in (a) and a function of current in (b). The data show that the lifetime of the down-state does decrease with applied current and with increasing temperature. However, the data do not show a corresponding increase in the up-state lifetime, as is

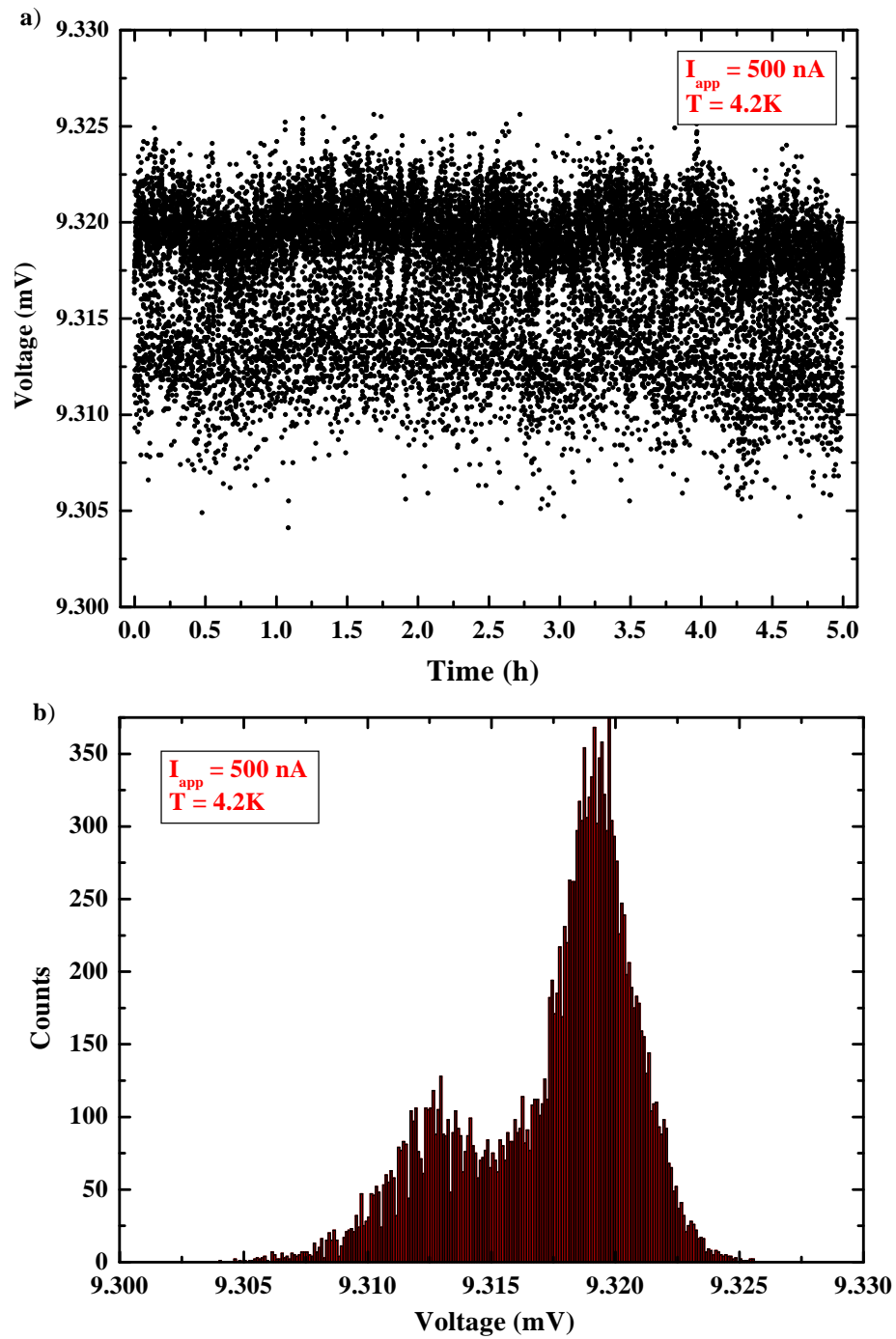


Figure 5.26.  $V(t)$  data taken from sample No. 66 showing two short lived states. The  $V(t)$  data shown in a) was acquired at 4 K over a 5 hour period with 500 nA applied to the sample. Figure b) shows a histogram of the  $V(t)$  data. The two levels of the system are seen in the histogram. The histogram also shows that the lower level had a shorter lifetime. The width of each peak is indicative of the excess noise of each level.

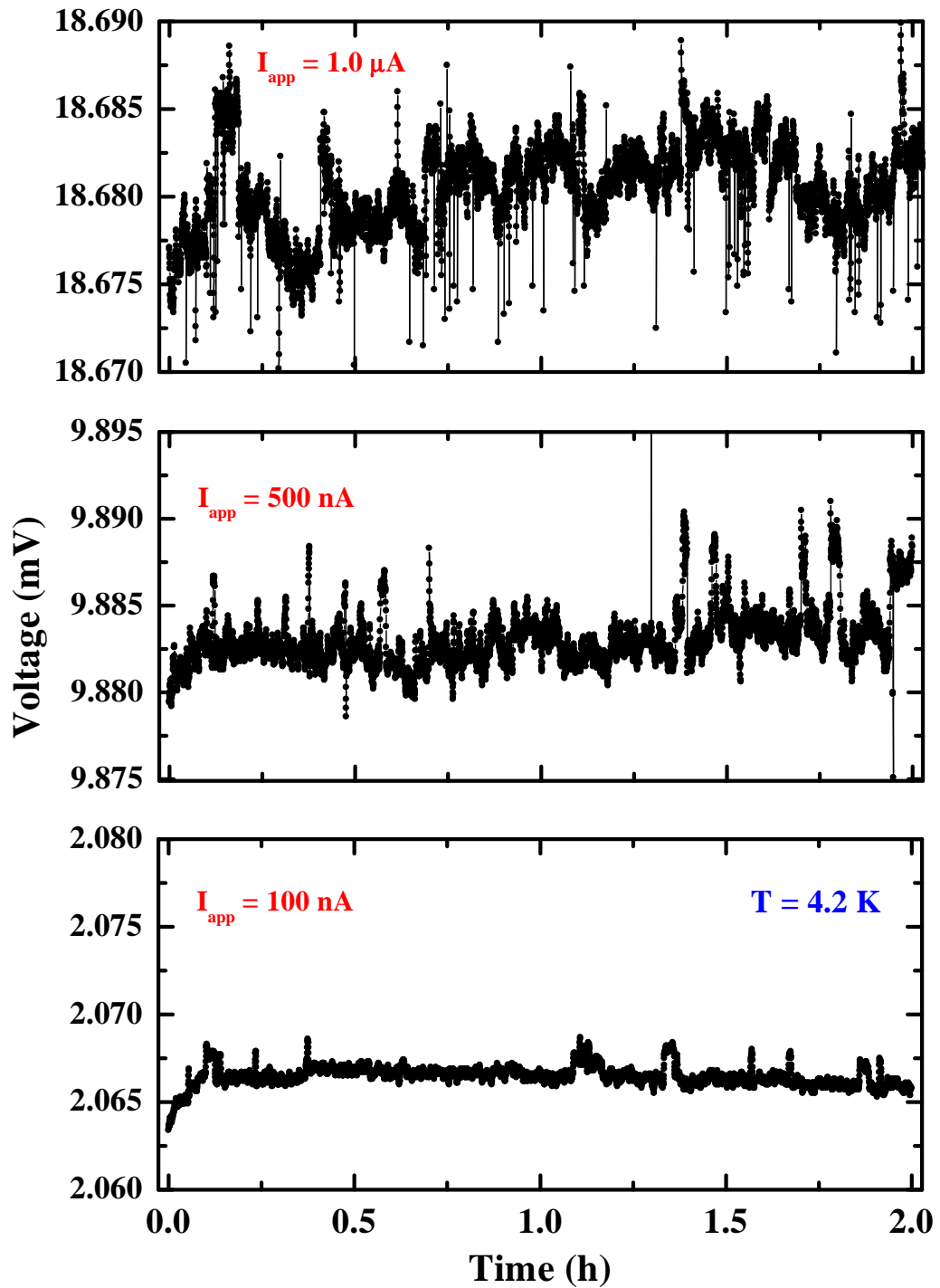


Figure 5.27.  $V(t)$  data from sample No. 66 taken at 4 K for three values of the applied current: 100 nA at bottom, 500 nA in the middle, and  $1 \mu\text{A}$  at top. The voltage scale for each plot is the same size. The fluctuations and the excess noise of the system increase with current.

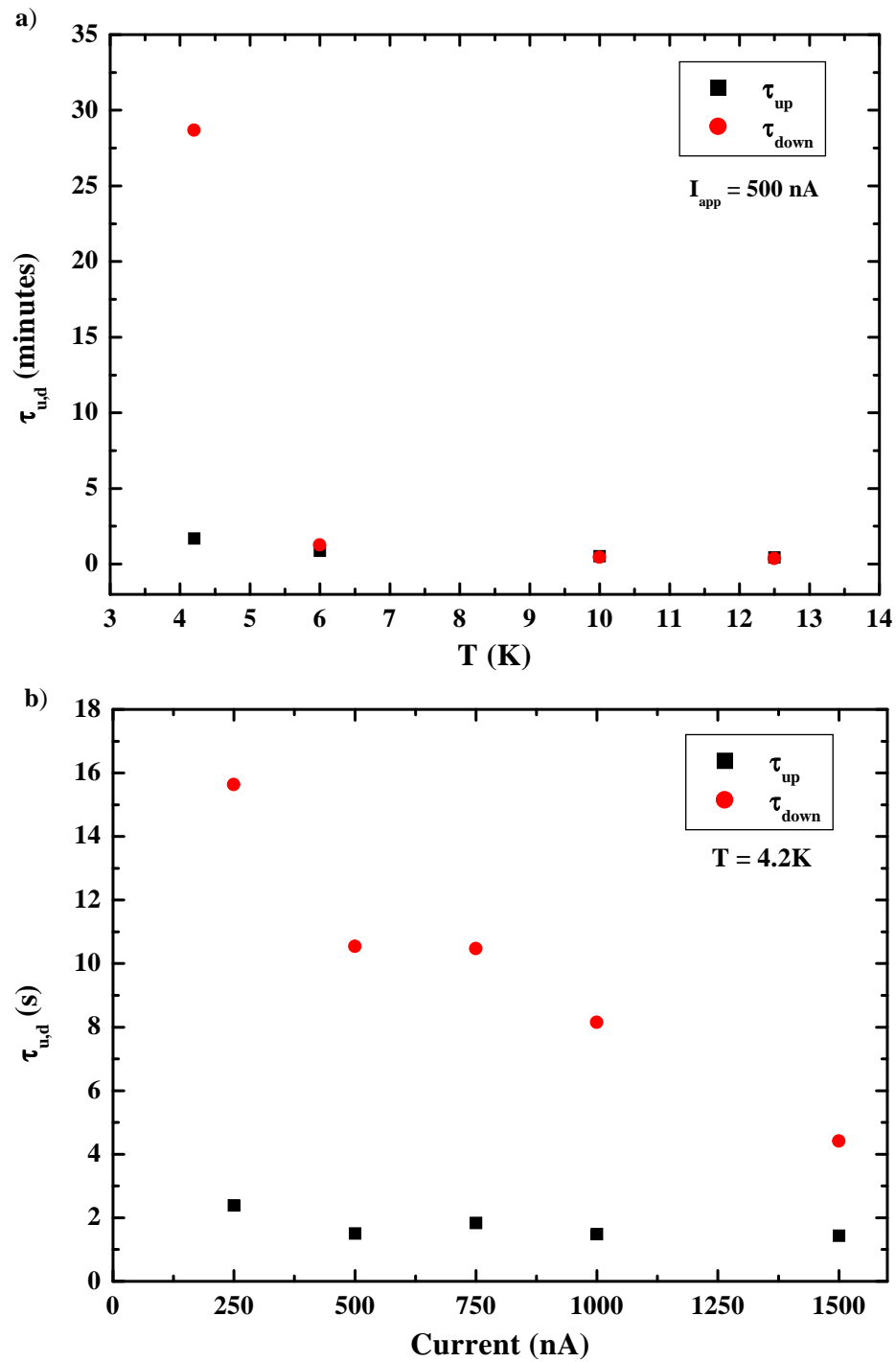


Figure 5.28. Figure a) shows a plot of lifetimes for the up and down states ( $\tau_{up}$  and  $\tau_{down}$ , respectively) versus temperature for sample No. 66. The data was taken at 500 nA applied to the sample. Figure b) shows a plot of the lifetimes versus applied current acquired at 4 K.

expected for RTN in a two-level system. [136] For both data sets there are not enough data points to provide clear indications of activated behavior for the lifetime of the down-state, although the data is suggestive. The fact that the lifetime of the up-state does not change over the range of measurements may suggest that the activation of this state appears at higher temperatures and currents. More likely is that the system has become multi-leveled as several other states become activated as the temperature and current are increased. This is the effect that is seen in the upper plot of Fig. 5.27. Thus, as the other levels become activated, the system acquires an equal probability for existing in each state.

In addition to RTN, as mentioned above there is a large amount of excess noise of the MWNT samples, as evidenced in every noise plot. The spectral density of the noise voltage may provide information regarding the nature of the excess noise. [135, 138] The most common forms of excess noise are Johnson noise, which is due to the thermal motion of the electrons, shot noise, which is a result of the quantization of the electron charge, and flicker noise ( $1/f$ ), which is caused by resistance fluctuations. [135] The origin of the resistance fluctuations is not universal, nor is the power of  $-1$  in the frequency dependence. Each type of noise may be distinguished by the current dependence of its noise power, given by [138]

$$S_V^j = 4Rk_bT \quad (\text{Johnson}), \quad (5.11)$$

$$S_V^s = 2R^2eI \quad (\text{Shot}), \quad (5.12)$$

$$S_V^f = \frac{A}{f^\beta} R^2 I^2 \quad (\text{Flicker}), \quad (5.13)$$

where  $R$  is the resistance.

For sample No. R4, the noise power is shown in Fig. 5.29 for RT in (a) and 4 K in (b). The noise power was calculated by performing an FFT on the  $V(t)$  data. Thus, the data acquisition rate of  $\sim 2$  points/sec. determined the maximum frequency of  $\sim 1$  Hz. The red lines shown in the figures have a slope of  $-1$  to indicate the  $1/f$  behavior of the data. In (a) the applied current is 100 nA, while in (b) the current is 0.1 nA. Although there is a difference of three orders of magnitude in the applied

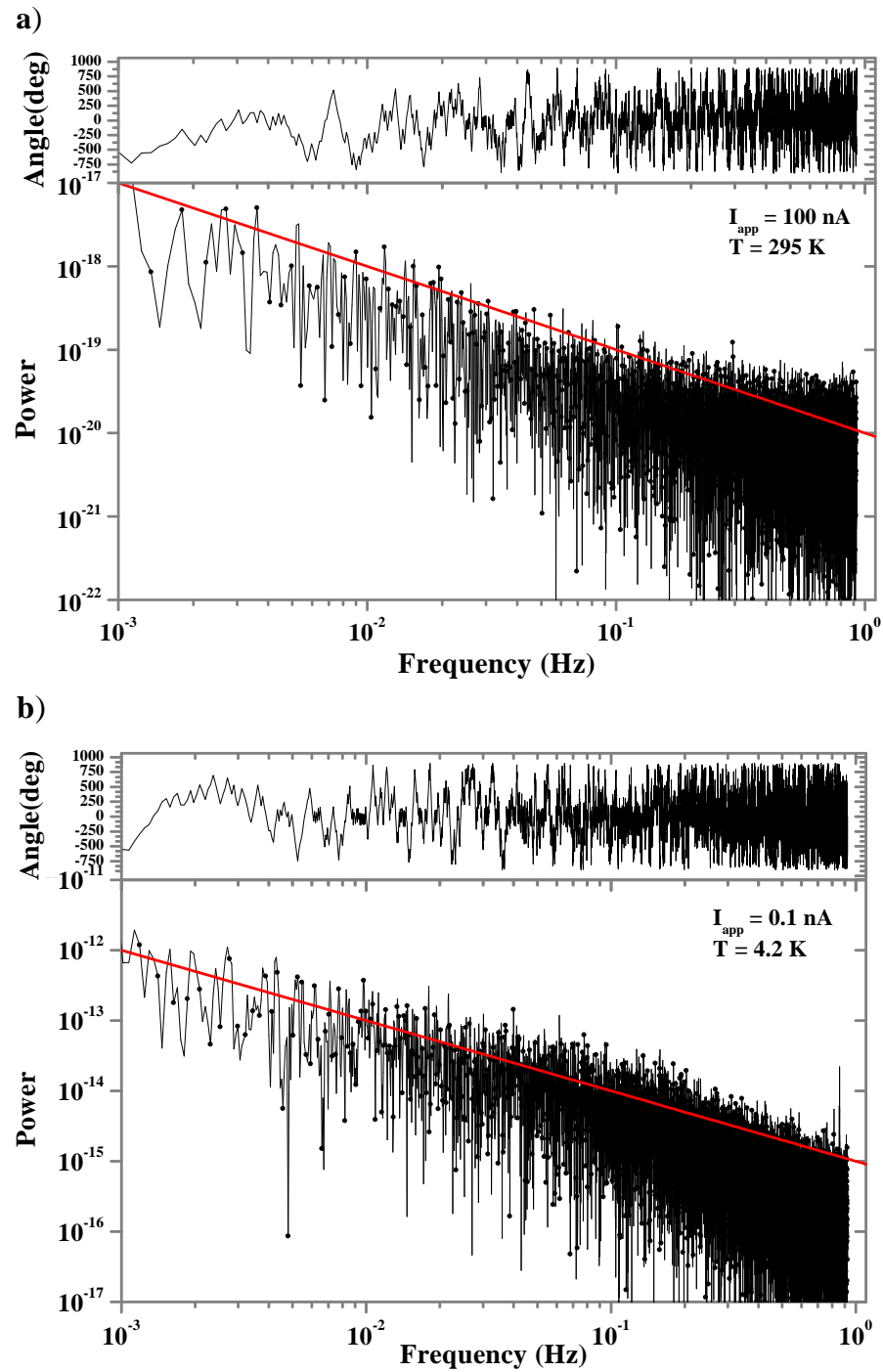


Figure 5.29. Noise power for sample No. R4 at RT in a) and 4 K in b). The data was calculated by performing an FFT on the  $V(t)$  data. The maximum frequency is one half the data acquisition rate, which here was  $\sim 2$  points/sec. The red line has a slope of  $-1$ .

currents, the noise power in (b) at 4 K is five orders of magnitude larger than the RT data in (a). However, the resistance of this sample increased by over four orders of magnitude from RT to 4 K, as shown in Fig. 5.19. From the fits to the data shown in Fig. 5.29, estimates of the coefficient  $A$  of Eqn. 5.13 are obtained. When this data was acquired, the resistance of sample No. R4 was  $\sim 9.4$  k $\Omega$  at RT and  $\sim 380$  M $\Omega$  at 4 K. From the fits in Fig. 5.29, the product of  $AR^2I^2$  of Eqn. 5.13 is  $\sim 10^{-20}$  at RT and  $\sim 10^{-15}$  at 4 K. Thus, we find a value for  $A$  of  $\sim 1 \times 10^{-14}$  at RT and  $\sim 7 \times 10^{-13}$  at 4 K. The agreement is not bad considering the estimates used, and these values for  $A$  are close to the values found by Collins *et al.* in their study of SWNT noise. However, they found  $A$  to change with sample resistance approximately as  $A/R \simeq 10^{-11} \Omega^{-1}$ . This puts their lowest measured value for  $A$  at  $\sim 3 \times 10^{-11}$ , and their highest value at  $\sim 5 \times 10^{-5}$ . These values are one to as much as eight orders of magnitude higher than the values determined for sample No. R4. This may indicate that SWNTs are even noisier than MWNTs.

The  $1/f$  behavior was also observed for the arc-grown MWNTs. Fig. 5.30 shows a plot of noise power versus current for sample No. 66. As predicted by Eqn. 5.13 for flicker noise, the noise power from this sample is proportional to the square of the current. This data was calculated from the standard deviation,  $\sigma_V$ , of the voltage data from 10 I(V) curves. The mean square voltage fluctuation is related to the standard deviation by

$$\sum_i^N \frac{(V_i - V_{ave})^2}{BN} = \frac{\sigma_V^2}{B} \frac{N-1}{N} = \langle S_V \rangle, \quad (5.14)$$

where  $N$  is the number of measurements and  $B$  is the equivalent noise bandwidth of the measurement, which for the Keithley 196 DMM is 300 kHz. To obtain the fit shown in Fig. 5.30, a least-squares fit was made to a plot of  $\langle S_V \rangle$  versus the square of the current. The value obtained is  $0.017 \Omega^2/\text{Hz}$ , which gives a value for  $A$  of  $4.2 \times 10^{-10}$ . This value is higher than the estimates for sample No. R4. In both cases, the values determined for the coefficient of  $1/f$  noise are higher or equal the values for a common carbon resistor of  $10^{-13}$ – $10^{-15}$  for resistances of 1 k $\Omega$  or less. [139]

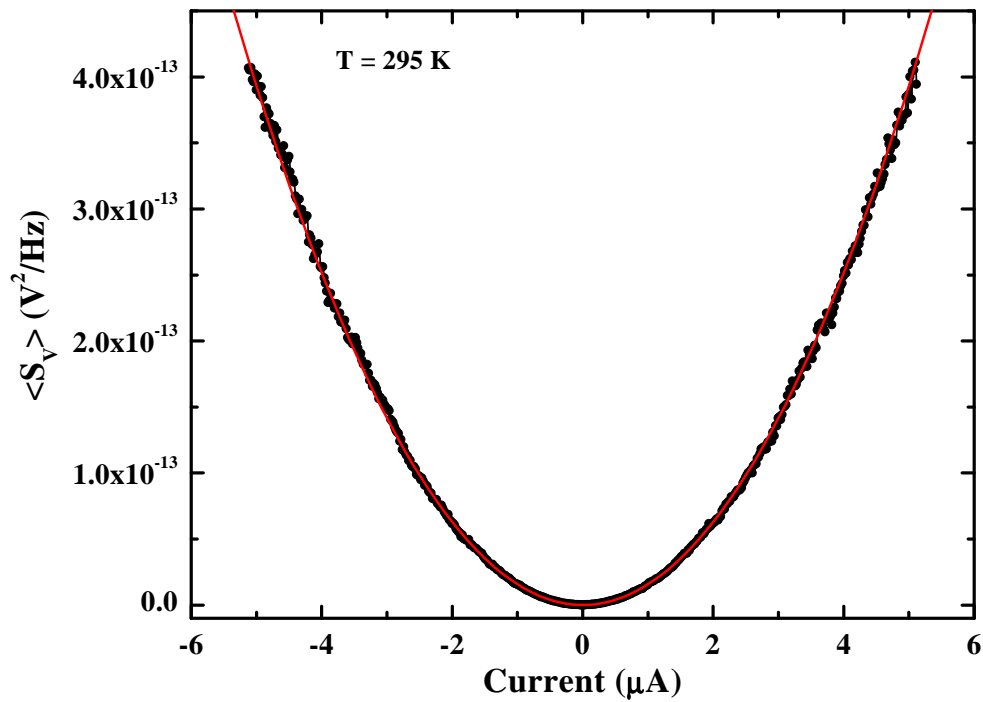


Figure 5.30. Noise power  $\langle S_V \rangle$  versus current at RT for sample No. 66. The data is parabolic in current, consistent with Eqn. 5.13. for  $1/f$  noise. The fit was determined from a least-squares fit the a plot of  $\langle S_V \rangle$  versus the square of the current. The value obtained is  $0.017 \Omega^2/\text{Hz}$ , which gives a value for  $A$  of  $4.2 \times 10^{-10}$ .

## 6. CONCLUSIONS

During the course of this work, the electronic properties of individual multi-walled carbon nanotubes were studied using field emission total energy distributions and temperature dependent transport measurements. Through the development of a novel technique for making electrical contacts to the ends of nanotubes, we were able to perform transport measurements, which have furthered our knowledge of the intrinsic behavior of multi-walled nanotubes.

### 6.1 Total Energy Distributions from Multi-walled Nanotubes

Using a technique developed by M. Buss [8] for mounting MWNTs to the ends of Pt FEM tips, we performed UHV energy-resolved field emission measurements. The field emission patterns obtained from MWNTs displayed no patterns or striations, as were found in other studies, [4, 93, 98] and the Fowler-Nordheim data show a slight non-linearity. This non-linearity may indicate a deviation from the standard Fowler-Nordheim theory, as is expected for emission from nanometer-sized objects. [99]

We obtained total electron energy distributions from individual multi-walled carbon nanotubes, which revealed a several peaks on the trailing edge. This structure in the distributions may be indicative of the predicted 1D electronic sub-bands of the nanotube, but further studies are needed. In the process of studying the field emission properties, the emission current was found to fluctuate randomly in time. The nature of this instability remains uncertain, yet it is crucial that the emission current be stable in order to reliably measure the energy distributions of the emitted electrons. Both the field emission current and the transport data show clear evidence for random telegraph noise (RTN) in nanotubes. [135] In addition, the energy distributions changed depending of the state of the emission current. For typical emission currents used (1–20 nA), the distributions contained peaks on the trailing edge. When

the MWNT entered a state of high emission current ( $\sim 200$  nA), the distribution was more free-electron like, often with no structure observed in the energy distribution. If the RTN is intrinsic to the nanotube, then the fluctuation of the emission current is related to the change in current paths along the nanotube's length, and not due to effects external to the nanotube. Thus, the change in the peak structure of the trailing edge of the energy distribution may reflect the 1D densities of states of the different current paths.

## 6.2 Electronic Transport in Multi-walled Nanotubes

To determine the source of the field emission current fluctuations and to study the fundamental electronic properties of multi-walled carbon nanotubes, we performed electronic transport measurements. For these measurements, we developed a novel technique for making reliable electrical contacts to nanotubes. Measurements of the conductance at room temperature on the resulting samples displays a large amount of noise, indicating that the current fluctuations may be intrinsic to multi-walled nanotubes. Random telegraph noise and  $1/f$  noise were also observed in the transport data, suggesting that the field emission current instability is related to the internal properties of the nanotube.

Despite the predictions for ballistic transport in MWNTs, [2, 60] we have seen no clear evidence for such behavior. Fig. 4.12 can serve as a histogram for our room temperature conductance data. The data do not provide a clear indication of quantized conductance, although the statistics are severely limited. We have measured a few samples whose conductance was close to quantized value, but these samples are merely suggestive. The fact that some samples can maintain a high current density ( $\sim 10^8$  A/cm<sup>2</sup>) is also suggestive of ballistic transport, but not a clear indication.

If transport in MWNTs is not ballistic, then the conductance values near integer numbers of  $G_o$  are misleading coincidences. The conductance values are then the result of transport through multiple layers, each conducting only a fraction of the total current. This is entirely possible considering the large distance of  $\sim 4$   $\mu\text{m}$  between contact pads. If on the other hand, multi-walled nanotubes are ballistic, then it

is surprising than the measured conductances are as low as they are. Since our fabrication technique opens the end of the MWNT, one would expect conductances on the order of  $NG_o$ , where  $N$  is the estimated number of metallic layers. Only once have we measured a conductance as high as  $27 G_o$ . Based on our MWNT samples, we estimate a value for  $N$  of  $\sim 4$ . We have measured a sample conductance near  $4 G_o$ , but only once. One sample was near  $3 G_o$  and two were near  $2 G_o$ . Several samples had conductances near  $1 G_o$ . If these data are interpreted as ballistic conductances, then it suggests that some mechanism is limiting the number of layers carrying current. The limit could be in the fabrication process or due to internal interactions between the nanotube layers. In the absence of clear evidence for ballistic transport, more studies are needed to develop a consistent data set which can be used to draw a conclusion about the measured conductance values.

Conductance measurements performed at low temperatures revealed several interesting features common to all samples studied. For each sample, the  $I(V)$  became non-linear at low temperatures. This feature was also observed as a decrease in the conductance as the temperature was lowered from room temperature (RT) to 4 K. The conductance was found to decrease fastest at zero-bias, roughly obeying a power law below  $\sim 100$  K. The conductance of each sample also increased with applied bias. In many instances, when  $eV > k_bT$ , the conductance at 4 K also displayed a power law in voltage. At low temperatures, the conductance also saturated with applied voltage. All of these features are explained by considering the low temperature conductance of the nanotube in terms of transport through a Luttinger liquid. This non-Fermi electron behavior, resulting from strong, repulsive electron-electron interactions, manifests itself as a power law suppression of the conductance as a function of the relevant energy scale ( $eV$  or  $k_bT$ ). In addition to the Luttinger component to the conductance, the conductance of the nanotube must also be considered. The measured system conductance contains contributions from the nanotube-contact (Luttinger) junction and from the nanotube itself. The main conclusion that can be drawn from this result is that the contact resistance does not dominate the resistance of the system. We believe

this is a direct result of the sample fabrication procedure. Based on our measurements we estimate the interaction parameter  $g$ , which controls the Luttinger behavior, to range from 0.17–0.21 for the case of a *bulk* contact to the nanotube, and 0.32–0.41 for the case of *end* contact to the nanotube, depending on the sample. Since the MWNTs are typically buried beneath the contacts longer than the critical length  $L_c$ , we expect *bulk* contact to the nanotubes. Both this expectation and the estimates from our data agree with the theoretical estimates for  $g$  of 0.18–0.3.

The noise measurements discussed in Section 5.4 are still preliminary and also require more investigation. Such a study is useful for a number of reasons. As evidenced from our data, MWNTs seem to exhibit more noise than ordinary carbon resistors. If the high noise level is truly an intrinsic property, then this excess noise could present a problem for the use of MWNTs in the field of molecular electronics. A large excess noise was also reported for SWNTs. [139] Thus, it is critical for the future of nanotube technology to determine the true source of the noise. It is now well known that nanotubes become oxygen doped under ambient conditions, which affects the resistance of SWNTs. Thus, it is reasonable to expect that the same process or some other external factors are responsible for the large amount of noise present in the nanotube samples. On the other hand, the presence of random telegraph noise may indicate that the nanotubes are sensitive to structural changes on the atomic scale. Fundamental studies are still needed to sort out the properties of the nanotube. In addition to providing information regarding the applications for nanotubes, noise studies will also provide information about the dominant conduction mechanisms in the nanotube. [112–115, 138] For instance, the fact that shot noise is suppressed by 1/3 in ballistic conductors may provide another method for investigating ballistic transport in nanotubes. [112, 113, 135] Clearly, there is much to be learned from a thorough investigation of noise in carbon nanotubes. The nanotube transport samples fabricated using the technique developed here provide excellent samples for noise studies.

### 6.3 Recommendations and Conclusion

Although the nanotube sample fabrication technique developed for this study is simple and reliable, it is not easy. In the course of two years only a little over 100 samples were fabricated, only a small fraction of which survived long enough to allow measurements to be performed. Even though much has been learned about the precautions needed to ensure a long sample life, a new technique is needed for sample preparation. The shadow mask aspect of the current technique is the most essential component to the fabrication process. At present, work is underway to extend the shadow mask method by patterning several masks on a single silicon wafer. This would allow 10's of samples to be fabricated by evaporating through the mask wafer to a substrate wafer. This method would provide the large number of samples needed to assemble meaningful transport statistics, and the shadow mask wafer may be patterned with a variety of contact configurations, such as multiple contacts to the nanotubes and varying lengths between contacts. This would allow for true 4-terminal measurements and very important length dependence studies. Although placing the nanotubes on the substrate layer is a possibility, we are currently learning to disperse the nanotubes on the substrate as was done in many other studies. This new method reduces the need for the precision manipulation of individual nanotubes, making the technique more accessible, yet still providing the clean contacts produced by the shadow mask method. Dispersions also enable the shadow mask method to be used for SWNTs.

In addition to extending the fabrication procedure, future work on nanotube transport must investigate alternate contact metals. The majority of measurements reported to date use either gold or platinum contacts. Aluminum contacts have been predicted to provide low resistance contacts to nanotubes. [140] We have tried to use nickel as a contact metal in order to investigate the spin coherence of nanotube transport, but we found that the nickel did not adhere to the glass substrate, nor to the nanotube. A thin layer of titanium could provide the adhesion layer needed to form good nickel contacts. There are many experiments which can be performed with

varying choices of contact metals.

The fabrication technique should also be extended to the field emission studies. Using a shadow mask, it is possible to evaporate a metal contact on top of a nanotube which has been mounted to the end of a FEM tip. This would provide a strong, reliable contact and remove the ambiguity regarding contact resistance fluctuation as a source of the emission current noise. Another method may be to electro-plate a metal contact to the tip/nanotube sample. This has been successfully accomplished once by Kevin Stavens of Prof. Andres' research group, but more control is needed. Clearly, either of these methods should be pursued in order to answer the questions raised by the FEM measurements. Related to further FEM studies, another avenue for further studies is Field-Ion Microscopy (FIM) of MWNTs, which provides atomic resolution of the emitter. I have attempted this experiment a few times with only a small degree of success, but is extremely useful for understanding the results of field emission, since the atomic configuration of the MWNT tip can be directly correlated with the field emission patterns and the total energy distributions.

In conclusion, the technique developed for fabricating electrical contacts has proven useful for obtaining fundamental knowledge of the electrical properties of multi-walled carbon nanotubes. This technique opens new avenues of research on nanometer-sized structures. As discussed above, the extension of this technique should prove valuable in many other studies, only a few of which have been mentioned.

## BIBLIOGRAPHY

## BIBLIOGRAPHY

- [1] S. Iijima, *Nature* **354**, 56 (1991).
- [2] J.W. Mintmire, B.I. Dunlap, and C.T. White, *Phys. Rev. Lett.* **1992**, 631 (1992).
- [3] Q.H. Wang, A.A. Setlur, J.M. Lauerhaus, J.Y. Dai, E.W. Seelig, and R.P.H. Chang, *Appl. Phys. Lett.* **72**, 2912 (1998).
- [4] K.A. Dean and B.R. Chalamala, *J. Appl. Phys.* **85**, 3832 (1999).
- [5] R. Martel, T. Schmidt, H.R. Shea, T. Hertel, and Ph. Avouris, *Appl. Phys. Lett.* **73**, 2447 (1998).
- [6] H.T. Soh, C.F. Quate, A.F. Morpurgo, C.M. Marcus, J. Kong, and H. Dai, *Appl. Phys. Lett.* **75**, 627 (1999).
- [7] S. J. Tans, A.R.M. Verschueren, and C. Dekker, *Nature* **393**, 49 (1998).
- [8] Michael Buss, PhD thesis, Purdue University, 1998.
- [9] K. Moloni, M.R. Buss, and R.P. Andres, *Ultramicroscopy* **80**, 237 (1999).
- [10] Dan Lovall, PhD thesis, Purdue University, 1997.
- [11] D. Lovall, M. Buss, E. Graugnard, R.P. Andres, and R. Reifenberger, *Phys. Rev. B* **61**, 5683 (2000).
- [12] A. Oberlin, M. Endo, and T. Koyama, *J. Crystal Growth* **32**, 335 (1976).
- [13] M.S. Dresselhaus, G. Dresselhaus, and P.C. Eklund, *Science of Fullerenes and Carbon Nanotubes*, Academic Press, New York, 1996.
- [14] R. Saito, M.S. Dresselhaus, and G. Dresselhaus, *Physical Properties of Carbon Nanotubes*, Imperial College Press, London, 1998.
- [15] W. Tian and S. Datta, *Phys. Rev.* **B49**, 5097 (1994).
- [16] M.F. Lin and K.W.-K. Shung, *Phys. Rev.* **B51**, 7592 (1995).
- [17] L. Chico, L.X. Benedict, S.G. Louie, and M.L. Cohen, *Phys. Rev.* **B54**, 2600 (1996).
- [18] C.L. Kane and E.J. Mele, *Phys. Rev. Lett.* **78**, 1932 (1997).
- [19] M.F. Lin, D.S. Chuu, and K.W.-K. Shung, *Phys. Rev. B* **56**, 1430 (1997).
- [20] O.M. Yevtushenko, G.Ya. Slepyan, S.A. Maksimenko, A. Lakhtakia, and D.A. Romanov, *Phys. Rev. Lett.* **79**, 1102 (1997).

- [21] R. Egger and A.O. Gogolin, Phys. Rev. Lett. **79**, 5082 (1997).
- [22] C. Kane, L. Balents, and M.P.A. Fisher, Phys. Rev. Lett. **79**, 5086 (1997).
- [23] C.T. White and J.W. Mintmire, Nature **394**, 29 (1998).
- [24] M.P. Anantram, J. Han, and T.R. Govindan, in *Molecular Electronics: Science and Technology*, edited by A. Aviram and M. Ratner, volume 852, New York Academy of Sciences, New York, NY, 1998.
- [25] K. Esfarjani, A.A. Farajian, Y. Hashi, and Y. Kawazoe, Appl. Phys. Lett. **74**, 79 (1999).
- [26] A.A. Farajian, K. Esfarjani, and Y. Kawazoe, Phys. Rev. Lett. **82**, 5084 (1999).
- [27] A. Rochefort, D.R. Salahub, and Ph. Avouris, J. Phys. Chem. B **108**, 641 (1999).
- [28] M.P. Anantram, S. Datta, and Y. Xue, Phys. Rev. **B61**, 14219 (2000).
- [29] R. Egger, Phys. Rev. Lett. **83**, 5547 (1999).
- [30] K. Sattler, Carbon **33**, 915 (1995).
- [31] J-P. Issi, L. Langer, J. Heremans, and C.H. Olk, Carbon **33**, 941 (1995).
- [32] D. L. Carroll, P. Redlich, P. M. Ajayan, J. C. Charlier, X. Blase, A. De Vita, and R. Car, Phys. Rev. Lett. **78**, 2811 (1997).
- [33] Jeroen W. G. Wildöer, L. C. Venema, A. G. Rinzler, R. E. Smalley, and C. Dekker, Nature **391**, 59 (1998).
- [34] T. W. Odom, J. L. Huang, P. Kim, and C. M. Lieber, Nature **391**, 62 (1998).
- [35] S.J. Tans, M.H. Devoret, H. Dai, A. Thess, R.E. Smalley, L.J. Geerligs, and C. Dekker, Nature **386**, 474 (1997).
- [36] A. Bezryadin, R.M. Verschueren, S.J. Tans, and C. Dekker, Phys. Rev. Lett. **80**, 4036 (1998).
- [37] M. Bockrath, D.H. Cobden, J. Lu, A.G. Rinzler, R.E. Smalley, L. Balents, and P.L. McEuen, Nature **397**, 598 (1999).
- [38] Z. Yao, H.W. Ch. Postma, L. Balents, and C. Dekker, Nature **402**, 273 (1999).
- [39] J. Kong, H. T. Soh, A. M. Cassell, C. F. Quate, and H. Dai, Nature **395**, 878 (1998).
- [40] L. Langer, V. Bayot, E. Grivei, J-P. Issi, J.P. Heremans, C.H. Olk, L. Stockman, C. Van Haesendonck, and Y. Bruynseraede, Phys. Rev. Lett. **76**, 479 (1996).
- [41] T.W. Ebbesen, H.J. Lezec, H. Hiura, J.W. Bennett, H.F. Ghaemi, and T. Thio, Nature **382**, 54 (1996).
- [42] A. Bachtold, M.S. Fuhrer, S. Plyasunov, M. Forero, E.H. Anderson, A. Zettl, and P.L. McEuen, Phys. Rev. Lett. **83**, 6082 (2000).

- [43] A.Yu. Kasumov, I.I. Khodos, P.M. Ajayan, and C. Colloex, *Europhys. Lett.* **34**, 429 (1996).
- [44] S. Frank, P. Poncharel, Z.L. Wang, and W. A. de Heer, *Science* **20**, 1744 (1998).
- [45] A. Bachtold, M. Henny, C. Terrier, C. Strunk, C. Schönenberger, J.-P. Salvetat, J.-M. Bonard, and L. Forró, *App. Phys. Lett.* **73**, 274 (1998).
- [46] H.W. Kroto, J.R. Heath, S.C. O'Brien, R.F. Curl, and R.E. Smalley, *Nature* **318**, 162 (1985).
- [47] Thomas W. Ebbesen, *Physics Today* **49**, 26 (1996).
- [48] L.A. Chernozatonskii, *Physics Letters A* **160**, 392 (1991).
- [49] Z.Ya. Kosakovskaya, L.A. Chernozatonskii, and E.A. Fedorov, *JETP Lett.* **56**, 26 (1992).
- [50] T.W. Ebbesen and P.M. Ajayan, *Nature* **358**, 220 (1992).
- [51] T.W. Ebbesen, *Annu. Rev. Mater. Sci.* **24**, 235 (1994).
- [52] P. Delaney, H.J. Choi, J. Ihm, S.G. Louie, and M.L. Cohen, *Nature* **391**, 466 (1998).
- [53] R. Tamura and M. Tsukada, *Phys. Rev. B* **52**, 6015 (1995).
- [54] J.-C. Charlier, T.W. Ebbesen, and Ph. Lambin, *Phys. Rev. B* **53**, 11108 (1996).
- [55] E.G. Gal'pern, I.V. Stankevich, A.L. Chistyakov, and L.A. Chernozatonskii, *JETP Lett.* **55**, 483 (1992).
- [56] J.W. Mintmire and C.T. White, *Phys. Rev. Lett.* **81**, 2506 (1998).
- [57] S. Datta, (Private Communication).
- [58] M.S. Dresselhaus, G. Dresselhaus, and R. Saito, *Carbon* **33**, 883 (1995).
- [59] P.R. Wallace, *Phys. Rev.* **71**, 622 (1947).
- [60] C.T. White and T.N. Todorov, *Nature* **393**, 240 (1998).
- [61] S. Datta, *Electronic Transport in Mesoscopic Systems*, Cambridge University Press, Cambridge, 1995.
- [62] Technically, the zero gap in metallic nanotubes will open due to curvature effects, an effect which is largest for smaller diameter tubes. See, for example, N. Hamada, S. Sawada and A. Oshiyama, *Phys. Rev. Lett.* **68**, 1579 (1992).
- [63] J. C. Charlier and Ph. Lambin, *Phys. Rev.* **B57**, R15037 (1998).
- [64] H.J. Choi, J. Ihm, Y.-G. Yoon, and S.G. Louie, *Phys. Rev. B* **60**, R14009 (1999).
- [65] P. Delaney, M. Di Ventra, and S.T. Pantelides, *Appl. Phys. Lett.* **75**, 3787 (1999).

- [66] P.F. Bagwell and T.P. Orlando, *Phys.Rev.* **B40**, 1456 (1989).
- [67] T.N. Todorov, in *Nanowires*, edited by P. Serena and N. Garcia, pages 79–90, Kluwer Academic, Dodrecht, 1997.
- [68] P.J. De Pablo, E. Graugnard, B. Walsh, R.P. Andres, S. Datta, and R. Reifengerger, *Appl. Phys. Lett.* **74**, 323 (1999).
- [69] M.P. Anantram, *Phys. Rev.* **B62**, R4837 (2000).
- [70] S. Datta and A.W. Ghosh, (Private Communication).
- [71] B. Walsh, MS thesis, 2000, Purdue University (unpublished).
- [72] R.H. Fowler and L.W. Nordheim, *Proc. Roy. Soc. Lond.* **A119**, 173 (1928).
- [73] R. Gomer, *Field Emission and Field Ionization*, Harvard University Press, 1961.
- [74] R. D. Young, *Phys. Rev.* **113**, 110 (1958).
- [75] J.W. Gadzuk and E.W. Plummer, *Rev. Mod. Phys.* **43**, 487 (1973).
- [76] A. Modinos, *Field, Thermionic and Secondary Electron Emission Spectroscopy*, Plenum Press, New York, 1984.
- [77] R.H. Good and E.W. Müller, Field emission, in *Handbuch der Physik, 2nd. edition, Vol 2*, page 176, Springer Verlag, 1956.
- [78] A. De Vita, J. C. Charlier, X. Blase, and R. Car, *Appl. Phys. A* **68**, 283 (1999).
- [79] E.W. Plummer and R.D. Young, *Phys. Rev.* **B1**, 2088 (1970).
- [80] R. Reifengerger, H.A. Goldberg, and M.J.G. Lee, *Surf. Sci.* **83**, 599 (1979).
- [81] H. Dai, J. H. Hafner, A. G. Rinzler, D. T. Colbert, and R. E. Smalley, *Nature* **384**, 147 (1996).
- [82] A.J. Melmed, *J. Vac. Sci. Technol.* **B9**, 601 (1991).
- [83] P.M. Ajayan, T.W. Ebbesen, T. Ichihashi, S. Iijima, K. Tanigaki, and H. Hiura, *Nature* **362**, 522 (1993).
- [84] S.H. Tsai, C.W. Chao, C.L. Lee, and H.C. Shih, *Appl. Phys. Lett.* **74**, 3462 (1999).
- [85] E. Graugnard, B. Walsh, P.J. de Pablo, R.P. Andres, S. Datta, and R. Reifengerger, in *Cluster and Nanostructured Interfaces*, edited by P. Jena, B.K. Rao, and S.N. Khanna, Plenum Press, New York, 2000.
- [86] M. A. More and D. S. Joag, *J. Phys. D: Appl. Phys.* **25**, 1844 (1992).
- [87] Yu.V. Gulyaev, Z.Ya. Kosakovskaya, N.I. Sinitsyn, G.V. Torgashov, E.A. Fedorov, Yu.F. Zakharchenko, and V.P. Val'chuk, *Mat. Res. Soc. Symp. Proc.* **359**, 99 (1995).

- [88] M.S. Mousa, *Appl. Surf. Sci.* **94/95**, 129 (1996).
- [89] B.H. Fishbine, C.J. Miglionico, K.E. Hackett, and K.J. Hendricks, *Mat. Res. Soc. Symp. Proc.* **349**, 319 (1994).
- [90] B.H. Fishbine, C.J. Miglionico, K.E. Hackett, K.J. Hendricks, X.K. Wang, R.P.H. Chang, J.D. Shovlin, and M.E. Kordesch, *Mat. Res. Soc. Symp. Proc.* **359**, 93 (1995).
- [91] Q.H. Wang, T.D. Corrigan, J.Y. Dai, R.P.H. Chang, and A.R. Krauss, *Appl. Phys. Lett.* **70**, 3308 (1997).
- [92] J.-M. Bonard, T. Stora, J.-P. Salvetat, F. Maier, T. Stöckli, C. Duschl, L. Forró, W.A. de Heer, and A. Châtelain, *Adv. Mater.* **9**, 827 (1997).
- [93] W. A. de Heer, J.-M. Bonard, K. Fauth, A. Châtelain, L. Forró, and D. Ugarte, *Adv. Mater.* **9**, 87 (1997).
- [94] A.G. Rinzler, J.H. Hafner, P. Nikolaev, L. Lou, S.G. Kim, D. Tománek, P. Nordlander, D. T. Colbert, and R.E. Smalley, *Science* **269**, 1550 (1995).
- [95] B.I. Yakobson and R.E. Smalley, *American Scientist* **85**, 324 (1997).
- [96] J.-M. Bonard, F. Maier, T. Stöckli, A. Châtelain, W.A. de Heer, J.-P. Salvetat, and L. Forró, *Ultramicroscopy* **73**, 7 (1997).
- [97] J.-M. Bonard, J.-P. Salvetat, T. Stöckli, W.A. de Heer, L. Forró, and A. Châtelain, *Appl. Phys. Lett.* **73**, 918 (1998).
- [98] J.-M. Bonard, T. Stöckli, W.A. de Heer, J.-C. Charlier, X. Blase, A. DeVita, R. Car, J.-P. Salvetat, and L. Forró, (preprint) (1997).
- [99] V.T. Binh and S.T. Purcell, *Appl. Surf. Sci.* **111**, 157 (1997).
- [100] E. McRae and J.F. Maréché, *J. Mater. Res.* **3**, 75 (1988).
- [101] G.U. Sumanasekera, C.K.W. Adu, S. Fang, and P.C. Eklund, *Phys. Rev. Lett.* **85**, 1096 (2000).
- [102] M.P. Anantram and T.R. Govindan, *Phys. Rev.* **B61**, 5020 (2000).
- [103] H.R. Shea, R. Martel, and Ph. Avouris, *Phys. Rev. Lett.* **84**, 4441 (2000).
- [104] A. Bachtold, C. Strunk, J.-P. Salvetat, J.-M. Bonard, L. Forró, T. Nussbaumer, and C. Schönenberger, *Nature* **397**, 673 (1999).
- [105] Pedro J. de Pablo, PhD thesis, Universidad Autónoma de Madrid, 2000.
- [106] The Nano-Tec scanning force system is available from Nanotec<sup>TM</sup>, FUAM, Edificio Rectorado, Universidad Autónoma de Madrid, E-28049 Madrid (Spain).
- [107] B. Anczykowski, D. Krüger, K.L. Babcock, and H. Fuchs, *Ultramicroscopy* **66**, 251 (1996).
- [108] J. Tamayo and R. García, *Appl. Phys. Lett.* **71**, 2394 (1997).

- [109] S.N. Magonov, V. Elings, and M.-H. Whangbo, *Surf. Sci.* **375**, 385 (1997).
- [110] M.S. Dresselhaus, G. Dresselhaus, K. Sugihara, I.L. Spain, and H.A. Goldberg, *Graphite Fibers and Filaments*, volume 5 of *Springer Series in Materials Science*, Springer-Verlag, New York, 1988.
- [111] For simplicity, this current density was estimated by assuming the current to flow uniformly through the entire cross-sectional area of this MWNT. Assuming this assumption is valid, the resistivity of this MWNT is about  $1.5 \times 10^{-7} \Omega \text{ m}$ , or about  $\sim 9 \rho_{Cu}$ .
- [112] R. Landauer and Th. Martin, *Physica B* **175**, 167 (1991).
- [113] R. Landauer, *Physica B* **227**, 156 (1996).
- [114] P.A.M. Holweg, J. Caro, A.H. Verbruggen, and S. Radelaar, *Phys. Rev.* **B45**, 9311 (1992).
- [115] Y. Naveh, *Phys. Rev.* **B58**, R13387 (1998).
- [116] D.H. Cobden, M. Bockrath, P.L. McEuen, A.G. Rinzler, and R.E. Smalley, *Phys. Rev. Lett.* **81**, 681 (1998).
- [117] P.L. McEuen, M. Bockrath, D.H. Cobden, Y.-G. Yoon, and S.G. Louie, *Phys. Rev. Lett.* **83**, 5098 (1999).
- [118] Neil W. Ashcroft and N. David Mermin, *Solid State Physics*, Holt, Rinehart and Winston, New York, 1976.
- [119] L. Langer, L. Stockman, J.P. Heremans, V. Bayot, C.H. Olk, C. Van Haendonck, Y. Bruynseraede, and J-P. Issi, *J. Mater. Res.* **9**, 927 (1994).
- [120] B.I. Shklovskii and A.L. Efros, *Electronic Properties of Doped Semiconductors*, volume 45 of *Springer Series in Solid-State Sciences*, Springer-Verlag, Berlin, 1984.
- [121] H. Kamimura and H. Aoki, *The Physics of Interacting Electrons in Disordered Systems*, Clarendon Press, Oxford, 1989.
- [122] O.E. Omel'yanovskii, V.I. Tsebro, O.I. Lebedev, A.N. Kiselev, V.I. Bondarenko, N.A. Kiselev, Z. Ja. Kosakovskaja, and L.A. Chernozatonskii, *JETP Lett.* **62**, 503 (1995).
- [123] C. Schönenberger, A. Bachtold, C. Strunk, J.-P. Salvetat, and L. Forró, *Appl. Phys. A* **69**, 283 (1999).
- [124] Johannes Voit, *Rep. Prog. Phys.* **57**, 977 (1995).
- [125] H.J. Schulz, in *Les Houches Summer School LXI*, edited by E. Akkermans, G. Montambaux, J. Pichard, and J. Zinn-Justin, page 533, Elsevier, Amsterdam, 1995.
- [126] H.J. Schulz, G. Cuniberti, and P. Pieri, Lectures at the summer school in Chia Laguna, Italy (1997), (cond-mat/9807366).
- [127] A.M. Chang, L.N. Pfeiffer, and K.W. West, *Phys. Rev. Lett.* **77**, 2538 (1996).

- [128] A. Yacoby, H.L. Stormer, N.S. Wingreen, L.N. Pfeiffer, K.W. Baldwin, and K.W. West, *Phys. Rev. Lett.* **77**, 4612 (1996).
- [129] M. Grayson, D.C. Tsui, L.N. Pfeiffer, K.W. West, and A.M. Chang, *Phys. Rev. Lett.* **80**, 1062 (1998).
- [130] A. Odinstsov and H. Yoshioka, *Phys. Rev.* **B59**, R10457 (1999).
- [131] H. Yoshioka and A. Odinstsov, *Phys. Rev. Lett.* **82**, 374 (1999).
- [132] L. Balents, in *XVIII Moriond Les Arcs Conference Proceedings*, edited by D.C. Glattli and M. Sanquer, Edition Frontiers, France, 1999.
- [133] H. W.Ch. Postma, M. de Jonge, Z. Yao, and C. Dekker, *Phys. Rev.* **B62**, (in press) (2000).
- [134] R. Andrews, D. Jacques, A.M. Rao, F. Derbyshire, D. Qian, X. Fan, E. C. Dickey, and J. Chen, *Chem. Phys. Lett.* **303**, 467 (1999).
- [135] Sh. Kogan, *Electronic Noise and Fluctuations in Solids*, Cambridge University Press, Cambridge, 1996.
- [136] Sh. Kogan, *Phys. Rev. Lett.* **81**, 2986 (1998).
- [137] R.T. Olson, G.R. Condon, J.A. Panitz, and P.R. Schwoebel, *J. Appl. Phys.* **87**, 2031 (2000).
- [138] A. Overhauser, (Statistical Mechanics Lecture Notes).
- [139] P.G. Collins, M.S. Fuhrer, and A. Zettl, *Appl. Phys. Lett.* **76**, 894 (2000).
- [140] J. Tersoff, *Appl. Phys. Lett.* **74**, 2122 (1999).
- [141] Y. Xue and S. Datta, *Phys. Rev. Lett.* **83**, 4844 (1999).
- [142] A. Rochefort, Ph. Avouris, F. Lesage, and D.R. Salahub, *Phys. Rev.* **B60**, 13824 (1999).
- [143] M.S. Dresselhaus, G. Dresselhaus, K. Sugihara, I.L. Spain, and H.A. Goldberg, in *Graphite Fibers and Filaments*, edited by M. Cardona, pages 188–202, Springer Series in Materials Science (5), New York, 1988.
- [144] G. Bergmann, *Phys. Rep.* **107**, 1 (1984).
- [145] R.A. Webb and S. Washburn, *Phys. Today* **41**, 46 (1988).
- [146] D.F. Holcomb, *Am. J. Phys.* **67**, 278 (1999).

## APPENDICES

## APPENDICES

**Appendix A: Nanotube Density of States Program**

This Appendix contains the C code for the program to calculate the density of states (DOS) for armchair ( $n, n$ ) or zigzag ( $n, 0$ ) nanotubes. Some of the lines of code are split to fit onto the page.

```

/* armdos - calculates Density of States for (n,n) armchair or (n,0)
 * zigzag nanotubes
 * Copyright (C) 1999 Brian L. Walsh
 * Copyright (C) 2000 Elton D. Graugnard

 * This program is free software; you can redistribute it and/or
 * modify it under the terms of the GNU General Public License as
 * published by the Free Software Foundation; either version 2 of the
 * License, or (at your option) any later version.

 * This program is distributed in the hope that it will be useful, but
 * WITHOUT ANY WARRANTY; without even the implied warranty of
 * MERCHANTABILITY or FITNESS FOR A PARTICULAR PURPOSE. See the GNU
 * General Public License for more details.

 * You should have received a copy of the GNU General Public License
 * along with this program; if not, write to the Free Software
 * Foundation, Inc., 675 Mass Ave, Cambridge, MA 02139, USA.

 * First written by Brian Walsh on 3/5/1999. Slightly modified by
 * Elton Graugnard on 3/6/1999. Major modifications to the code made
 * by Elton on 7/17/2000 - the sorting algorithm was changed.
 */

#include <stdio.h>
#include <stdlib.h>
#include <math.h>

#define ARR_SIZE 80000
#define PI 3.141592654
/*#define A sqrt(3.0)*1.421 *//* The c-c bond distance in graphite. */
#define A sqrt(3.0)*1.44 /* This is the value for C60. */
#define T 2.9 /* The value of the overlap integral. */

/* This function calculates the analytical E(k) relations for a (n,n)
 * armchair nanotube. */
double armEofK(double,double,double);

/* This function calculates the analytical density of states versus k,
 * DOS(k), for a (n,n) armchair nanotube. */

```

```

double armdEdKofK(double,double,double);

/* This function calculates the analytical E(k) relations for a (n,0)
 * zigzag nanotube. */
double zigEofK(double,double,double);

/* This function calculates the analytical density of states versus k,
 * DOS(k), for a (n,0) zigzag nanotube. */
double zigdEdKofK(double,double,double);

FILE *fout;

struct ekDataStruct
{
    double E;
    double k;    /* k is not used unless you uncomment below in order to
                  get the actual E(k) data. */
    double dEdK;
};

struct DOSstruct {
    double Ebin;
    double DOS;
};

int main(int argc, char **argv)
{
    int i;
    int bins = ARR_SIZE;    /* Number of bins */
    double res;            /* Inverse of the Energy resolution */
    double Ebinval;        /* Holds the scaled energy */
    double Emax = 3.0;     /* Maximum energy to be plotted */
    double krange = 2*PI;  /* 2*Pi */
    double kd;
    double q;
    double N;
    char s[100];
    char choice={'n'};

    ekDataStruct ekData[ARR_SIZE];
    DOSstruct DOSstr[ARR_SIZE]; /* Holds the DOS(E) data. */

    printf ("Nanotube DOS(E) program.\n");
    printf ("ntdos version 1, Copyright (C) 2000 Elton D. Graugnard\n");
    printf ("ntdos comes with ABSOLUTELY NO WARRANTY; This is free ");
    printf ("software,\n and you are welcome to redistribute it under");
    printf (" certain conditions;\n rerun the program with the ");
    printf ("argument 'G' to see the details.\n");

    if (argc != 2)
    {
        printf("Usage: ntdos <outfile> or 'G' \n");
        for (i = 0; i < argc; i++)
        {
            printf("argv[i] = %s\n",argv[i]);
        }
    }
}

```

```

    }
    exit(1);
}

if ((argc == 2)&&(*argv[1] == 'G'))
{
    system ("more gpl.txt");
    exit(0);
}

while ((choice != 'a')&&(choice != 'z'))
{
    printf("\nEnter 'a' for armchair DOS and 'z' for zigzag DOS: ");
    fflush(stdout);
    gets(s);
    sscanf(s,"%c",&choice);
}

N=0;
while (N <= 0)
{
    if (choice == 'a')
    {
        printf("\nEnter n for a (n,n) armchair nanotube: ");
    }
    else
    {
        printf("\nEnter n for a (n,0) zigzag nanotube: ");
    }
    fflush(stdout);
    gets(s);
    sscanf(s,"%lf",&N);
}

res=0.0;
/* (res*Emax) cannot be larger than ARR_SIZE, so 10000 is fine. */
while ((res < 10.0)|| (res > 10000.0))
{
    printf("\nEnter the resolution (larger num. = better res): ");
    fflush(stdout);
    gets(s);
    sscanf(s,"%lf",&res);
}

/* initializing data structure */
for(i = 0; i < bins; i++)
{
    DOSstr[i].Ebin = 0;
    DOSstr[i].DOS = 0;
}

/* Iterating over q from 1 to 2N+1 to match theory of 0 to 2n. Each
 * N is a different E(k) curve. We calculate DOS(E) for each curve
 * incrementally. Since 'if' statements are slow, I first check for
 * armchair or zigzag. */
if (choice == 'a')
```

```

{
printf ("\nArmchair\n");
for(q = 1; q < 2*N+1; q++)
{
printf("q = %g\n",q);

/* calculate armchair E(K) and dEdK(K). The functions are
* sent kd for the value of K.*/
for(i = 0; i < bins; i++)
{
kd=((double)i/bins)*krange-PI/(3*1.4);
ekData[i].E = armEofK(kd,q,N);
/* ekData[i].k = kd; */ /* Uncomment if you want the
E(k) data itself. */
ekData[i].dEdK = armdEdKofK(kd,q,N);
}

/* We have E(K) and dEdK(K). We want dEdK(E) - start
* binning. This does the energy binning in one pass, so
* it's not too slow. First we limit the energy to the
* desired range, set by 0.0 and Emax. Then we make sure
* the E(K) has the right slope, so dEdK > 0. Next we scale
* the actual energy by the inverse of the resolution. The
* larger res, the better the energy resolution. We then
* add 0.5 and floor the scaled energy to toggle the value
* into the right bin. This make the (int) type cast give
* the right scaled energy value. Lastly, we use the scaled
* energy value (as an int) as the index of the DOSstr array
* (so res*Emax must be < ARR_SIZE). We use the toggled and
* scaled energy value divided by res as the energy value
* and then add 1/(pi * dEdK) to the previous DOS array
* value. */
for(i = 0; i < bins; i++)
{
if ((ekData[i].E >= 0.0)&&(ekData[i].E <= Emax))
{
if (ekData[i].dEdK > 0)
{
Ebinval = floor(res * ekData[i].E + 0.5);
DOSstr[(int)Ebinval].Ebin = Ebinval/res;
DOSstr[(int)Ebinval].DOS
+= 1/(PI * ekData[i].dEdK);
}
}
}
}
}
else
{
printf ("\nZigzag\n");
for(q = 1; q < 2*N+1; q++)
{
printf("q = %g\n",q);

/* calculate zigzag E(K) and dEdK(K) */

```

```

for(i = 0; i < bins; i++)
{
    kd=((double)i/bins)*krange-PI/(3*1.4);
    ekData[i].E = zigEofK(kd,q,N);
    /* ekData[i].k = kd; */ /* Uncomment if you want the
        E(k) itself. */
    ekData[i].dEdK = zigdEdKofK(kd,q,N);
}

/* We have E(K) and dEdK(K). We want dEdK(E) - start
 * binning. This does the binning in one pass, so it's not
 * too slow. See comments above for explanation. */
for(i = 0; i < bins; i++)
{
    if ((ekData[i].E >= 0.0)&&(ekData[i].E <= Emax))
    {
        if (ekData[i].dEdK > 0)
        {
            Ebinval = floor(res * ekData[i].E + 0.5);
            DOSstr[(int)Ebinval].Ebin = Ebinval/res;
            DOSstr[(int)Ebinval].DOS
                += 1/(PI * ekData[i].dEdK);
        }
    }
}

}

}

/* Writing out results to a 2 column data file. */
if ((fout = fopen(argv[1],"w")) == NULL)
{
    printf("\nCannot open output file!\n");
    exit(1);
}

for (i = 0; i < bins; i++)
{
    if(DOSstr[i].DOS != 0)
    {
        fprintf(fout,"%g\t%g\n", DOSstr[i].Ebin,DOSstr[i].DOS);
    }
}
fclose(fout);

} /* End of main. */

/* This function calculates the analytical E(k) relations for a (n,n)
 * armchair nanotube. */
double armEofK(double kval, double qval,double nval)
{
    double En;
    double q=qval;
    double n=nval;

```

```

    En = T*sqrt(1.0+4.0*cos(q*PI/n)*cos(kval*A*0.5)+4.0*cos(kval*A*0.5)*
               cos(kval*A*0.5));
    return En;
}

/* This function calculates the analytical density of states versus k,
 * DOS(k), for a (n,n) armchair nantoube. */
double armdEdKofK(double kval,double qval,double nval)
{
    double En,dEdK;
    double q=qval;
    double n=nval;

    En = T*sqrt(1.0+4.0*cos(q*PI/n)*cos(kval*A*0.5)+4.0*cos(kval*A*0.5)*
               cos(kval*A*0.5));
    dEdK =
        -T*T*A*((2.0*cos(kval*A*0.5)+cos(q*PI/n))*(sin(0.5*A*kval)))/En;
    return dEdK;
}

/* This function calculates the analytical E(k) relations for a (n,0)
 * zigzag nantoube. */
double zigEofK(double kval, double qval,double nval)
{
    double En;
    double q=qval;
    double n=nval;

    En = T*sqrt(1.0+4.0*cos(sqrt(3.0)*kval*A*0.5)*cos(q*PI/n)+4.0*
               cos(q*PI/n)*cos(q*PI/n));
    return En;
}

/* This function calculates the analytical density of states versus k,
 * DOS(k), for a (n,0) zigzag nantoube. */
double zigdEdKofK(double kval,double qval,double nval)
{
    double En,dEdK;
    double q=qval;
    double n=nval;

    En = T*sqrt(1.0+4.0*cos(sqrt(3.0)*kval*A*0.5)*cos(q*PI/n)+4.0*
               cos(q*PI/n)*cos(q*PI/n));
    dEdK =
        -T*T*(sqrt(3.0)*A*cos(q*PI/n))*(sin(0.5*sqrt(3.0)*A*kval))/En;
    return dEdK;
}

```

## Appendix B: The FEM Chamber and an Indexed FEM of a Pt tip

Figs. B.1 and B.2 show photographs of the FEM chamber used in this study. The components of the chamber are labeled. The TEDs from the MWNT FEM samples were taken with the Omicron CSA-300 electron energy analyzer shown in Fig. B.2. The work function for our analyzer is 4.52 eV. A schematic top view of the chamber is shown in Fig. B.3. When we performed our MWNT experiments the deceleration lens (a UHV phosphor screen) was not present at the analyzer entrance.

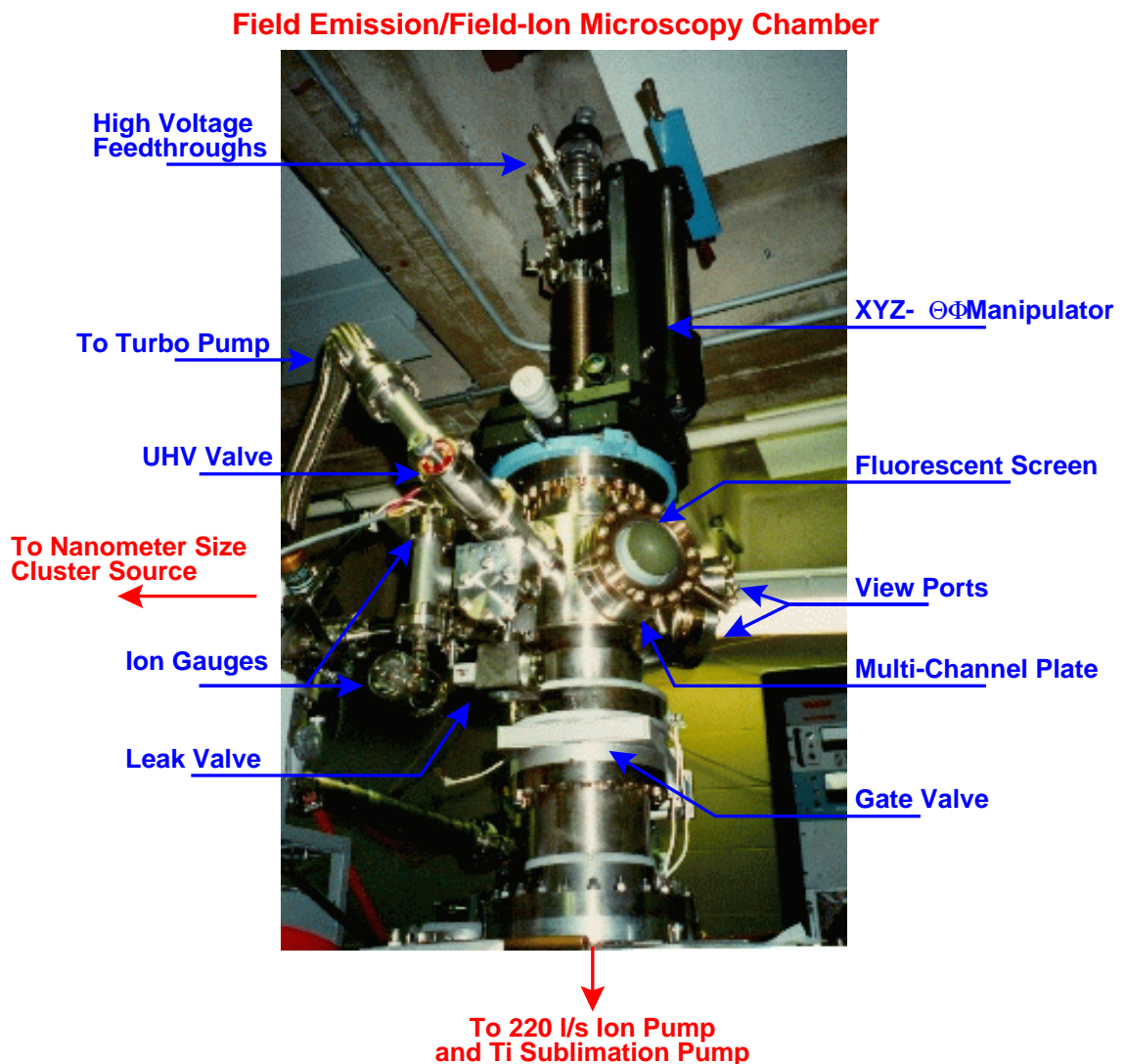


Figure B.1. A labeled photograph of the front of the FEM chamber.

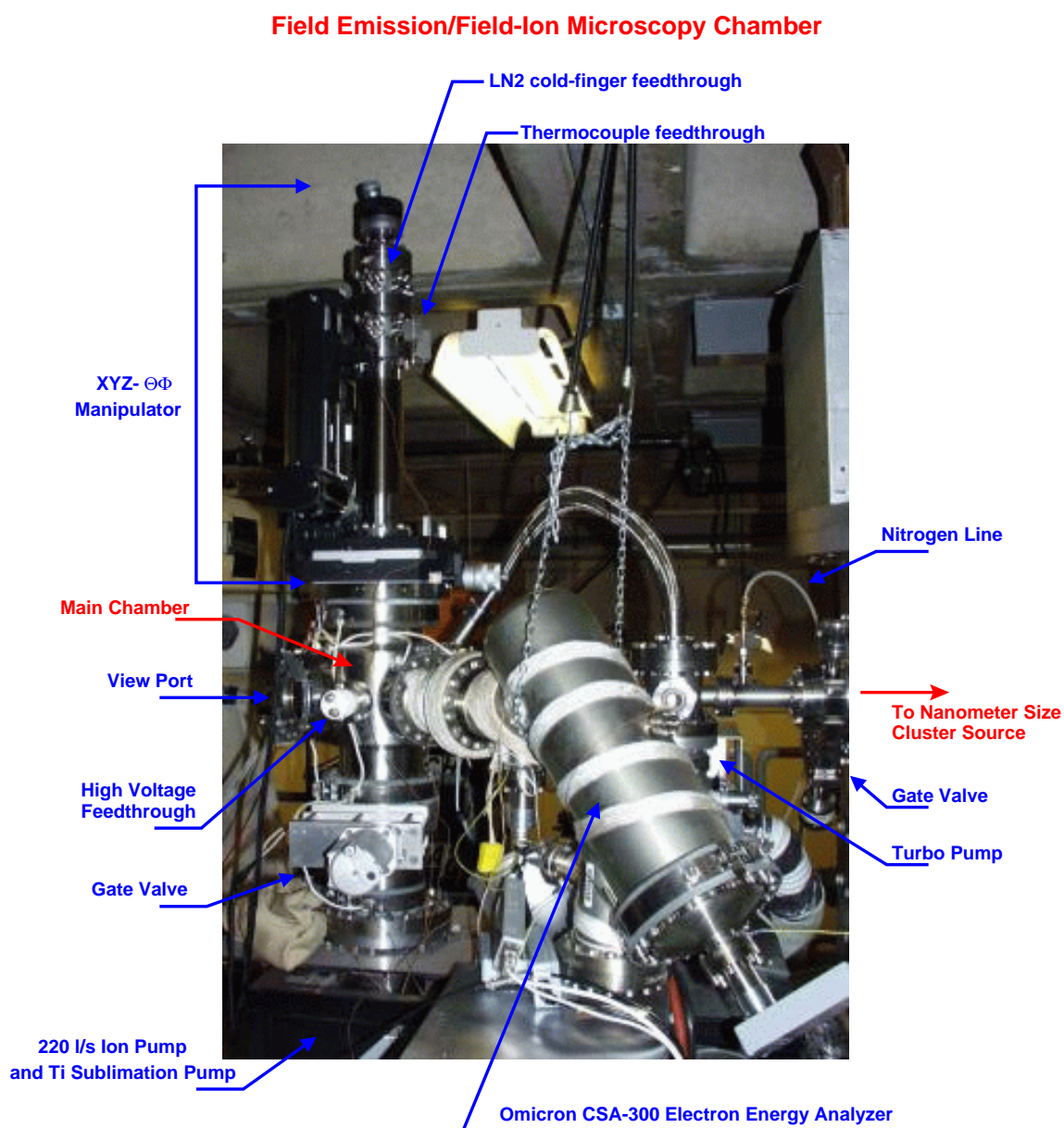


Figure B.2. A labeled photograph of the rear of the FEM chamber.

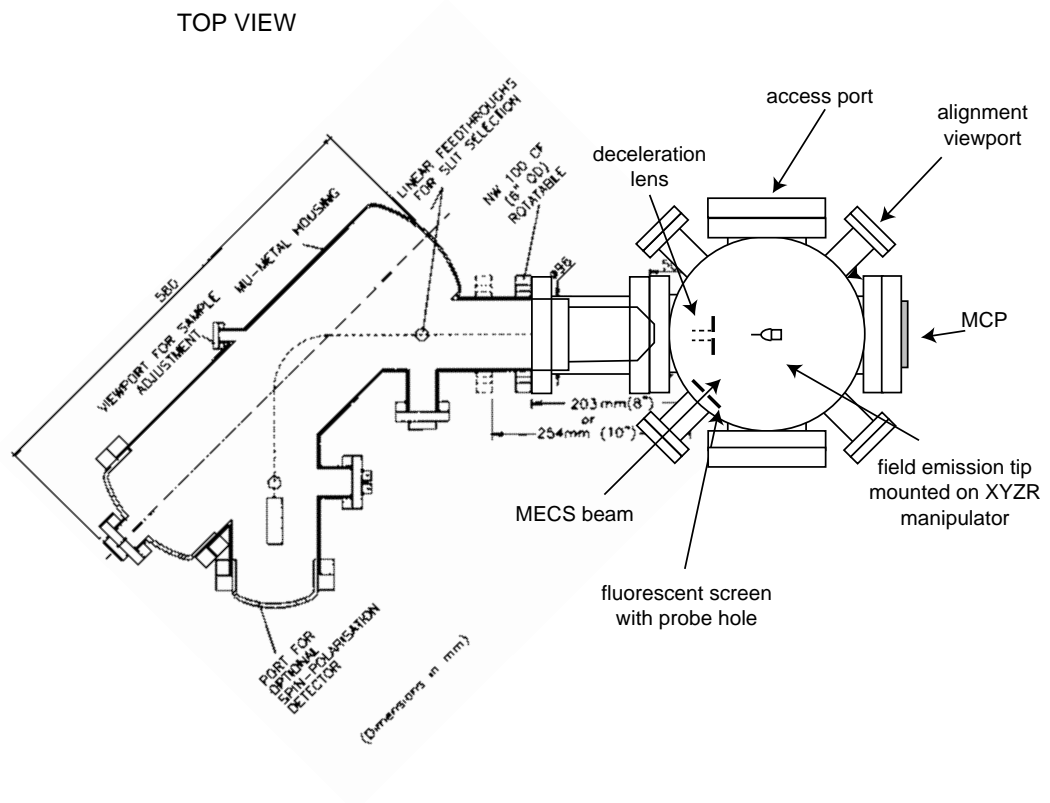


Figure B.3. A schematic top view of the FEM chamber showing some of the details of the energy analyzer.

The image in Fig. B.4 was taken with -6500V applied to the tip and recorded with a CCD camera. The large voltage required for this image indicates that the tip had a rather large end radius.

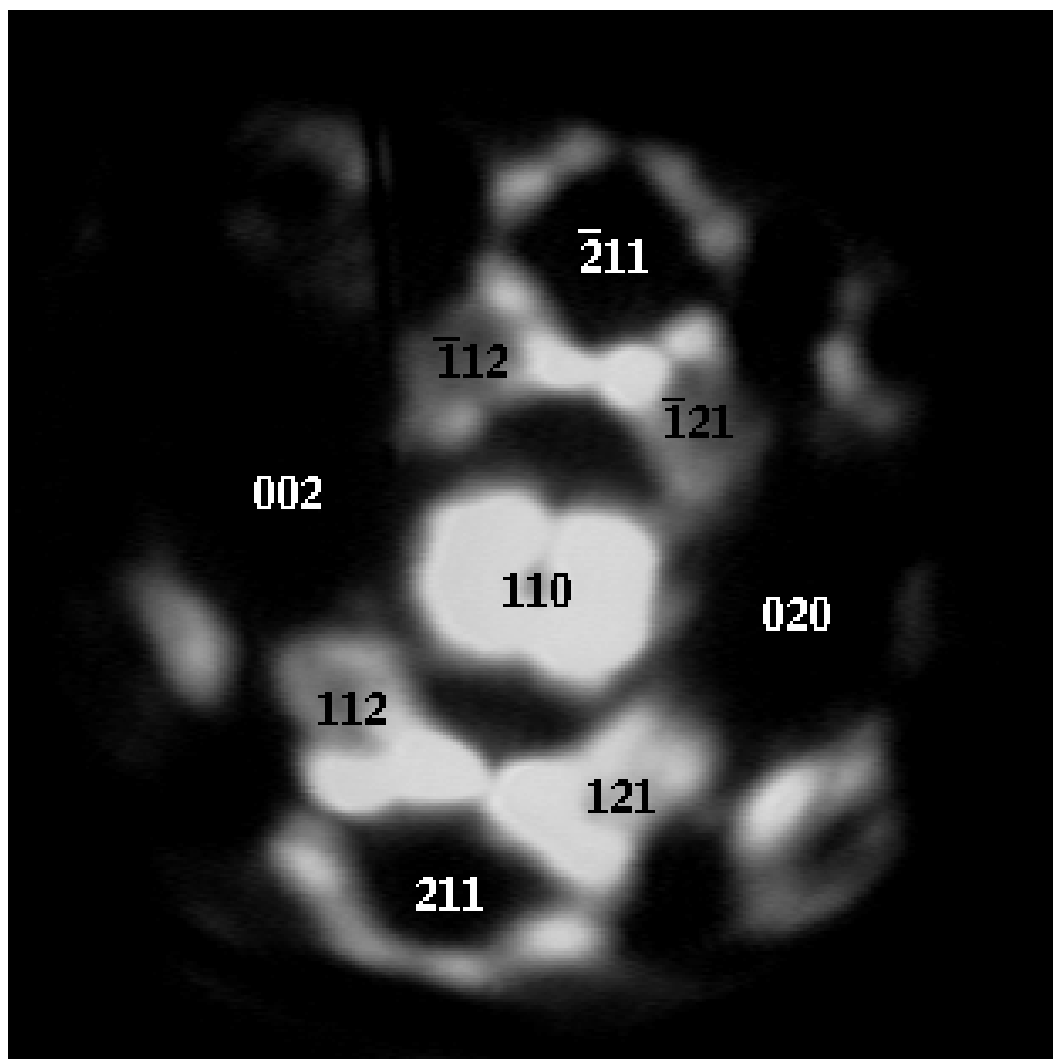


Figure B.4. A crystallographically indexed field emission micrograph from a (110) oriented platinum tip.

### Appendix C: FEM and TEDs of a Single-walled Nanotube Rope

The SWNT rope shown in Fig. C.1 was mounted to the Pt FEM tip using the procedure described in Section 3.2.1. This sample was one of only two made in a year. The field emission data taken from this rope was reported in Dan Lovall's PhD dissertation. [10]

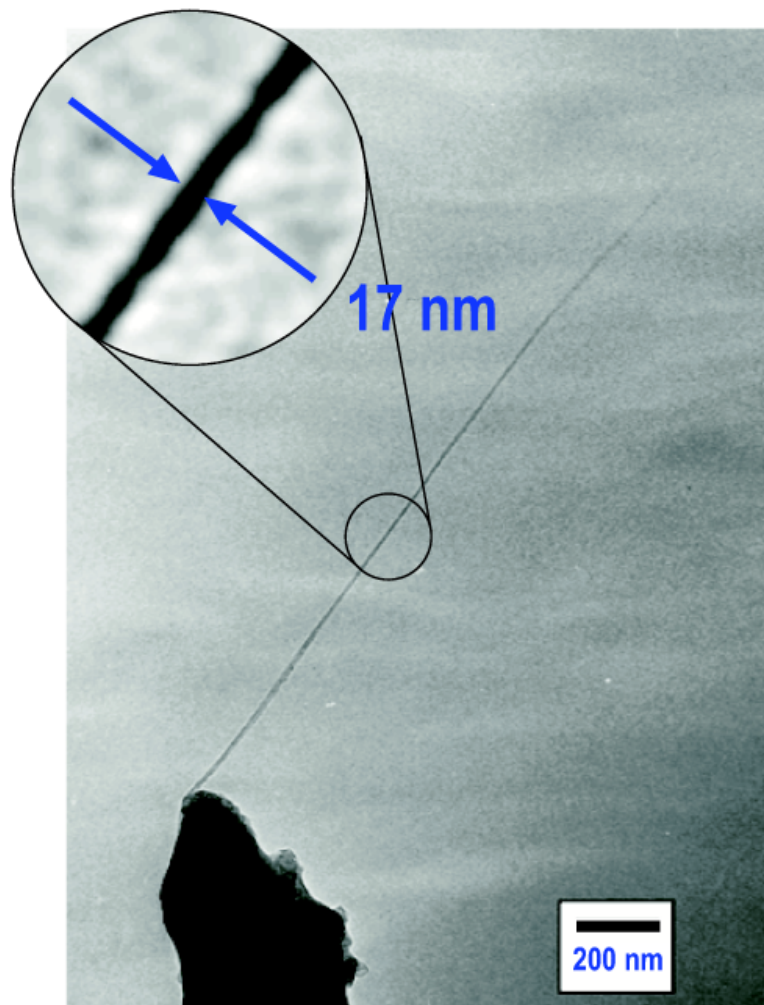


Figure C.1. A TEM image of a SWNT rope mounted to the end of a Pt FEM tip. The diameter of the rope (as seen in the magnified region) is  $D \simeq 17$  nm. Due to vibrations of the rope in the electron beam, the end cannot be resolved.

Later analysis of the field emission properties of this rope are published in the following reference. [11] The emitted current from this rope was stable and did not change with time. Total energy distributions for this SWNT rope were recorded using a commercial electron energy analyzer (Omicron CSA 300). A typical TED from the rope is shown in Fig. C.2. The inset of the image shows the data with the background subtracted, highlighting the peak structure in the trailing edge of the TED.

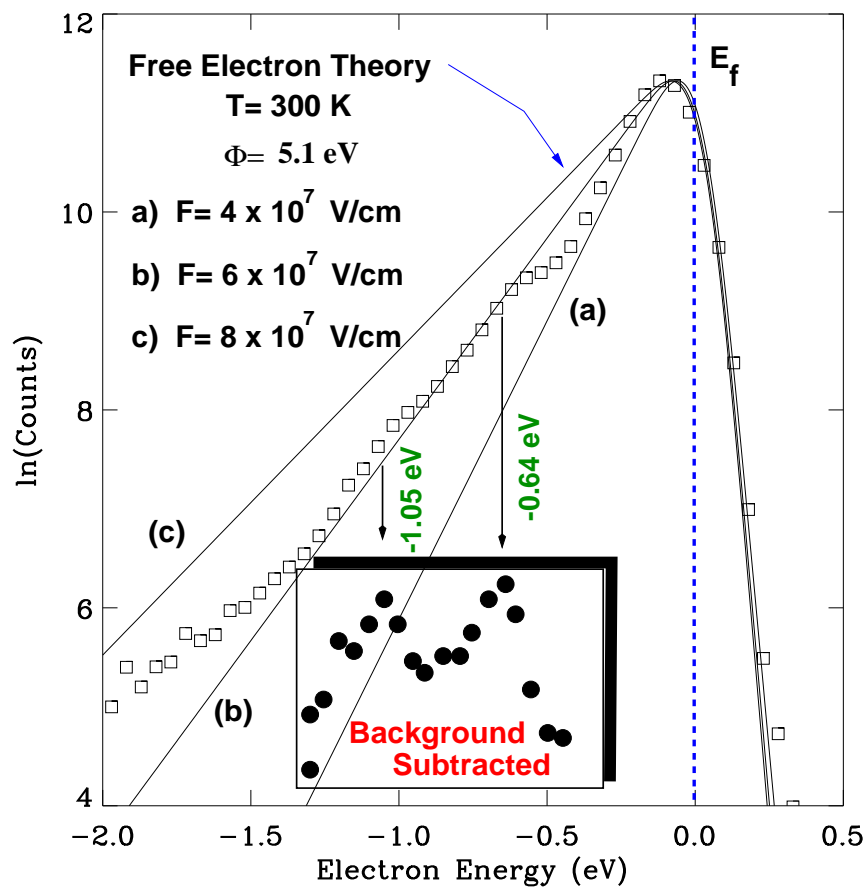


Figure C.2. The TED for a SWNT rope. Here we plot the natural log of the detected counts versus the electron energy relative to the Fermi level ( $E_F = 0$ ). By subtracting the monotonically decreasing component of the data (due to the deformed barrier width), we are able to extract the peaks shown in the inset. These peaks signal peaks in the DOS of the nanotubes in the rope.

### Appendix D: Optical Microscope used for Sample Fabrication

The photograph shown in Figs. D.1 and D.2 were taken from the PhD dissertation of Michael Buss. [8] Fig. D.1 shows the Nikon Epiphot 200 inverted dark-field microscope, the microscope stage, and the two Newport M-460A-XYZ manipulators. This system was used for fabricating samples for the field emission experiments discussed in Chapter 3 and for the transport samples discussed in Chapters 4 and 5.

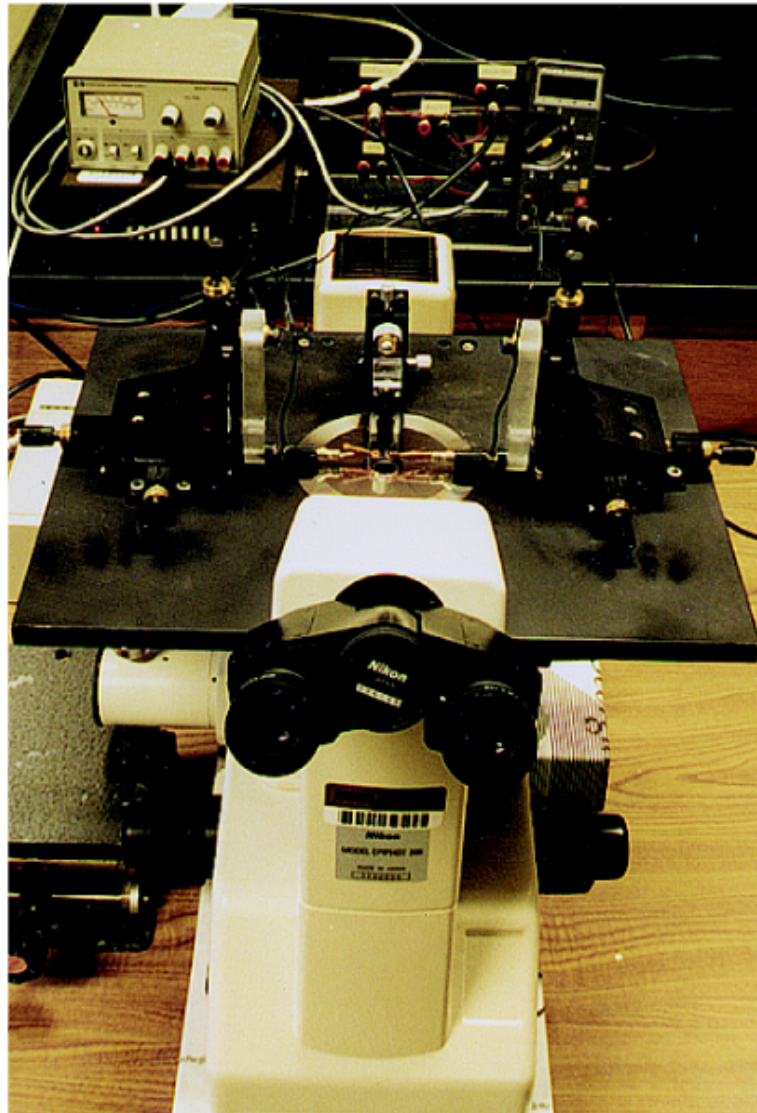


Figure D.1. A photograph of the optical microscope system used to fabricate field emission and transport samples.

Fig. D.2 shows a photograph of the various holders used with the manipulators on the optical microscope stage shown in Fig. D.1. The Pt tips used for selecting and manipulating the nanotubes were fabricated on small stainless steel tabs, as shown in Fig. D.3. The Pt wire was first spot welded to the steel tab, then the tip was etched. Holder 'A' in Fig. D.2 was used for holding the small steel tabs onto which the Pt tips were attached.

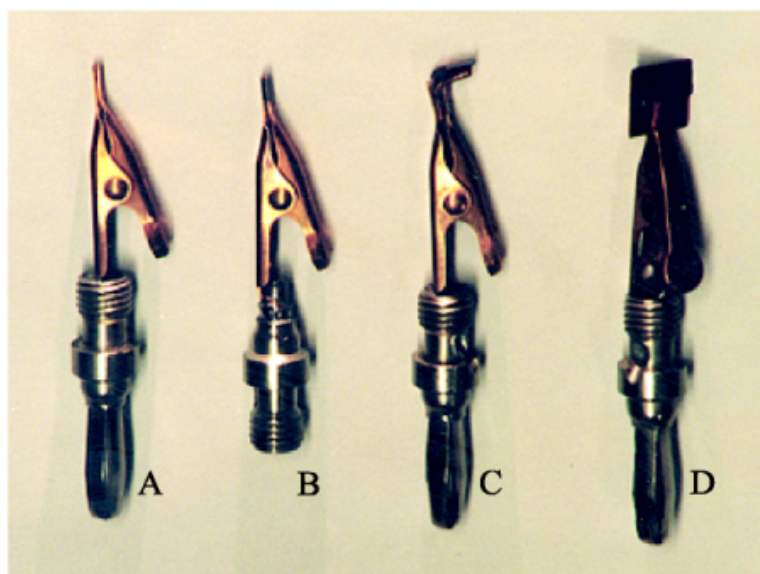


Figure D.2. A photograph of the holders used with the manipulators on the optical microscope stage.

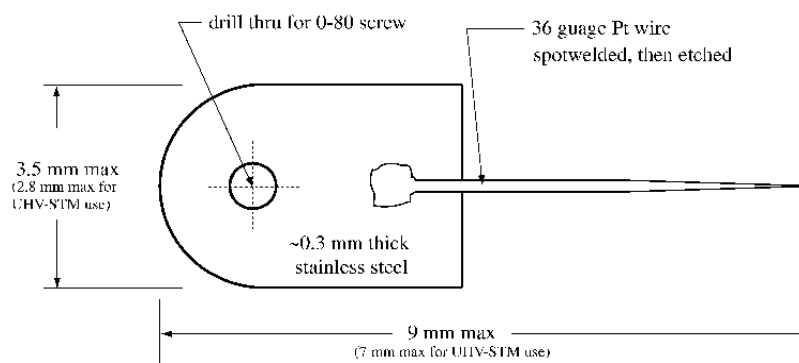


Figure D.3. A schematic of the stainless steel tabs used to hold the Pt FEM tips.

## Appendix E: Low Temperature Sample Mount

In order to study the electronic properties of our samples as a function of temperature, we built a probe to hold the sample in a cryogenic dip experiment. A simple schematic of the experiment is shown in Fig. E.1. The probe consists of a brass mounting plate, attached to the end of a 190 cm long, thin-walled, stainless-steel tube. A schematic of the mounting plate is shown in Fig. E.2. The brass plate is electrically and thermally isolated from the steel tube with a short section of Bakelite. The sample is mounted to the brass plate using thermally conductive Apiezon N grease. Four electrical leads are attached to the Ti/Au contact pads with a small amount of silver paint. Two of the leads carry the current to and from the sample. The other two measure the voltage dropped across the contact pads. This method prevents the measurement of the voltage drops along the electrical leads to the sample. This is not a true four-terminal technique since there are only two contacts to the nanotube (see Fig. E.2 and Section 4.1). To measure the temperature, a silicon diode thermometer (DT-470-SD-13A, LakeShore Inc.) is thermally anchored to the brass plate, opposite the sample. Four leads connect the silicon diode thermometer to a LakeShore DRC-91C temperature controller.

The brass sample/thermometer plate is inserted into a stainless-steel can, which is sealed to the steel tube using two indium o-rings. Using a valve at the top of the probe, the entire assembly is repeatedly flushed with dry-nitrogen and evacuated to fore-pump pressures ( $< 5$  Torr). The temperature of the sample is varied by placing the steel can inside of a liquid helium dewar. We control the temperature of the sample by carefully positioning the steel can with respect to the liquid He level within the dewar. At low temperatures, most of the residual gases within the probe (other than helium) condense to the walls, leaving the sample thermally isolated from the steel probe. Thus, to ensure accurate temperature readings and to achieve the lowest possible temperature, before inserting the probe into the dewar, we introduce a small amount of helium gas into the probe. This exchange gas facilitates the heat exchange between the sample and the walls of the steel can. Thus, the helium exchange gas

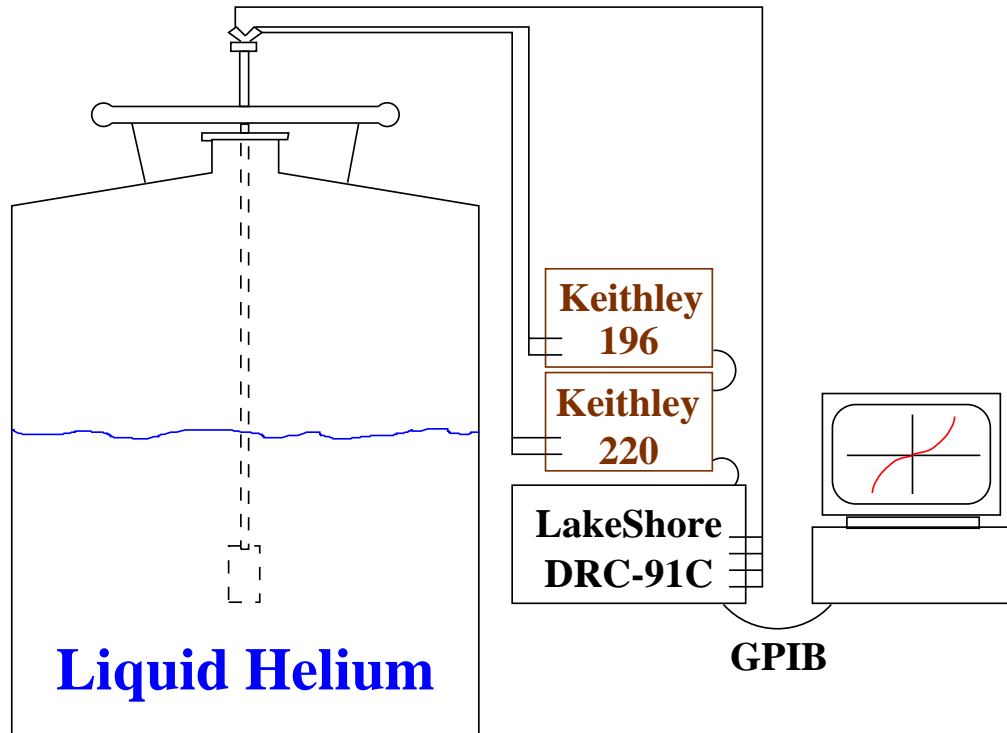


Figure E.1. A schematic of the low temperature conductance experimental setup. A Keithley 220 current source is used to send a specified current through the sample, and a Keithley 196 DMM is used to measure the voltage drop across the sample.

is necessary to achieve the 4.2 K temperature of liquid helium. Once the sample temperature stabilizes,  $I(V)$  data are acquired. The data are obtained using a Keithley 220 current source in conjunction with a Keithley 196 system digital multimeter, which are computer controlled over the General Purpose Interface Bus. Several computer programs (written in C) control the data acquisition from the samples. For  $I(V)$  data, current ramps are applied to the sample and the voltage drop is measured with a resolution of  $0.5 \mu\text{V}$ .<sup>1</sup> The  $I(V)$  data curves obtained in this manner contain up to 512 points, with a maximum acquisition rate of  $\sim 3$  points/sec. The entire data acquisition system was checked repeatedly with variety of carbon resistors of known resistance.

<sup>1</sup>Technically, since the current is applied and the voltage is measured, the data acquired is more accurately called  $V(I)$  data. We use “ $I(V)$ ” by convention.

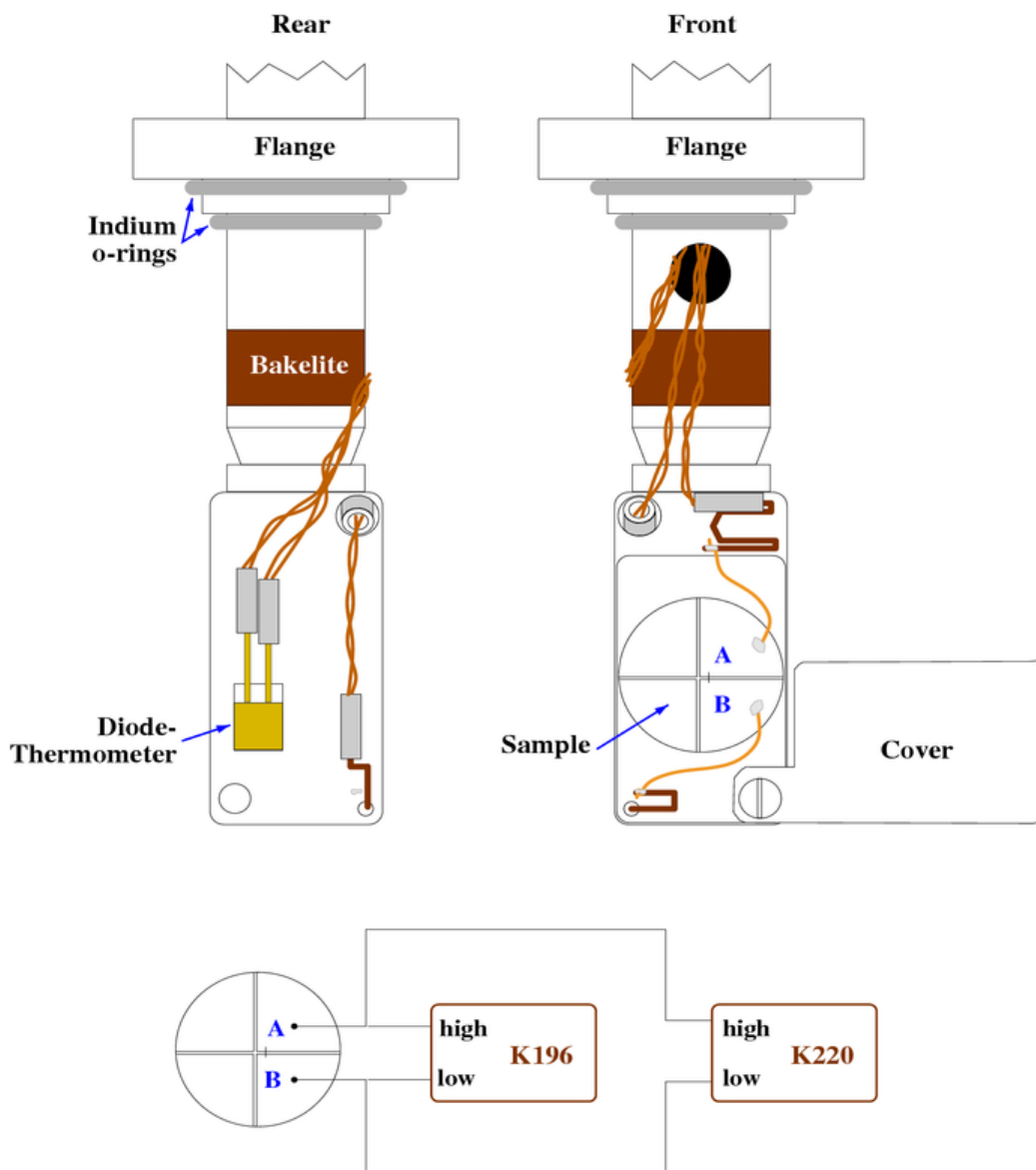


Figure E.2. A schematic of the sample mounting plate. The plate is electrically and thermally insulated from the steel tube with a section of Bakelite. The wires from the Keithley 220 current source and the Keithley 196 DMM travel down the tube to a hole in the tube wall. The “high” wires of each instrument are attached to the upper binding-post, while the “low” wires are routed along the back of the plate to the lower binding-post. For clarification, the instrument configuration is also shown at bottom. The diode thermometer is thermally anchored to the back of the mounting plate.

## Appendix F: Investigated Transport Models

In addition to the Luttinger liquid theory, we investigated several other temperature dependent transport models in an attempt to explain the observed behavior in the nanotube conductance. The models considered are i) thermally activated conduction, [118] ii) simple two-band model for graphite, [119] iii) a zero in the transmission probability induced by gap states, [24] iv) variable range hopping mechanisms, [121, 122] v) weak-localization, [40, 123] and vi) the Luttinger Liquid model. [21, 22, 29] Although several of these models may fit a portion of the conductance versus temperature data, the Luttinger liquid model (discussed in Section 5.2) provides the most consistent explanation for the temperature *and* voltage dependence of the data. For completeness, here we include a brief discussion for each model listed above (other than the Luttinger model) with a plot of the best fit to the conductance data. It should be noted that none of the models discussed here incorporated the strong electron-electron interactions, which are the focus of the Luttinger model.

### F.1 Thermally Activation Conduction

If the temperature dependence of the nanotube sample conductance is due to transport through multiple layers, several of these layers could be semiconducting. The semiconducting layers will contribute to the conductance through an activation process, given by the general form [37, 118]

$$G \propto \exp\left[-\frac{E_g}{k_b T}\right], \quad (\text{F.1})$$

where  $E_g$  is the size of the energy gap. Fig. 4.13 shows a plot of energy gap versus nanotube diameter for semiconducting nanotubes. As the temperature increases the conductance through any semiconducting layers increases exponentially. This type of behavior is also expected for a 1D tunnel barrier. If the conductance is dominated by tunneling processes between metallic layers in the MWNT, the conductance will also be activated. If the dominant conduction process is activation a plot of  $\ln(G)$  versus  $1/T$  should yield a straight line with a slope of  $-E_g/K_b$ . This type of plot is called an Arrhenius plot and is shown in Fig. F.1 for the six samples discussed in Chapter 5.

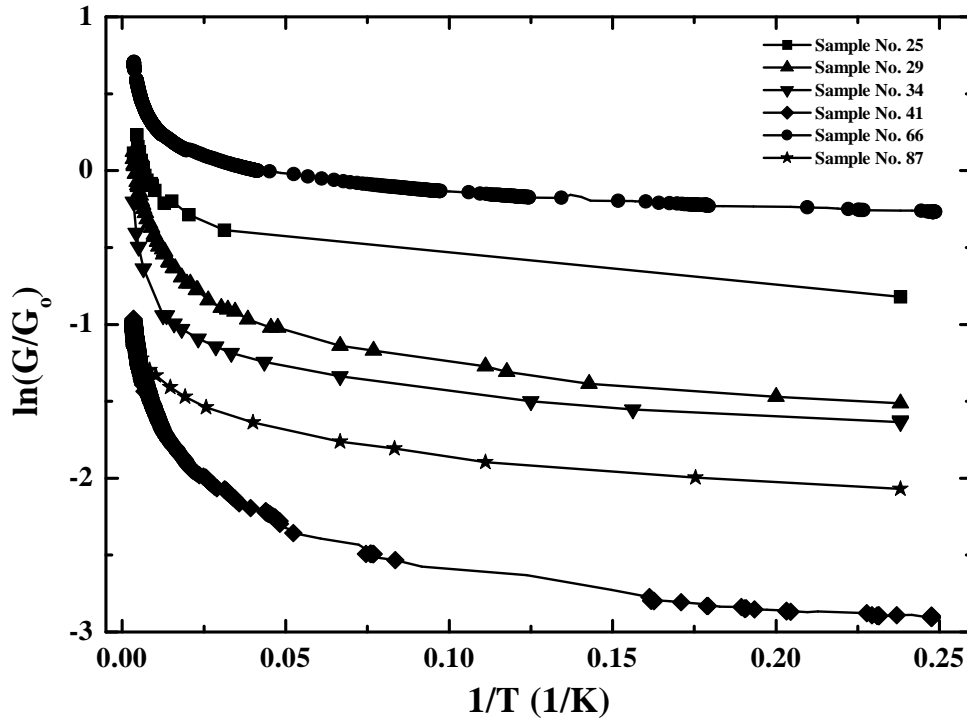


Figure F.1. An Arrhenius plot for the six samples discussed in Chapter 5.

The large curvature of the data plotted in this way indicates that the conduction process is not activated. If we consider only low temperatures the data is linear. The slopes to the low temperature data, determined by least-squares fits, give values for  $E_g$  that range from 0.06–0.2 meV, which is extremely small. If these energy gaps are related to semiconducting nanotubes, the estimates for the tube diameters (from Eqn. 2.14) range from 4118 nm to 13,727 nm! Clearly, these values are unreasonable.

The voltage dependence of the conductance for semiconducting layers is not as straight forward as the temperature dependence. As is well known, there are a variety of scenarios which may describe a metal-semiconductor (M-S) interface. As discussed in Chapter 4, we have seen evidence for Schottky diode behavior in our samples, presumably from a M-S junction. The voltage dependence of this junction was highly asymmetric (see Fig. 4.10) and completely different than the voltage dependence of the six samples studied here. Another issue concerning semiconductor voltage dependence and Schottky barrier formation is the question of the Fermi level alignment between

the nanotube and the contacts. The position of the semiconductor energy bands depends strongly on the coupling between the nanotube and the contacts, as well as any defects or distortions of the nanotube at the contacts. [141, 142] Thus, it is not clear what the voltage dependence of the conductance should be for a semiconducting nanotube. Given the ambiguity in the voltage dependence and the lack of a strong asymmetry with voltage combined with the large curvature shown in Fig. F.1 and the extremely small energy gaps, we do not believe the behavior is due to semiconducting layers.

## F.2 Simple Two-band Model

The simple two-band model has been used to explain the conductance versus temperature behavior for graphite and for carbon nanotubes. [119, 143] This model describes the conductance when the valence band and the conduction band overlap each other by an amount  $\Delta$ , as shown in Fig. F.2 (from Langer *et al.*). [119] In this model, the conductance is related to the carrier densities and may be expressed as

$$\begin{aligned} G \propto n + p &= C_n k_b T \ln[1 + e^{E_F/k_b T}] + C_p k_b T \ln[1 + e^{(\Delta - E_F)/k_b T}], \\ \Rightarrow G &\propto C k_b T \ln\left[(1 + e^{E_F/k_b T})(1 + e^{(\Delta - E_F)/k_b T})\right], \end{aligned} \quad (\text{F.2})$$

where  $C_n$  and  $C_p$  constants related to the effective masses of the carriers, which we assume to be equal, and the zero of energy is the bottom of the conduction band. A plot of Eqn. F.2 is given in Fig. F.2 where we see that the curvature of Eqn. F.2 at low temperatures is in the opposite direction of the data. The parameters of the fit are  $C = 1.7 \times 10^{-3} (\text{eV})^{-1}$ ,  $\Delta = 24 \text{ meV}$  and  $E_F = 0$ , which produced the least upward curvature at low temperatures. For the conductance to fit this model, the data would have to saturate at low temperatures, which we have only seen for sample No. R4. The conductance for sample No. R4, discussed in Section 5.3, does show saturation at low temperatures, perhaps indicating a more graphitic nature. Sample No. R4 was grown by a CVD method, [134] and TEM images showed the tubes to be more kinked than the arc-grown nanotubes (see Fig. 5.16).

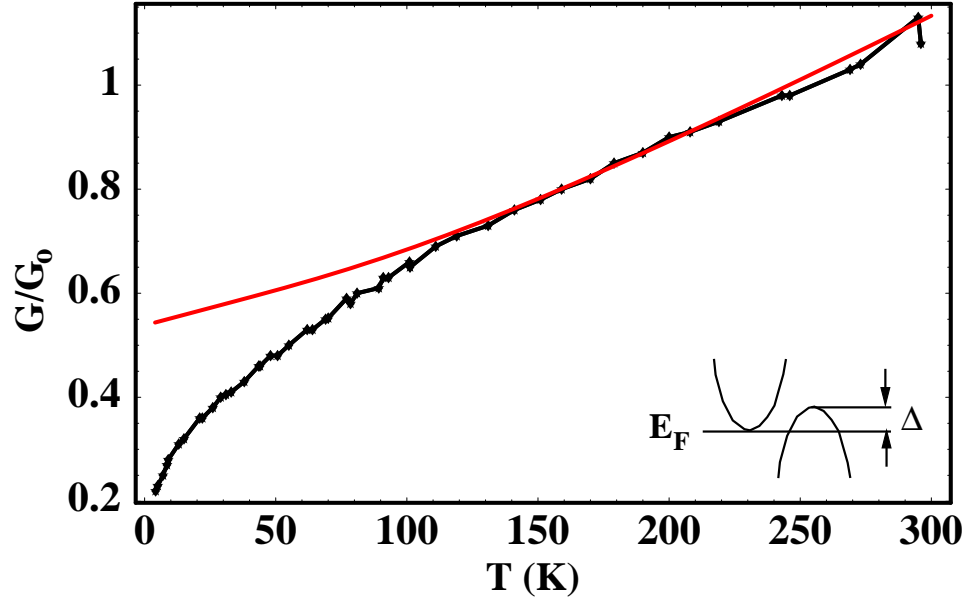


Figure F.2. The conductance of the simple two-band model shown with the conductance data for sample No. 29. The schematic illustrates the model. The parameters of the fit are  $C = 1.7 \times 10^{-3} (\Omega \text{eV})^{-1}$ ,  $\Delta = 24 \text{ meV}$  and  $E_F = 0$ .

### F.3 A Zero in the Transmission Probability

In a report by Anantram *et al.* it was found that defects in a carbon nanotube could create regions in the transmission probability at certain energies where the transmission probability goes to zero. [24] The size of the gaps depends on the nature of the defect and how much it affects the system. Using Eqn. 2.17 we calculate the current through a system with a gap of width  $\Delta$  located at the Fermi energy. We insert the gap into the transmission function by changing the limits of integration:

$$I \propto \int_{-\infty}^{-\Delta/2} \mathcal{T}(E) [f(E - \mu_1) - f(E - \mu_2)] dE + \int_{\Delta/2}^{\infty} \mathcal{T}(E) [f(E - \mu_1) - f(E - \mu_2)] dE. \quad (\text{F.3})$$

If we assume that the transmission probability is constant everywhere else, we obtain the results shown in Fig. F.3. The conductance displays a pronounced dip at low temperatures as the reduction of thermal broadening allows the gap in the transmission to be resolved. This behavior is similar to our conductance data except that here, the

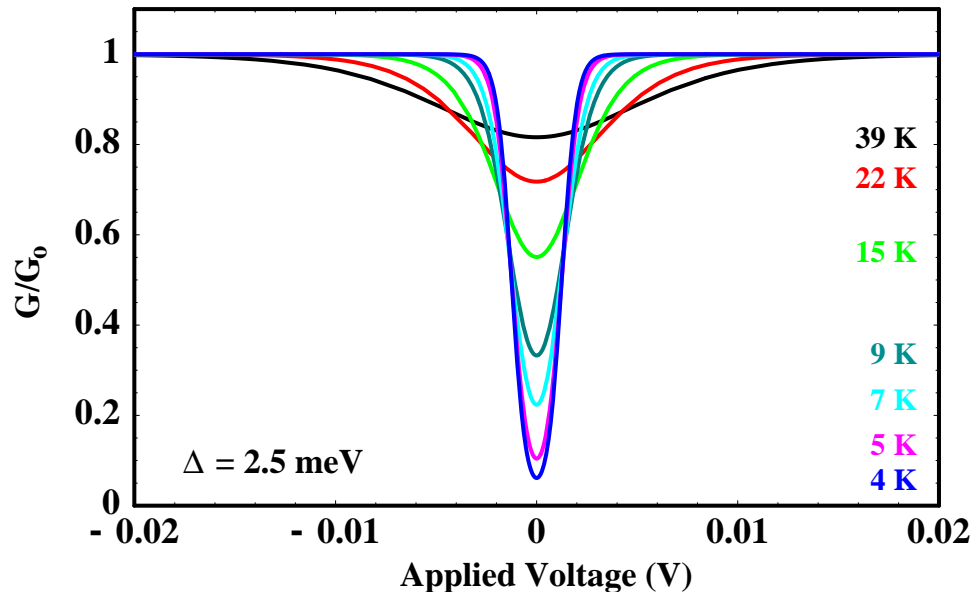


Figure F.3. The conductance of a ballistic conductor at several temperatures calculated with a gap in the transmission function, using Eqn. F.3. The calculations were performed at several of the temperatures shown in Fig. 5.10 for sample No. 29.

conductance at low temperatures does not saturate with applied voltage until well away from the gap where the model saturates at  $1G_o$ . Also, at lower temperatures, the conductance increases to  $1G_o$  faster than at higher temperatures, contrary to our conductance data. Another feature of this model is that the temperature dependence of the conductance at zero-bias is essentially the same as the activation model, which, as we have already seen, does not fit our conductance data.

#### F.4 1D and 2D Hopping Conduction

Hopping conduction and Anderson localization have been studied extensively over the past several decades. [120–122] Variable range hopping conduction in the Anderson localized regime was proposed by Mott. [120, 121] In this regime, due to disorder in a material, the electron states have become localized. Phonon-assisted hopping from one localized state to another can occur at finite temperatures in an activated manner. However, the spatial extent of the electron wavefunctions is also important,

so this is not the same as the previous thermal activation model. For  $D$ -dimensional systems, one finds [120–122]

$$\sigma \propto \exp\left[-\left(\frac{T_0}{T}\right)^{\frac{1}{D+1}}\right], \quad (\text{F.4})$$

where  $T_0$  depends on the dimension and may reflect electron-electron interactions. Thus, for carbon nanotubes, one might expect  $D = 1$  or  $2$  in Eqn. F.4. In order to analyze this transport mechanism, we can re-write Eqn. F.4 in terms of conductance and take the natural log of both sides to get:

$$\ln(G) \propto -\left(\frac{T_0}{T}\right)^{\frac{1}{D+1}}. \quad (\text{F.5})$$

Thus for hopping conduction in  $D$ -dimensions, a plot of  $\ln(G)$  versus  $T^{-1/(D+1)}$  should yield a straight line. In Fig. F.4 we plot the natural log of the conductance data versus  $T^{-1/2}$  (1D) in (a) and versus  $T^{-1/3}$  (2D) in (b). In each case the calculations fit the low temperature data well, until about 25 K. The temperature below which Eqn. F.4 is valid is related to the interaction energy for electrons in the localized states and to  $T_0$ . For both dimensions, the quantity  $T_0$  depends on the average number of hopping sites, the localization lengths and the density of states. It is not clear what values of  $T_0$  are reasonable. If we interpret  $T_0$  as the activation energy one obtains  $k_b T_0^{(1D)} = 0.28$  meV and  $k_b T_0^{(2D)} = 0.61$  meV, both of which are very small. It is also not clear what to expect for the voltage dependence of this model. Since the low temperature conductance data is well fit by a hopping mechanism, we cannot exclude this model as a possible explanation of the observed nanotube behavior. A voltage dependence for this model would help further distinguish this mechanism. Magnetotransport data would also help since there are clear predictions for hopping conduction in the presence of a magnetic field. [120, 121] Furthermore, the above analysis is for the single electron model. It has also been shown that hopping conduction is affected by many-body correlations. [120] Furthermore, for finite levels of disorder, such that the system has localized electron states, a ‘‘Coulomb Gap’’ forms in the density of states at the Fermi level. [120] This gap in the DOS has dramatic effects on hopping

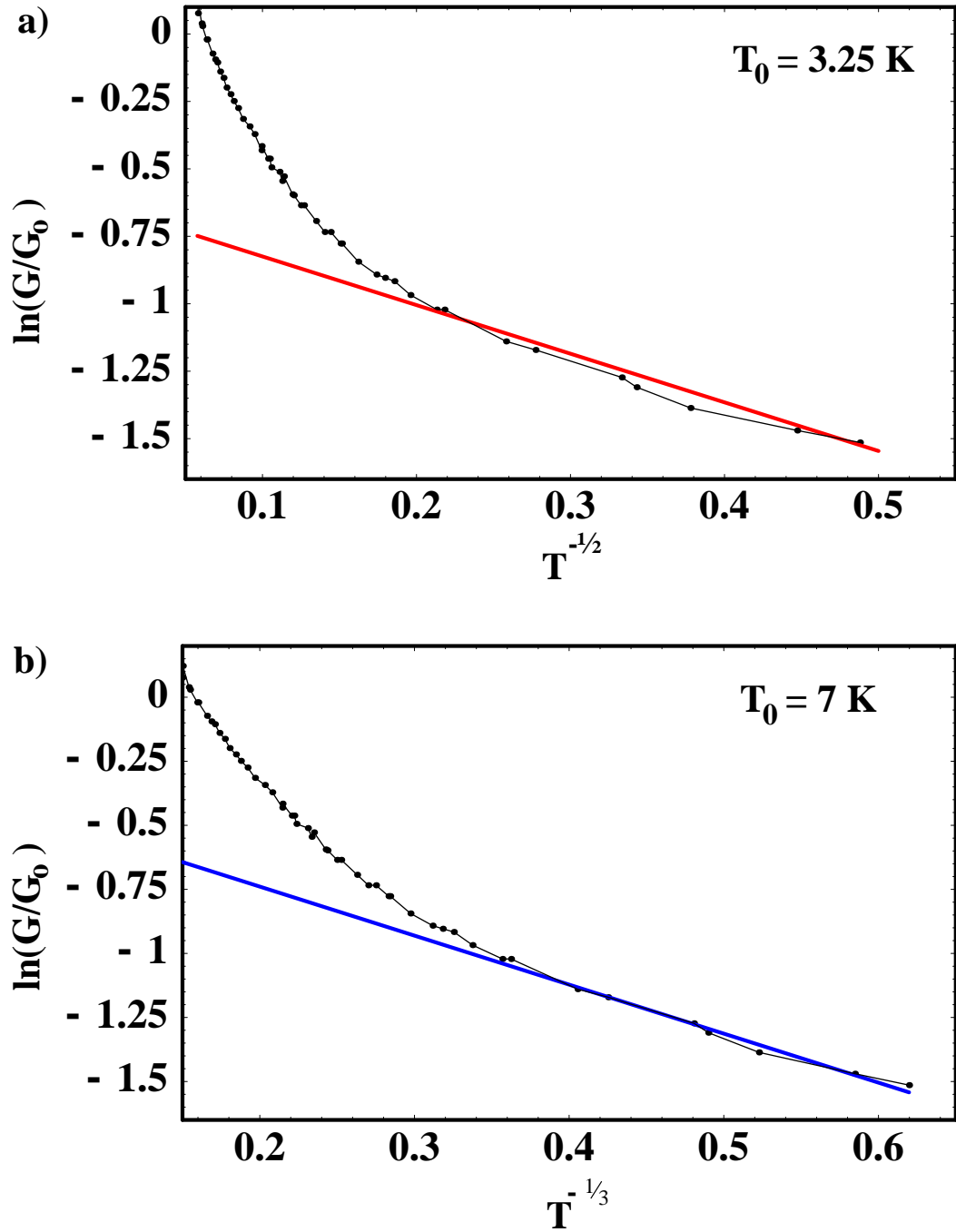


Figure F.4. In (a) a plot of  $\ln(G/G_0)$  versus  $T^{-1/2}$  with a fit using Eqn. F.4 for 1D. In (b) the  $x$ -axis is  $T^{-1/3}$  with a fit using Eqn. F.4 for 2D. The conductance data shown is for sample No. 29.

conduction and must be included in the parameter  $T_0$  of Eqn. F.4. This gap may affect both the temperature and voltage dependence of hopping conduction. Thus, we cannot completely exclude this model, and further work is needed.

### F.5 1D and 2D Weak Localization

Closely related to hopping conduction, weak localization in one and two dimensions addresses the issue of electron transport through disordered wires (1D) and thin films (2D). [144–146] In the regime of weak localization, the conduction electrons scatter elastically at the randomly distributed scattering centers of the material. The phase of the electron wavefunction is not destroyed by these collisions. This property allows for the constructive interference of electrons counter-propagating through a series of scatterers, an effect which is known as weak localization. This constructive interference leads to an enhanced backscattering probability and thus, to a decrease in conductance. The phase coherence of the electron wavefunctions is destroyed by inelastic scattering events, which reduces the interference. The temperature dependence of the inelastic scattering time is the source of the temperature dependence of the interference effects and thus, weak localization.

In 1D the conductance is given by [103, 123]

$$G = G_* - \frac{2e^2}{hL} \left( \frac{1}{l_\phi^2} + \frac{w^2}{3l_m^2} \right)^{-1/2}, \quad (\text{F.6})$$

where  $L$  and  $w$  are the length and width of the sample, respectively. The parameter  $l_m$  is the magnetic length, which is inversely proportional to the magnetic field, and the parameter  $l_\phi$  is the phase coherence length, which is related to the temperature by  $l_\phi \propto T^{-1/3}$  below  $\sim 20$  K and  $l_\phi \propto T^{-1/2}$  above  $\sim 20$  K. Thus, in the absence of a magnetic field, we find (below  $\sim 20$  K) [123]

$$G - G_* = - \frac{2e^2}{hL} \left( \frac{\mathcal{D}G_D L \hbar^2}{2e^2 kT} \right)^{1/3}, \quad (\text{F.7})$$

where  $\mathcal{D}$  is the diffusion coefficient and  $G_D$  is the Drude conductance for elastic scattering only.

In 2D the temperature dependent weak localization conductance for a nanotube with  $N$  conducting layers is given by [40]

$$G = G_* + \frac{e^2 d N}{h L} \ln \left[ 1 + \left( \frac{T}{T_c} \right)^p \right], \quad (\text{F.8})$$

where  $d$  is the tube diameter,  $L$  is the length, and  $T_c$  is related to various scattering lengths. The parameter  $p$  depends on the scattering mechanism and was found to be 1 by Langer *et al.* for a MWNT sample. [40]

In both formulations it is not clear what the value of  $G_*$  should be. Typically the value used is the value of the conductance at zero magnetic field, however this value could change with temperature. For our purposes  $G_*$  is used as a fitting parameter. For 1D weak localization from Eqn. F.6, a plot of  $G$  versus  $T^{-1/3}$  should be a straight line in the region below  $\sim 20$  K ( $20^{-1/3} \simeq 0.37$ ). The data plotted in this way for samples No. 29 and 87 are shown in Fig. F.5 with least-squares fits to the low temperature portions of the data. Thus, we see that the data do conform to a straight line on such a plot, consistent with 1D weak localization. The parameters (slope,  $y$ -intercept) determined by the fits are  $(-0.55, 0.55)$  for sample No. 29,  $(-0.53, 1.10)$  for sample No. 66, and  $(-0.21, 0.26)$  for sample No. 87.

A similar analysis can be performed for a  $T^{-1/2}$  dependence above 20 K. Such an analysis was performed for sample No. 29. Again, the data are linear when plotted in this manner. For this sample the values of the (slope,  $y$ -intercept) obtained from least-squares fits in the region of  $\sim 20$ – $60$  K are  $(-1.69, 0.72)$ . Fig. F.6 plots the  $G(T)$  data for sample No. 29 on a linear scale. The red line is the fit valid in the region less than 20 K, and the blue line is the fit for higher temperatures, which departs from the data near 55 K.

For 2D weak localization we can obtain fits of similar quality to the 1D fits. In Fig.F.7 we show fits to sample No. 29 using Eqn. F.8, and in Fig.F.8 we show fits for sample No. 66. For our samples the length between contacts  $L$  is  $4.3 \mu\text{m}$ . In each fit we used  $p = 1$ , as was found in previous studies. [40] The parameters used to make the fit are:

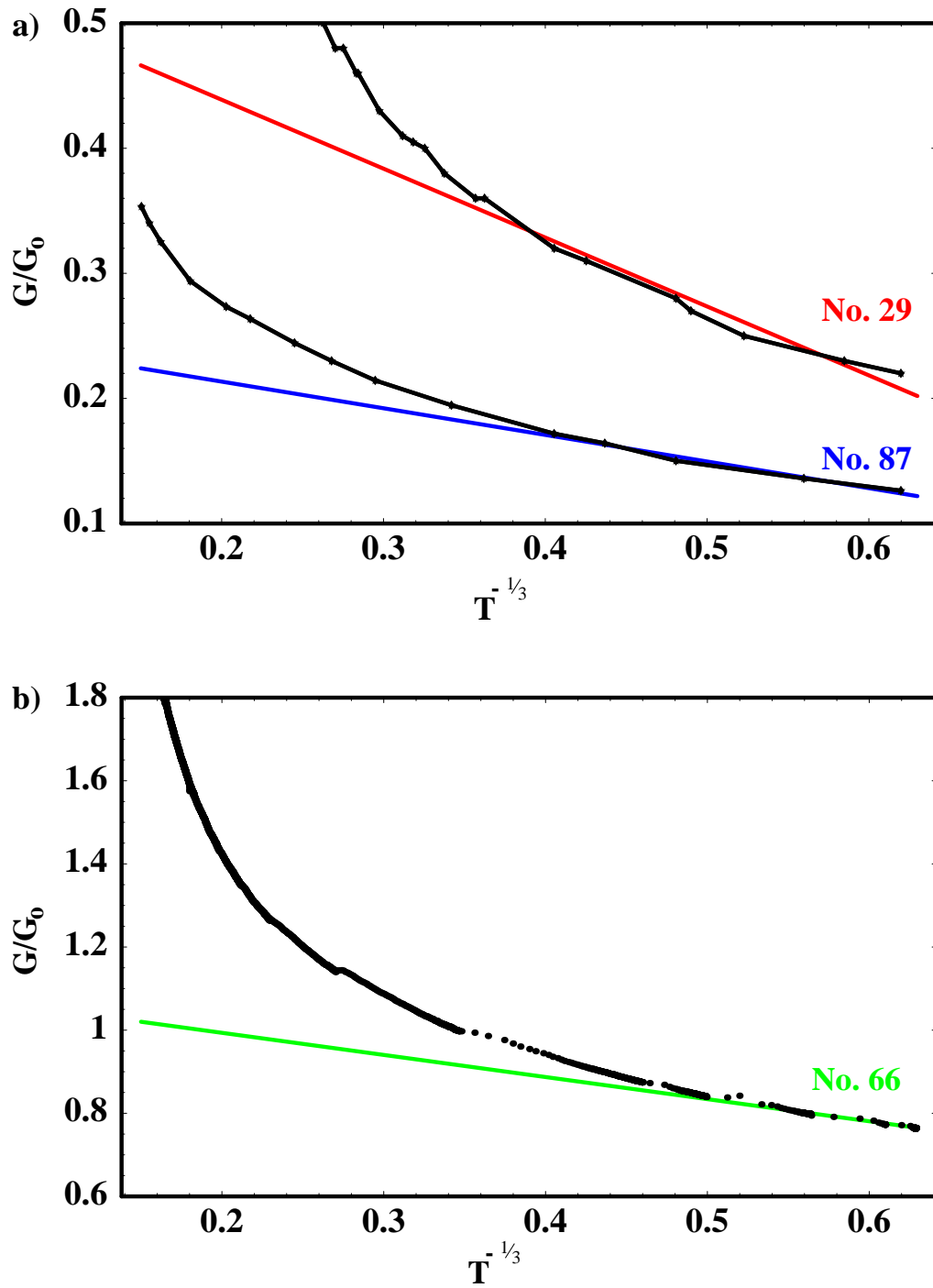


Figure F.5. A plot of  $G/G_0$  versus  $T^{-1/3}$  with a least-squares fit to the low temperature data for samples No. 29 and No. 87 in (a) and sample No. 66 in b). The values of the (slope,  $y$ -intercept) determined by the fits are No. 29:(-0.55, 0.55), No. 87:(-0.21, 0.26), and No. 66:(-0.53, 1.10).

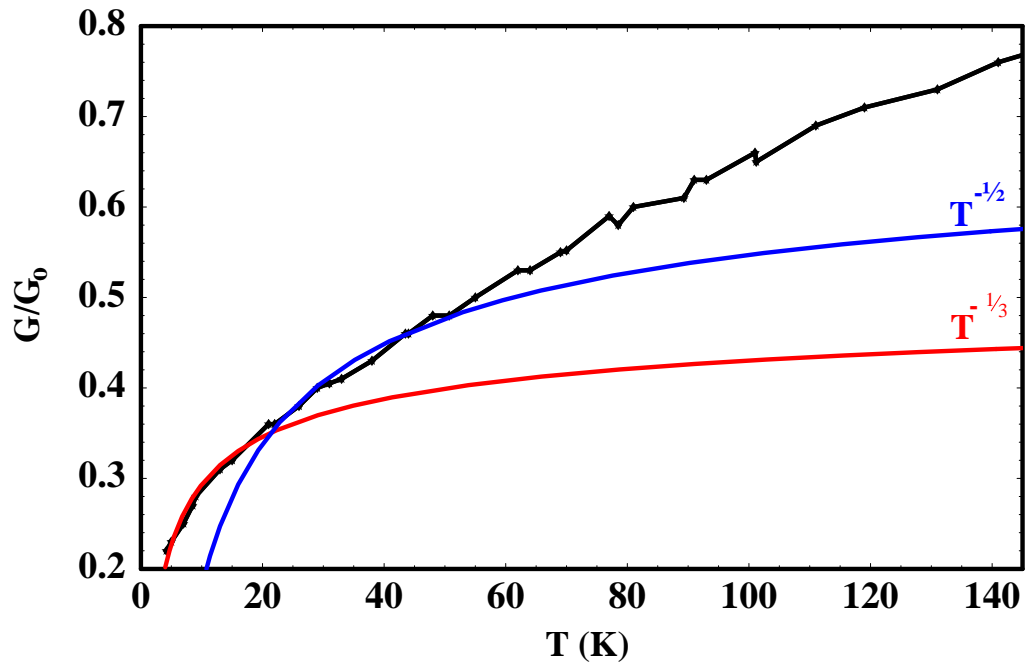


Figure F.6. A plot of  $G/G_o$  versus  $T$  for sample No. 29 with least-squares fits to the data. The red curve was fit to the data below 10K using a  $T^{-1/3}$  dependence and the blue curve was fit in the region of  $\sim 20$ –60 K using a  $T^{-1/2}$  dependence.

No. 29:  $G_* = 0.01 G_o$ ,  $d = 15$  nm,  $N = 45$ , and  $T_c = 0.3$  K,

No. 66:  $G_* = 0.45 G_o$ ,  $d = 25$  nm,  $N = 50$ , and  $T_c = 0.5$  K.

The value of  $T_c$  in zero magnetic field was found in another study to be 0.3 K, [40] thus these values are consistent with previous results. The parameters  $d$  and  $N$  cannot be uniquely determined since only their product enters Eqn. F.8 and we have no way of knowing the diameter of the individual MWNT layers, nor the precise outer diameter of the individual MWNT. However, the values listed are not unreasonable for our samples.

The essential result from the above analyses is that both 1D and 2D weak localization fit the conductance data at low temperatures, which is the region that the theories are applicable, as phase-breaking mechanisms decrease with temperature (i.e., phonon scattering). To fully exclude weak localization as a possible model requires magneto-resistance (MR) data, which we do not have at this time. In lieu of

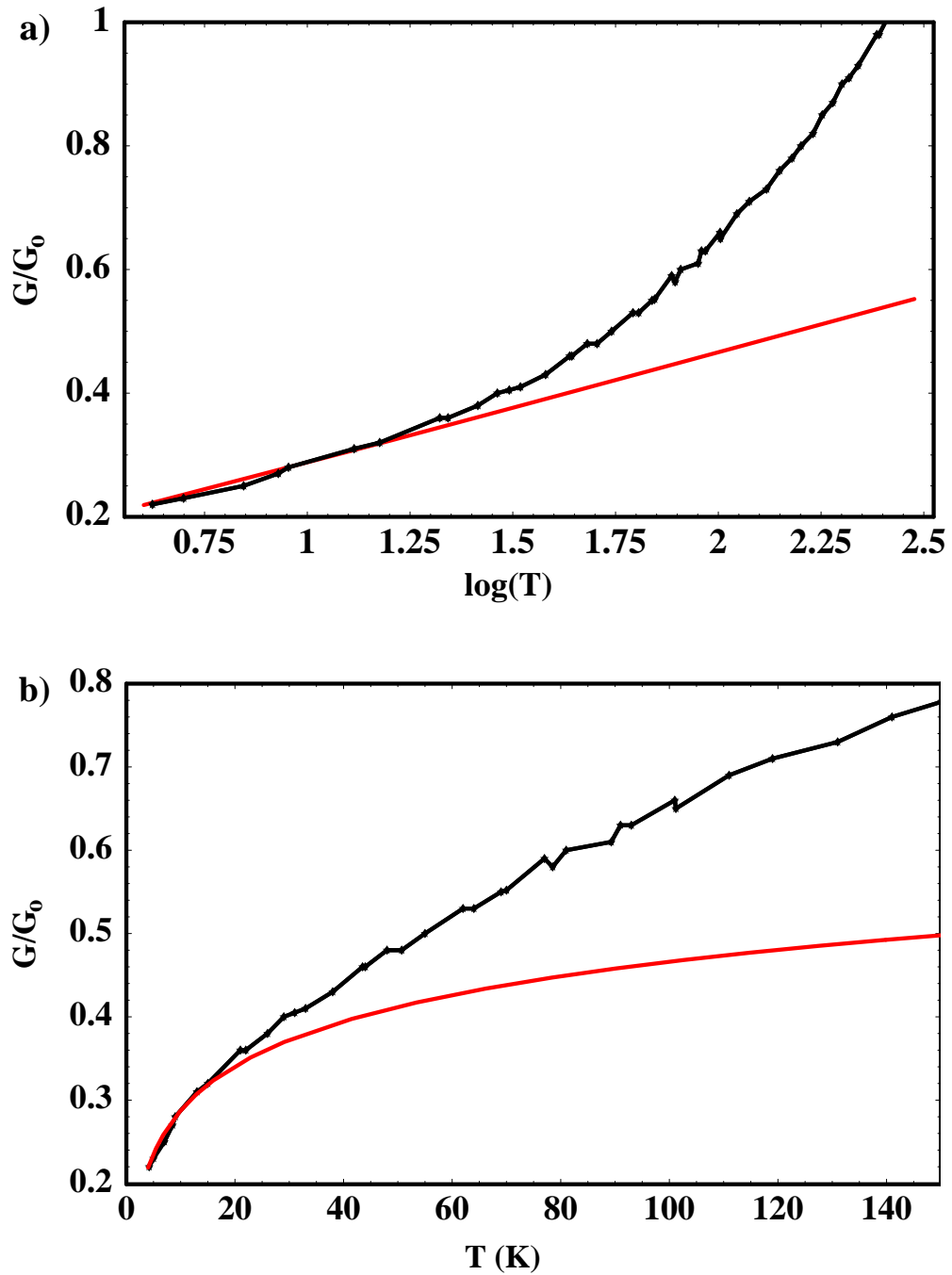


Figure F.7. a) A plot of  $G/G_0$  versus  $\log(T)$  with a fit to the low temperature data for sample No. 29. In b) we show the same fit on a plot of  $G/G_0$  versus  $T$ . The parameters used in the fits are discussed in the text.

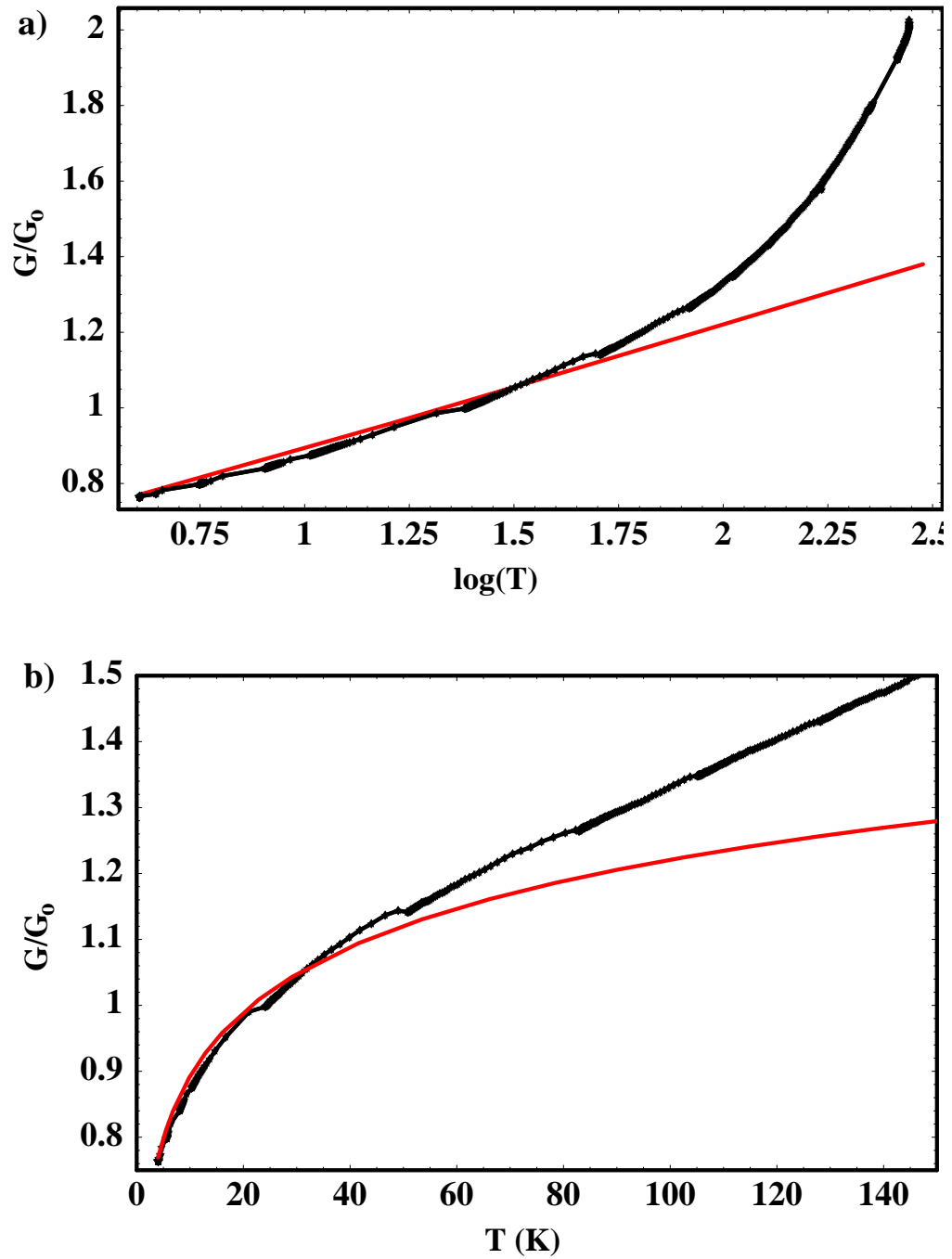


Figure F.8. In a) we plot  $G/G_0$  versus  $\log(T)$  with a fit to the low temperature data for sample No. 66. Figure b) shows the same fit of a linear scale. The parameters used in the fits are discussed in the text.

MR data, we have the voltage dependence of the conductance, which shows behavior consistent with the Luttinger model. To our knowledge the only voltage dependence of the weak localization model stems from electron heating at high current values. However, our  $I(V)$  data show non-linear behavior even at low bias. Also, it is not clear what the magnetic field dependence of a Luttinger liquid would be. Thus, the MR data would have to display Aharonov-Bohm oscillations, the signature of weak localization, and not simply a positive or negative MR. Aharonov-Bohm oscillations have been reported for MWNTs, which demonstrates that the theory is applicable in certain cases. [104] Shea *at al.* have also reported data supporting 1D weak localization and strong localization. [103] Interestingly, they also reported a voltage dependence for the low temperature conductance, which they ascribed to Luttinger liquid behavior. Thus, it is not clear that weak localization and Luttinger liquid theories are incompatible. Presumably, in any given sample both transport mechanisms are present and it becomes a question of the dominant mechanism. More work is needed to ascertain why one mechanism dominates in one instance and not in another.

## Appendix G: Mathematica Routine for Least-squares Fits

This Appendix contains the *Mathematica* code for the routine to find the least-squares fit to the nanotube conductance data. The routine below was used for sample No. 34. The object `t34k4ave` is an array of voltage and conductance data for sample No. 34 at 4 K. The functions `ETA` and `Gtotal` were pre-defined and are given by Eqns. 5.10 and 5.8, respectively. The routine loops through the specified fitting parameters: `A` (the overall coefficient  $A$  of Eqn. 5.3), `alpha` (the exponent  $\alpha$  in Eqn. 5.3), and `Gnt` (the nanotube conductance  $G_{NT}$  in Eqn. 5.8). For each set of parameters, the `While` loop calculates  $\eta$  (Eqn. 5.10) self-consistently, at each voltage point. Thus, this routine results in a least-squares fit which is completely self-consistent. The  $\eta$  values at each voltage are stored in the `HHH` array. The conductance, calculated at each voltage value with the value of  $\eta$  for that voltage, is stored in the array `tmpGtotlist`. The difference between the fit and the data at each voltage point is stored in the list `gvdif`, which is then squared and summed. The same is done for the low temperature conductance at zero-bias. When a fit is within the specified tolerance, it is appended to `t34results`. When the parameter loops are finished, `t34results` is sorted according to the sum of the squared difference of the conductance versus voltage fits.

```
(* Define results list column headers and tables. *)
(* HHH stores V and \[Eta]. *)
t34results = {{0.0, "sumlogsq", "lowgvdif", "highgvdif", "Gnt", "A",
  "\[Alpha]", "\[Eta]", "dif"}};
HHH = Table[0, {i, 126}, {j, 2}];
tmplog = Table[0, {i, 7}]; loggtdif = Table[0, {i, 7}];
(* Start loops : First A, then \[Alpha], then Gnt. *)
For[A = 0.79, A < 1.0, A += 0.01;
  {
  Print["A = ", A],
  For[alpha = 0.39, alpha < 0.6, alpha += 0.01;
    {
    For[Gnt = 0.39, Gnt < 0.55, Gnt += 0.01;
      {
      (* For the given values of A, \[Alpha], Gnt, *)
      (* calculate \[Eta] self-consistently at each V value. *)
      For[i = 0, i < 126, i++;
        {
        HHH[[i, 1]] = t34k4ave[[i, 1]],
        dif = 0.5, eta = 0.5, j = 0,
```



VITA

## VITA

Elton D. Graugnard was born in Port Hueneme, California, on April Fool's Day, 1974. Nine days later he moved to Mobile, Alabama, where he lived until 1980. From 1980 to 1990 he lived in south Louisiana, the crawfish captial of the world. There he lived in his great-grandmother's house on the Bayou Teche in the small farm town of Parks. In 1986, he moved to Baton Rouge, where he lived for four years while his parents were in professional schools. In 1990 he moved to Shreveport in the northwest corner of Louisiana.

Elton attended Centenary College of Louisiana in Shreveport, where he met Melanie J. Mendenhall, a small town Oklahoma girl. Elton graduated from Centenary in May, 1996 with a B.S. in Physics. He began graduate school in physics at Purdue University in June of 1996. In May, 1998 he received his M.S. in physics.

On June 12, 1999 Elton and Melanie were married in All Souls' Episcopal Church, Oklahoma City, Oklahoma.